

ABSTRACT

LI, ANG. Evaluation of Laminated Hull Material for High Altitude Airship. (Under the direction of Dr. Abdel-Fattah M. Seyam and Dr. Philip D. Bradford).

High altitude airship, being able to hover at a stationary position 20 *km* away from the ground for extended time, are extremely useful for multitude of applications. Yet, with tremendous interests in the development of these airships, the past attempts failed. The development of hull materials being able to survive the complicated high-altitude environment is extremely challenging task.

In this work, a multilayer laminate envelope from carefully selected constituents (fiber reinforcement, adhesives, and weathering materials) for stratospheric airship with highest strength-to-weight ratio produced so far and high gas barrier property were successfully produced. By characterizing all different properties required for high altitude applications, these constituents were proved advantageous over state-of-art materials found in the literature regarding strength and gas permeability. To continue modifying current structure and obtain a more comprehensive understanding of the laminate adhesion mechanism, a parametric study of the lamination process involving process parameters i.e. temperature and speed, as well as different reinforcement fabric structures was conducted. Various mechanical testing and helium permeation testing were carried out. It was found (1) in the lamination process temperature has a more significant impact on adhesion improvement and (2) woven fabrics formed with flat yarns is preferable to reach strong bonding in the multilayer laminate structure. Subsequently, the best candidate laminates produced using woven fabric from flat Zylon® yarn at a temperature of 215 °C and with a dwell time in the heated zone for 2.1 *s* were then taken for seaming evaluation. For comparison purpose, a

commercially produced similar structured laminate with a proprietary adhesive was also used for seaming study.

The creep resistance performance of the butt seam with different overlap and underlap combinations was assessed. It was determined that double side butt seam can significantly improve the creep resistance performance in comparison with single side butt seam. Yet, with given overlap length, longer underlap length does not necessarily lead to better creep resistance performance. For the laminate with a proprietary adhesive, the issue of yarn pull-out was identified as the major reason for seam failure in creep test. However, EVOH (Ethylene Vinyl Alcohol) adhesive laminate exhibited strong adhesion within the laminate to prevent the yarns from being pulled out. With the use of EVOH adhesives, the duration of the creep test went almost ten times higher.

Extremely low helium permeability was achieved by the laminated fabric made in the lamination parametric study, being two orders of magnitude lower than the required number from the industry. Helium permeation modelling is thus crucial to understand the mechanism of gas blocking and may help in laminate material selection and reduce/eliminate unnecessary expensive trials. A modified ideal laminate theory combining the coverage and pinhole models was used to effectively evaluate the helium permeation. It was also proved that the lamination process considerably promoted the helium barrier property because the melted adhesive flowed into and filled the pinholes in the VDA coating to effectively hinder the permeation of helium gas molecules.

© Copyright 2018 Ang Li

All Rights Reserved

Evaluation of Laminated Hull Material for High Altitude Airship

by
Ang Li

A dissertation submitted to the Graduate Faculty of
North Carolina State University
in partial fulfillment of the
requirements for the degree of
Doctor of Philosophy

Fiber and Polymer Science

Raleigh, North Carolina

2018

APPROVED BY:

Dr. Abdel-Fattah Seyam
Co-Chair of Advisory Committee

Dr. Philip D. Bradford
Co-Chair of Advisory Committee

Dr. Xiangwu Zhang

Dr. Mohammed A. Zikry

DEDICATION

This work is dedicated to my parents and grandparents. Growing up in such a family full of love and happiness, I feel so spoiled in my life growing up. Their cherishing and nourishing inspire and encourage me to chase my dream in whatever situations. Their comfort and understanding sustain me through the valleys in my life journey.

To my beloved wife Yalin Zhang, who is my No.1 supporter and always willing to listen to my crazy thoughts and complaints. She is more than my wife, but the closest friend, my soul mate and my spiritual companion.

To my dear Lord, for His mercy and grace, the everlasting love and overflowing life.

BIOGRAPHY

Ang Li was born in Xuancheng, China, in 1991. He grew up in a beautiful small town, attended local middle and high schools, and graduated from Jingde high school in 2008. The same year, Ang was enrolled in Anhui Polytechnic University where he spent four years of his college life in the city of Wu Hu. College education opened his eyes and helped Ang develop his interest in science and engineering. Therefore, after obtaining a B.S. degree in Textile Engineering, he continued his pursuit of a M.S. degree in the College of Textiles at North Carolina State University starting from 2012 fall. With the advisory of Dr. Philip Bradford, Ang successfully completed his Master's Thesis on the topic of CNT strain sensor in 2014. Being passionate about scientific research and open to all kinds of challenges, Ang took an opportunity to continue his education pursuing a Ph.D. degree in Fiber and Polymer Science, at the College of Textiles, North Carolina State University. Since then, he has been working on an amazing project developing high altitude airship materials under the advisory of Dr. Abdel-Fattah Seyam and Dr. Philip Bradford. After graduation, Ang is planning to seek for a career in the US, in a textile related industry that involves product development and innovative research.

ACKNOWLEDGMENTS

I would first owe my sincerest gratitude to my advisor, Dr. Abdel-Fattah M. Seyam, for his guidance and intellect in research and for always inspiring and trusting in me. He trained me to conduct good research work and helped me build a thoughtful mind. I am so grateful for his dedication of time and energy directing and keeping me on track all the way to the final goal of my research. His revisions and comments on my dissertation are definitely inspiring and indispensable for the completion of the whole research work.

I would like to extend my thanks to other members of my committee: Dr. Philip Bradford, Dr. Xiangwu Zhang, Dr. Mohammed A. Zikry and Dr. Andre Mazzoleni for serving on my Ph.D. Advisory Committee. Their inputs to my research surely make this work a better one.

I would like to give special thanks to Rahul Vallabh and Prateeti Ugale for their helpful discussions and great help with the experimental work. You are the best coworkers to work with.

I would also like to thank David Kim and SCEYE S.A. for giving me an opportunity to be part of a great project and sponsor me financially to complete my PhD. degree.

TABLE OF CONTENTS

LIST OF TABLES.....	ix
LIST OF FIGURES	xiv
1 Introduction and Background	1
1.1 Stratospheric Airship Applications – Significance.....	1
2 Literature Review	13
2.1 Load-Bearing Component.....	13
2.1.1 High Performance Fibers.....	13
2.1.2 Structures of Load-bearing Textile Fabrics	19
2.2 Gas retention layer.....	23
2.2.1 Polymeric Films	24
2.3 Weathering Layer	26
2.3.1 Ultraviolet (UV) Radiation	28
2.3.2 Ozone and Atomic Oxygen Degradation	32
2.3.3 Temperature.....	33
2.4 Adhesives	35
2.4.1 Lamination of Hull Material	35
2.4.2 Seaming of Hull Material.....	40
2.5 Evaluations of Laminated Envelope Materials	45
2.5.1 Mechanical Characterizations.....	48
2.5.2 Gas Permeability Characterization	64
3 Motivation and Research Objectives.....	81
4 Preliminary Work	84

5	Experimental	85
5.1	Materials	85
5.1.1	High Performance Fibers.....	86
5.1.2	Functional Polymeric Thin Films and Coatings.....	87
5.1.3	Adhesives.....	89
5.2	Experimental Design.....	90
5.2.1	Lamination Parametric Study.....	90
5.2.2	Seam Evaluation	92
5.2.3	Helium Permeation Study.....	94
5.3	Laminate Fabrication	95
5.4	Seam Formation	96
5.5	Testing and Evaluation	98
5.5.1	T-peel Test.....	98
5.5.2	Tensile Test	100
5.5.3	Tear Test	102
5.5.4	Helium Permeation Test.....	103
5.5.5	Creep Test.....	106
6	Results and Discussions	107
6.1	Lamination Parametric Study	107
6.1.1	Main Effects of Lamination Parameters on Tensile Property.....	108
6.1.2	Main Effects of Lamination Parameters on Peel Property	113
6.1.3	Main Effects of Lamination Parameters on Tear Property	119
6.1.4	Main Effects of Lamination Parameters on Gas Barrier Property ...	146

6.1.5	Conclusion	149
6.2	Seam Evaluation.....	150
6.2.1	Parametric Study of Seaming.....	150
6.2.2	Effect of Seam Configuration on Tensile Property.....	156
6.2.3	Seam Creep Properties.....	158
6.2.4	Conclusion	171
6.3	Helium Permeation Study	171
6.3.1	Helium Permeation Model of Flexible Composite Laminate	171
6.3.2	Experimental Verification of the Models.....	177
6.3.3	Conclusion	179
7	Overall Summary.....	180
REFERENCES.....		182
APPENDICES		188
Appendix A Preliminary Work		189
A.1	Concept of Design	189
A.2	Laminate Fabrication	190
A.3	Laminate Prototype Development.....	192
A.4	Characterizations	195
A.4.1	Laminate Tensile Strength.....	195
A.4.1.1	Effect of Thermal and UV Weathering	197
A.4.2	Laminate Tear Strength.....	200
A.4.3	Laminate Creep Resistance.....	201
A.4.4	Helium permeation	202

A.4.5 Ozone Resistance.....	204
A.5 Summary.....	205
Appendix B Statistical analysis of laminate tensile test in warp direction for lamination parametric study	207
Appendix C Statistical analysis of laminate tensile test in weft direction for lamination parametric study	212
Appendix D Statistical analysis of T-peel test for lamination parametric study .	217
Appendix E Statistical analysis of laminate tear test in warp direction for lamination parametric study	221
Appendix F Statistical analysis of laminate tear test in weft direction for lamination parametric study	225
Appendix G Statistical analysis of varied laminate adhesion levels for lamination parametric study	229
Appendix H Statistical analysis of peel strength for seaming parametric study .	230
Appendix I Statistical analysis of tensile strength of butt seams with different seam configurations	234

LIST OF TABLES

Table 1.1	Stratospheric Airship Hull Material Design Considerations (Zhai & Euler 2005)	9
Table 2.1	High Performance Fibers Comparison (Zhai & Euler 2005).....	19
Table 2.2	Desirable Environmental Protective and Gas Holding Polymeric Materials (Zhai & Euler 2005).....	24
Table 2.3	Material Surface Thermal Properties (Zhai & Euler 2005)	34
Table 2.4	Fabric configurations and corresponding properties (Miller & Mandel 2000)	46
Table 2.5	Sample Testing for Airship Hull Materials (Miller & Mandel 2000)	48
Table 2.6	Detailed Structural Information of Laminate Materials developed in the Literature (Komotsu et al. 2003; Maekawa et al. 2008; Mcdaniels et al. 2009; Kang et al. 2006; Gu 2007; Xu 2009; Li et al. 2010)	52
Table 5.1	Specifications of woven fabrics	86
Table 5.2	Typical properties of Polyimide film (50 DE Plasma MBS Kapton/DB25).....	87
Table 5.3	Typical properties of Polyethylene terephthalate film (DE025)	88
Table 5.4	Typical properties of EVOH film (EF-F grade).....	89
Table 5.5	Properties of EXF-951 TPU film adhesive	90
Table 5.6	Designs of experiment for lamination parametric study	92
Table 5.7	Experimental design for seaming parameter study	94
Table 6.1	Sample IDs and their variable parameters of lamination parametric study	107
Table 6.2	Laminate tensile test results	110
Table 6.3	Peel strength of laminate.....	115
Table 6.4	Laminate tear test results	138
Table 6.5	GTR results of selective laminate samples	147
Table 6.6	Peel strength of seams.....	153
Table 6.7	Extrapolation results of laminate creep test	160
Table 6.8	Extrapolation results of the creep test of BS 10.16-0	167
Table 6.9	Extrapolation results of the creep test for BS 10.16-3.81	169
Table 6.10	Helium Permeation Results for Modelling	178
Table A.1	Tensile Strength of laminate prototypes P4, P9, and P10	196

Table A.2	Tear Strength of laminate prototypes P4 and P9	201
Table A.3	Helium permeability of laminate prototype P3 and P4.....	202
Table A.4	Helium Permeability of Modified Laminate Prototype.	203
Table A.5	Ozone resistance testing results	205
Table B.6	Between subject-effects on tensile strength – Analysis of Variance.....	207
Table B.7	Between subject-effects on tensile strength – Effect Tests	207
Table B.8	ANOVA of fabric effect on tensile strength.....	208
Table B.9	Means for one-way ANOVA – Estimates of fabric effect on tensile strength .	208
Table B.10	Tukey-Kramer HSD post hoc test of fabric effect on tensile strength	208
Table B.11	ANOVA of temperature effect on tensile strength	209
Table B.12	Calculated means for one-way ANOVA – Estimates of temperature effect on tensile strength	209
Table B.13	Tukey-Kramer HSD post hoc test of temperature effect on tensile strength ...	209
Table B.14	ANOVA of dwell time effect on tensile strength	210
Table B.15	Calculated means for one-way ANOVA – Estimates of dwell time effect on tensile strength	210
Table B.16	Tukey-Kramer HSD post hoc test of dwell time effect on tensile strength	210
Table D.17	ANOVA of simple effects on tensile strength	211
Table D.18	Tukey-Kramer HSD post hoc test of simple effects on tensile strength	211
Table C.1	Between subject-effects on tensile strength – Analysis of Variance.....	212
Table C.2	Between subject-effects on tensile strength – Effect Tests	212
Table C.3	ANOVA of fabric effect on tensile strength.....	213
Table C.4	Calculated means for one-way ANOVA – Estimates of fabric effect on tensile strength	213
Table C.5	Tukey-Kramer HSD post hoc test of fabric effect on tensile strength	213
Table C.6	ANOVA of temperature effect on tensile strength	214
Table C.7	Calculated means for one-way ANOVA – Estimates of temperature effect on tensile strength	214
Table C.8	Tukey-Kramer HSD post hoc test of temperature effect on tensile strength ...	214
Table C.9	ANOVA of dwell time effect on tensile strength	215

Table C.10	Calculated means for one-way ANOVA – Estimates of dwell time effect on tensile strength	215
Table C.11	Tukey-Kramer HSD post hoc test of dwell time effect on tensile strength	215
Table C.12	ANOVA of simple effects on tensile strength	216
Table C.13	Tukey-Kramer HSD post hoc test of simple effects on tensile strength	216
Table D.1	Between subject-effects on peel strength – Analysis of Variance.....	217
Table D.2	Between subject-effects on peel strength – Effect Tests.....	217
Table D.3	ANOVA of fabric effect on peel strength.....	218
Table D.4	Means for one-way ANOVA – Estimates of fabric effect on peel strength	218
Table D.5	Tukey-Kramer HSD post hoc test of fabric effect on peel strength.....	218
Table D.6	ANOVA of temperature effect on peel strength.....	219
Table D.7	Means for one-way ANOVA – Estimates of temperature effect on peel strength.....	219
Table D.8	Tukey-Kramer HSD post hoc test of temperature effect on peel strength.....	219
Table D.9	ANOVA of dwell time effect on peel strength	220
Table D.10	Means for one-way ANOVA – Estimates of dwell time effect on peel strength.....	220
Table D.11	Tukey-Kramer HSD post hoc test of dwell time effect on peel strength	220
Table E.1	Between subject-effects on tear strength – Analysis of Variance	221
Table E.2	Between subject-effects on tear strength – Effect Tests.....	221
Table E.3	ANOVA of fabric effect on tear strength	222
Table E.4	Means for one-way ANOVA – Estimates of fabric effect on tear strength.....	222
Table E.5	Tukey-Kramer HSD post hoc test of fabric effect on tear strength	222
Table E.6	ANOVA of temperature effect on tear strength.....	223
Table E.7	Means for one-way ANOVA – Estimates of temperature effect on tear strength.....	223
Table E.8	Tukey-Kramer HSD post hoc test of temperature effect on tear strength.....	223
Table E.9	ANOVA of dwell time effect on tear strength.....	224
Table E.10	Means for one-way ANOVA – Estimates of dwell time effect on tear strength.....	224
Table E.11	Tukey-Kramer HSD post hoc test of dwell time effect on tear strength.....	224

Table F.1	Between subject-effects on tear strength – Analysis of Variance	225
Table F.2	Between subject-effects on tear strength – Effect Tests.....	225
Table F.3	ANOVA of fabric effect on tear strength	226
Table F.4	Means for one-way ANOVA – Estimates of fabric effect on tear strength.....	226
Table F.5	Tukey-Kramer HSD post hoc test of fabric effect on tear strength	226
Table F.6	ANOVA of temperature effect on tear strength.....	227
Table F.7	Means for one-way ANOVA – Estimates of temperature effect on tear strength.....	227
Table F.8	Tukey-Kramer HSD post hoc test of temperature effect on tear strength.....	227
Table F.9	ANOVA of dwell time effect on tear strength.....	228
Table F.10	Means for one-way ANOVA – Estimates of dwell time effect on tear strength.....	228
Table F.11	Tukey-Kramer HSD post hoc test of dwell time effect on tear strength.....	228
Table G.1	Chi-Square test for correlation of adhesion level and fabrics	229
Table G.2	Chi-Square test for correlation of adhesion level and temperature.....	229
Table G.3	Chi-Square test for correlation of adhesion level and dwell time.....	229
Table H.1	Between subject-effects on seam peel strength – Analysis of Variance	230
Table H.2	ANOVA of temperature effect on seam peel strength.....	231
Table H.3	Calculated means for one-way ANOVA – Estimates of temperature effect on seam peel strength	231
Table H.4	Tukey-Kramer HSD post hoc test of temperature effect on seam peel strength.....	231
Table H.5	ANOVA of seaming pressure effect on seam peel strength	232
Table H.6	Means for one-way ANOVA – Estimates of seaming pressure effect on seam peel strength.....	232
Table H.7	Tukey-Kramer HSD post hoc test of seaming pressure effect on peel strength of the seams.....	232
Table H.8	ANOVA of seaming speed effect on seam peel strength	233
Table H.9	Means for one-way ANOVA – Estimates of seaming speed effect on seam peel strength	233

Table H.10	Tukey-Kramer HSD post hoc test of seaming speed effect on peel strength of the seams.....	233
Table I.1	ANOVA of seaming speed effect on seam peel strength	234
Table I.2	Tukey-Kramer HSD post hoc test of seaming speed effect on seam peel strength.....	234

LIST OF FIGURES

Figure 1.1.	HAA Line-of-Sight Radius	2
Figure 1.2.	Typical Annual Winds Aloft (Jamison et al. 2005).	5
Figure 1.3.	Typical non-rigid airship design (Liao & Pasternak 2009).	7
Figure 1.4.	Layout of typical laminated flexible composite (Islam & Bradley 2012).	10
Figure 2.1.	Timeline of Performance Textile Fiber Development (Zhai & Euler 2005).....	14
Figure 2.2.	Magnified Image of Woven Polyester and Crimp Diagram. Tensile loading of woven fabric induces transverse loads at thread overlap intersections due to straightening of crimped fibers (McDaniels et al. 2009).	22
Figure 2.3.	(a) Comparative Stress-Strain of materials with and without creep; (b) Conceptual Drawing of non-crimp fabric (McDaniels et al. 2009).....	22
Figure 2.4.	Layer composition of Z2929T-AB (Maekawa et al. 2008).....	29
Figure 2.5.	Residual strength of Z2929T-AB material and its joint after accelerated UV and Ozone exposure (Maekawa et al. 2008).	30
Figure 2.6.	Test panels mounted on top of an outdoor exposure rack facing the south (Nakadate et al. 2011).	31
Figure 2.7.	Summary of supplemental outdoor exposure test, effects of an additional protection layer, humidity, and temperature (Nakadate et al. 2011).	31
Figure 2.8.	Tensile strength of Z2929T-AB and its joints in warp and weft direction (Maekawa et al. 2008).....	34
Figure 2.9.	Interfacial tensions and the static contact angle (https://www.kruss.de/services/education-theory/glossary/contact-angle/).	38
Figure 2.10.	Typical seam designs for airship hull materials (Islam & Bradley 2012).	41
Figure 2.11.	(a) Zeppelin LZ N07, (b) Envelope Material (Miller & Mandel 2000).....	46
Figure 2.12.	Comparison of the tensile strength and weight of the laminate materials developed in the literature (Komotsu et al. 2003; Maekawa et al. 2008; McDaniels et al. 2009; Kang et al. 2006; Gu 2007; Xu 2009; Li et al. 2010)....	50
Figure 2.13.	Comparison of the strength-to-weight ratio of the laminate materials developed in the literature (Komotsu et al. 2003; Maekawa et al. 2008; McDaniels et al. 2009; Kang et al. 2006; Gu 2007; Xu 2009; Li et al. 2010)....	50

Figure 2.14. Tensile stress-strain curve of Vectran® fabric incorporated envelope material (Kang et al. 2006)	54
Figure 2.15. Tensile test results at various temperatures (Kang et al. 2006).	55
Figure 2.16. SEM image of failed specimens: (a) delamination and (b) fiber breakage (Meng et al. 2016).....	55
Figure 2.17. Measured force-displacement curves of the uni-axial tensile tests; (a) global curve and (b) magnification at the low strain range (Meng et al. 2016).....	56
Figure 2.18. The stress-strain model of the coated fabric (Chen et al. 2014).	57
Figure 2.19. Cut slit tear test (Maekawa et al. 2008).	58
Figure 2.20. Pressurized cylinder test specimen (Maekawa et al. 2008).	59
Figure 2.21. Schematic of ILC cylinder (Miller & Mandel 2000).....	60
Figure 2.22. Stress vs. Cut slit length: compatibility of Thiele's formula with test data (Miller & Mandel 2000).....	61
Figure 2.23. Allowable slit size of the technology demonstrator (Maekawa et al. 2008).	62
Figure 2.24. Comparison between experimental data and the theoretical values for uni- axial specimens (a) the warp specimens and (b) the weft specimens (F. X. Wang et al. 2016).	63
Figure 2.25. A schematic of the basic permeation mechanism of a barrier material (Duncan et al. 2005).....	65
Figure 2.26. Effect of temperature on the permeation of oxygen through PET film (Auras et al. 2004).	69
Figure 2.27. Effect of temperature on water vapor diffusion in an epoxy adhesive seam (Gledhill et al. 1980).	70
Figure 2.28. Effect of tensile stress on oxygen permeability of various plastic films (Boersma et al. 2003).	71
Figure 2.29. Diffusion in multi-layer structures with interfaces (i) through thickness, in series: interfaces won't affect the overall property if they cannot provide an additional barrier; (ii) along layers, in parallel: diffusion possible between layers and along interfaces (Duncan et al. 2005).	72
Figure 2.30. Geometrical configuration and microstructure of flexible film-fabric laminated composites (Yao et al. 2011).	77

Figure 2.31. An example of representative volume element (RVE) of plain woven structure (Yao et al. 2012).....	79
Figure 5.1. Laminate structural and material design	85
Figure 5.2. Pratix OK-12L Seamless Teflon Belt Drum Laminator (http://practix-usa.com/heat-transfer-machines/laminating-machines/).....	96
Figure 5.3. (a) Schematic of continuous fusing machine and (b) Images of the fusing machine showing the seaming process.	97
Figure 5.4. A schematic of butt seam with detailed material and structure description.....	98
Figure 5.5. Test panel and specimen for T-peel test (ASTM 2015a).....	98
Figure 5.6. MTS Q-Test/5 Universal Testing Machine (https://textiles.ncsu.edu/zte/physical-testing-laboratory/mts-q-test5-universal-testing-machine-212x375/).	99
Figure 5.7. MTS Landmark servo hydraulic 250 kN testing machine.	101
Figure 5.8. Schematic diagram of a cut-slit tear specimen.	102
Figure 5.9. The Labthink® PERME® VAC-V2 gas permeability tester (http://en.labthink.com/en-us/product/vac-v2-gas-permeability-tester.html). .	104
Figure 5.10. Schematic of pressure differential method utilized in the Labthink® PERME® VAC-V2 gas permeability tester (http://en.labthink.com/en-us/product/vac-v2-gas-permeability-tester.html).	104
Figure 6.1. Typical Stress vs. strain curves of laminates in warp and weft directions.....	108
Figure 6.2. Typical modes of failure after tensile test	110
Figure 6.3. Main effects of (a) Fabric types, (b) Temperature and (c) Dwell time on tensile strength of laminate in warp and weft directions; (d) Tensile strength of pure fabrics in warp and weft direction.	112
Figure 6.4. Specimens failed after T-peel test with different mode of failure on PI film... 114	
Figure 6.5. Main effects of (a) Fabric types, (b) Temperature and (c) Dwell time on peel strength/resistance of laminate.	117
Figure 6.6. Typical load vs. displacement curve of a laminate central slit tear testing specimen (a commercial laminate sample from production line).	120
Figure 6.7. (a) Central slit tear test specimen gripped on the MTS machine, (b) The slit opening process.....	122

Figure 6.8. Typical tear propagation process of central slit tear testing specimen under uni-axial tensile loading.....	123
Figure 6.9. Images of the failed commercial laminate sample from production line after tear test	126
Figure 6.10. The Load-displacement curve of a typical brutal failure of a central slit laminate specimen with excellent adhesion.....	127
Figure 6.11. Brutal failure of laminate tear test specimen.....	128
Figure 6.12. The Load-displacement curve of a typical immediate tear propagation of a central slit laminate specimen with good adhesion.....	129
Figure 6.13. An image showing progressive failure of laminate tear test specimen with immediate tear propagation.....	130
Figure 6.14. The Load-displacement curve of a typical delayed tear propagation of a central slit laminate specimen with fair adhesion.....	131
Figure 6.15. An image showing progressive failure of laminate tear test specimen with delayed tear propagation.....	132
Figure 6.16. The Load-displacement curve of a typical principal yarn pull-out of a central slit laminate specimen with poor adhesion.....	133
Figure 6.17. An image showing progressive failure of laminate tear test specimen with principal yarn pull-out.....	134
Figure 6.18. The Load-displacement curve of a typical principal yarn pull-out of a central slit laminate specimen with poor adhesion.....	135
Figure 6.19. (a) Typical Load-Displacement curve of central slit specimen of pure fabric (b) Zylon® fabric failed due to shear.....	136
Figure 6.20. An image showing progressive failure of laminate tear test specimen with fabric shear deformation.....	137
Figure 6.21. Main effects of (a) Fabric types, (b) Temperature and (c) Dwell time on tear strength/resistance of laminate.....	140
Figure 6.22. Contingency tables correlating adhesion levels with (a) Fabrics, (b) Temperature and (c) Dwell Time.....	143
Figure 6.23. Effects of temperature, dwell time, and fabric type on the helium permeation of laminate.....	148

Figure 6.24. Testing samples for T-peel test to determine the adhesive bonding strength ..	151
Figure 6.25. T-peel test (a) adhesive failure, (b) adhesive layer fractured and (c) VDA coating peeled off from laminate and PI film delaminated from both VDA coatings (highlighted in the dashed rectangles).	152
Figure 6.26. Typical load-to-displacement curve of T-peel test.....	153
Figure 6.27. Main effects of seaming temperature, pressure and speed on peel strength of seamed samples.....	154
Figure 6.28. Peel strength of all eight seamed samples.	155
Figure 6.29. Tensile strength of butt seams made in different geometrical configurations..	157
Figure 6.30. (a) Butt seam samples for tensile testing, (b) fractured butt seam samples after tensile testing.	158
Figure 6.31. Creep strain and stress curves of a laminate sample.	159
Figure 6.32. A typical curve for creep test of butt seam specimen.	160
Figure 6.33. Effect of underlap length on time to failure of creep test for <i>10.16 cm</i> overlap butt seams.....	161
Figure 6.34. Failure analysis after creep test of (a) BS 10.16-0, (b) BS 10.16-5.08, (c) BS 10.16-7.62 and (d) BS 10.16-10.16.....	162
Figure 6.35. Effect of underlap length on creep resistance property for <i>12.7 cm</i> overlap butt seams.....	164
Figure 6.36. Failure analysis after creep test of (a) BS 12.7-0 and (b) BS 12.7-2.54.....	165
Figure 6.37. Creep strain and stress curves of sample BS 10.16-0 under a static load of <i>303 N/cm</i>	166
Figure 6.38. Creep strain and stress curves of sample BS 10.16-3.81 under a static load of <i>303 N/cm</i>	168
Figure 6.39. Creep strain extrapolation of sample BS 10.16-3.81 with correct curve fitting after data deduction.	169
Figure 6.40. A schematic of the three typical model types for gas permeability: (a) Ideal laminate theory, (b) Coverage model and (c) Pinhole model (Bishop 2015)..	172
Figure 6.41. A schematic of multilayer structure of the laminate material for ILT.....	174
Figure 6.42. A schematic of the gas flow in single side VDA coated PET film.	174
Figure 6.43. A schematic of double VDA coating affecting the gas flow.	175

Figure 6.44. A schematic of multilayer structure with detailed compositions of the laminate material for modified ILT	176
Figure A.1. General design concept of the laminate material	189
Figure A.2. Schematic of laminate between aluminum plates during hot press lamination	190
Figure A.3. Layer notations of the laminate fabricated on lab-scale lamination machine..	191
Figure A.4. Schematic design of laminate prototype P4.....	193
Figure A.5. Outside and inside of laminate prototype P4	193
Figure A.6. Schematic design of laminate prototype P9.....	194
Figure A.7. Outside and inside of laminate prototype P9	194
Figure A.8. Schematic design of laminate prototype P10.....	195
Figure A.9. Outside and inside of laminate prototype P10	195
Figure A.10. Comparison of the strength and weight of the new laminate prototypes and laminate materials developed in other studies	197
Figure A.11. Comparison of the strength-to-weight ratio of the new laminate prototypes and laminate materials developed in other studies	197
Figure A.12. Specimens mounted on metal frames for UV-Vis weathering.....	198
Figure A.13. Specimen frames mounted inside the weathering chamber of Atlas Ci 3000+ Weather-Ometer	199
Figure A.14. Comparison of tensile strength of prototypes before and after thermal exposure and accelerated UV-Vis weathering.....	199
Figure A.15. Strength loss after thermal exposure and accelerated UV-Vis weathering	200
Figure A.16. Example of cut-slit tear test load-displacement curve (prototype P9 weft)....	200
Figure A.17. Load-displacement curve of prototype subjected to a constant load of 1250 N.....	202
Figure A.18. Schematic design of modified laminate prototype.	203
Figure A.19. The schematic of the sample set-up of Ozone resistance exposure testing.	204

LIST OF ABRREVIATIONS

HAP	High Altitude Platform
LTA	Lighter-Than-Air
SSA	Stratospheric Airship
LEO	Low Earth Orbit
JAXA	Japan Aerospace Exploration Agency
FAA	Federal Aviation Administration
UHMWPE	Ultra High Molecular Weight Polyethylene
LCP	Liquid Crystal Polymer
PBO	Polybenzaxole
PET	Polyester
PI	Polyimide
EVOH	Ethylene Vinyl Alcohol
PVF	Polyvinylfluoride
PU	Polyurethane
TPU	Thermoplastic Polyurethane
TOR	Triton Oxygen Resistant
VDA	Vacuum Deposited Aluminum
CTE	Coefficient of Thermal Expansion
LPD	Liquid-Phase Deposition
ILT	Ideal Laminate Theory
RVE	Representative Volume Element
OFAT	One-Factor-At-a-Time

1 Introduction and Background

1.1 Stratospheric Airship Applications – Significance

The term High Altitude Platform (HAP) generally refers to an aircraft, usually unmanned airship, aerostat or airplane, positioned above an altitude of 20 *km*. It was established at the World Radiocommunication Conference 1997 (WRC-97), defined as a telecommunications station located at an altitude of 20 to 50 *km* and at a specified fixed-point relative to the Earth (D’Oliveira et al. 2016). This fact attracted a growing interest in HAP utilization as a complement to terrestrial and satellite-based communications networks. In the past two decades, great efforts have been made to explore the potential application of HAPs for extended surveillance and telecommunications support. Despite the fact that many projects all over the world were initiated, none of them had been successfully executed to the end. In 2014, two Internet giants Google and Facebook, announced investments in new HAP projects to provide Internet access in regions without communication infrastructure (terrestrial or satellite), bringing attention back to the development of HAPs.

Commercially, with efforts to expand high-bandwidth data services, manufacturers are motivated to develop HAPs to serve as an alternative to extremely expensive satellites for the same purpose. It is anticipated that they can play roles similar to those of artificial satellites. Generally, HAPs have the advantages of being closer to the ground for low propagation loss, shorter transmission distances for relaying ground-based communications, short transmission delay time (Komotsu et al. 2003) and the possibility of return for maintenance or payload reconfiguration (D’Oliveira et al. 2016).

Persistent surveillance from a fixed position is also an important need that HAPs can meet (Jamison et al. 2005), showing obvious advantage over low earth orbit satellites. Additionally,

being closer to the covered area permits better resolution images (Komotsu et al. 2003). The main issue in high altitude flight is generating lift in the rarefied atmosphere. The majority of the vehicles that operate at these altitudes do so by flying very fast (Colozza et al. 2005). Hence, flight at high altitude (say, over 70,000 feet) for extended periods (several days or more) is an extreme technical challenge for fixed wing aircrafts. However, Lighter-Than-Air (LTA) system, unlike fixed wing aircraft, do not need to stay in motion to remain aloft because they generate lift from buoyancy instead of through aerodynamics. In this arena, the LTA system (airship or aerostat) has great potential and is envisioned as a persistent eye-in-the-sky that can provide electronic and optical observation of a large country. For instance, from 21.3 km (70,000 ft.), an airship would have line-of-sight coverage of 325 miles and could almost cover the whole area in Texas shown in Figure 1.1.



Figure 1.1. HAA Line-of-Sight Radius

Moreover, an airship equipped with an efficient power storage system can maintain station at specific geographic location as well as move around to a new location and adjust the

body orientation accordingly (Colozza et al. 2005). These characteristics make LTA systems superb candidates for long-term high-altitude surveillance missions.

Another important application for HAP would be wide-field, high resolution optical and near-infrared imaging of astronomical targets. A reliable LTA system hovering at an altitude of 20 *km* or higher should be able to serve as an observatory to provide image quality competitive with space-based telescopes. The response times are short, and the operational cost are much lower than a comparable space-based telescope. Since at such a high altitude, the platform is above the weather and $\approx 95\%$ or more of the atmosphere (Fesen & Brown 2015). Being above the weather, it would experience virtually perfectly clear skies every night and could provide high data quality day and night as long as the platform remained at this altitude. Finally, a stratospheric astronomical observatory could also provide reliable science support for a host of space-based missions at an estimated cost of only a few percent of a conventional low earth orbit satellite (Fesen & Brown 2015).

LTA systems, being able to hover at a stationary position 20 *km* away from the ground for extended periods of time, make them very useful for many purposes. For example, 24-hour border surveillance, detection of oil spills and pirate ships in the ocean, reinforcement of GPS in high traffic areas, analysis of coastal erosion and monitoring of beach cleanliness can all be realized easily at such high altitude. Moreover, LTA systems can also be used as a cheaper alternative to satellites for meteorological analysis and natural disaster management. In this information era, the other huge impact of LTA systems, would be to enhance access to mobile internet service and serve as reinforcement of connection in deserted, difficult to access areas, facilitating globalization of internet connectedness. With so many potential benefits discussed, it is not surprising that many organizations around the world, commercial and military, are

interested in these systems or platforms. It was mentioned in a 2004 report (Jamison et al. 2005) that more than thirty companies were already involved in the development of commercially available airships and aerostats in many countries e.g. China, France, Germany, India, Japan, South Korea, Russia, United Kingdom, and the United States.

Generally, there are two basic types of LTA systems: either tethered (aerostat) or un-tethered (airship). The tethered high-altitude aerostat is operated from a fixed location. Lift is provided solely by a lifting gas, such as helium or hydrogen, which is contained in the envelope. The tether provides a structural link to the mooring system, power for the aerostat and payload, and secure command and communications. The tethered high-altitude aerostat is very power efficient, requiring no power for station keeping or altitude control. It is also easily recoverable for payload maintenance. However, according to a report back to 2005, the aerostat's altitude was still limited to *5 km* by the weight of its tether cable at that time. Nonetheless, high performance nano-material technology investments could someday yield extremely light-weight tethers with high strength to sustain aerostats operations above *18 km* (Colozza et al. 2005). Even though the length of tether cables seemed not to be a problem, the aerostats will still be somewhat restricted by the fixed ground location. In contrast, an un-tethered high-altitude airship is an unmanned, self-powered, free flying vehicle. Lift is produced by a combination of aerodynamics and lifting gas contained in the hull. The combination of photovoltaic and advanced energy storage systems delivers the necessary power to perform specific airship mission that requires mobility. Generally speaking, the potential of airships is superior to aerostats for the fulfillment of more versatile missions. Thus, most research in the literature has tended towards the development of airships rather than aerostats. Per the bibliometric analysis in one of the most recent review papers published in 2009, countries that

published most often on HAP were US, Italy, UK and Japan. More recently, China has joined the competition and has quickly become the major generator of scientific articles in HAP area as of December 2015, with emphasis on airships (D’Oliveira et al. 2016).

It has long been realized that high wind speed and unpredictable turbulences at certain altitudes in the atmosphere will cause extreme difficulties for airship operation. Figure 1.2 shows a typical profile of peak wind speeds annually, demonstrating significant wind speed variations relative to the altitude (Jamison et al. 2005). Clearly, there are still desirable regions where wind speed is low and turbulence is minimal. Specifically for the operation of HAP, a certain part of stratosphere (between 65,000 and 80,000 ft.) that is above the jet stream, severe weather, the FAA air traffic layer (Zhai & Euler 2005), and below the upper layers of the stratosphere, is the most suitable region. Hence, a stratospheric airship (SSA) flying between 65k and 80k ft. seems necessary to realize the concept of HAPs, which unsurprisingly, has attracted a considerable amount of interest from many research teams (Kang et al. 2006; Zhai & Euler 2005; Gu 2007; Xu 2009; Komotsu et al. 2003; Xu et al. 2008).

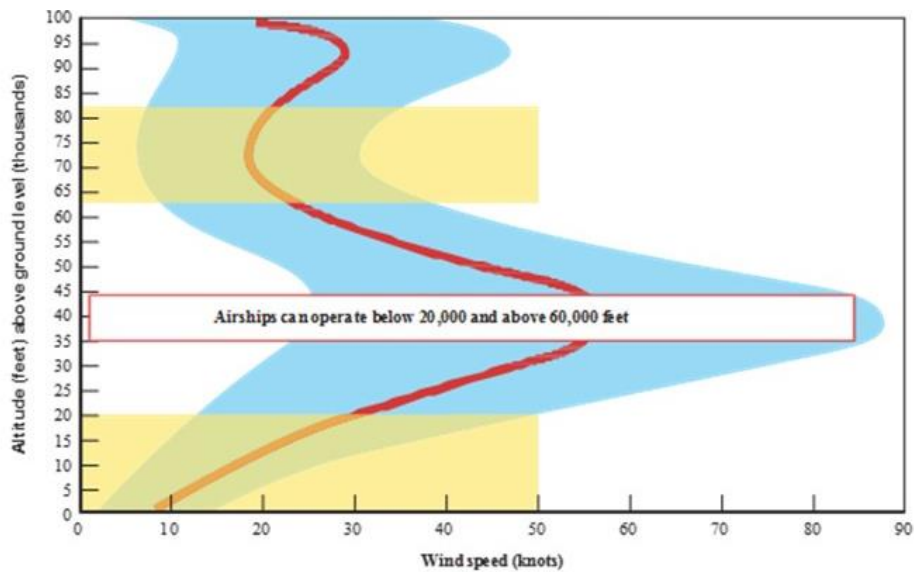


Figure 1.2. Typical Annual Winds Aloft (Jamison et al. 2005).

Due to the fact that the air at this altitude is very thin, with a density of about 7% of the sea level, a SSA floating at this region has to be a vehicle with large volume in order to generate sufficient lifting force (Guchi et al. 2000). To fulfill its size and light structure requirement, the airship with non-rigid hull configuration is preferred. Practically, non-rigid airships have simple structures and are easy to design, build, and maintain. In comparison with rigid airships, the fabrication cost of non-rigid airships is also lower, and the manufacturing time cycle is shorter. Non-rigid airships overcome the issue of weight penalty inherent in the use of rigid structures (Liao & Pasternak 2009). Figure 1.3 shows a typical configuration of classical non-rigid airships. The shape of a non-rigid airship is sustained by a pressure differential between the lifting gas in the hull and the atmosphere. An envelope as the gas containment membrane encloses the lifting gas and the ballonets and provides protection from the environment. Ballonets are filled with air to maintain a fixed pressure inside as the temperature of the lifting gas or the airship altitude changes. Ballonets permit the envelope pressure to be controlled. Adjustment of air volume in ballonets and gas volume in the airship envelope produces the change of buoyancy. With all these advantages provided, much more efforts have been predominantly put into the study of non-rigid airship in order to effectively materialize the HAP concept (Komotsu et al. 2003).

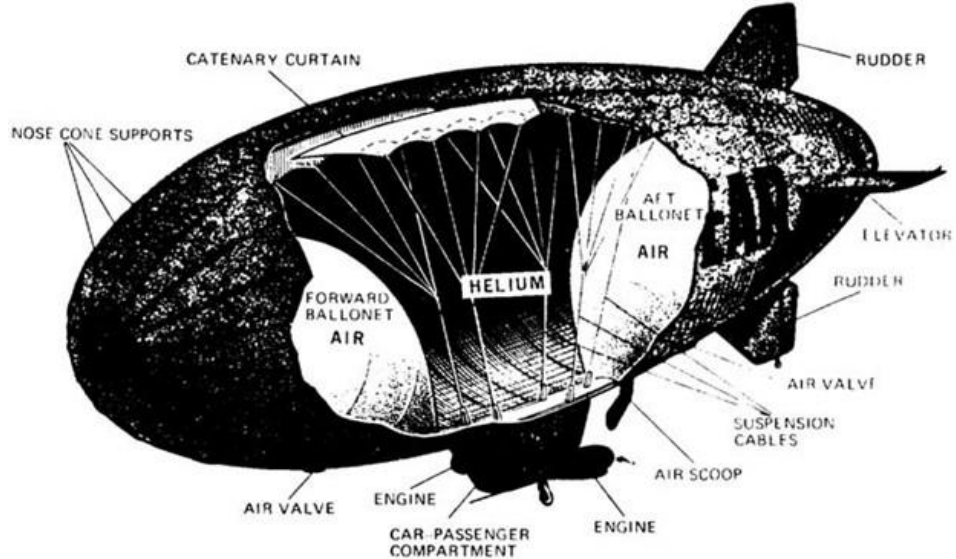


Figure 1.3. Typical non-rigid airship design (Liao & Pasternak 2009).

For non-rigid airships, the envelope/hull is one of the major structural elements. It contains the lifting gas and keeps the aerodynamic shape of the airship. It is, therefore, required that this part of an airship deserves a high level of engineering and quality control (Miller & Mandel 2000). Although great advances have been made in airship fabric technology over the last three decades, SSAs have unique requirements that demand further improvements. Generally, the challenge is to develop a very lightweight yet strong material that is capable of containing lifting gas and resistant to the environment.

The strength-to-weight ratio of the hull material significantly affects the feasible size of a non-rigid airship. Besides the aerodynamic stresses, hoop stresses from the gas pressure differential also rise with diameter, and in a non-rigid airship, this diameter must be relatively large because of the need to resist hull-bending moments (Jamison et al. 2005). As previously mentioned, the SSA is required to be large to produce sufficient lifting force due to the rarefied air in stratosphere. Stronger yet lighter materials are needed to build a SSA in optimized dimensions. On the other hand, to allow the airship to float at a certain altitude for long periods, the non-rigid SSA is designed to be a super-pressure structure, where the volume of the airship

is maintained relatively constant in the face of changes in the temperature of the contained lifting gas. This means that diurnal temperature variations have the effect of raising and lowering airship internal gas pressures. Consequently, this design also requires the use of stronger and tougher hull materials due to the high stresses brought to the hull fabric via significant pressure variations. In addition, the material must also be designed to have a good control of vehicle thermal changes, minimizing the impact of diurnal temperature variation on hull material durability. The stratosphere is also called the “ozone layer” because 90% of the earth's ozone is concentrated in this region. The high ozone concentration and intense UV radiation can deteriorate hull material, resulting in a loss of strength and permeability over time. A desirable SSA must stay aloft for a period of months to years to provide valuable and consistent services. Consequently, leakage of the lifting gas through the hull must be minimized, which is an enormously challenging task. For example, as an effective lifting gas capable of providing significant buoyancy, helium is a monatomic gas and has the smallest molecular diameter of all gases. Thus, the leakage of helium gas cannot be completely prevented because helium will simply diffuse through any envelope materials over time, even the aluminum alloy skin (Islam & Bradley 2012). The loss of lifting gas will result in loss of operational capability and increased operational cost. It is likely that gas permeation will represent the binding constraint to the endurance of SSA. At this altitude, the extremely low temperature can also cause the material to become brittle with a resultant loss of flexibility. However, enough flexibility to inflate and deflate the envelope is critical over its long service life cycle. High tear resistance is also needed to maximize damage tolerance and prevent catastrophic tear propagation. Low creep is extremely important that the envelope shape and its dimensional stability can be maintained throughout its life. It is strictly required that the

joining technique is capable to produce strong and reliable seams to withstand peel and creep rupture. The overall considerations in the design of an envelope material are summarized by Zhai and Euler (Zhai & Euler 2005) as listed in Table 1.1.

Table 1.1 Stratospheric Airship Hull Material Design Considerations (Zhai & Euler 2005)

Requirements	Criteria
Structural	Pressure load, Safety factor <ul style="list-style-type: none"> • Tensile and shear strength • Tear resistance • Strength-to-weight Ratio
System	Service life <ul style="list-style-type: none"> • Environmental resistance (UV, ozone, temperature, etc.) • Lifting gas permeability
Material Performance	Flexing (unaffected by folding), Blocking, Inter-layer bonding
Material Producibility	Repeatable process control (consistency) Yield percentage
Envelope Manufacturability	Bondability Handling
Thermal Control	Solar absorptivity, α Infrared emissivity, ϵ

All these requirements are not able to be fulfilled by a single type of existing material. To meet all these challenging requirements of SSA hull material design, laminated multi-layer flexible composite materials are typically considered an effective approach. Currently, the most modern materials which have been developed as hull materials have been laminated composite materials. The feature of laminate material is that overall properties of the laminate can be tailored and optimized by the cautious selection of appropriate components. In the case of SSA envelope material, the laminate should be made to optimize the resulting balance between strength-to-weight ratio, tear resistance, gas retention, Ozone and UV resistance, flexibility and service durability. Hence, the laminate will be comprised of load-bearing

component, gas barrier element and layers to protect against weathering and the environment. Moreover, these components need to be efficiently bonded together with an adhesive that allows for ease of laminate manufacture and of material joining (Islam & Bradley 2012). A typical laminate configuration is shown in Figure 1.4.

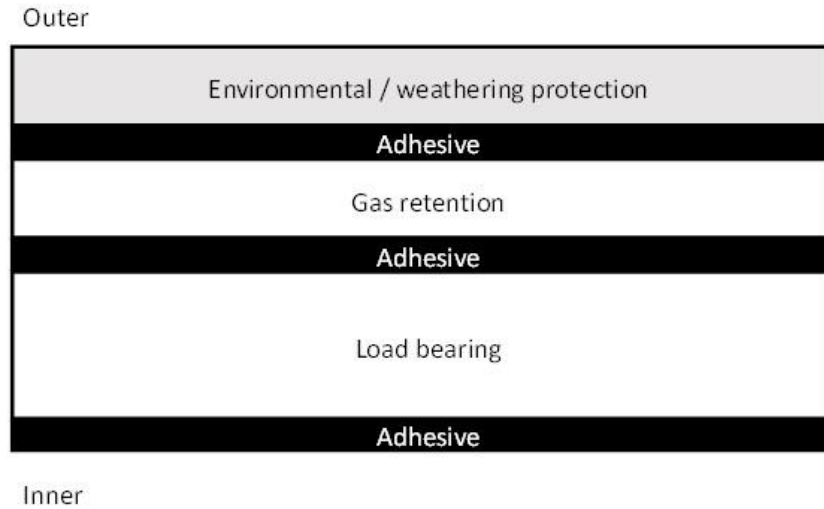


Figure 1.4. Layout of typical laminated flexible composite (Islam & Bradley 2012).

The structure typically has distinct inner and outer sides, with the gas-retention component incorporated between the weathering protection and load-bearing layers, allowing for the direct bonding of load-bearing components via widely available seaming technique e.g. heat sealing or cementing. In this case, the load transfer efficiency is greatly ensured. The outer sides were designed to be exposed to weather, UV, and ozone, whereas inner sides are usually in direct contact with lighter gases (hydrogen/helium) and to sustain high pressure. Prior to the progressing of high performance fibers and polymeric films, adhesives were the main target to be modified to achieve improved functional properties for the laminate structure. Many additives can be blended in the adhesive system to enhance the functional features of the multilayer laminates, including UV inhibitors, antifungal agents, adhesion promoters, cross-linkers, light and hydrolytic stabilizers, pigments, and the like (Islam & Bradley 2012). Mater

et al. mentioned making multi-layer laminated hull material by using polyester (PET) and polyurethane (PU) films being formed of polymers to which additives for ultraviolet stability, micro-organism resistance, and hydrolytic stability have been added (Mater & Hartly 1992). The patent claimed that the multi-layer laminate structures created could achieve improved physical and gas retention properties with the integration of additives blended high-modulus thermoplastic polyester films.

Despite considerable effort and expense in the past decades, no self-propelled airship built by any manufacturer has flown at stratospheric altitudes for more than one day. The first successful stratospheric powered airship flight took place in the late 1960s, reaching 20.4 km (67k ft.) for two hours with a five pounds payload (Fesen & Brown 2015). In 2005, Raven Industries announced the historic eight-hour flight of a powered stratospheric airship, reaching the altitude of 20 km (66k ft.). This may still be the current world record for a high-altitude airship flight duration (Smith et al. 2011). However, it is the major development in textile engineering (high performance fibers and polymeric films) that continued to push the boundaries in airship design and development (Jamison et al. 2005). The emergence of novel high-performance fiber and polymeric films is very likely to change the game completely.

Most recent examples of laminated lightweight gas-holding multilayer structures found in the literature typically combine high-performance polymers, fibers, fabrics, and film substrates for LTA airships. It is typical observed from these structures that the high-tenacity fabrics made from high-performance fibers (e.g. Zylon[®], Vectran[®]) and high modulus film (e.g. Kapton[®], Mylar[®]) substrates are pressed together under controlled pressure and temperature with primarily polyether/polycarbonate-based polyurethane adhesive systems which have high flex at low temperature, tensile strength, modulus. However, there is still much room for the

improvement on modifications of the existing SSA hull structures and materials as well as manufacturing processes. Therefore, a review of the most recent research and developments about the new materials and their applications in airship industry is critical to enlighten the design and materialization of next-generation SSA envelope material, which could possibly provide a brand-new solution for the fulfillment of the HAP system in the near future.

2 Literature Review

In the scope of this review, only envelope materials developed in a basic configuration of laminated, textile reinforced composite will be emphasized. Due to the strict requirements of high-altitude applications, these materials share similarities in their structures, including at least load-bearing, gas-retention, weathering and adhesive components. In some unique scenarios, eliminating one or two layers by incorporating multi-functional components into the laminate structure can achieve the goal of further weight reduction. This chapter will cover some generic discussions about the most critical functional components in the laminate structure, followed by more in-depth evaluation and analysis toward some uniquely designed airship hull material.

2.1 Load-Bearing Component

2.1.1 High Performance Fibers

To make an envelope material flexible, it is required that the load-bearing component to be textile fabric, either single or multiple layers (not preferred because of weight penalty). The most challenging aspect of designing the load-bearing layer is the identification of a high-performance fiber with extra light weight. The low strength-to-weight ratio of traditional natural fibers are not able to meet the mechanical property requirements of high-altitude LTA systems. With the continuous development of synthetic fibers, the textiles used in airship industry have witnessed many significant breakthroughs, providing the highest possible strength-to-weight ratios. Figure 2.1 shows the history of modern textile fiber development.

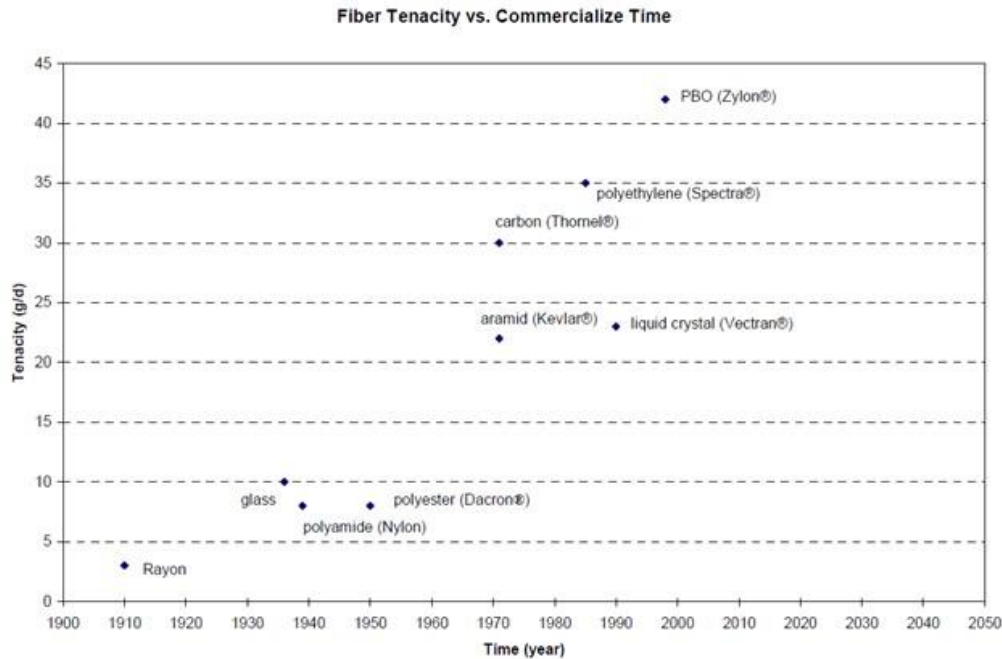


Figure 2.1. Timeline of Performance Textile Fiber Development (Zhai & Euler 2005)

At an early stage of airship development, the combination of high strength-to-weight ratio, low creep, low moisture regains, and improved hydrolysis resistance made polyester fiber a good choice for LTA applications. Almost all the earlier synthetic fiber reinforced LTA hull materials were made with high tenacity polyester fiber woven fabrics. However, most of those materials produced with polyester fibers were designed only for low and medium altitude LTA systems. It is not until late twentieth century that the high-performance fibers with higher modulus (over 300 *g/denier*) and tenacity (over 20 *g/denier*) became available. The strongest commercially available fibers in the aspect of specific strength (Strength/Density) are Zylon®, Dyneema® and Spectra®. Other high performance fibers, including Vectran® and Kevlar®, also possess great properties (Zhai & Euler 2005).

2.1.1.1 Para-aramids - Kevlar®

Comparing to the conventional low strength textile fibers, fully aromatic polyamides, have a much higher strength-to-weight ratio, a greater modulus which inevitably lead to a much lower failure strain. With the linear density being comparable to carbon fibers, they could significantly reduce the weight of an envelope considering only strength. However, their major disadvantage is apparently the degradation issue when exposed to ultraviolet radiation from sunlight (Islam & Bradley 2012). It was also found that a para-aramid fiber reinforced laminate is not capable of effectively dispersing the stress concentrations, which will be unavoidably introduced during the manufacture of large structures. According to conventional knowledge, the tensile deformation of para-aramid fiber is dominated by rotation of its crystallites toward the fiber axis. Tensile load application induces an immediate elastic rotation and a time-dependent creep rotation. Crystallite rotation stiffens the fiber, reducing elastic and creep compliance. Thus, the stress concentrations cannot be relieved effectively in a timely manner. The unrelieved stress concentrations can then initiate catastrophic tear propagation. Before this problem been properly solved or completely eliminated, there won't be further development of stronger and lighter aramid envelopes (Islam & Bradley 2012).

2.1.1.2 Ultra High Molecular Weight Polyethylene - Spectra® & Dyneema®

The fibers made from ultra-high modulus polyethylene (UHMWPE) are very different from the polyethylene material that we are familiar with. In normal polyethylene, the long polymer chains are less oriented, which allows the material to stretch dramatically before failure. The molecular weight is low, and the crystallinity is usually lower than 60%. While in these purposely designed high molecular weight, high-performance fibers, the long chains have

been straightened (crystallinity can be as high as 95%) and lie along the fiber length, giving considerably higher strength with much lower failure strain. Although they have the potential to produce the lightest fabrics for a given high strength, with similar strain to failure and modulus as para-aramids, they may be expected to suffer from the same inability to relieve induced time-dependent stress concentration, creep, and poor flexural properties, which could initiate catastrophic tear propagation. UHMWPE fibers are not compatible with many industrial resins and adhesives e.g. epoxy, because the presence of a weak boundary of low molecular weight fragments as well as its non-polar nature of molecular structure (Silverstein & Breuer 1993). . They are also restricted by the low melting point, with a heat resistance only up to ~150 °C. But notably, UHMWPE fibers under the trade name of Dyneema® are very resistant to moisture and UV light (DSM 2008), which is an outstanding property over Zylon® and Vectran®. It was also claimed in (McDaniels et al. 2009) that the tradeoff of Dyneema® being with less than ideal creep but excellent UV performance may be easier to design for, and determine life factors from, than from materials with opposite trade-offs. Unfortunately, there is no research found attempting to make laminated envelope material with Dyneema® fabrics for airship applications so far.

2.1.1.3 Polyarylate - Vectran®

Vectran® fiber is a commercial product from Kuraray Inc. and is produced by melt spinning from thermotropic liquid crystal polymer (LCP). As a fully aromatic polyester fiber, it has a tensile strength of 27 g/denier and tensile modulus of 600 g/denier. The micro-fibrillation nature of Vectran® fiber makes it difficult to process and requires significant effort to weave a defect-free fabric. A high tenacity (HT) polyarylate fiber (Vectran® HT) offers

desirable combinations of performance, structure, and properties critical to LTA application material development. They include high strength and modulus, excellent creep resistance, high abrasion resistance, superior flex/fold fatigue resistance, minimal moisture regain and excellent chemical resistance (Islam & Bradley 2012). In addition, other properties like low coefficient of thermal expansion (CTE), and excellent cut resistance, superior property retention at low and elevated temperatures, outstanding damping damping and impact resistance provide this type of fibers with more advantages to be used for diverse structural engineering applications. Regardless of its lower specific strength, Vectran® offers a superior balance of different properties in comparison to other high-performance fibers. Vectran® is particularly an excellent choice for airship balloonet material because of its outstanding abrasion resistance and flex-fatigue performance, as balloonets in a non-rigid airship are required to inflate and deflate frequently over their long service life cycle (McDaniels et al. 2009). However, Vectran® fibers possess much lower specific strength when compared with Zylon® and HMWPE fibers (compared in Table 2.1 below), which inevitably restricted its applications in high-altitude airships.

2.1.1.4 Poly(p-phenylene-2,6-benzobisoxazole) - Zylon®

Zylon® fiber, made from rigid-rod chain of an aromatic heterocyclic lyotropic polymer, polybenzoxazole (PBO), is produced from an air-gap wet spinning process in the coagulation bath with a low spinning rate. The world leading technique of Toyobo Inc. allows them to produce Zylon® fiber with a tensile strength as high as *42 g/denier* and tensile modulus of *2000 g/denier*. In spite of a larger density, Zylon® still possess a higher specific strength over Dyneema®, and is therefore claimed as the strongest fiber in the world (Islam & Bradley 2012).

The fiber has better abrasion resistance than aramid fibers but performs significantly lower than Dyneema®. Nevertheless, the extremely high flame resistance and excellent creep resistance are not matched by any other types of high-performance fibers. With all these impressive properties, this “super fiber” looks very promising for SSA application. However, the weaknesses of Zylon® fiber was gradually unveiled after many investigations into different types of properties. It is widely known that prolong exposure to visible light and UV radiation degrades Zylon® fibers over time (Said et al. 2006). Moreover, the strength will also drop significantly when being exposed to an environment with high humidity and heat. As a result, it must be very carefully protected during all the processes from weaving preparation to weaving and ultimately lamination. Finally, Zylon® fiber is fairly more expensive when compared to other types of high-performance fibers.

To sum up, high performance fibers are attractive to the LTA industry. However, concerns remain for these fibers, such as inability to effectively relieve stress concentrations (e.g. Kevlar®), poor creep resistant properties (e.g. Spectra®), moisture and UV degradations (e.g. Spectra® and Zylon®). This may change as more scientific investigations and more working experience with these fibers are gained, so that their less desirable properties can be improved or compensated for by some other methods (Islam & Bradley 2012). Another important consideration is that most high-performance fibers are developed for special military purposes rather than for more commonly civil uses, which determines their excessive cost. This directly results in limited availability, research, and technical information of these high-performance fibers. For a clear comparison, Table 2.1 shows several high-performance fibers as well as more cost-effective and readily available high tenacity polyester, KoSa® (Zhai & Euler 2005).

Table 2.1 High Performance Fibers Comparison (Zhai & Euler 2005)

Material		Strength, g/den	Pros	Cons
Zylon®	PBO	42	Strong, excellent creep resistance, And extremely high temperature resistance	Low flex resistance, poor UV, visible light, and moisture resistance
Spectra®	UHMWPE	25-40	Strong, flexible, and good weatherability	Low melting point, poor UV and creep resistance, and difficult to bond
Vectran®	LCP	23	Good overall properties and excellent cut resistance	Not as strong as Spectra® or Zylon®, poor UV Resistance
Kevlar®	Aramid	22	Strength comparable to Vectran®	Poor folding and abrasion resistance
Kosa®	PET	7-9	Tough, durable, inexpensive, fully evaluated	Low strength

There are several lab-scale samples and pilot line materials that have been made to further evaluate more comprehensive properties of high-performance fiber reinforced laminates for LTA applications, which will be discussed in more details in the next section.

2.1.2 Structures of Load-bearing Textile Fabrics

Another challenge in the core strength material development is to achieve efficient strength transfer from the theoretical yarn strength to the end-use laminated composite material. To satisfy the strict standard on the hull weight, single layer woven fabric is predominantly used in high strength, lightweight hull material as the core strength element. Beyond that, the weave pattern design, weaving preparation and weaving process as well as other textile technologies also significantly influence the physical properties of the finished textile fabric (Zhai & Euler 2005). The design of weave pattern determines how the warp and weft yarns interlaced with each other (usually orthogonal to each other) in a woven fabric. Plain weave is the most common and simple weave design, and it provides very high interlacements between

the warp and weft yarns. Due to the high interlacements, the crimp in the finished fabric is usually high. On the other hand, plain woven fabrics are dimensionally stable structure, so that the handling is improved. There will be less distortion of the yarns. Plain weave is a basic weave pattern with many variations. A plain weave fabric can be produced with various yarn counts (*denier/tex*) and fabric thread density (number of yarns per *inch* in the warp and weft directions) to modify the tensile strength and openness of the finished fabric. A common variation of plain weave is the basket weave and ‘rip stop’ which improves the tear resistance. Compared with a simple plain weave fabric, basket weave fabrics have lower thickness and crimp, leading to a relatively higher tear strength. In rip stop patterns, thicker or double yarns are usually woven at intervals to achieve the purpose of preventing tear propagations in one or both directions (Islam & Bradley 2012). With a similar overall structure to the widely investigated coated fabrics, the laminated structure should share some principles when it comes to the hybrid structure of fibers and polymers. For example, the woven fabric design has a significant impact on tear resistance. But, the higher original tear strength of a basket weave, as compared with a plain weave, may not be retained when such fabric is coated with a thick layer of polymer. The increased openness of the basket weave causes greater polymer coating to penetrate through the thickness and strike into the fabric structure. Yarns may thus become less mobile and unable to slide and jam together. The yarns then break individually rather than in groups, causing the tear strength to reduce significantly. However, proper coating or lamination restricts the rotation and slippage of the yarns in the hybrid structure and therefore would increase shear resistance (Schwartz 2008).

An unconventional “non-crimp” structure was discussed in a high strength-to-weight ratio technical fabric study by Cubic Tech (CT) Corp., which can be likened to a classic composite

laminate structure called “Cross-ply” where the layers were only stacked orthogonally. With the same principle, CT has developed improved capability to further produce multidirectional, non-interlaced laminates from oriented filament plies and high-performance films or surface coatings. In this paper, removal of crimp was particularly emphasized to be able to effectively increase the tensile strength of the as-produced laminate (McDaniels et al. 2009). It is claimed that “non-crimp” fabrics have many technical and performance advantages over woven fabrics with high crimp, being easier to manufacture as well as more flexibility to optimize weight and thickness. Additionally, for woven fabrics with high crimp which is unavoidable due to yarn interlacing, the fabric strength will be substantially damaged. Tensile loading of high crimp woven fabric brings transverse loads at yarn overlap areas as crimped yarns are to be straighten; this reduces the conversion of yarn strength to fabric strength and also affects fatigue performance and creep property. It is also stated by McDaniels et al. that crimp induced degradation in properties is more noticeable with higher performance structural fibers. Because most of these fibers are optimized in the axial direction of the fiber filaments properties, which weakens transverse properties consequently. Figure 2.2 is a magnified image of a woven polyester fabric followed by an illustration of crimp in woven fabrics as load is applied (McDaniels et al. 2009).

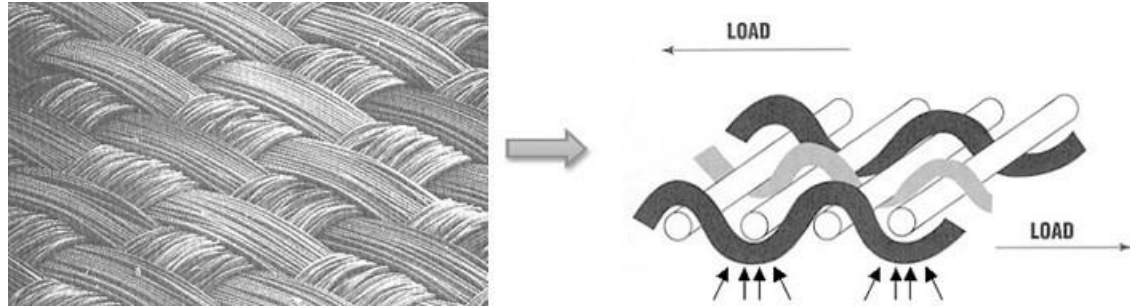


Figure 2.2. Magnified Image of Woven Polyester and Crimp Diagram. Tensile loading of woven fabric induces transverse loads at thread overlap intersections due to straightening of crimped fibers (McDaniels et al. 2009).

In contrast, their proposed non-crimp composite laminates are free from these limitations and may be produced with multiple oriented layers positioned at any angles. The most important advantage of multi-directional oriented laminates is the ability to optimize weight, thickness, and strengths at varied locations or in fixed load directions. (McDaniels et al. 2009).

Figure 2.3(a) illustrates this point with a stress-strain graph of a non-crimp material, with no crimp, and a woven fabric having crimp. A conceptual drawing of a non-crimp fabric is also included in Figure 2.3(b).

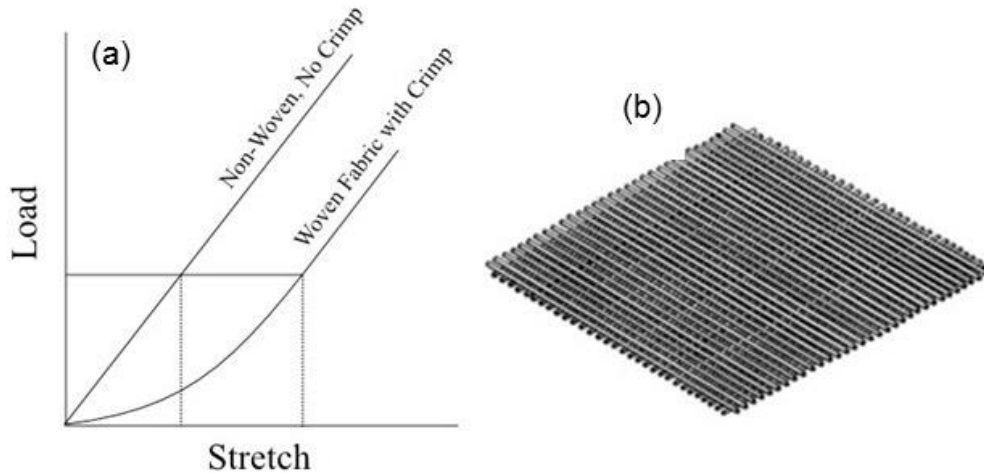


Figure 2.3. (a) Comparative Stress-Strain of materials with and without creep; (b) Conceptual Drawing of non-crimp fabric (McDaniels et al. 2009).

The key factor affecting the mechanical performance of the woven fabric is load sharing between the yarns. This is more important for high-performance fibers which normally have

very low elongation at break (Zhai & Euler 2005). In a plain weave fabric, the interlacing of warp and weft yarns can help the load sharing in the yarns when the loaded yarns are properly aligned. The strength of a single yarn is determined by the weakest spot according to the weak-link theory (WLT) first proposed by Pierce in 1926. Therefore, the interlacing woven structure can effectively increase the fabric strength and stabilize the dimension. Moreover, with ribbon like, flat filament yarns used for weaving, negligible crimps will be produced in contrast to the exaggerated demonstration drawn in Figure 2.2. While, in the case of “non-woven” structure, since there is no assistance from the fabric interlacing structure, the overall strength of the fabrics can be weakened by a bunch of yarns with non-uniform quality along the length. To achieve higher strength, the requirement of the tension control on each single yarn should be more rigorous. Because, a number of yarns may rupture earlier due to overstretching while another set of yarns can still be loose and bearing no stress at all. Careful tension control has to be applied on both warp and weft yarns during lamination process to ensure the proper load sharing of the “non-woven” fabric.

2.2 Gas retention layer

Helium gas loss has two principal effects: 1) causing reduction of lift and thus a decrease in operational capability of the airship, which is not a safety issue because the leakage rate is normally known; 2) increasing the operational expenses because the lifting gas needs to be replaced to maintain the normal high-altitude operations. Back in 2011, the average market price of 99.9% helium in the U.S. can be estimated between 1.77 and 2.47 USD/m^3 (Bonnici et al. 2014). It is already emphasized that the size of SSA envelope material would be fairly large in order to provide sufficient lift in the stratosphere with rarefied air. In financial terms, the

larger the envelope the greater the volume of helium lost for a given permeability. On the other hand, helium is a non-renewable resource. Once it is released into the atmosphere, it will escape earth. The need to minimize helium loss has always been present.

2.2.1 Polymeric Films

Generally, a thick layer of coating or film is absolutely necessary to provide satisfactory gas barrier property for airship operation. All the earlier airship hull materials used coatings as the gas barrier, while lightweight polymeric film materials are usually incorporated as the major gas barrier for the modern hull laminates (Islam & Bradley 2012). The properties of polymeric film materials which have the potential to be used as gas retention component were summarized in a review paper on airship material (Zhai & Euler 2005), as shown in Table 2.2.

Table 2.2 Desirable Environmental Protective and Gas Holding Polymeric Materials (Zhai & Euler 2005)

Material	Permeability	Weatherability	Flex Fatigue	Adhesion to Fabric/Film	Heat Sealability
PVF (Tedlar®)	Good	Excellent	Good	Poor	No
PTFE (Teflon®)	Good	Excellent	Good	Poor	Yes (> 500 °F)
Polyurethane	Fair	Good	Excellent	Excellent	Yes
PVC	Fair	Good	Good	Excellent	Yes
PVDC (Saran®)	Excellent	Poor	Fair	Fair	Yes
Nylon	Excellent	Poor	Excellent	Fair	Yes
Polyester (Mylar®)	Good	Fair	Fair	Fair	No

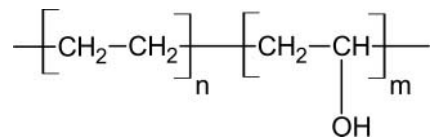
In addition to low permeability, it is also desirable for the film to have good shear stiffness to enhance the overall stiffness of the whole laminate as much as possible. Bondability is also important because poor adherence to other components could result in delamination. In practice, polyester is a preferred material, with high-modulus polyester film (Mylar®; DuPont-

Teijin) being the most commonly used gas barrier element on existing airship materials. Mylar® has low permeability and relatively high strength and stiffness as well.

Notably, it is recommended in an airship material review (Islam & Bradley 2012) that polyimide (PI) film, Kapton®, provides outstanding mechanical strength and high modulus and is also suitable to be used as an effective gas barrier component. Aerospace grade PI films are widely used on external surfaces of satellites and spacecraft, yet their applications are still scarcely found in airship, potentially due to their excessive cost. There is only one case of airship envelope found in the literature integrating PI film as a gas barrier layer, being protected by another layer of PVF film as weathering component. This particular airship envelope material can be operated at an altitude of ~ 21.3 km (70,000 ft.). and with a service temperature from -100 °C to +60 °C (Laven & Kelly 2005). Many researchers have made efforts to improve the durability of PI film in aerospace applications, mainly addressing the erosion issue caused by the atomic oxygen (AO). A recent study (Gouzman et al. 2010) have shown that a thin layer of Titania coated on the surface of PI films via liquid-phase deposition (LPD) can effectively reduce surface erosions induced by AO. With a practical solution to endure AO, which is also richly existing in the stratosphere, using modified PI films as weathering component seems feasible. In combination with a decent gas barrier property, they can be used as multi-functional layer so as to reduce the overall weight of the envelope material. The decrease in the number of layers will also help to reduce the use of adhesives, reducing the weight as well as the number of locations where delamination can occur.

The other unique polymeric film frequently used as gas retention component in more recent airship material laminate structures is EVAL™ film (EVOH, Kuraray). Without any exceptions, the EVOH (ethylene vinyl alcohol) films were laminated together with other

components through various bonding agents (Komotsu et al. 2003; Maekawa et al. 2007). EVOH is a semi-crystalline copolymer of ethylene and vinyl alcohol monomer units (Mokwena & Tang 2012). The repeating unit of EVOH has the following chemical structure:



In general, the good gas barrier properties of EVOH copolymers are primarily attributed to their inherent high degree of crystallinity. Because it is known that gas transfer occurs mainly through the amorphous regions, and crystallinity hinders the diffusion of gas molecules. Thus, the presence of large amount of impermeable crystalline regions in EVOH reduces gas permeability by creating more complicated and tortuous diffusive pathways for gas molecules (Lagaron et al. 2004). In the molecular structure, the large amount of hydroxyl groups in EVOH copolymers result in high intermolecular and intramolecular forces and therefore lead to a high cohesive energy (Lagaron et al. 2004). Significant cohesion between adjacent polymer chains is also helpful for polymer molecules to aggregate together into a crystalline solid. Other than the excellent gas barrier property, EVOH is also known to be very sensitive to moisture, which is primarily caused by the associations between water molecules and the polar hydroxyl groups in EVOH. Thus, care needs to be taken on the handling and storage of EVOH polymers in order to optimize the barrier performances (Mokwena & Tang 2012).

2.3 Weathering Layer

Polyvinylfluoride (PVF) film, commonly known by the trade name, Tedlar® (DuPont), has been used for most large LTA hull material applications. Tedlar® has excellent resistance to solar degradation. Pigmented Tedlar® film offers the highest level of UV protection which

means the load-bearing layer underneath will not be greatly influenced by destructive aging and UV-induced heat. Tedlar® also has non-staining properties, chemical and solvent inertness, toughness, flexibility over a wide temperature range (-72 to 107 °C), and good gas containing properties for low-altitude airship applications (Kang et al. 2006). To understand the long-term weathering effects on SSA hull materials, Nakadate et al. (Nakadate et al. 2011) applied Aluminum evaporated Tedlar® Film as the weathering protection component, incorporating with Zylon® woven fabric as the load-bearing component and polyurethane as adhesives. The thin reflective metallic coating was intended to improve the UV radiation resistance of the envelope material. However, the results from weathering exposure testing indicates that the addition of an extra layer of Aluminum was able to significantly improve the moisture barrier property and thus sustaining long-term outdoor exposure in high humidity environment.

Another widely acceptable and readily used material for weathering resistant purpose is polyurethane (PU). PU is available in many formulations and possesses an excellent balance of properties, making it a superior coating material for textile fabrics to meet diverse end uses. It has outstanding overall toughness, high tensile strength, tear strength, abrasion resistance, low temperature flexibility, fair gas permeability, good handling properties, crease resistance, and good UV and ozone resistance (Islam & Bradley 2012). While most polyurethanes are thermosetting polymers that do not melt when heated, thermoplastic polyurethanes (TPUs) are also available. TPU can be heat sealed, adhesively bonded, and laminated to other substrates. Kang et al. integrated a TPU film at the inner side of the envelope material for thermal bonding. Different from the PU layer traditionally coated onto the textile fabrics, it is mentioned in (Kang et al. 2006) that laminated TPU film can serve as another gas barrier within the envelope.

In particular, when the external weathering and gas retention layers are damaged, the internal TPU layer can block gas leakage to some extent.

2.3.1 Ultraviolet (UV) Radiation

To adapt to the working environment in the stratosphere, the surface materials of an envelope, in contact with the atmosphere, must also be able to resist the intense UV radiation. Not only does the material need to withstand the degradation from the UV radiation for an extended period of time, but also prevents the UV radiation and visible light from transmitting through. Because, in most cases of the modern envelope material for SSA applications, the high-performance fibers used to fabricate the core strength layer are UV and even visible light sensitive. The fibers tend to lose strength significantly upon exposure to UV radiation for an extended period of time (Said et al. 2006). Such degradation induced by UV radiation becomes a challenging issue for the development of SSA hull materials. There have been a number of works investigating different methods of effectively protecting the high performance fibers from UV radiations, among which a sheath structure containing UV inhibitors was found to be highly effective in improving the UV-Vis resistance of PBO braids (Vallabh et al. 2016). In the other study, Hassanin et al. sheathed the PBO braided tendon with a PU membrane loaded with TiO₂ nanoparticles. The strength of the protected sample retained at a significantly higher level when the fillers loading was optimally controlled. For airship materials, the lightweight need requires the UV protection method to be effective without adding too much weight. The application of UV inhibitor loaded materials will inevitably bring unwanted weight to the airship envelope. Thus, another approach to protect the high-performance fibers with minimum weight penalty is to deposit consistent quality thin metallic coatings to reflect the UV radiations

and prevent the penetrations. However, the introduction of the metallic surface could potentially cause adhesion issues.

To validate the effectiveness of metallic coating, an envelope material (Z2929T-AB) consists of Aluminum evaporated Tedlar® layer, was developed using Zylon® (PBO, Toyobo) as core strength fabric. The detailed layer notation of this laminated envelope material is shown in Figure 2.4.

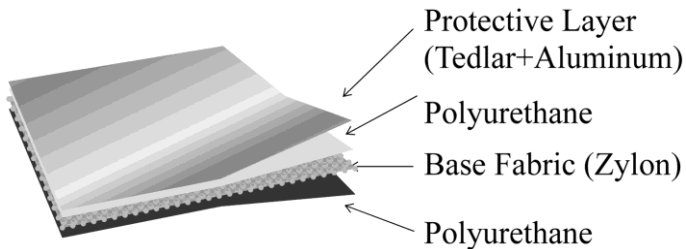


Figure 2.4. Layer composition of Z2929T-AB (Maekawa et al. 2008).

The xenon tests were conducted where the specimens are exposed to 180 W/m^2 xenon lights for 100 hrs, which is equivalent to half of a year's exposure to UV radiations on the ground. Per the data presented in Figure 2.5, the strength retention rate is close to 100% with a negligible reduction of tensile strength, proving that the addition of a thin layer of evaporated Aluminum can effectively block the UV radiations and protect the high-performance fibers. However, a prolonged stratosphere-level-intensity UV-Vis exposure test needs to be done to further confirm the long-term reliability of the UV resistant performance of Aluminum reflective coating. Moreover, in the real operation environment, stresses are constantly applied to the envelop material, which in turn will cause fatigue degradation on material properties. Therefore, whether the integrity of the metallic coating can be maintained during long-term use is a key issue for UV resistance property (Maekawa et al. 2008).

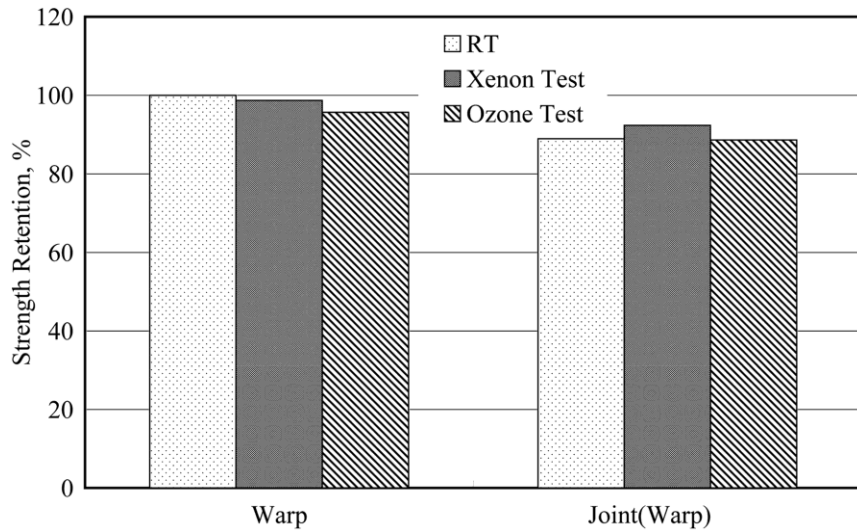


Figure 2.5. Residual strength of Z2929T-AB material and its joint after accelerated UV and Ozone exposure (Maekawa et al. 2008).

Since it takes considerable amount of time to build a large airship before launching, ground level moisture is also an important factor which tends to affect the performance of the multi-layer envelope laminate materials. Subtle effects can be accumulated and transformed into a significant impact over time. Thus, a two-year long outdoor exposure test (Figure 2.6) was conducted by Nakadate et al. (Nakadate et al. 2011) to investigate on the extended impact of weathering to airship envelope materials. Indeed, testing results from this work showed a unique seasonal effect on the tensile strength. Specifically, it was observed that substantial decrease in tensile strength occurred during late spring to early fall of the second year as well as the first year, whereas negligible decrease took place during other seasons.

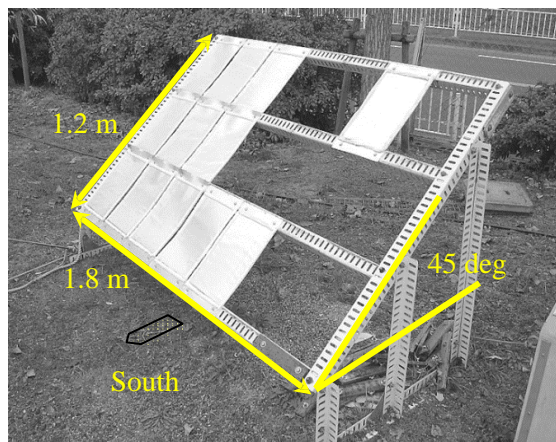


Figure 2.6. Test panels mounted on top of an outdoor exposure rack facing the south (Nakadate et al. 2011).

These results suggested that the high humidity and/or the high temperature during these seasons were/was the cause of the decrease in tensile strength. A six month long supplemental outdoor exposure test was conducted to separate humidity effect from temperature effect (Figure 2.7).

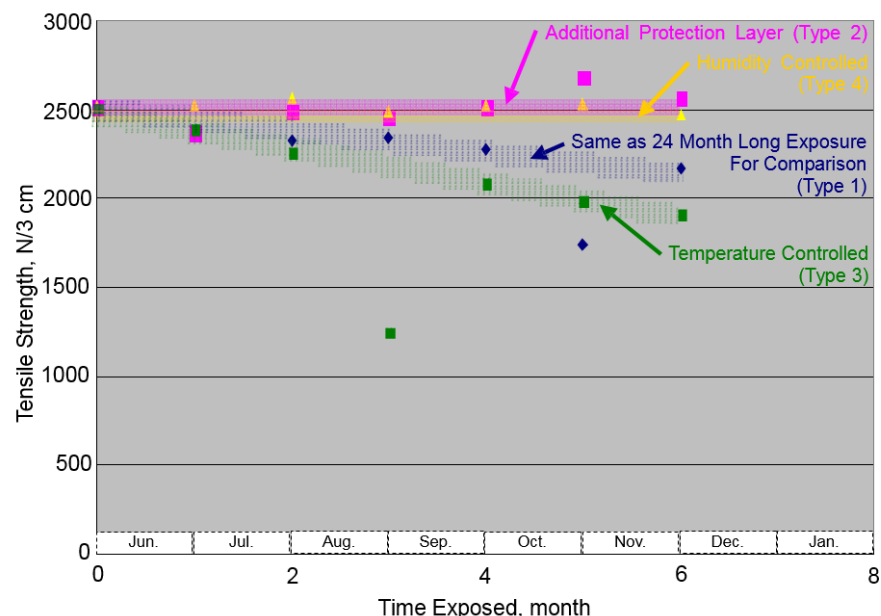


Figure 2.7. Summary of supplemental outdoor exposure test, effects of an additional protection layer, humidity, and temperature (Nakadate et al. 2011).

The test results suggested that the high humidity was obviously the primary factor causing the decrease in tensile strength. Notable in Figure 2.7, the tensile strength of the material with

an additional protection layer (evaporated Aluminum Tedlar[®], Type 2) decreased as negligibly for months as that with humidity controlled (Type 4). The added layer to the outer surface might have reduced the overall permeability of the material and block the humidity from passing though the material and penetrating into the core fabric. However, since the primary effect of the aluminum evaporated Tedlar[®] protection layer is to block the light, the effect of light should be separated from other factors for future work. To sum up, it is suggested by Nakadate el al. that dried air needs to be filled in final airship assembly to maintain its shape and strength for months before launching to the stratosphere where moisture barely exist. Moreover, it is also recommended that the addition of one thin layer or two (e.g. aluminum coating) with low permeability to gas and vapor can be effective for humidity resistance.

2.3.2 Ozone and Atomic Oxygen Degradation

Ozone is a strong oxidant and could break some of the molecular chain structures, resulting in degradation of polymer material. Per the study of Maekawa et al. (Maekawa et al. 2008), Ozone at $50 \pm 5 \text{ ppm}$ is applied to the specimen for 24 hrs in the exposure test. This ozone concentration is five times higher than that at the altitude of 20 km. From the high strength retention percentage displayed in Figure 2.5, it is also confirmed that Tedlar[®] functioned as a great ozone resistant element even at a higher concentration. Nonetheless, the short exposure time of the exposure test is not able to validate the long-term ozone resistant performance. Due to the existence of the Tedlar[®] film, it takes time for ozone to erode and penetrate into the interior structure of the laminate to cause critical damage. It can be true that Tedlar[®] film is capable to shield load-bearing fabric from the attack of ozone for certain amount of time. But long-term ozone resistance merely from Tedlar[®] is not guaranteed which

needs to be further verified by exposure to high concentration ozone for extended period of time. A hybrid exposure test of intensive UV and high concentration ozone can also help to identify the real weathering resistant performance because that will be more closely simulated to real situation in stratosphere.

Other than ozone, the richly existing Atomic Oxygen (AO) in the stratosphere is also extremely hazardous due to strong erosion to nearly all the polymers (Lin et al. 2011). It is reported by Zhai and Euler (Zhai & Euler 2005) that Triton Oxygen Resistant (TOR) polymers may be a promising candidate for the protective film layer of SSA. TOR polymers were tested in low earth orbit (LEO) by NASA and appeared to have potential as weather resistant films or coatings in extreme environments. Preliminary data indicates these polymers have a high resistance to degradation from AO, ozone and UV radiation (Triton 2001). The most unique feature of this polymer is that an outer oxidized layer can not only be formed to protect against abrasion, but also be capable of reforming if surface damage does not penetrate completely through the material.

2.3.3 Temperature

The diurnal temperature changes of LTA structures impose significant challenges concerning altitude control and power consumption. The material surface properties significantly influence system thermal control. A low solar absorptivity with a high infrared emissivity (low α / ϵ ratio) is desirable to minimize system temperature fluctuations. In this case, a reflective metallic backing is theoretically more effective than a white non-metallic surface. Table 2.3 compares several material combinations, white Tedlar®, silvered Teflon®, quartz over silver, and a lab-scale sample produced for a high-altitude LTA system study (Zhai

& Euler 2005). As shown in Table 2.3, it is apparent that the metallic lab made sample demonstrated brilliant thermal control parameters.

Table 2.3 Material Surface Thermal Properties (Zhai & Euler 2005)

	Solar absorptivity, α	Infrared emissivity, ϵ	α/ϵ ratio
White Tedlar®	0.3	0.85	0.35
Silvered Teflon®	0.08	0.6	0.13
Quartz over Silver	0.077	0.79	0.1
LTA hull coupon	0.07	0.75	0.09

The effect of temperature on mechanical properties of Z2929T-AB airship envelope material was also investigated by Maekawa et al. (Maekawa et al. 2008). Tensile tests were performed at different temperature levels from low to high, obtaining the tensile strength of the laminates and their seams. The respective tensile strength results to temperature variations are plotted in Figure 2.8.

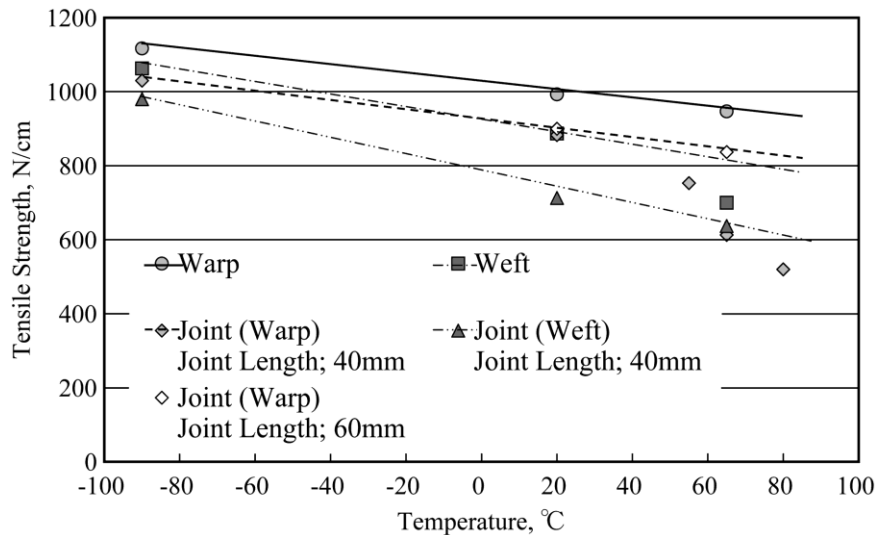


Figure 2.8. Tensile strength of Z2929T-AB and its joints in warp and weft direction (Maekawa et al. 2008).

A similar trend is observed from all the different samples that the tensile strength reduced when the temperature increases, regardless of laminates or seams of varied length. Due to the limited data points collected over a relatively wide temperature range, the variations of mechanical response of laminate and seams cannot be rigorously analyzed. Yet, it is apparent that effective thermal control to maintain a relatively lower temperature will be beneficial for the prevention of mechanical failure in the laminate or seams induced by high heat degradation.

2.4 Adhesives

2.4.1 Lamination of Hull Material

Most of the conventional low-altitude airship hull materials were coated fabrics produced by a coating process in which one or several layers of materials are deposited on the surface of a textile substrate. The majority of coating materials are liquid polymer compounds with gas retention and weathering resistant properties. With the evolutions of airship material requirements, coated fabrics were gradually replaced by flexible multi-layer laminate structures produced by lamination process, integrating multiple functional polymeric films and fabrics by using adhesives. Adhesive is often used in multi-layer composite material to bond the various components together. The intermediate adhesive layers can be either thermoset or thermoplastic. A thin adhesive layer(s) is critical to minimize the overall areal weight of the material. Adequate flexibility of the multi-layer structure and good bondability to each component (to prevent delamination) are essential requirements for the adhesive, which are primarily determined by adjusting the bonding process parameters. In addition to the bulk properties of the adhesive selected, substrate surface conditions, physical and chemical treatments, and processing method also significantly affect the weight, flexibility, interfacial

bonding and other physical properties of the finished material product. A good combination of the adhesive compound, substrate surface treatment, and the proper parameters control of integration technique are key factors to achieve a well-engineered laminate material in general as well as for SSA applications.

2.4.1.1 Basic principles of lamination process

Lamination has been proved to be an effective process that combines multiple substrates together. The goal of lamination is to produce a stable, multi-layer structure with properties that cannot be achieved by a single material.

2.4.1.1.1 Adhesion in laminating

Strong adhesions between layers are the fundamental requirement of lamination process, which can be attained by adhesives, heat, pressure, or mechanical bonding. There is direct interactions between adhesion and other properties, such as tear strength, peel strength, and flexing property (Dartman & Shishoo 1993). Adhesion can be described as the attraction between two contacting surfaces, which is mainly determined by cohesion forces of bulk materials and interactions between the layers (Wicks et al. 2007). In a simple case of a flat and smooth interface, the work of adhesion, W_a , i.e. the required energy to separate two contacting surfaces, is defined as:

$$W_a = \gamma_1 + \gamma_2 - \gamma_{12} \quad (1)$$

where γ_1 and γ_2 are the surface tensions of the two components in contact, respectively, and γ_{12} is the interfacial tension (Dartman & Shishoo 1993). The adhesion on the interface is summarized in Equation (1) concerning surface energy, indicating that adhesion is a function of the surface/interfacial energies of materials, which are highly related to the nature of

intermolecular interactions (Dartman & Shishoo 1993). Generally, larger work of adhesion will provide stronger adhesion. Two materials with high molecular affinity will yield strong adhesion simply because high work of adhesion can be generated. Since the work of adhesion is mainly determined by the chemical properties of materials, the molecular affinities of polymer, fabric substrates and adhesives are the foundations to obtain good adhesion in laminated structures. When different components in a laminated structure do not have adequate chemical affinity to each other, a third material (usually called ‘tie-layer’) with good affinity to both components can be added to effectively enhance the adhesion strength (Cole & Macosko 2000).

In addition, interfacial diffusion of polymer chains can also affect the adhesion. When there are two phases interacting with each other sufficiently, polymer molecules will possibly diffuse beyond the interface to form entangled structures of the two phases (Shim 2010). This process can be fairly active when polymer molecules are highly mobile and free to vibrate and rotate. At low temperatures, polymers exist as solids in which the molecular chains vibrate gently. As the temperature of the polymer is increasing, a temperature range is reached in which the molecules gradually become more flexible and mobile and can penetrate deeper into a different phase by diffusion over permitted period of time. The temperature required to cause this increase in molecular freedom is known as the glass transition temperature (T_g) (Jacob et al. 2008). Therefore, time and temperature in lamination processes play important roles to achieve high adhesion strength.

Mentioned in Shim’s review (Shim 2010) on coated and laminated fabrics, it is claimed that wetting and spreading are also very important factors concerning the formation of an adhesive interface between two components in the lamination process. In the wetting

phenomena, interactions between liquid-solid, liquid-liquid and liquid-air are involved and represented by respective interfacial tensions (Shim 2010). As shown in Figure 2.9, when a liquid and a flat solid body are in contact, the liquid may form beads where the angle between the liquid-air and liquid-solid interfaces stabilizes and reaches a certain value, which is known as the contact angle.

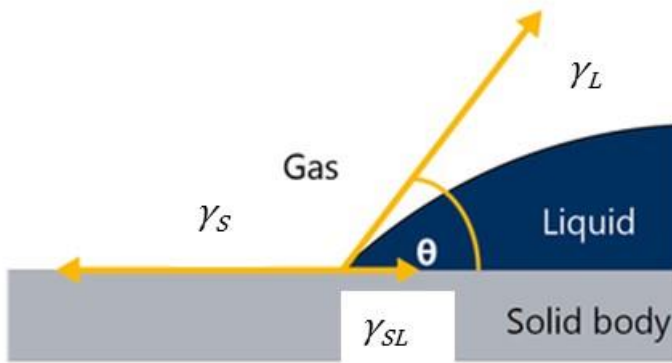


Figure 2.9. Interfacial tensions and the static contact angle (<https://www.kruss.de/services/education-theory/glossary/contact-angle/>).

If there is no relative motion of the contact line with the solid body, this angle is then called a static contact angle. The static contact angle is determined by the balance of interfacial tensions in the three-phase contact line. It can be derived from the balance of interfacial tensions, see Figure 2.9, and is given by Young in 1805 (Shim 2010):

$$\cos\theta = \frac{\gamma_s - \gamma_{SL}}{\gamma_L} \quad (2)$$

where θ is the static contact angle, γ_s the solid-air interfacial tension, γ_{SL} the liquid-solid interfacial tension, and γ_L is the liquid-air interfacial tension. Wetting phenomena can be characterized by the value of the static contact angle. A low value means high wettability and a high value indicates poor wettability. Thus, wetting and spreading are important criteria for obtaining good adhesion (Dartman & Shishoo 1993). However, in many laminating processes,

the contact line is in motion, where the viscosity of the fluid will also influence interface formation and adhesion. In practice, the interface between two components in laminated materials is normally rough and with grooves and pores. Depending on the wettability of the liquid adhesive, the roughness of surfaces can affect the adhesion strength differently. A liquid adhesive with good wettability spreads on a rough substrate surface and fills grooves and pores. As a result, the actual area of contact is larger than the geometrical area, causing the formation of an intimately bonded interface between the adhesive and the substrate surface. A moderate level of surface roughness thus enhances bonding strength (Fung 2002). However, when the wettability of the liquid adhesive is poor, the effective area of contact for bonding is even reduced, leading to a weaker adhesion strength eventually.

Textile fabric substrates used for lamination are usually porous, so penetration through the structure is fairly common. If the liquid adhesives penetrate into fibrous structures, a considerably larger interface area can be obtained, producing a strong mechanical interlocking. As a result, adhesions between two layers in laminated fabrics is more complicated and usually a combination of mechanical interlocking and interfacial interactions (Dartman & Shishoo 1993). Adhesion is therefore closely dependent on adhesive penetrations. However, there is an optimum degree of penetration beyond which degradations of mechanical properties will become more significant. When the liquid adhesives penetrate deep into the fibrous structures, adhesion increases due to the mechanical interlocking effects. However, the yarns within the fabric structures lose the freedom of moving and rotating and becomes stiff. This will cause the laminated structure to be weakened due to its inability to relieve stress concentrations (Farboodmanesh et al. 2005). Moreover, excessive flowing of the liquid adhesive, in extreme cases, will strike through the thickness of the whole fabric and flow away from the surface,

hence resulting in the formation of a poor bond (Fung 2002). Thus, penetration in the laminating process should be controlled to balance good interfacial adhesion and preserve the flexibility of the structure. Here, it is necessary to understand that wettability is not the only factor to determine the penetration process. Other factors, such as fabric structure, viscosity of the liquid adhesive, temperature, pressure applied during the process and method of lamination, all have some impact on the degree of penetration (Shim 2010).

The controlling the parameters in the lamination process is critical to producing high quality laminate composite materials with balanced properties. The fundamental property of the laminated structure is undoubtedly the interfacial adhesion between all the components in contact. To achieve strong interfacial bonding with any given adhesive and material combinations, optimum temperature, pressure and speed settings must be established by thorough trials. The best conditions can be specific for different material compositions, so a well-designed parametric study based on a good understanding of raw material properties is very important. However, there is barely a few publicly available studies focusing on the adhesion evaluation and discussion to establish optimum process parameters. Therefore, it is worth conducting a lamination process parametric study to understand the effects of all the parameters on the adhesion property on any given set of laminated materials.

2.4.2 Seaming of Hull Material

Seaming process is as important as the design and development of the base material to build airship hull. Although it is the base material that carries the load, the seams connecting the base materials must be able to effectively and efficiently transfer the load from one piece of the base material to another. The load transfer process would inevitably create tensile as

well as shear forces on the seamed areas. Thus, a good seam must be able to provide tensile strength that is equal to or greater than the strength of the base material, so that the integrity of the whole hull structure can be preserved (Zhai & Euler 2005). Butt seams and lap seams are the two most typical seam designs for hull envelope material seaming. As shown in Figure 2.10 below, for a typical butt seam, the base material is butt-joined with a special structural tape as the butt strap. The seam needs to be heated and cooled under pressure to ensure good bonding (Islam & Bradley 2012). This strap carries the entire load across the seam, whereas the outer strip of weather-resistant material is bonded there purely to seal the seam against the environment and add some extra gas barrier properties to the whole seam structure. The structural tape used as the butt strap is specially woven to have high strength across its width and is impregnated with the bonding agent.

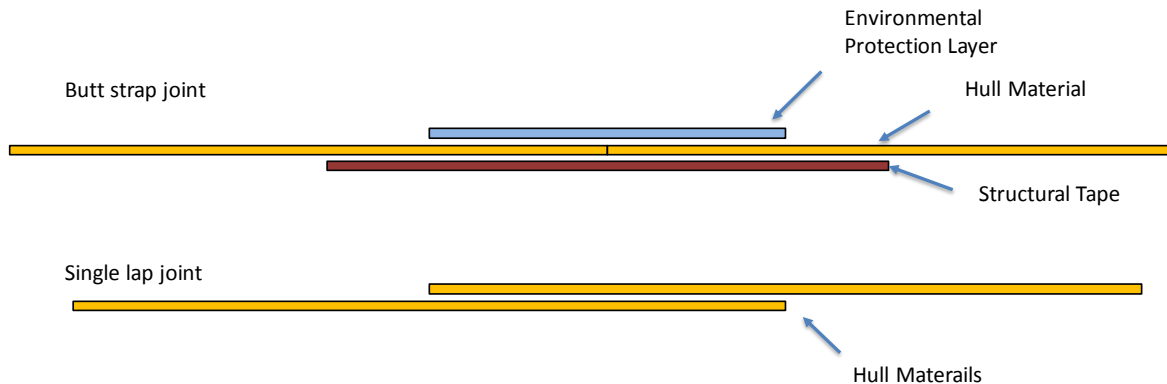


Figure 2.10. Typical seam designs for airship hull materials (Islam & Bradley 2012).

Compared with the butt seam, a lap seam is a much simpler design providing significant convenience to the real industrial seam production. However, there is a big restriction namely, the base laminate material is required to be structurally bondable on both sides (Zhai & Euler 2005).

Besides the strength requirement, severe conditions in the airship operational environment such as the cryogenic temperature and thermal cycling are also hazardous for seam integrity in

the long term. The seam is required to absorb stresses and have high failure strength even at extreme service temperatures varied during a day. One major factor determines the seam performance is the adhesive polymer bulk properties. As previously mentioned, glass transition temperature (T_g), is a very useful measurement of physical property, reflecting the behavior of polymeric adhesives. In general, tensile strength and elastic modulus increase below the T_g , whereas flexibility, toughness and interfacial adhesion decrease. Therefore, the relationship between the T_g and the service temperature limits is a significant factor in predicting the property requirements of polymeric adhesives (Edward M. Petrie 2003a). Overall speaking, polymers with low T_g are more resistant to cryogenic temperature which imposes greatest challenges. Several adhesives are considered good candidates for structural and cryogenic temperature application. First, polyurethane has the most outstanding low temperature properties compared with other commercially available adhesives. In general, the polyurethane adhesives are easy to process and bond well to a diverse collection of substrates. Certain grade of polyurethanes can also serve as good gas barrier component to stop helium leakage per Kang et al. (Kang et al. 2006). Next, silicone adhesives exhibit consistently good performances over a wide temperature range from cryogenic temperatures up to as high as 250 °C. Generally, silicone elastomer seams show superior performance when peel resistance rather than tensile or shear, is primarily considered. However, most of the silicone-based adhesives by nature have poor gas barrier property. Last but not the least, thermosetting acrylic resins are usually considered great structural adhesives at temperatures down to -40 °C, which also possess fair peel and creep resistance. Another principal factor to be considered is the effect of thermal cycling, which will result internal stress concentrations at the seam interfaces. Different coefficients of thermal expansion (CTE) and thermal conductivity between the adhesive and

the base laminate material can issue in severe residual stress. These internal stresses tend to be magnified at cryogenic temperatures, and is able to induce adhesive rupture of seams (Edward M Petrie 2003b).

As discussed in the previous section, some of the adhesion mechanisms, including wetting, thermal diffusion of polymer molecules across the interfaces and chemistry bonding between molecules, also apply to the scenarios of adhesively joined seams. Thus, a good control of time, temperature and pressure is also able to have significant impact in seaming process to attain high adhesion strength between the surfaces of the base laminate envelope materials. When bonding problems with films and plastics are still experienced, surface treatment of the film or plastic with corona discharge or a plasma process sometimes helps. Chemical cleaning or pretreatments with flame are also reported to be helpful. Normally, adequate shear strength of the adhesives can be achieved as long as the area of the bonding overlap is sufficiently large. However, the peel resistance is directly related with the level of interfacial adhesion. To achieve a higher peel strength of the seams, the seaming process must be optimized to obtain maximum adhesion.

Komatsu et al. (Komotsu et al. 2003) evaluated the bonding strength of some high-specific-strength laminated fabric for SSA applications, focusing on the high-temperature tensile strength and creep properties because the strength of the envelope structure is determined by the seam shear strength. As stated in (Komotsu et al. 2003), the bonded seam strength is determined by the bonding shear strength of the layer in contact with the adhesive. The adhesive layer was made of materials with rubber properties, such as polyurethane, silicon, and polyester elastomers. In that work, polyurethane was first applied to the protective layer and adhesive. Polyurethane keeps its flexibility and strength at temperatures from -80 °C to

+70 °C. For the Zylon® fabric reinforced envelope, creep properties and overlap bonding width effects were investigated in a high-temperature environment. For almost all the test specimens, the initial rupture point was at the edge of the seam. As suggested by that work, an overlap width of 40 mm is enough for practical use in a broad temperature band (Komotsu et al. 2003). The average tensile strength of the 20 mm seams was tested to be significantly lower than those from 40 mm, 60 mm and 80 mm. Then a creep test was conducted using the same envelope. It is already mentioned previously that, among high-performance fibers, Zylon® fibers had the best creep properties, with a creep failure time of 2 years at 60% breaking load at room temperature. However, the lifetime of the envelope structure with adhesive seams may be much shorter when it is exposed to a high-temperature environment. The seam tensile strength was evaluated at about 1000 N/cm, and the creep failure time was 69 days under the conditions of 20% maximum load at a temperature of 70 °C and under a 35% load at only 7 days. This fact shows that some method must be introduced to keep the envelope-bonding part at a low temperature or under low-stress conditions.

It is unlikely to eliminate seams completely from the building of airship hull structure using traditional technologies. Strength wise, seams are demanded to be as strong if not stronger than the base envelope material. However, to achieve a relatively high tolerance in manufacturing, seams are usually made with extra amount of adhesive and thus inevitably become rigid and heavy. Even though most adhesives for seaming purpose are capable to provide high shear strength to prevent seam adhesive failure, poor peel resistance is still known as the most troublesome weak spot. Additionally, for SSA applications, the gas barrier property of the seamed area is also a critical challenging factor. The gas permeation through the seams would not only be determined by the intrinsic properties of adhesives but also the structure

integrity of the seams concerning the interfaces between adhesives and envelope materials. Given that the measuring of gas permeation rate through seams is intrinsically challenging, the understanding of the permeation mechanism is far from adequate. For airship material seams specifically, there is no related research found in the era of gas permeability study. There is an urgent need to investigate and establish some reliable methods to accurately measure the gas permeation through the seams made with flexible composite laminates.

2.5 Evaluations of Laminated Envelope Materials

The proper design of an airship envelope material can be affected by many material properties. In this section, the background of some of the more critical properties is considered. The previous sections have shown that the laminated envelope materials are complex manufactured structure. The behavior of the laminated envelope materials usually cannot be directly related back to the properties of their component parts. Therefore, small changes in the manufacture or structure can also have significant effects on these properties.

Miller et al. discussed information on the design requirements of low altitude non-rigid and semi-rigid airship envelopes and materials from a designer's point of view, as well as material development and qualification information from a manufacturer's point of view. Special consideration is given to material tear resistance. For the Zeppelin LZ N07 shown in Figure 2.11 (a), a laminate of polyester base cloth and Tedlar® film was selected for the main hull material (Figure 2.11(b)). The outer cover of PVF film serves as great weathering and environmental barrier to protect the rest of functional and structural elements. Although the protection from PVF film is proved sufficient for most of the low-altitude airship applications, long endurance of the hull material cannot be guaranteed by using merely PVF film at

stratosphere since the envelop material is facing much harsher environment with intensive UV radiation, high concentration of Ozone and Atomic Oxygen and large diurnal temperature variations.

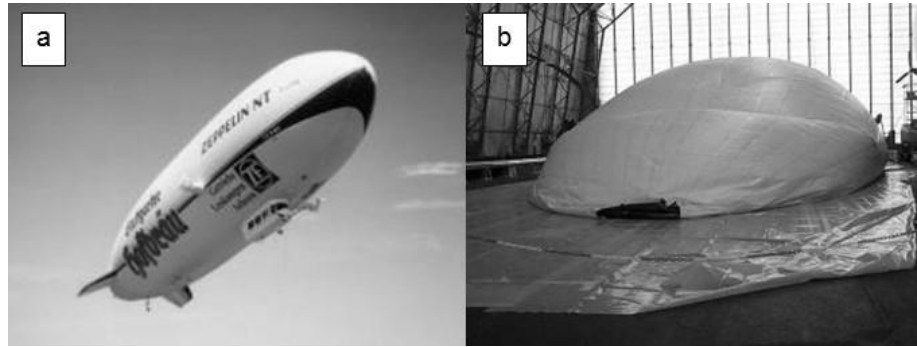


Figure 2.11. (a) Zeppelin LZ N07, (b) Envelope Material (Miller & Mandel 2000).

Per their discussion in (Miller & Mandel 2000), one critical property for airship envelop is its tear resistance ability after damage is introduced. As the tear resistant property is determined by the overall design of the textile fabric, Table 2.4 is created to help understand the effects of varying fabric configurations in correlation with performance properties. It presents the effect on selected more critical properties as the fabric configurations are varied for the same given mass of yarns. In general, these trends hold true for most laminated woven fabrics(Miller & Mandel 2000).

Table 2.4 Fabric configurations and corresponding properties (Miller & Mandel 2000)

Fabric Attributes	Properties			
	Tensile Strength	Tear Strength	Amount of Coating (Mass)	Fabric Stability
Smaller Yarn Denier	Same	-	-	+
Plain Weave	Same	-	-	-
Ripstop Weave	Same	+	+	-
Higher Yarn Count	Same	-	-	+

* decrease (-) and increase (+)

Table 2.4 shows the intricate balance in the design of textile materials. For instance, to minimize the weight, a small denier, high count, plain weave fabric would be more desirable. While to maximize the tear strength, the exactly opposite selections would be made to weave a high denier, low count, rip-stop fabric. Nevertheless, it might not be the case when the fabrics were thickly coated or well laminated that the yarns could be securely anchored by the polymeric adhesive compound (Miller & Mandel 2000). Miller and Mandel also constructed a table of the required testing with standards or related descriptions where standard is not applicable. In Table 2.5, most of the necessary tests for airship hull material qualification can be found.

Table 2.5 Sample Testing for Airship Hull Materials (Miller & Mandel 2000)

TEST	TEST METHOD
Weight	FED-STD-191 TM5041
Bow and Skewness	ASTM D 3882
Surface Finish – Interior	Visual Inspection
Surface Finish - Exterior	Visual Inspection
Water Release - Exterior	FED-STD-191 TM5504
Blocking at Elevated Temperature	FED-STD-191 TM5872
Surface Polymer Characterization	Infrared Spectrophotometry
Tensile Modulus	ASTM D 751
Breaking Strength/Elongation - Strip Method Ultimate Tensile	FED-STD-191 TM5102
Breaking Strength/Elongation - Strip Method, Ultimate Tensile after Weather Exposure (QUV Chamber)	FED-STD-191 TM5102
Seam Tensile Strength - Heat Seal	FED-STD-191 TM5102
Seam Tensile Strength at Elevated Temperature Heat Seal	FED-STD-191 TM5102
Base Cloth Breaking Strength - Ravel Strip Method Ultimate Tensile	FED-STD-191 TM5104
Creep/Hysteresis Evaluation	Vendor Test Method
Tear Strength - Cut Slit	MIL-C-21189 Para 10.2.4 FAA P-8110-2, Appendix A
Tear Strength -Tongue	FED-STD-191 TM5134
Coating Adhesion -Heat Seal Seam, Back/Structural Tape	FED-STD-191 TM5970
Coating Adhesion - Heat Seal Seam, Cover Tape	FED-STD-191 TM5970
Coating Adhesion - Cement	FED-STD-191 TM5970
Film Ply Bond Adhesion (Dry)	FED-STD-191 TM5970
Film Ply Bond Adhesion (Elevated Humidity)	FED-STD-191 TM5970
Seam Deadload - Elevated Temp (Underwater) Heat Seal	Vendor Test Method
Seam Deadload - Elevated Temp (Hot Air) Heat Seal	Vendor Test Method
Seam Deadload -Elevated Temp (Underwater) Cement	Vendor Test Method
Seam Deadload - Elevated Temp (Hot Air) Cement	Vendor Test Method
Cylinder Deadload - Elevated Temp (Underwater)	Vendor Test Method
Inflated Cylinder Flex Testing	Vendor Test Method
Low Temp Flex	ASTM D 2136
Helium Permeability	ASTM D 1434 or Vendor Test Method
Helium Permeability after Weather Exposure (QUV Chamber)	ASTM D 1434 or Vendor Test Method
Seam Helium Permeability	ASTM D 1434 or Vendor Test Method

2.5.1 Mechanical Characterizations

2.5.1.1 Tensile Properties

Uni-axial tensile strength is probably the property most often quoted for an envelope material. Serving as the most fundamental data to support the SSA design, high specific strength (strength/density) is always preferred. Komatsu et al. (Komatsu et al. 2003) from Japan Aerospace Exploration Agency (JAXA) experimentally developed and evaluated the tensile strength of more than thirty high-specific-strength laminated fabric for SSA platform,

involving the applications of a large number of different high performance fiber and film materials. Among all these laminated envelope prototypes, high performance fibers including Vectran®, Kevlar® and Zylon® were used as the load-bearing components. Tedlar films with and without Aluminum evaporation were used as the weathering layer, and Mylar and ethylene vinyl alcohol (EVOH) films integrated as gas retention layers. Based upon the comparisons of strength results, laminated envelope with Zylon® fabrics as the core layers exhibit the most satisfactory mechanical performance. Further study of the temperature effects on mechanical properties also verified that the high specific strength of Zylon® based envelope materials can be well maintained at both high and low temperatures. Among high-performance fibers, Zylon® fibers also have the best creep resistant performance, with a creep failure time of two years at 60 % breaking load at room temperature (PBO, Toyobo). Hence, it was confirmed that Zylon® fiber is undoubtedly the most promising candidate to build a reliable, enduring load-bearing element for SSA applications.

To visualize the strength and weight correlations of envelope materials in development, some published results in the literature (Komotsu et al. 2003; Maekawa et al. 2008; McDaniels et al. 2009; Kang et al. 2006; Gu 2007; Xu 2009; Li et al. 2010) were put together to obtain a more comprehensive evaluation. Comparisons of the material tenacity vs. weight and the strength-to-weight ratio vs. weight of the laminate materials are presented in Figure 2.12 and Figure 2.13, respectively.

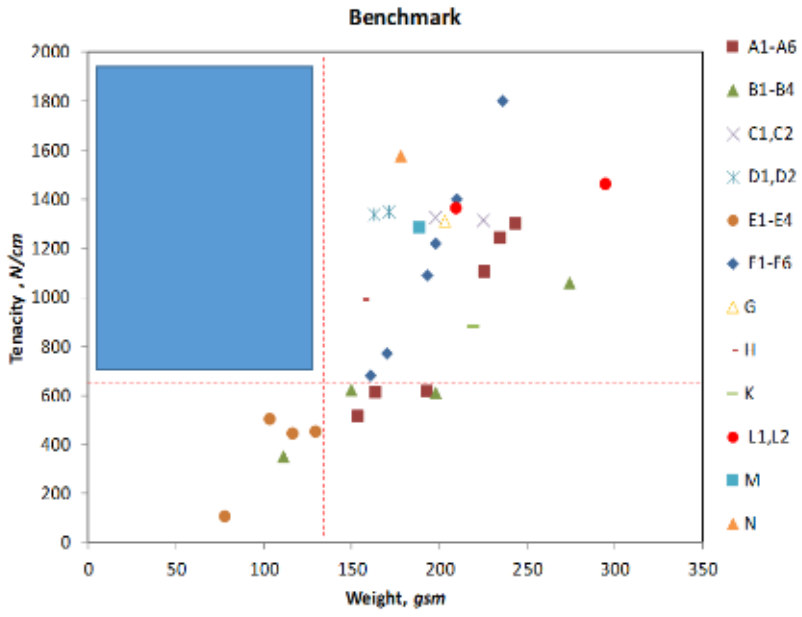


Figure 2.12. Comparison of the tensile strength and weight of the laminate materials developed in the literature (Komotsu et al. 2003; Maekawa et al. 2008; McDaniels et al. 2009; Kang et al. 2006; Gu 2007; Xu 2009; Li et al. 2010).

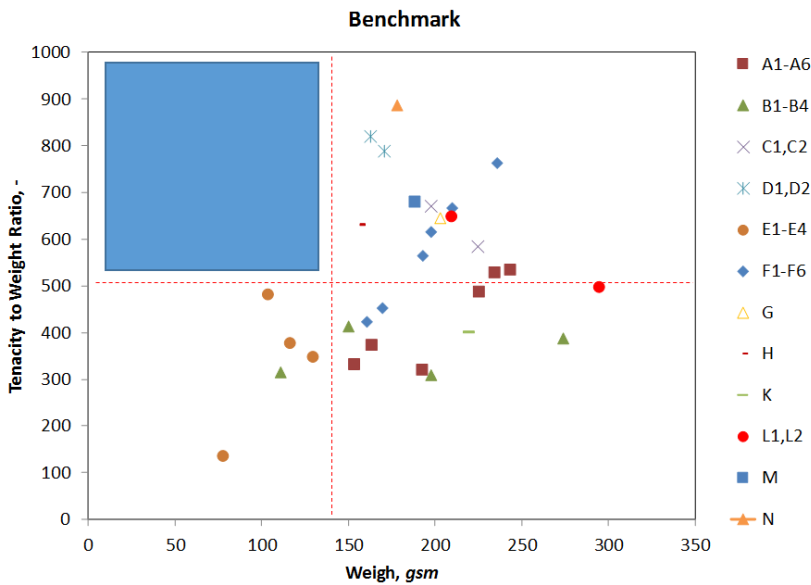


Figure 2.13. Comparison of the strength-to-weight ratio of the laminate materials developed in the literature (Komotsu et al. 2003; Maekawa et al. 2008; McDaniels et al. 2009; Kang et al. 2006; Gu 2007; Xu 2009; Li et al. 2010).

Detailed material information of all collected airship envelope samples can be found in Table 2.6. It is obvious that Zylon® is predominantly used as the core strength element of the

laminated envelope materials studied in most recent years. Generally, we saw a leap in the specific strength of the Zylon® fabric reinforced envelope materials. Nonetheless, there is still room for further specific strength improvement, namely reducing the laminate weight by integrating thinner and lighter polymeric films and depositing considerably thinner functional coatings to eliminate one or two unnecessary layers. Besides modifications of gas retention and weathering components, load-bearing layer and adhesives layers can also be adjusted for the purpose of weight reduction. The most direct approach has to be making woven fabrics with lower denier Zylon® yarns to further reduce the net weight and thickness of the textile reinforcement. Observed from the collected data in the literature, the lowest linear density of Zylon® yarns used to make woven fabrics was 250 *denier*. Preliminary work has been done in this regard to have successfully woven structurally stable plain weave fabrics with 150 *denier* Zylon® yarns, attaining a significantly reduced weight when compared with the fabric weight values reported in the literature. In addition to the fabric net weight reduction, the thinner fabrics obtained also allow less adhesives to be applied to achieve adequate level of interfacial adhesion. This also facilitate the reduction of the overall weight of the composite laminate by avoiding thick layers of adhesives only adding a lot of dead weight.

Table 2.6 Detailed Structural Information of Laminate Materials developed in the Literature (Komotsu et al. 2003; Maekawa et al. 2008; Mcdaniels et al. 2009; Kang et al. 2006; Gu 2007; Xu 2009; Li et al. 2010)

ID	Scientific Work	Remarks	Material Description	Tenacity, N/cm	Weight, gsm	Tenacity-to-Weight Ratio, kN.m/kg
A1	Komatsu et al. 2003	"Z500_100" means 500 denier Zylon fibers are used and fabric weight is 100 gsm, PU:Poly urethane, XL:EVOH	Z500_100-PU-XL	1300	244	533
A2			Z250_94-PU-XL	1240	235	528
A3			Z250_79-PU-XL	1100	226	487
A4			Z250_47-PU-XL	615	193	319
A5			Z250_47-PU	610	164	372
A6			Z250_40-PU	510	154	331
B1	Komatsu et al. 2003	V:Vectran, PE:Polyethylene, XLA:Aluminum stuck EVOH	V-PU-XL	610	198	308
B2			V100_31-PE-XLA	620	150	413
B3			V-PU-XL	350	111	315
B4			V200_102-PU-XL	1060	274	387
C1	Komatsu et al. 2003	TA:Tedlar with Aluminium deposit, T: Tedlar, PUA: Poly urethane with Aluminum deposit	TA-Z250_110-PU	1327	198	670
C2			T-Z250_110-PU	1313	225	584
D1	Komatsu et al. 2003	Z250_110-PUA-XLD	Z250_110-PUA-XLD	1337	163	820
D2			Z250_110-PU-XLD	1350	171	789
E1	Komatsu et al. 2003	N:Nylon, K: Kevlar, H:Hydrel, MI: Mictron (for internal gas bag or light weight use)	N30_40-PU-XLD	105	78	135
E2			K200-H-MI	450	130	346
E3			V-H-MI	500	104	481
E4			Z-H-MI	440	117	376
F1	Komatsu et al. 2003	M: Mylar Thick Zylon fibers are sandwiched by two Mylar films	Z500_37-M	680	161	422
F2			Z1000_74-M	1220	198	616
F3			Z1500_111-M	1800	236	763
F4			Z1000_44-M	770	170	453
F5			Z1500_67-M	1090	193	565
F6			Z2000_89-M	1400	210	667

Table 2.6 Continued

G1	Sasaki et al. 2005	For 250 m long airship (Z4040T-AB)	Al&PVF-PU-Z-PU	1310	203	645
H1	Maekawa et al. 2005	For 150 m long airship (Z2929T-AB)	Al&PVF-PU-Z-PU	993	157	632
J1	McDaniels et al. 2009	Heavy Zylon Nonwoven Fabric	Z(NW)_349	2833	>349	<812
J2	McDaniels et al. 2009	Medium Vectran Nonwoven Fabric	V(NW)_139	916	>139	<659
K1	Kang et al 2006	Vectran woven Fabric, PUC: PU coating	V_109-PUC-PVF-PU	883	220	401
L1	Gu 2007	Lindstrand HALE Airship Envelope	V (NW)	1460	295	495
L2	Gu 2007	For 200 m long airship	na	1360	210	648
M1	Cao & Gao 2009	Zylon plain weave (Warp)	Z_87-PVF_52-PU_25*2-PUC_5~8	1013	189	536
		Zylon plain weave (Weft)		1281		678
N1	Li et al. 2010	Zylon plain weave (Warp)	Z990_78-M_40-PVF_30-PU_30	1578	178	887
		Zylon plain weave (Weft)		1356		762

The goal of next generation laminated envelope materials should be not only lighter than any other laminates with similar tensile strength, but also stronger than any laminate with the similar weight. The strength-to-weight ratios are expected to be higher than all the laminates developed in previous studies. Generally speaking, the mechanical strength data should fall into the blue square zones in Figure 2.12 and Figure 2.13 to be qualified as promising candidate for SSA applications.

More comprehensive and in-depth studies on the tensile property of the laminated envelope materials were also conducted to help better understand their behaviors toward the mechanical loading in varied conditions. Kang et al. (Kang et al. 2006) conducted uni-axial tensile tests for the Vectran® fabric reinforced envelope materials to attain experimental results of tensile properties and then compared with the results predicted by the geometrically non-linear finite element analyses. As shown in Figure 2.14, the stress-strain curve of an envelope material was simply considered as a smooth curve with significant nonlinearity. The modulus

of the material increased to the tensile strain, and a modulus of about 9.5 GPa was found at higher strain range when the steady state is reached.

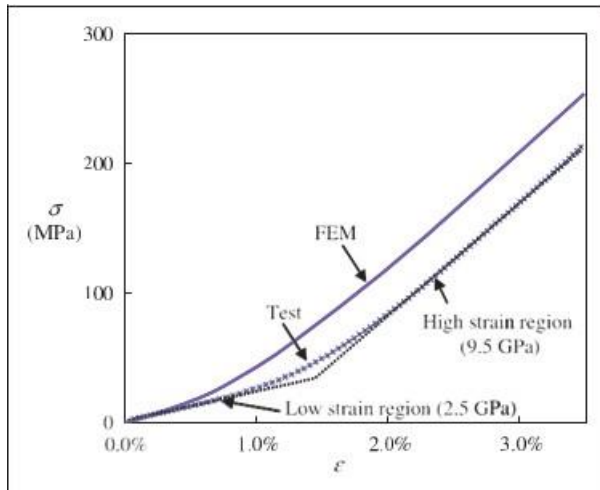


Figure 2.14. Tensile stress-strain curve of Vectran® fabric incorporated envelope material (Kang et al. 2006)

They also performed uni-axial tensile tests in a thermal chamber at low, medium (room condition), and high temperatures to investigate the dependence of tensile strength on temperature. The stress-strain curves generated from the tensile tests for various temperatures are shown in Figure 2.15. It can be clearly observed that curves with steeper slope were obtained for decreased temperatures resulting in higher modulus. The steady-state stiffness modulus calculated at the lowest temperature of -75 °C was 47% larger than that calculated at the room temperature of approximately 25 °C. This behavior correlates well with the stiffening of Vectran® fibers with a 40% modulus increase at a cryogenic temperature.

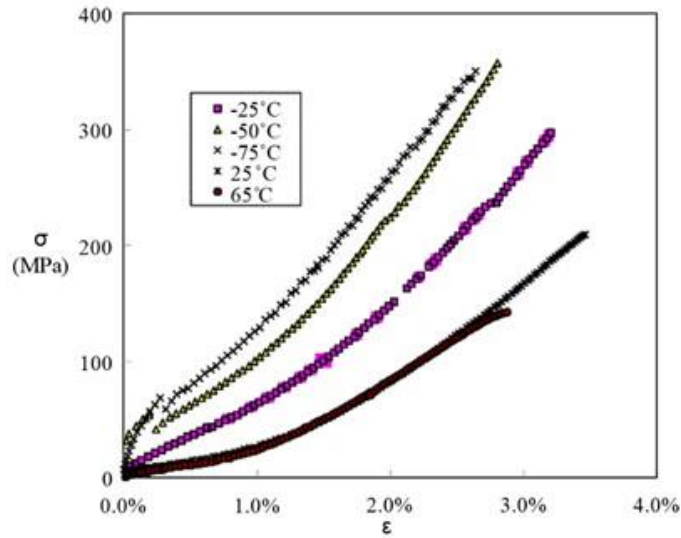


Figure 2.15. Tensile test results at various temperatures (Kang et al. 2006).

With a similar Kevlar® fabric as reinforcement in envelope material, Meng et al. continued on with some more in-depth investigations based on results from uni-axial tensile testing. By observing the SEM images of the fractured specimens (Figure 2.16), two distinct failure modes of the envelope material are identified, namely interface failure and fiber bundle fracture. The failure mode of debonding between fibers and polymer films correlates well with the force-displacement curve obtained, shown in Figure 2.17 (Meng et al. 2016).

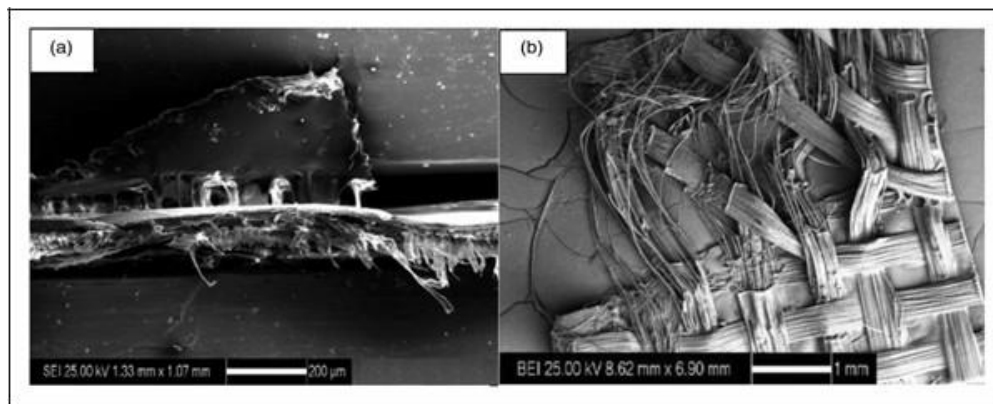


Figure 2.16. SEM image of failed specimens: (a) delamination and (b) fiber breakage (Meng et al. 2016).

As can be seen from Figure 2.17(a), a significant orthotropy is observed for the load-displacement curve of the envelope material. Potentially due to the fact that weft yarns have slightly higher initial crimps, the maximum tensile force in the weft direction is about 13.4% lower than that in the warp direction. As is shown in Figure 2.17(b), there are two significant nonlinear regions on the force-displacement curves in both warp and weft directions. This may be attributed to the occurrence of debonding between the fabric substrate and the polymeric adhesives/coating, which is also found by Chen et al. in their research (Chen et al. 2014).

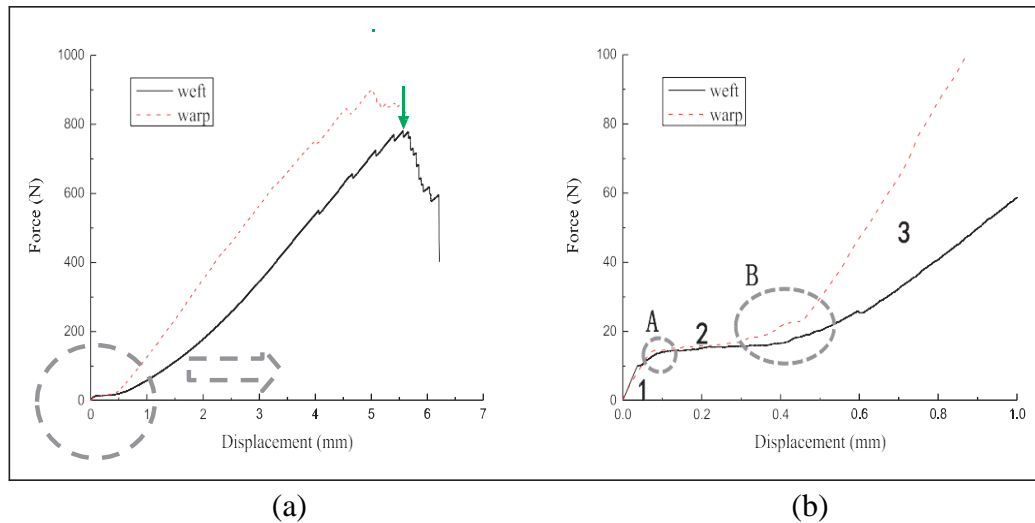


Figure 2.17. Measured force-displacement curves of the uni-axial tensile tests; (a) global curve and (b) magnification at the low strain range (Meng et al. 2016).

For the specific coated/laminated fabric, Chen et al. further proposed a simple and concise stress-strain model as shown in Figure 2.18. The stress-strain curve consists of three linear regions and two non-linear regions. The five characteristic regions in total can be described (Chen et al. 2014):

OA: initially, the composite behaves as an undamaged, linear elastic material, indicating that the fabric and coating are extended together;

AB and CD: the first and second non-linear regions, respectively. The coating may be debonded from the fabric, and the fabric behaves as a non-linear material;

BC: the second linear stage, where the whole material properties are primarily controlled by the yarns. The yarns elongate linearly again with a smaller slope (elastic modulus) than that of OA region;

DE: fabric elongate linearly again after point D, and at point E most of yarns fractured.

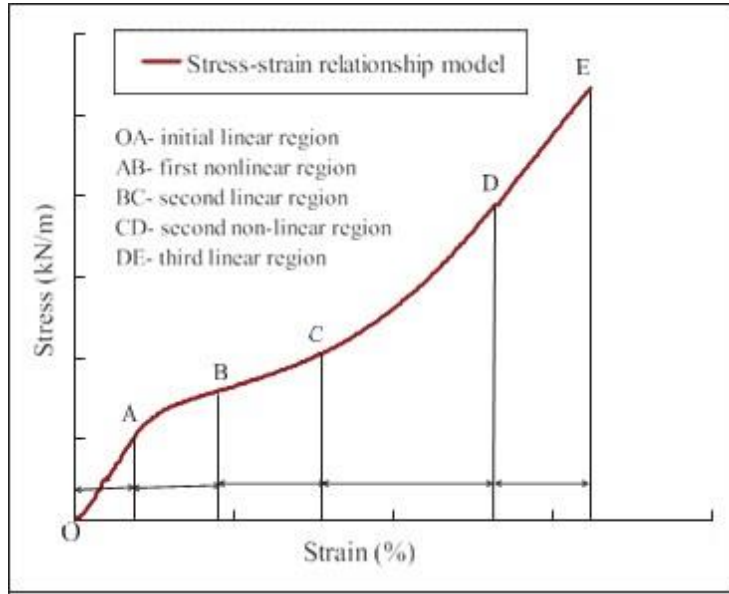


Figure 2.18. The stress-strain model of the coated fabric (Chen et al. 2014).

In the five regions, the stress-strain relationships were expressed as:

$$OA, BC, DE: \sigma = a \cdot \varepsilon + b \quad (3)$$

$$AB: \sigma = a \cdot \ln \varepsilon + b \quad (4)$$

$$CD: \sigma = a \cdot e^{b \cdot \varepsilon} \quad (5)$$

where σ is the stress, ε is the strain, and a and b are the best-fit parameters that were determined by the experimental data (Chen et al. 2014).

2.5.1.2 Tear Strength

2.5.1.2.1 Central Slit Tear Testing

It is mentioned in an airship design and manufacture report (Miller & Mandel 2000) that central slit tear testing is an effective method of measuring the material capability to resist tearing after initial damaged. The Federal Aviation Administration (FAA) adopted this test in FAA P-8110-2, “Airship Design Criteria”, 10 Oct 86, Appendix A. The Test setup is briefly shown in Figure 2.19 below.

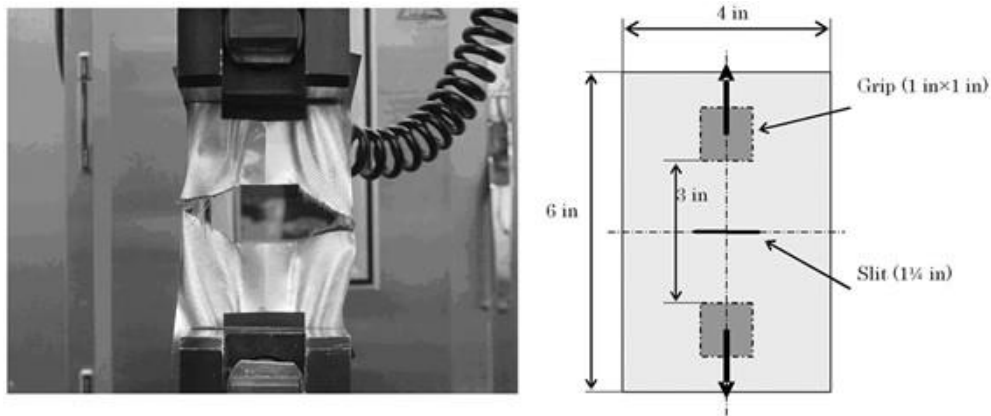


Figure 2.19. Cut slit tear test (Maekawa et al. 2008).

This method can better simulate the tearing action of a damaged material than do other standard tear testing methods, e.g. tongue tear test and trapezoid tear test. This method is normally used to determine merely the tear strength of the material. As is shown in Figure 2.19, the test sample is required to be 101.6 mm (4 inch) wide x 152.4 mm (6 inch) long, having a 32 mm (1-1/4 inch) wide razor cut slit across the center of the sample normal to the longest dimension. Then the specimen is put symmetrically into jaws of a tensile testing machine with the longest direction being parallel to the loading direction. The jaws must be 25.4 mm (1 inch) wide and securely grip the yarns that were already cut in the material, and a gauge length of 76.2 mm (3 inch) is required to be set at the beginning of the test.

2.5.1.3 Tear Propagation

As mentioned above, in the design criterion of FAA-P-8110-2, it is only specified to measure the tear strength of an envelope material. However, the tear strength itself has no definite relationship with the actual tear propagation characteristics of the airship envelope material. Therefore, there have been several studies to establish the relationship (Maekawa et al. 2008).

2.5.1.3.1 Pressurized Cylinder Test

Using the air-pressurized cylinder to generate the bi-axial tensile field is the most reliable method for the development of airships (Maekawa et al. 2008; Miller & Mandel 2000). This method is able to maximally simulate the actual stress field, and longer tear length can be tested compared to the bi-axial tensile test (Chen & Chen 2016; Zhang et al. 2012; F. Wang et al. 2016; Chen et al. 2017; Liu et al. 2015). In this test, the bi-axial load is applied in stress-control mode. A generic sketch and a picture of the real specimen produced were shown in Figure 2.20.

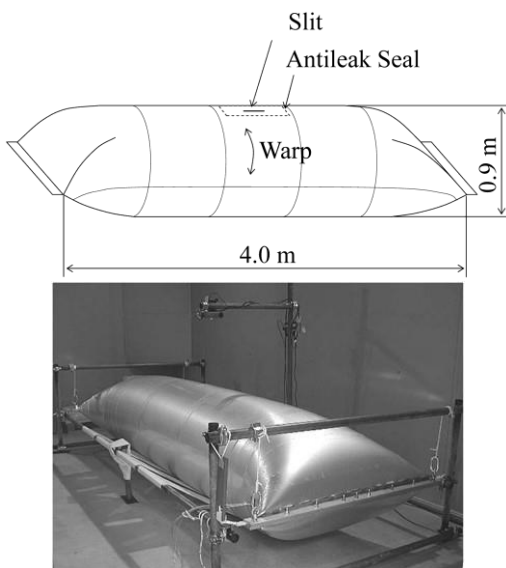


Figure 2.20. Pressurized cylinder test specimen (Maekawa et al. 2008).

The specimen is a cylinder closed at both ends and the slit is covered from inside by an expandable film to prevent air leakage. The specimen will be set in a stand and the pressure is increased at a constant speed. The slit is watched and recorded by a video camera. The gas filling will be stopped immediately when the tear starts to propagate, and depressurization is made.

2.5.1.3.2 Thiele's Empirical Formula

The general expression of Thiele's empirical formula can be written as follow:

$$\sigma = pr = \frac{C_l C_s}{L^n(1 + L/r)} \quad (6)$$

where p is the inflation pressure, r is the cylinder radius, C_s is the cut slit tear strength, L is the cut slit length. In this equation, C_l and n are the constants, which can be calculated via least-square method. The application of this method is beyond the range of this dissertation and thus not reviewed.

To establish the relationship between the tear strength, slit length and tear propagation property, many researches have been conducted. Miller and Mandel (Miller & Mandel 2000) carried out the tear propagation test with ILC cylinders (ILC Dover), as shown in Figure 2.21.

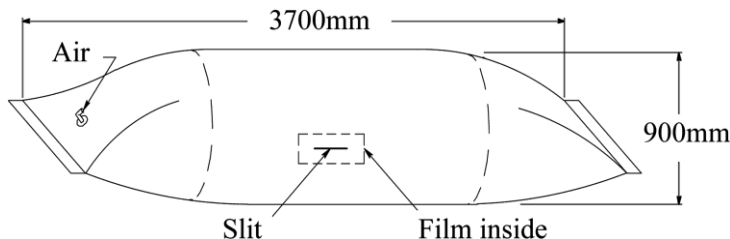


Figure 2.21. Schematic of ILC cylinder (Miller & Mandel 2000).

It was also confirmed that Thiele's empirical formula, which correlates tear strength with tear propagation stress, can be applied to the envelope used on Zeppelin NT (Figure 2.22).

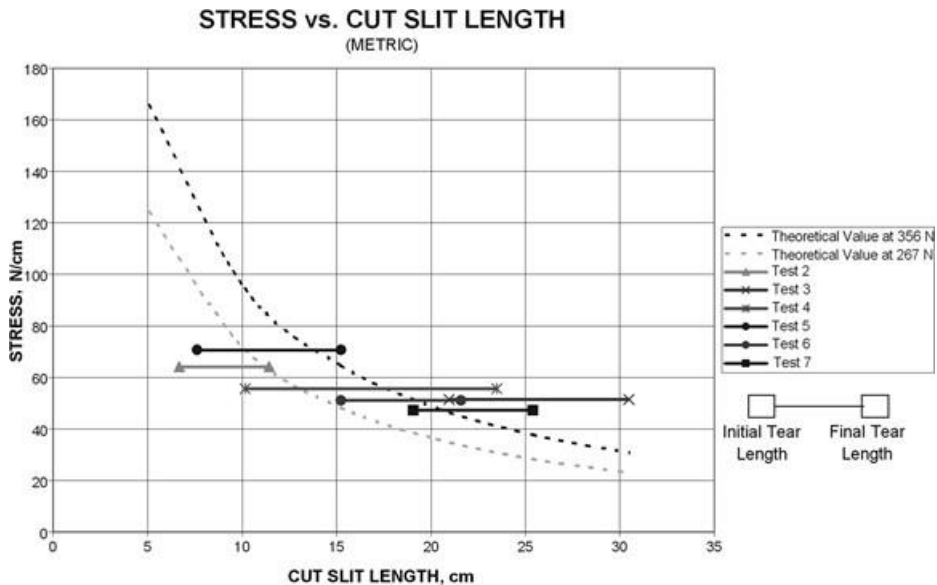


Figure 2.22. Stress vs. Cut slit length: compatibility of Thiele's formula with test data (Miller & Mandel 2000).

Maekawa et al. (Maekawa et al. 2008) completed another well-designed tear propagation study of a type of lightweight and high strength Zylon® envelope material using the same pressurized cylinder method. The envelope material used in this work, Z2929T-AB, was developed using Zylon® fabric as its load-bearing component. The tensile strength in the warp direction is averaged at 997 N/cm and the density is measured to be 157 gsm . The measurements were made to find the stress that initiates the tear propagation, and the experimental results are fitted to Thiele's empirical formula with a good correlation. Moreover, by using Thiele's empirical equation, the minimum slit length of the tear propagation under the limit load condition is estimated to be $\sim 40 \text{ mm}$ (Figure 2.23).

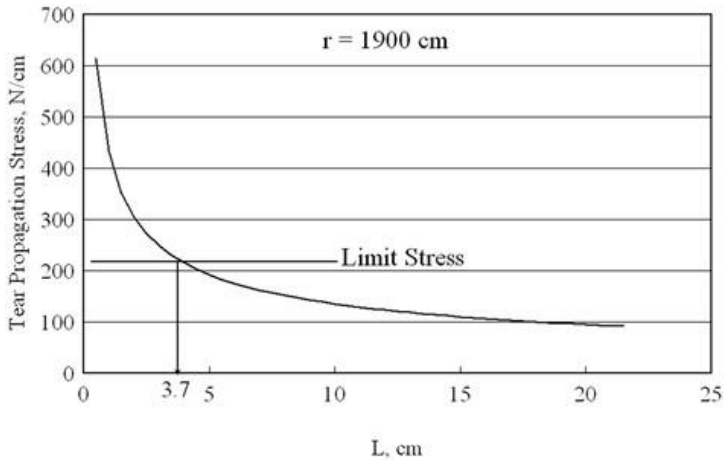


Figure 2.23. Allowable slit size of the technology demonstrator (Maekawa et al. 2008).

2.5.1.3.3 Tear Propagation Theory for Uni-axial Tear Test

Although satisfactory results were generated from previous work on tear propagation, the testing procedures for both the bi-axial tensile test or pressurized cylinder test are much more complicated than that of uni-axial tear test. Regardless of the inability to better simulate the real stress field on the hull material, uni-axial tear test is still an effective way to evaluate the tear strength. Wang et al. (F. X. Wang et al. 2016) experimentally investigated the tearing properties of a new coated woven fabric, GQ-6, made of ultra-high molecular weight polyethylene (UHMWPE) fiber for airship applications. Effects of the stretching rate, the initial crack length, and the initial crack orientation on the tear strength of the material were evaluated. By analyzing three of the most critical methods for tear propagation modelling, i.e. Griffith energy theory, the stress intensity factor theory, and the Thiele's empirical theory, it was found that the stress intensity factor theory gives the best correlation with the test data, shown in Figure 2.24.

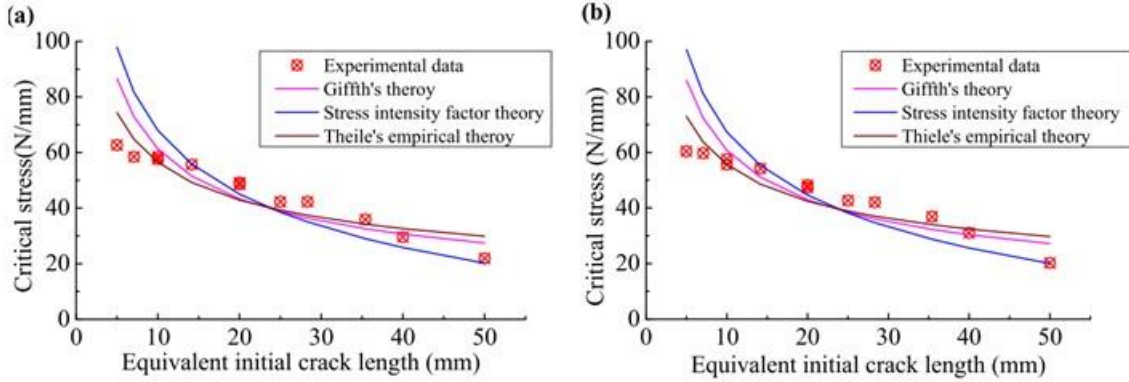


Figure 2.24. Comparison between experimental data and the theoretical values for uni-axial specimens (a) the warp specimens and (b) the weft specimens (F. X. Wang et al. 2016).

From the fitting results, the theoretical resolutions were found to be close to the experimental results during the equivalent initial crack length from 10 mm to 40 mm . However, the variation became more obvious with the increase of the crack length. At the crack lengths higher than 40 mm , the stress intensity factor theory is obviously the most approximate to the experimental results, whereas resolutions of the other two theories are higher than the experimental results. The form of stress intensity factor (K_I) is applied as:

$$K_I = F_T \sigma (\pi a)^{1/2} \quad (7)$$

where σ is maximum tensile stress, a is half of the initial central crack length ($L/2$), and F_T is a geometrical factor calculated from specimen dimensions. According to the research output of Isida (Isida 1973), when the specific geometric ratio γ is < 0.8 , the fitting function is written as:

$$F_T = 2.08(\gamma)^2 + 0.078\gamma + 1 \quad (8)$$

Hence, the stress intensity factor, K_I , can then be deduced by the warp and weft experimental data, respectively. Considering that Griffith theory is based on the infinite plank and the Thiele's empirical theory based on the pressurized cylinder tests, the influence of sample dimension is thought to be insignificant. Whereas, for the stress intensity factor theory

presented above, the specimen's dimension is strictly considered and therefore such theory is the most suitable one for the uni-axial loading tear tests (F. X. Wang et al. 2016).

2.5.2 Gas Permeability Characterization

Polymeric films are often used in multi-layer structure of varied materials, to obtain the desired mixture of properties. Therefore, permeation through multi-layers is a principal issue in the design of many polymer film incorporated hybrid structures. The scientific work on gas permeability of airship envelope materials is quite limited, but experimental and modeling work accomplished on other similar multi-layer laminated structures can also provide valuable information. Since the airship envelope is under pressure all the time during operation, the effect of applied stress on the permeability, although still unknown, is thought to be significant for permeation performance. Permeation along macroscopic interfaces may occur in many applications (adhesive seams, coatings and laminated structures), but not currently well measured owing to a lack of suitable measuring techniques. There is a potential need for the development a suitable technique to measure seam structure of airship envelope laminate in an effective and reliable way. Modelling of gas diffusion in multi-layer polymeric structures is often utilized to predict the gas permeation performance degradation over time. With the help of appropriate modelling, the gas permeation of the airship envelope can be well evaluated and further used for helium leakage prediction of larger scale airships.

2.5.2.1 Gas Permeability Theories

Gas permeation is a gas diffusive process in which gas molecules transfer through a polymer from the high concentration side to the low concentration side, Figure 2.25. Gas

molecules transportation in polymers consists of absorption at the polymer surface, dissolution in the polymer, diffusion of molecules through the material and desorption from the surface of the material.

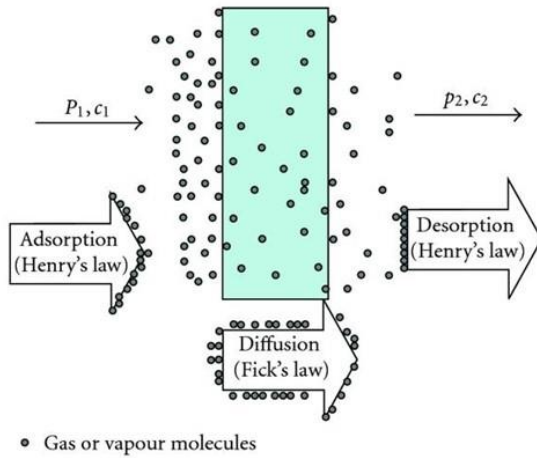


Figure 2.25. A schematic of the basic permeation mechanism of a barrier material (Duncan et al. 2005).

The ideal absorption and desorption of gas molecules are defined by Henry's Law where the amount of gas dissolved in a material is proportional to the pressure of gas above it at a given temperature. Henry's Law:

$$C = Sp \quad (9)$$

where C is concentration, S is solubility and p is pressure. Henry's Law only applies where there is no chemical reaction between the gas and the material. It is also mentioned in a report (Crank 1975) that many polymer/gas combinations do not follow this absorption and desorption behavior due to the existence of holes, voids or fillers in the material. The equation then should be written as:

$$C = Sp + C_H \quad (10)$$

where C_H is the concentration of molecules of holes or voids. In this model, it is assumed that the total concentration is the sum of the concentrations of molecules dissolved in the polymer and those merely adsorbed into 'holes'.

Diffusion occurs through random molecular motions and will eventually reach an equilibrium state. The rate of diffusion is proportional to the concentration gradient of the permeate (substance permeating through the polymer). With Fick's 1st law of diffusion, the diffusion rate with diffusion coefficient D can be calculated. In combination with the ideal Henry's Law, we can find the permeability.

$$P = \text{Permeability coefficient} = (D)(S) \quad (11)$$

where D is diffusion coefficient, which is a measure of how rapidly gas molecules are transporting through the polymer, in the direction of lower concentration. It is a kinetic term that describes how fast gas molecules transport through the polymer. S is solubility coefficient, which is the number of transferring molecules dissolved in the polymer when equilibrium status is reached. It is a thermodynamic term that relates to the number of gas molecules dissolved in the polymer.

Fick's 1st law of diffusion, expresses the flux of gas molecules (J) through the polymer with given thickness (h) as a function of the concentration gradient when the steady state is reached, where c is the concentration of diffusing gas molecules.

$$\frac{dJ}{dt} = -D \frac{dc}{dh} \quad (12)$$

where D is known as the diffusion coefficient, which is temperature dependent. For ideal systems, it follows an Arrhenius relationship, involving activation energy (E_D).

$$D = D_0 \exp\left(-\frac{E_D}{RT}\right) \quad (13)$$

where R is the universal gas constant, T is the absolute temperature. For polymers, Arrhenius relationships of D to $1/T$ are typically linear. However, some discontinuities may be observed close to the phase transitions in the diffusion coefficient-temperature curves. For instance, a

significant increase of diffusion rates can be observed when the temperature is higher than the T_g . Diffusion can be dependent on other factors, which will be discussed later (Duncan et al. 2005).

Permeability at the steady state, the unit pressure flux across a polymer film, can be obtained when boundary conditions are fixed and the gas molecule concentration within the film is in equilibrium. For a polymer membrane with fixed thickness x , at constant temperature and with gas concentration c_1 and c_2 at the two surfaces ($c_1 > c_2$), then the permeation (Q) across the thickness can be obtained through Equation (12):

$$\frac{dQ}{dt} = -D \frac{dc}{dh} = D \frac{(c_1 - c_2)}{h} \quad (14)$$

To express concentrations in terms of pressure following Henry's law, the equation can be rewritten:

$$\frac{dQ}{dt} = DS \frac{(p_1 - p_2)}{h} = P \frac{(p_1 - p_2)}{h} \quad (15)$$

As discussed above in Equation (16), the product DS is known as the permeability coefficient, P . In laminated multi-layer membrane structures, the total permeation (Q_L) with n layers can be calculated using the ideal laminate theory (ILT) as:

$$\frac{1}{Q_L} = \frac{1}{h} \sum_{i=1}^{i=n} \frac{h_i}{P_i^*} \quad (17)$$

where h_i is the thickness of each layer and P_i^* is the permeability of each layer (Permeation = Permeability/thickness) (Duncan et al. 2005).

2.5.2.2 Factors Affecting Gas Transfer

2.5.2.2.1 Intrinsic Properties of Polymers

For polymer materials, free volumes as well as pores and voids are the main intrinsic factors influencing the gas transferring performance of gas molecules. Free volume exists

intrinsically in polymers and arises from the gaps formed between entangled polymer chains. Free volume can be likened to extremely tiny pores, but free volume pores are dynamic in nature since their formation is determined by the polymer chain vibrations. The active motions of the polymer chains can open and close ‘pores’ and alter channels between pores, providing ‘pathways’ for gas molecule diffusions. The variations of free volume are mainly dependent on the density and physical state of the polymer. It is known that crystalline regions in polymers are more ordered than amorphous regions, leading to lower volume in these regions. The crystalline region is often assumed to be impermeable and that the diffusion rate of gas molecules is related merely to the amorphous phase (Gorrasí et al. 2003). Higher volume fractions of the amorphous phase tend to cause higher solubility constants of polymers. In addition, when a polymer is processed by a method that enhances the molecular orientation, then the free volume will also be reduced in comparison to a random orientated polymer. For instance, the crystallization of a semi-crystalline polymer can be improved significantly by molecular orientation, which will in turn cause the reduction of free volume.

Pores and voids are considerably larger than free volumes and are features which are not dependent to the vibrations and motions of polymer chains. However, the volume fraction of voids will be affected by the variation of the imposed stress, because tensile load tends to open voids while compression load will close pores. Like free volume, pores and voids offer spots where gas molecules can be attached to and are far less of a barrier to transport. If pores or voids are open and connected to form a channel, then diffusion rates through these locations will be much higher than if the pores are closed and isolated. (Duncan et al. 2005).

2.5.2.2.2 Environmental Effects

Despite the intrinsic properties of the polymer materials, other factors e.g. temperature and mechanical stress, from the material operational environment also strongly affect the gas permeation properties. Temperature can significantly influence the diffusion properties of gas molecules in polymers, shown in Figure 2.26 (Auras et al. 2004). With the increase of temperature, the mobility of the polymer chains increases, leading to polymer thermal expansion and therefore a lower density as a result. In this case, the free volume in the polymer will increase, resulting in a higher solubility.

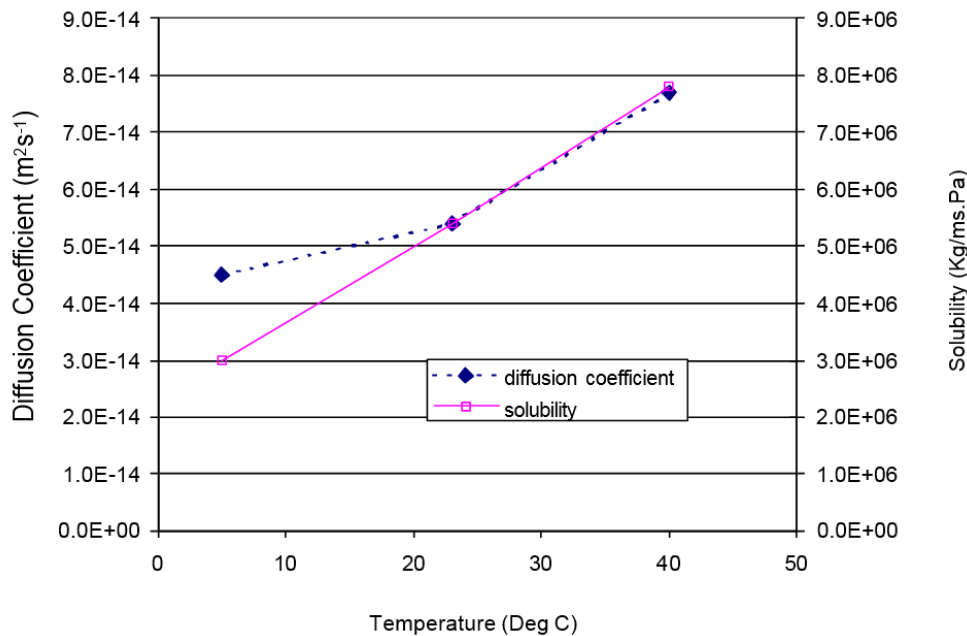


Figure 2.26. Effect of temperature on the permeation of oxygen through PET film (Auras et al. 2004).

Moreover, discontinuity of the solubility may occur near phase transitions of the polymers. The diffusion coefficients and saturation levels for water vapor in an epoxy adhesive is shown in Figure 2.27 (Gledhill et al. 1980). When the highest test temperature was applied at $90\text{ }^\circ\text{C}$ which is slightly above the glass transition temperature (T_g) at $85\text{ }^\circ\text{C}$, both diffusion coefficient and saturation level (solubility) are significantly higher than they are at temperatures below T_g . At temperatures above T_g , segmental motions of the polymer chains are

greatly increased, creating larger fractions of free volumes for the diffusing gas molecules to rapidly pass through.

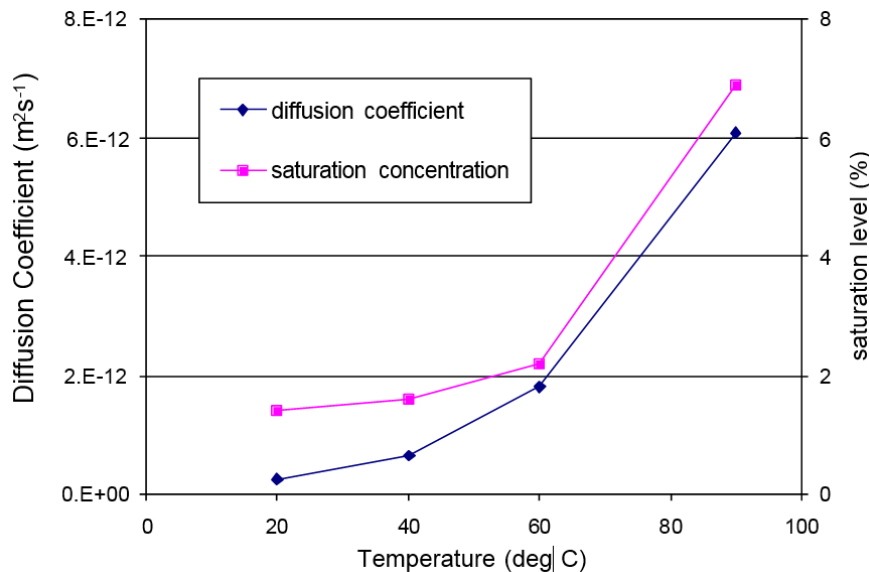


Figure 2.27. Effect of temperature on water vapor diffusion in an epoxy adhesive seam (Gledhill et al. 1980).

Results from experimental standard permeation tests may not fully represent the performance of materials in service, because the mechanical stresses experienced in operational environment will change the molecular solubility by opening and closing the pores and voids. Data collected from tests performed with tensile stresses have been reported in the literature. Boersma et al. (Boersma et al. 2003) investigated on the effects of tensile stress applied to plastic films on their oxygen permeation properties. It was reported that the permeation rate will increase as the stress increases, (see Figure 2.28). Michaeli et al. (Michaeli et al. 2004) also tested the permeability of polymer films at different strain levels. A group of polymer films with barrier coatings were also tested, and the results were compared and contrasted with the control (non-coated). In both cases, the increased strain caused the increase of gas permeability, while much greater impact was observed for the coated polymer films. In

the unstrained condition, the permeability of uncoated polymer film is measured to be five times higher than that of a coated film. However, the differences between the two groups at the strain of 5 – 8% became insignificant. As concluded in this work, the substantial increases in gas permeability of the coated sample at high level of strain could be attributed to the stress/strain induced microscopic cracks in the brittle barrier coatings.

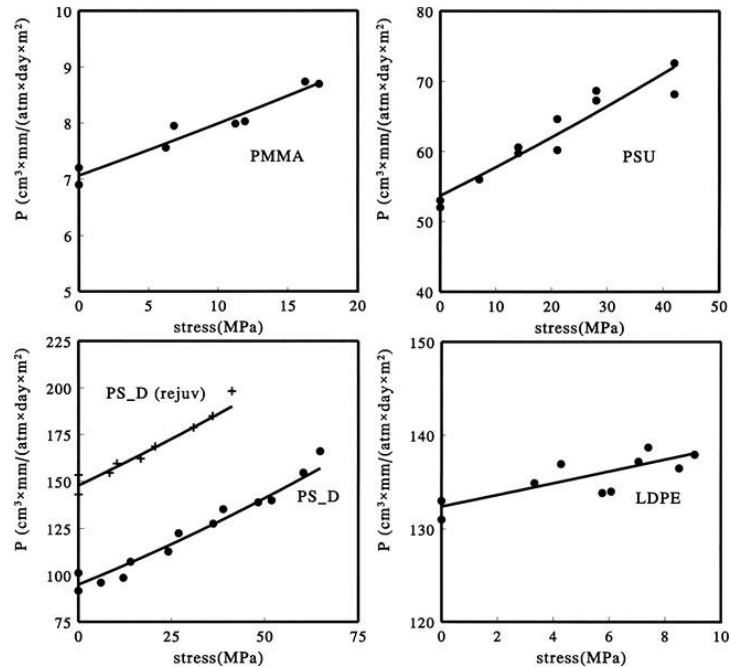


Figure 2.28. Effect of tensile stress on oxygen permeability of various plastic films (Boersma et al. 2003).

2.5.2.2.3 Effects of Interfaces

Generally, there are two types of distinct scenarios for multi-layer laminate shown in Figure 2.29. The gas would either pass through the thickness of the laminate normal to the interfaces, scenario (i) or transfer parallel to the interfaces, scenario (ii).

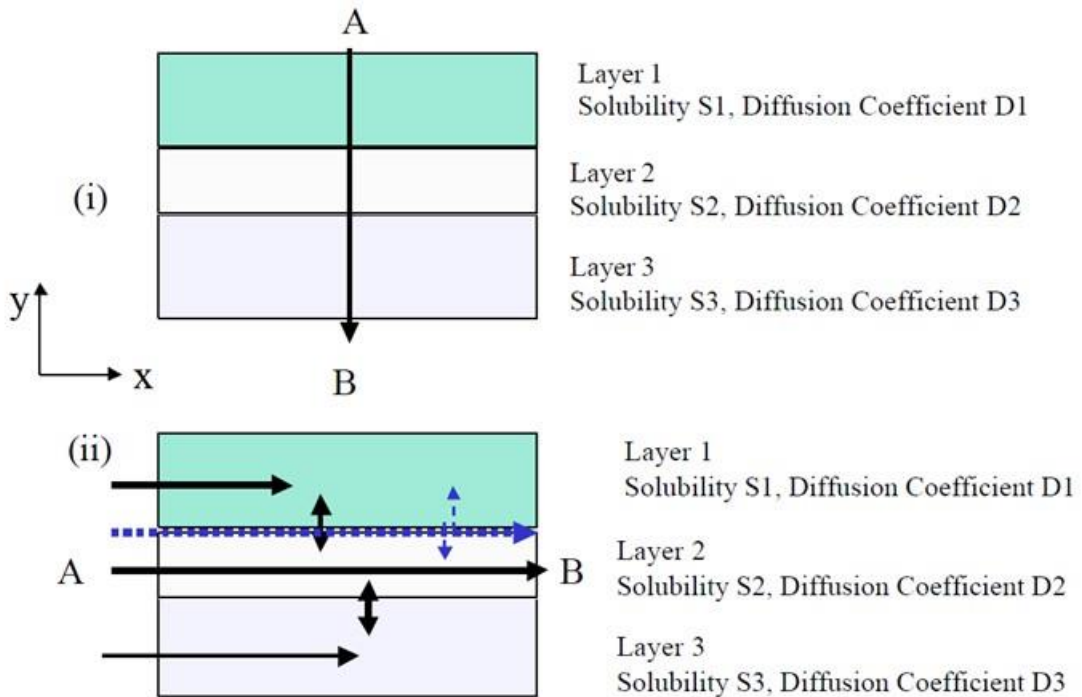


Figure 2.29. Diffusion in multi-layer structures with interfaces (i) through thickness, in series: interfaces won't affect the overall property if they cannot provide an additional barrier; (ii) along layers, in parallel: diffusion possible between layers and along interfaces (Duncan et al. 2005).

Scenario (i) is comparable to a multi-layer membrane or coated laminates. Diffusion takes place in series and concentration is uniform in the x-direction. Normally, with the impact of interfaces being ignored, the overall diffusion could be modelled as a series of one-dimensional processes. The concentration at the interfaces can be used as the boundary condition for each layer. Scenario (ii) is perhaps more analogous to adhesive seams or long-fiber reinforced composites. The gas molecules diffuse through all the layers parallelly, and thus it is considered as a two-dimensional problem. Since the permeation rates within each layer would be different, there will be concentration gradients across all the interfaces, causing inter-layer diffusion consequently.

However, these evaluations become unreliable when the interfaces have impacts on gas transfer processes. For instance, at interfaces like metal/adhesive or metal-coating bonds, the

strong affinities between the interfaces and polar gas species (e.g. water vapor) will cause the increase of the available sites for absorption and therefore the increase of the uptake of these polar gas species. In this scenario, high saturation concentrations at the interfaces will change diffusion boundary conditions, leading to increased gas transmission rates. The effects may not be significant in case (i), but in case (ii) a strong absorption at the interface may cause the formation of a rapid diffusion channel along the interfaces (Figure 2.29). Diffusion occurred at a particular interface will be accelerated, leading to a higher transmission rate than that expected from bulk material properties (Duncan et al. 2005).

2.5.2.3 Permeation Measurement Methods

All gas permeation methods follow the same fundamental principle which is having one side of the sample exposed to the gas to be evaluated. This can be done statically or with a continuous stream of permeant gas so that a constant pressure can be maintained throughout the test. On the other side of the film material tested, the gas permeated is taken away with a carrier gas and fed into a sensor. In most of the gas permeability testing, instead of measuring the absolute quantity of the permeant in the carrier gas, a relative difference between the permeant and carrier gas mixture and the pure carrier gas is calculated (Duncan et al. 2005). The permeability of the film material is determined from the experimental parameters such as pressure difference, testing area, sample thickness, time, etc.

2.5.2.3.1 Gas Permeation Tests

Manometric Methods – It is specified in ASTM D 1434 - 82 that the gas permeation rates can be determined by evaluating the pressure changes which are recorded by a manometer. In this method, the test gas is fed into a chamber until the atmospheric pressure is reached. The

chamber on the opposite side of the film sample is hermetically sealed to ensure accurate measurement. As gas diffuses through the film sample and accumulated in the low-pressure chamber, the pressure will increase gradually over time. After an initial delay of the pressure increase, the pressure-time curve will finally become linear. The gas permeation rate can be calculated from the rate of pressure increase (Duncan et al. 2005).

2.5.2.3.2 Conditioning of the Test Sample

The physical condition of the polymer film sample is very important for getting reliable gas permeability results. Any damages to the surface will create defects or pinholes through the sample, which will lead to a higher permeation rate (Duncan et al. 2005). Samples need to be handled carefully when being mounted between feeding and detecting chambers prior to testing. Thin film samples may need to be supported by filter papers to prevent bowing, stretching or damaging if pressure differentials or high gas flow rates are used. The grade of filter papers is strictly required to provide support without interfering with the permeation mechanism, e.g. by providing an additional barrier. Composites materials, multi-layer fabrics or coated films may have different solubility and permeability in different directions. These samples should always be tested with the correct surface facing the test gas according to specific end uses. Samples need to be pre-conditioned carefully to avoid the absorption of moisture from the atmosphere. Because the presence of absorbed moisture is reported to be able to significantly increase gas permeation rates in hydrophilic polymers (Auras et al. 2004). Therefore, pre-conditioning of samples need to be done properly in order to achieve stable and consistent moisture content before the start of every single test. This may be accomplished by conditioning the samples in an environment with fixed temperature and humidity for certain period of time until equilibrium is reached. The application of plastic strain may change the

properties of the polymeric materials and is thus a source of measurement uncertainty. (Duncan et al. 2005).

2.5.2.4 Gas permeability modelling for multi-layer flexible composite

It was reported by Ashford et al. (Ashford et al. 1973) that the helium permeability measured by standard methods was found to be variable, and the measurements did not correlate with the achieved daily lift loss. Therefore, the U.S. based airship and aerostats builder TCOM initiated an investigation into an accurate and reliable measurement method of helium permeability of its laminated airship hull materials. The permeability, or more strictly speaking, permeation of these multi-layer airship materials was measured by independent test laboratories. However, large variations in the results were obtained from nominally the same test devices and following the same standard gas permeability testing methods. By carefully re-design the experimental details and rigorously conduct the methodology, TCOM succeeded in developing a reliable and most importantly repeatable test method (Islam & Bradley 2012). With the permeability of all the functioning laminate components obtained directly from the manufacturers, a theoretical value of material gas permeation was able to be calculated for a tri-laminate, which is comprised by Tedlar®, Mylar® and Dacron® using Hytrel® as the adhesive. This theoretical calculated value was $1140 \text{ cc}/\text{m}^2.24\text{h}.0.1\text{MPa}$ and compared well with the experimentally measured permeation data of $990 \text{ cc}/\text{m}^2.24\text{h}.0.1\text{MPa}$. A difference of 13% in the permeation values might be good compared to the predictions made with previous permeability testing methods. But this simple calculation method can never be identified as accurate because it is based on the ideal laminate theory (ILT) previously discussed for perfect multi-layer membrane. The value of total permeation of the multi-layer laminate will not be

the same as that measured as it assumes there are no defects and the layers are homogeneous which is not true in practice. The existence of woven fabric structure sandwiched in-between the polymeric films also makes the gas transmission process more complicated. Therefore, modified models for more accurate prediction of the gas permeation through multi-layer laminated film/fabric hybrid structures need to be established, taking the woven fabric structure and potential defects and pinholes in polymeric films into account.

Yao et al. (X. F. Yao et al. 2010) experimentally studied the helium leakage mechanisms of flexible Vectran® fabric laminated composites under different damage models and a multi-layer permeation model was developed mainly on the basis of continuity theorem. This principle indicates that, when the steady state of gas diffusion is reached, the helium gas molecules transferring through the upper layer must also pass the layer next to it within the whole structure. Yet, this is only true when the horizontal flow within all the layers as well as their interfaces is ignored. The detailed structure information can be observed in Figure 2.30.

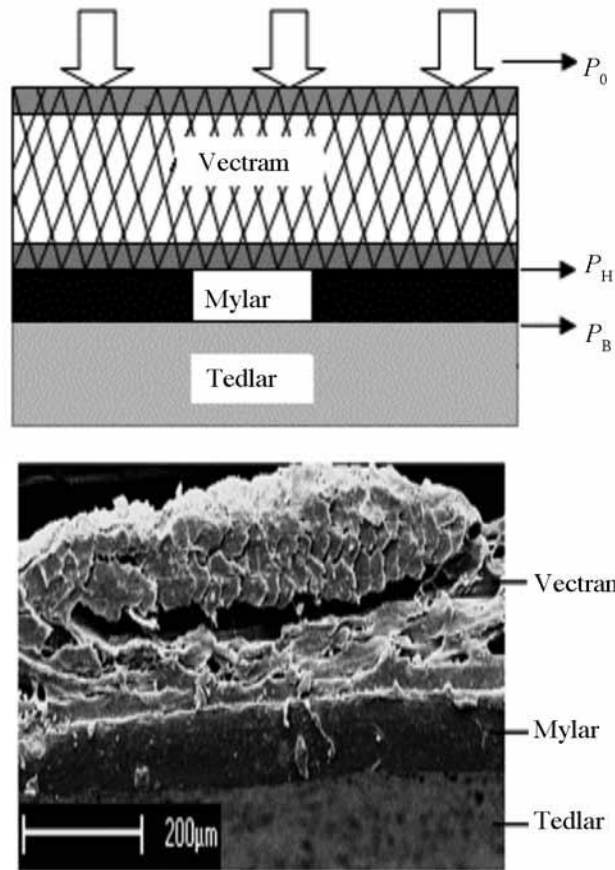


Figure 2.30. Geometrical configuration and microstructure of flexible film-fabric laminated composites (Yao et al. 2011).

According to Equation (15) discussed above, the helium flux per unit time and area in the flow direction (J) of each single layer of this composite material can be written as:

$$J = P \frac{p_0 - p_1}{h} \quad (18)$$

where P is the permeability coefficient; $p_0 - p_1$ is the pressure difference across a barrier layer; h is the thickness across each component of the laminated composite. Therefore, the helium flux for each layer per unit area of the flexible film-fabric laminated composite can be expressed as follows:

$$q_L = P_L^{eff} \frac{p_0 - p_H}{h_L} \quad (19)$$

$$q_H = P_H \frac{p_H - p_B}{h_H}$$

$$q_B = P_B \frac{p_B}{h_B}$$

where q_L , q_H and q_B are the helium flux per unit area and time of the load-bearing layer, gas barrier layer and weather protective layer, respectively. Also, h_L , h_H and h_B are the thickness across each of the component, respectively. P_L^{eff} , P_H and P_B are the permeability coefficient of each component, respectively. p_0 , p_H and p_B are the pressure of each layer as demonstrated in Figure 2.30, respectively (Yao et al. 2011).

According to the aforementioned continuity theorem, we have:

$$q_L = q_H = q_B$$

Being different from continuous polymeric films, the woven fabric load-bearing layer should undergo a different mechanism of helium permeation. Due to the porous nature of textile fabrics, the Fick's law for film diffusion is not suitable to be applied directly. The size of the pore from a textile fabric is substantially larger than the free path of helium gas molecules on average. Therefore, Hagen-Poiseuille's law was applied to express the helium flux through the textile load-bearing layer (Yao et al. 2011):

$$J = \frac{\varepsilon (\bar{d}/2)^4 \Delta p}{h \eta \tau h_l} \quad (20)$$

where ε is the porosity; \bar{d} is the average diameter of pores in the textile fabric; η is the viscosity coefficient of helium; τ is the tortuosity ratio; Δp is the pressure difference across the textile fabric.

Although the modified helium permeability of textile load-bearing layer was able to be calculated using this model, the total helium flux of the flexible film-fabric laminated

composite was still calculated to be 22.4% higher than experimental data. Being much higher than the 13% error obtained in the multi-layer helium permeation study by Ashford et al. (Ashford et al. 1973), this model needs further modifications to improve the prediction accuracy of gas permeation rate.

In the following study of helium leakage modeling, Yao et al. (Yao et al. 2012) further developed a model adjusting the simulation of the gas transmission through load-bearing fabric layer. In this paper, the individual component of a multi-layer composite structure was analyzed respectively. A new ‘porous-medium leakage model’ was introduced, assuming that when steady state was reached eventually, helium permeates not only in the transverse direction but also back and forth for the woven load-bearing layer. Moreover, the distribution of gas density and pressure through the layer thickness are assumed to be non-linear. Based on a typical representative volume element (RVE) of woven structure (Figure 2.31), a square hole is formed outside the cross area of the warp and weft yarns. The side length of the square hole is defined as d .

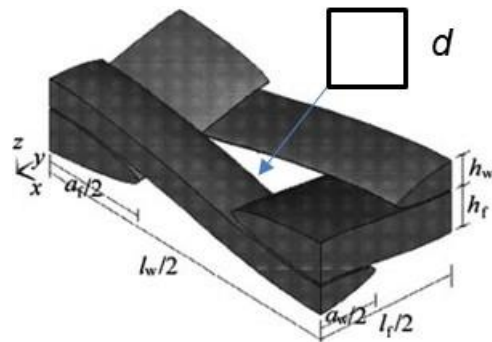


Figure 2.31. An example of representative volume element (RVE) of plain woven structure (Yao et al. 2012).

According to the Poiseuille’s law, the flow rate passing through the small square pore per unit time is

$$Q = \frac{d^4}{12\eta L_0} (P_1^2 - P_2^2) \quad (21)$$

where η is the gas viscosity for helium gas, L_0 is the thickness of the pore, and the P_1 and P_2 are the upper and bottom pressure of the square pore.

Then following the principle of continuity condition, when the helium permeation reaches the steady state, the helium mass permeation rate per unit area and per unit time for each layer must be the same. With the modified load-bearing permeation model, in this specific work, the equivalent helium leakage rate from a flexible film-fabric composite with $250 \mu m$ in thickness and $0.1 MPa$ in pressure difference was calculated to be lower than the measured data (pressure difference method). This is the first time observed in the literature that the predicted data was lower than the measured results, which is possibly owing to the inevitable gas leakage from the chamber edge in a real experiment per the author's explanation (Yao et al. 2012).

A good management of lifting gas containment (leakage rate analysis) for the stratospheric airship envelope material is critical to accurate altitude control. The theory and modelling of gas leakage through the laminated envelope material is able to provide valuable information to help leakage control. Apparently, some scientists already stepped out to explore possible routes toward the goal. However, so far, not enough effort has been made to develop a comprehensive model to simulate the gas permeation accurately. Hence, there is a heavy need to make some significant progression to build a reliable model for multi-layer film/fabric hybrid structure, which is typically used for airship envelop material.

3 Motivation and Research Objectives

It is clear from the literature review that a multi-layer laminated composite structure involving many different high-performance fibers, functional polymeric films and versatile adhesives is the mainstream approach to obtain an effective solution of materials to build high-altitude LTA platforms. The literature review shows that some of the prior research were dedicated to identifying a good fit or balance of various high-performance materials. It is noted that Zylon® fiber is predominantly used to build the core strength element of the laminated envelope materials in the most recent studies. Generally, we saw a leap in the specific strength of the Zylon® fabric reinforced envelope materials compared to previously developed airship materials for high-altitude applications. Nonetheless, the common issues of relatively heavy weight obtained still remains as the major hindrance for material breakthrough. Further improvement on the material and structure design of the laminated composite is required to reach a higher strength-to-weight ratio. Great efforts have also been made experimentally and analytically to obtain an in-depth understanding of the mechanical behavior of the airship envelope material concerning uni-axial and bi-axial tensile as well as tear and creep properties. However, adhesion studies of these laminated materials have been minimal and have not been investigated systematically. Generally speaking, interfacial adhesion in the laminated structure is the most fundamental and critical property based on which other functionalities can then be realized. It is important to understand how the process parameter variations can affect the adhesion property and overall performance of the laminated composite materials. Speaking of adhesion, seaming is another key element to ensure a strong and durable airship hull structure can be built. Research on seaming has mainly focused on the tensile and creep performances in various environmental conditions and over time. Yet, gas permeation study on adhesively

seamed structure is scarcely seen in the literature, primarily because no reliable method has been established to measure accurate permeation rate through a seamed structure. In the aspect of the gas retention property, there are also major gaps to be filled, concerning the development of a suitable gas permeation model for multi-layer hybrid film/fabric structure. Prior works on the gas permeation of laminated envelope material showed relatively inaccurate prediction results when compared to the experimental data. Therefore, research is still needed to: 1) theoretically study the gas permeation/diffusion mechanisms of polymeric films and coated fabrics and 2) experimentally establish a good testing method to eliminate operational and environmental errors, ensuring accurate permeability measurement and modelling verification.

Since it is quite challenging to follow the existing laminate structure design and process method to achieve higher strength-to-weight ratio of the airship envelope material, the main goal of this research is to first develop a flexible multi-layer structure by integrating multi-functional components through a highly efficient dry heat lamination process. Then, a parametric study and adhesion evaluation need to be accomplished in order to identify the best candidate of laminate for subsequently seaming study and gas permeability investigations. The specific objectives to achieve the goal of the proposed research are:

1. Produce a multi-layer laminate envelope material for stratospheric airship with extraordinarily high strength-to-weight ratio and outstanding gas barrier property based on a unique structural design and material combination.
2. Conduct a parametric study of the lamination process to understand the effects of lamination parameters i.e. temperature and speed, as well as the fabric structure on the properties of the laminate.

3. Conduct a parametric study to develop overlap seams with seam strength that is higher than the laminate strength to effectively transfer the load using a two-factorial design of experiment considering temperature, time (seaming speed), applied pressure and seam overlap length. This would enable identifying and quantifying the critical factors that produces highest seam strength with minimum seam weight penalty (lowest seam overlap length).
4. Develop an analytical gas permeation model for an entire airship in terms of experimentally measured permeation of individual laminate components, the entire laminate, seamed area, and non-seamed area.

4 Preliminary Work

Considering the only past success on stratospheric airship flight last only for less than 10 *hrs* and reasons for failure not reported, there is not really much in the public domain regarding the requirements for the hull material to be benchmarked to. We have to start from nothing and build up our own knowledge base concerning the specifications of the envelope materials potentially required to endure the long-term stratospheric flight. Therefore, we initiated some fundamental work from the very basic material sourcing and screening to the material structural designs, and ultimately a list of various testing and post-test evaluations. All the invaluable information we obtained from these works laid foundations for subsequent researches on other interesting and more challenging topics. Moreover, the results from the preliminary work directed the experimental designs that include key independent parameters and responses related to the laminate performance characteristics. Summary of the preliminary work is reported in Appendix A.

5 Experimental

This section explains the detailed experimental procedures structured to achieve the research goals through set of experimental designs. Guided by the preliminary research results, the experimental plans include details of the key materials used to make different types of laminate samples, designs of experiments, sample production methods, and various testing protocols.

5.1 Materials

The finalized laminate design is shown in Figure 5.1. The constituents of the laminate are load bearing layer made from PBO fiber (Zylon[®]), two EVOH films (EVALTM, ethylene vinyl alcohol copolymer) as adhesive layers, thin PET film (Mylar[®]) with vacuum deposited aluminum (VDA) coating as bottom gas barrier layer, and top weathering layer built from PI film (Kapton[®]) with double sided VDA coatings and corrosion resistant coating (CRC) on the top.

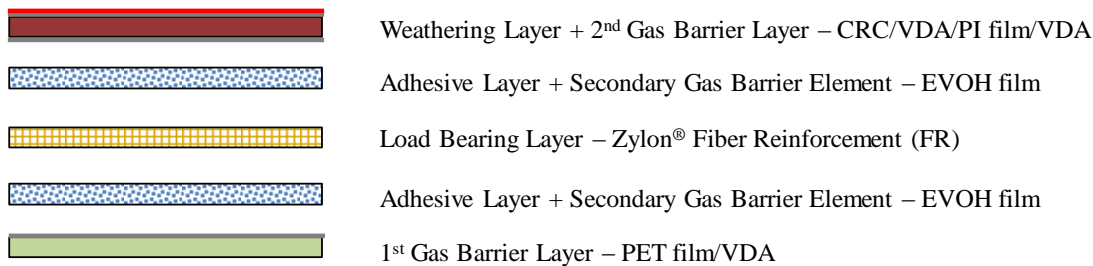


Figure 5.1. Laminate structural and material design.

To seam the laminate, TPU (Thermoplastic Polyurethane) film adhesive is used to provide strong bonding between the seamed laminate parts, adequate tensile and shear strength, as well as low temperature flexibility. All these raw materials used to make laminate and seam samples can be largely categorized into three sections: 1) fibers and fabrics, 2) thin polymeric films and

coatings, and 3) adhesives. The following sections describe and justify the reasons behind the selection of specific laminate materials.

5.1.1 High Performance Fibers

In this research, yarns from Zylon® (PBO) fiber were produced and supplied by Toyobo Co., Ltd to make high strength woven fabrics. Zylon® has the highest specific strength and specific modulus among the commercially available high-performance fibers. With excellent creep resistant property, these yarns are selected for the textile reinforcement in the laminate material. Zylon® multi-filament yarns (99 *fil*) with a linear density of 150 *denier* are used to weave lightweight and thin woven fabrics. For the parametric study of lamination, two types of slightly distinct woven fabrics are used, which were produced and supplied by Textum Inc. and OEM for Toyobo Co., Ltd, respectively. The specifications of woven fabrics are listed in Table 5.1.

Table 5.1 Specifications of woven fabrics

Fabric ID	Textum	OEM-Toyobo
Warp Yarn:	150 Denier/99 fil/106.3 tpm/Zylon®	150 Denier/99 fil/0 tpm/Zylon®
Weft Yarn:	150 Denier/99 fil/106.3 tpm/Zylon®	150 Denier/99 fil/0 tpm/Zylon®
Warp Density:	15.1 ends/cm	15.6 ends/cm
Pick Density:	15.4 picks/cm	15.4 picks/cm
Fabric Width:	160 cm	120 cm
Weave	Plain	Plain
Area Density:	52.6 gsm	51.9 gsm
Thickness:	120 μm	80 μm
Crimp (Warp/Weft):	1.0%/2.3%	0.0/0.0

5.1.2 Functional Polymeric Thin Films and Coatings

5.1.2.1 Polyimide film (Kapton®)

In addition to its high modulus, the PI film is proved to be a multi-functional material that is ozone stable (confirmed in the preliminary work at low concentration), gas tight and high temperature resistant. 50 DE Plasma MBS Kapton/DB25 is a 50-gauge polyimide-based product that is aluminized on both surfaces, being deposited with corrosion resistant coating (CRC) on single side, and offers excellent physical, thermal, and optical properties with low emittance and solar absorptance values. The surface properties of PI film are improved by plasma treatment to ensure strong interfacial bonding between PI and thin Aluminum coating. The structure of this particular multi-layer film material is CRC/VDA/50 GA Dupont™ Kapton® HN Polyimide Film/VDA. It is particularly suited for broad temperature ranges and complies with the requirement of ASTM D-5213. The detailed properties are listed in Table 5.2.

Table 5.2 Typical properties of Polyimide film (50 DE Plasma MBS Kapton/DB25)

Property		Value	Method
Physical	Tensile strength, MPa	165	ASTM D882-91-A
	Elongation at break, %	35	ASTM D882-91
	Thickness, μm	13.2	-
	Density, g/cc	1.42	
	Area density, gsm	21	
Thermal	Operating temperature, °C	-250 to 290	-
	Moisture absorption, %	4	
Metallization	Type, % pure aluminum	99.99	
	Deposition, Å	> 300	
	Electrical Resistance	≤ 300	ASTM D257
Optical	Emittance	< 0.04	ASTM E408
	Absorptance	≤ 0.14	ASTM E903/ ASTM E490

5.1.2.2 Polyethylene terephthalate film (Mylar®)

DE025 is a 25-gauge polyethylene terephthalate (PET) based product that is aluminized on one surface and offers excellent physical, thermal, and optical properties with low emittance and solar absorptance values. It is engineered for use in multi-layer insulation (MLI) blanket applications and complies with the requirements of Federal Specification LP-377. The detailed product information is listed in Table 5.3.

Table 5.3 Typical properties of Polyethylene terephthalate film (DE025)

Property		Value		Method	
Physical	Tensile strength, MPa	MD	200	ASTM D882A	
		TD	255		
	Elongation at break, %	MD	160		
		TD	100		
	Thickness, μm	6.35			
	Density, g/cc	1.4			
Thermal	Area density, gsm	8		-	
	Operating temperature, °C	-250 to 120			
	Shrinkage, %	MD	3.5		
		TD	3.5		
Metallization	Type, % pure aluminum	99.99		ASTM D257	
	Deposition, Å	> 300			
	Electrical Resistance	≤ 300			
Optical	Emittance	< 0.04		ASTM E408	
	Absorptance	≤ 0.14		ASTM E903/ ASTM E490	

5.1.2.3 Vacuum deposited aluminum (VDA) Coating

The VDA layer, also known as metallization, which is an extremely thin coating applied to the polymeric film prior to lamination, is used to reinforce the gas holding property with minimal weight penalty. The VDA coatings are positioned on the outer side of the laminate will also effectively reflect the heat and UV radiations and thereby protect Zylon® fabric from degradation. Detailed information is listed in Table 5.2 and Table 5.3.

5.1.3 Adhesives

5.1.3.1 EVOH film adhesive (EVALTM) – Lamination

EVOH is a crystalline ethylene vinyl-alcohol copolymer. Its monolayer films have outstanding gas barrier properties. From the preliminary work, EVOH films were also proved strong adhesive components bonding polymeric films with metallic coating to Zylon[®] textile fabrics. Typical properties of the EF-F grade EVOH films are listed in Table 5.4.

Table 5.4 Typical properties of EVOH film (EF-F grade)

Property			Value	Method
Physical	Tensile strength, MPa	MD	110	ISO1184
		TD	40	
	Elongation at break, %	MD	300	
		TD	100	
	Thickness, μm		15	
	Area density, gsm		18	
Thermal	Melting point, °C		183	NA
	Shrinkage, %	MD	2.7	Kuraray Method
		TD	1.8	

Due to its hydrophilic nature, EVOH films are sensitive to moisture. When the EVOH films are exposed to moisture, it may cause bagginess and wrinkles of the films. Therefore, much attention needs to be paid for appropriate packing and storage of EVOH films before and after every use.

5.1.3.2 Polyurethane film adhesive – Seaming

Polyurethane has the best low temperature properties of all commercially available adhesives. In general, the polyurethane adhesives are easily processed and bond well to many substrates. EXF-951 is a single layer of solvent free thermoplastic ether-based polyurethane

(TPU) adhesive polymer extruded onto a paper release liner and supplied by Adhesive Films, Inc. The detailed properties of this TPU film adhesive is listed in Table 5.5.

Table 5.5 Properties of EXF-951 TPU film adhesive

Property	Value	Method
Shore hardness A	83	ASTM D-2240
Specific gravity, g/cc	1.105	ASTM D-792
Thickness, μm	50.8	
Tensile strength, KPa	400	-
Ultimate elongation, %	670	
Melting point, $^{\circ}C$	135 - 145	Gradient Heat Bar
T_g , $^{\circ}C$	-46	DMA
Appearance	Water clear	Visual

5.2 Experimental Design

Three designs of experiment are developed to achieve the following goals: (i) to conduct a parametric study of the lamination process to understand the effects of lamination process parameters (temperature and speed), as well as the reinforcement fabric structure on properties of the laminate, (ii) to conduct a parametric study for the fabrication of double-sided butt seams with effective load transfer via a two-factorial design of experiment regarding temperature, time (seaming speed), applied pressure and seam dimensions, and (iii) to develop an analytical gas permeation model for an entire airship in terms of experimentally measured permeation of individual laminate components, the entire laminate, seamed area, and non-seamed area.

5.2.1 Lamination Parametric Study

All components of the laminate were passed through a heated roller under pressure at various speeds. With the nipping pressure being set, temperature and the feed speed were varied in order to achieve laminate samples with different physical properties. Two types of

Zylon® plain woven fabrics with slightly distinct structures and physical properties were utilized for lamination. One fabric was woven from twisted yarns (TY) and the other from flat yarns (FY). The two fabrics' specifications are depicted in Table 5.1.

Temperature can directly influence the melting and flowing of the polymer, and more importantly the activation of the adhesion property. Considering the melting point of the EF-F grade EVOH films selected for this research is 183 °C, the lowest level of lamination temperature was thus set at 185 °C, being slightly higher than the melting point to ensure the melting of EVOH films. Per preliminary trials of lamination with this grade of EVOH films, ~200 °C was determined to be a sufficiently level temperature to activate the adhesion of EVOH polymer, at the same time, without being too high to damage the rest of the laminate components, especially for the ultra-thin PET films. A higher level of temperature at 215 °C was also selected as a third level for the investigations of the temperature and adhesion effect on the laminate performance properties. According to the discussion from the literature on lamination process, the lamination speed and reinforced fabric structure (e.g., openness) usually play key roles affecting the penetration of the flowing polymer through the interstices of the woven fibrous structure. With several trials conducted on this specific lamination machine, a high and a low level of speed were finally determined as ~1.6 and ~1.0 m/min to ensure consistent lamination quality. The dwell time in the heated zone at each of the speed level are calculated to be ~2.1 s and ~3.5 s, respectively. The 150 denier multi-filament Zylon® yarns were used to produce plain-weave fabric with similar structure (Table 5.1). The twisted and flat (non-twisted) yarns will cause certain degree of difference regarding fabric openness, crimp ratio and fabric thickness.

After several pre-trials, lamination pressure (generated indirectly by the tension in the conveying belt of the lamination machine) is decided to be fixed at 80 *psi* to ensure sufficient contact between raw materials and adhesives, so as to obtain high bonding strength. The pressure at an exceedingly high level is not desirable because that will cause over penetration of the melted EVOH, which will inevitably lead to laminate sample stiffening. On the other hand, according to our observations while conducting the pre-trials, high pressure applied improperly caused damage to the polymeric films and create surface unevenness. Moreover, the integrity of the ultra-thin deposited coatings was also subjected to notable degradation. Taking all these factors into account, a parametric study on lamination process was designed. The experimental design variables and their levels are shown in Table 5.6.

Table 5.6 Designs of experiment for lamination parametric study

Variables	Levels	Parameters
Temperature, °C	3	185, 200, 215
Dwell time, s	2	2.1, 3.5
Fabrics	2	150 <i>Denier</i> , TY 150 <i>Denier</i> , FY
Replica	2	
Total Runs:		(3 x 2 x 2 x 2) = 24
Fixed Parameters:		
Adhesive	Pressure	Fabrication Method
EVOH (Eval® EF-F)	550 <i>KPa</i>	Laminator

5.2.2 Seam Evaluation

To better achieve the goal of this study, the experimental work was divided into two parts. In the first part, a two-factorial design of experiment was conducted to study the optimal

parameters for seaming process with a goal to determine the best candidate of the laminates. Two-factorial designs in which each factor is studied at two-level (high and low) are very important in factor screening experiments and practiced in many scientific investigations. Compared with one-factor-at-a-time (OFAT), the factorial designs are more efficient to get the same precision for effect estimation. Generally, the relative efficiency of factorial continues to increase with more factors added. In addition, factorial designs have wider inductive basis to draw inferences about certain process. Interactions of factors are able to be revealed, which proved to be the key to understanding a process (Anderson & Whitcomb 2007).

With some preliminary results on seaming process, double side butt seams were made with high and low levels of temperature, seaming time (controlled by the speed of the seaming equipment) and pressure. Per the preliminary results from hand press seaming, the temperature applied needs to be sufficiently high in order to activate the adhesive for better interfacial adhesion. Short seaming duration will cause poor peel strength, which is used to judge the adhesion strength, due to insufficient contact between adhesive and laminates. For the pressure applied during seaming, low level of hand press was already found to be effective in obtaining high peel strength. It was still unknown that how high pressure performs regarding seam formation. Pre-trials are conducted to determine the exact high and low levels for this two-factorial design of experiment since the process used for seaming are completely different from hand pressing with an iron.

In the second part, the seam with highest load transfer efficiency (strength-to-weight ratio) was selected by comparing the tensile testing results. Seams with different overlap and underlap lengths were produced following the same procedure with controlled parameters

decided in the previous experimental section. The details of experimental design are listed in Table 5.7.

Table 5.7 Experimental design for seaming parameter study

Variables		Levels		
I	Temperature, °C	2	150, 180	
	Seaming speed, m/min	2	3, 6	
	Pressure, KPa	2	100, 400	
Total Runs:		(2 x 2 x 2) = 8		
II	Seam Dimensions, cm (Overlap – Underlap)	3	10.16 – 0	
			10.16 – 3.81	
Total Runs (Levels):		3		
Fixed parameters:				
Adhesive		Thickness	Fabrication Method	
TPU film		50.8 μ m	Fusing Machine	

5.2.3 Helium Permeation Study

The helium barrier property of the best candidate laminate(s) and their seams were studied. Based on the experimental measurements of all the laminate components, an analytical gas permeation model for hybrid film/fabric multi-layer flexible composite was developed that enabled the calculation of permeation of an entire airship with known dimensions and areas of seams. The effect of controlled stress/strain on the helium permeation rate of the laminate was investigated.

Since the laminate consists of multiple components of various materials, it is valuable to measure the helium permeation rate of each single component to understand the gas permeation mechanisms and develop a reasonable model of gas permeation through multi-layer laminate

structures. To develop the analytical model for helium permeation process through the multi-layer film/fabric laminate, the helium transmission rate of each single component was measured strictly following the pre-test conditioning. With the experimental results of the multi-layer laminate and its seam, the analytical model for multi-layer flexible composite structure was verified.

5.3 Laminate Fabrication

The lamination process was conducted on the Pratix OK-12L Seamless Teflon Belt Drum Laminator available at the Textile Technology and Filament Lab, College of Textiles, NCSU, shown in Figure 5.2. Since the laminator does not have a properly functioning tension system, a unique jig with a pair of Teflon coated woven fabrics was used to help produce continuous, wide, and wrinkle-free laminate samples. The major function of the pair of Teflon coated woven fabrics is to release the tension and force which the materials encountered during the pressing between the heated roller and conveying belt. Since the PI film is more rigid and less stretchy compared to PET film and EVOH film, there is always wrinkles formed on PI side if tension is not controlled. To resolve the wrinkling issue of PI film, a two-step lamination process was followed. The first step is to pass the PI film, which is sandwiched by the Teflon coated fabric, to adhere the PI film smoothly onto one of the Teflon coated fabric carriers. Then, lay all the components according to the correct sequence between two Teflon coated fabric carriers and feed the materials into the laminator. Depending on the condition of the lamination, the laminated composite sample may be passed through the laminator for a third time. Usually, after the third pass, laminate composite samples with minor wrinkles were

successfully produced. The Zylon® fabric was pressed using iron to flatten it out before lamination to provide smooth surface suitable for adhesion.



Figure 5.2. Pratix OK-12L Seamless Teflon Belt Drum Laminator (<http://practix-usa.com/heat-transfer-machines/laminating-machines/>).

5.4 Seam Formation

The selection of Kannegger Fusing Machine (K-FM) (Figure 5.3(a)) for seaming is mainly due to its nature of continuous process and more precise parameters control, which will potentially produce seam samples with more consistent qualities. As is shown in Figure 5.3(b), this machine is a continuous seaming machine features multiple pairs of heating elements and one pair of pressure roller at the end. Generally, the process follows the steps of pre-heating under moderate pressure, pressing at elevated pressure and temperature, and ultimately fast cooling. The dwell time at the heated zone can be controlled by tuning the speed of the conveying belt.

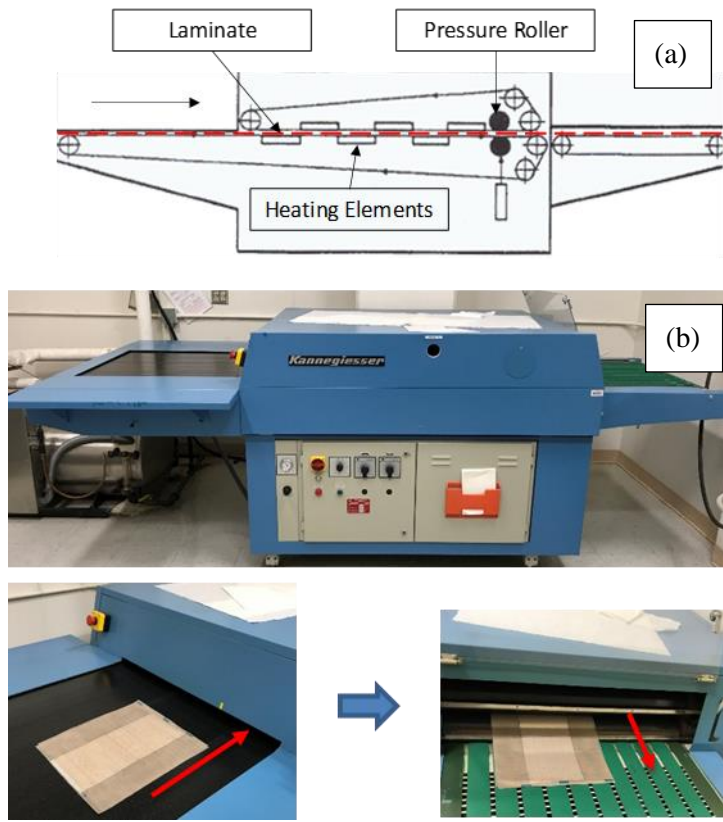


Figure 5.3. (a) Schematic of continuous fusing machine and (b) Images of the fusing machine showing the seaming process.

The whole seaming process is automatic and with high efficiency. Parameters can be readily adjusted from the control panel. Only manual work needs to be done is to lay multiple components for seaming correctly in between two sheets of non-sticky Teflon fabrics for protection. All the parameters for seaming needs to be confirmed before positioning the materials onto the conveying belt. The temperature from the nip roller surface was measured by an IR gun in order to ensure an accurate control. A schematic of a typical butt seam is shown in Figure 5.4. All the butt seam samples with varied configurations were made following the drawing.

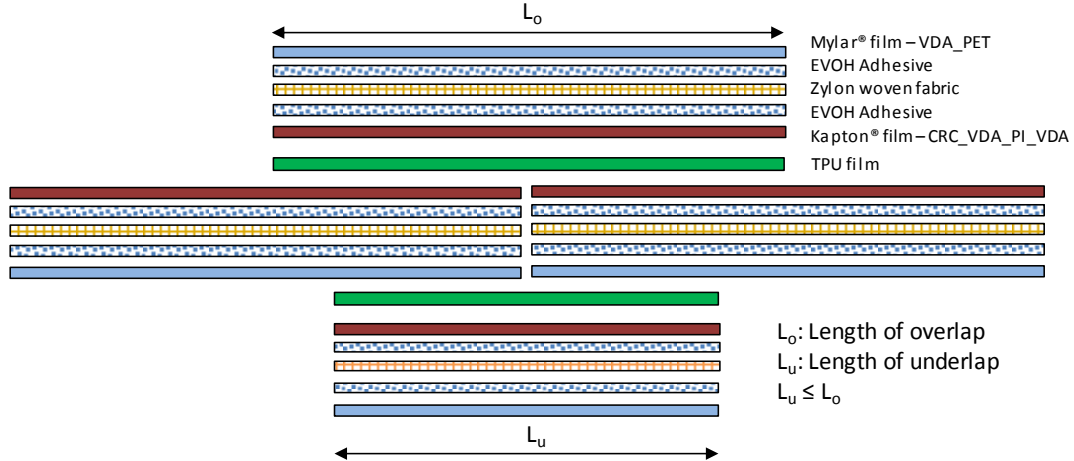


Figure 5.4. A schematic of butt seam with detailed material and structure description.

5.5 Testing and Evaluation

5.5.1 T-peel Test

To characterize adhesion properties of the laminate material, T-peel test was applied following ASTM D1876 (ASTM 2015a). This method is primarily intended for determining the relative peel resistance of adhesive bonds between flexible adherents by means of a T-type specimen. A schematic of T-peel test specimens is shown in Figure 5.5.

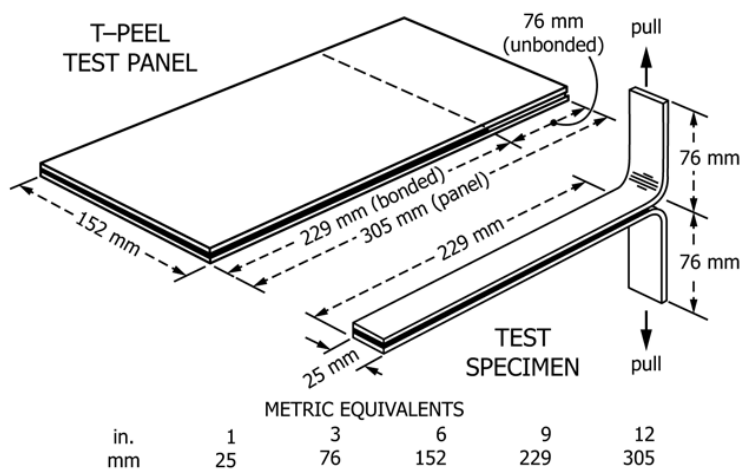


Figure 5.5. Test panel and specimen for T-peel test (ASTM 2015a).

A tensile testing machine with proper loading range and suitable grips capable of clamping the specimens firmly and without slippage throughout the tests is required. The MTS Q-Test/5 Universal Testing Machine was selected to perform the T-peel test, shown in Figure 5.6. Per the testing method, the peel strength/resistance of a specimen will be calculated by averaging the load values over at least a *12.7 cm (5 inch)* length of the bond line after the initial peak.



Figure 5.6. MTS Q-Test/5 Universal Testing Machine (<https://textiles.ncsu.edu/zte/physical-testing-laboratory/mts-q-test5-universal-testing-machine-212x375/>).

5.5.1.1 Parametric study – Laminate

To make the laminate samples for T-peel test, a piece of ultra-thin Teflon sheet needs to be applied at certain areas to prevent the EVOH film adhesives from bonding the PI and PET films to the fabric. Due to the weak strength of the ultra-thin PET film, the peeling always ends very soon because films rupture at the laminated and non-laminated boundary. Thus, only the

adhesion of EVOH on PI side can be quantitatively evaluated through T-peel Test. Five specimens from each sample were tested.

5.5.1.2 Seam study – Seam

T-peel test was performed to screen out the most critical factor(s) affecting the adhesive bonding strength and identify the best combination(s) of parameters to produce seam(s) with the best peel resistant property. To characterize peel resistance of the adhesive used for seaming, T-peel test was also applied on MTS Q-Test/5 Universal Testing Machine following ASTM D1876 (ASTM 2015a). Tensile tests were performed on the MTS Landmark servo hydraulic 250 kN testing machine, following ASTM D5035 (ASTM 2015b). It should be noted that a desirable seam failure is anticipated to occur away from the seamed region and the failure strength of the seam is higher than that of the laminate. To make the T-peel test successful, a two-step seaming process needs was followed. First, the TPU film adhesive with the same length of the laminate (30.48 cm) was adhered onto the PI side of one laminate. And then, the other laminate was bonded to the TPU adhesive by passing through the fusing machine for a second time. Five specimens from each seam sample were tested.

5.5.2 Tensile Test

High tensile strength is strictly required for envelope material in order to bear the pressure during airship operation at high altitude. Tensile strength of the laminate samples was determined using the guidelines provided in ASTM standard D5035 (ASTM 2015c). With all the high-performance materials being integrated, the laminate sample was expected to possess

high tensile strength. Therefore, the MTS Landmark servo hydraulic 250 kN testing machine was used (Figure 5.7).



Figure 5.7. MTS Landmark servo hydraulic 250 kN testing machine.

5.5.2.1 Parametric study – Laminate

In accordance with the ASTM standard, the effective gauge length was 7.62 cm and the width of the strip specimen was 2.54 cm (1 inch). Three specimens cut from each replica were tested in both warp and weft directions. During the cutting, care was given for the alignment of the yarns in the test direction, because tensile testing specimens with angled yarns can lead to different modes of failure and thus significantly lower measured strength values. On the other hand, it helps to minimize damage of the yarns at the two parallel edges, which will also cause decline of the measured tensile strength.

5.5.2.2 Seam evaluation – Seam

Double-side butt seams made in $10.16 - 0$, $10.16 - 3.81$, $10.16 - 7.62$ cm (overlap – underlap) respectively were tested for tensile strength with three specimens per replica. In order to be qualified as a strong seam, these seam specimens should be broken on the laminate, away from the seamed area.

5.5.3 Tear Test

The Tear Strength of the laminate material was measured using the central cut-slit tear testing method described in MIL-C-21189 (FAA 1995) on the MTS Landmark servo hydraulic 250 kN testing machine. A schematic diagram of a tear specimen is shown in Figure 5.8.

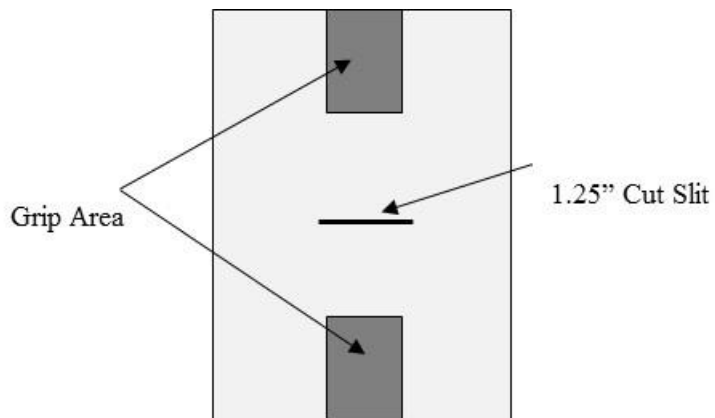


Figure 5.8. Schematic diagram of a cut-slit tear specimen.

The specimens are required to be 10.16 cm (4 inch) wide and 15.24 cm (6 inch) long. A 3.175 cm (1.25 inch) long slit was made with a razor across the center of the laminate specimen perpendicular to the direction of the load. The specimen must be placed symmetrically in the clamps of the machine with the long dimension parallel and the short dimension perpendicular to the direction of the application of the load. The yarn running parallel to the long dimension must be aligned parallel with one outside edge of the front jaw of each clamp to ensure the

same yarns being gripped in both clamps. The clamps must be 2.54 cm (1 inch) wide and must grip the yarns that have been slit. The distance between clamps must be 7.62 cm (3 inch) at the start of the test with the slit in the specimen an equal distance from each clamp jaw. The testing speed is suggested as $3.048 \pm 0.127\text{ m/min}$ ($12.0 \pm 0.5\text{ inch/min}$). Five specimens in both warp and weft directions were tested. The tearing strength is determined as the average load of the highest recorded peaks of the five specimens (FAA 1995).

5.5.4 Helium Permeation Test

To contain the helium gas inside the airship envelope, the laminate material is required to be helium tight and being able to hold helium gas over time. Helium permeation tests were conducted following the M – Manometric method provided in ASTM D1434 (ASTM 2015d). This method is used to estimate the steady-state rate of transmission of a gas through materials in the form of film, sheeting, laminates, and coated fabrics. To conform to this ASTM standard, the Labthink® PERME® VAC-V2 gas permeability tester (shown in Figure 5.9) is capable to be operated based on the differential pressure method. Gas transmission rate as well as solubility coefficient, diffusion coefficient and permeability coefficient can be measured with the equipment. Gas of interest for this research is helium. The test temperature is controlled by water bath constantly at $23\text{ }^{\circ}\text{C}$.



Figure 5.9. The Labthink® PERME® VAC-V2 gas permeability tester (<http://en.labthink.com/en-us/product/vac-v2-gas-permeability-tester.html>).

The basic principle of pressure differential method is shown in Figure 5.10. In this method, a pressure difference of 0.1 MPa is formed on two sides of the specimen. After the transmitting process has become stable, the barrier property of material can be calculated with the obtained pressure variation of lower chamber. There is no specific requirement to the property of test gas, and gas consumption is very small.

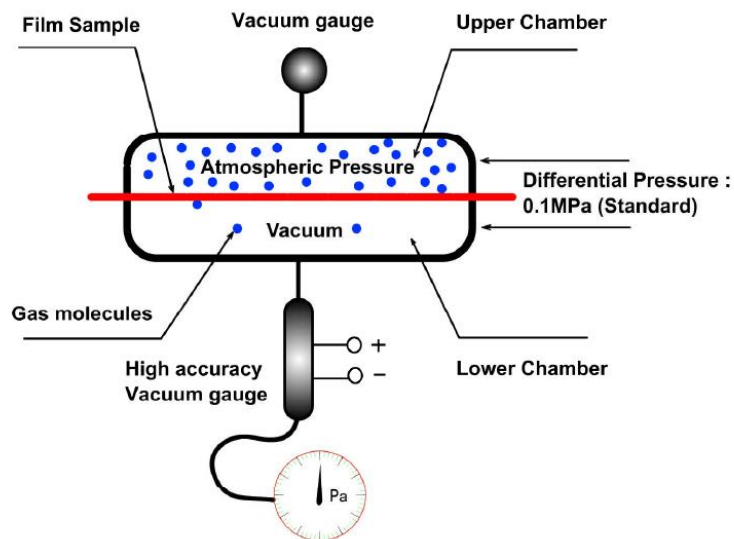


Figure 5.10. Schematic of pressure differential method utilized in the Labthink® PERME® VAC-V2 gas permeability tester (<http://en.labthink.com/en-us/product/vac-v2-gas-permeability-tester.html>).

In this test, the effective penetration area is a circle with a 35-mm diameter. The regular testing procedures are listed as follow:

- 1) Prepare specimen. The laminate composite is clipped into roundness with a diameter of 97 mm, which is matching the diameter of the outward O-ring seal.
- 2) Apply the vacuum grease carefully at the targeted annular area on the surface of bottom chamber to achieve best sealing effect, so that gas will not leak from the brim of the specimen.
- 3) Deposit specimen. The specimen is placed in the middle position of the two chambers. Especially, the specimen is within the area of the O-ring from outside to avoid the gas leakage from the brim of the specimen. On the other hand, specific grade of quantitative filter papers is used to support the specimen to avoid deformation of the specimen under the pressure difference and improve the test validity.
- 4) Tighten the chamber bolts, and then vacuum for 12 hrs.
- 5) If the required vacuum level is successfully achieved (a sign of good sealing), the test will be automatically initiated by the system.

The gas valve will be open, allowing the helium gas to flow into the top chamber to form a standard pressure of 0.1 MPa. Once the test is started, the pressure in the bottom chamber will be measured in real time and ultimately a $p-t$ curve is processed to obtain the gas transmission rate.

5.5.4.1 Parametric study – Laminate

Helium permeation tests are required to be strictly applied on good laminate (3 specimens) with rigorously controlled pre-test conditioning to eliminate any unwanted variations that the

gas permeation test results will be potentially affected by. The test specimen shall be representative of the material, free of wrinkles, creases, pinholes, and other imperfections, and shall be of uniform thickness. The test specimen was cut to an appropriate size (generally circular) to fit the test cell. The thickness of the specimen was measured to the nearest $2.5 \mu\text{m}$ with a calibrated dial gauge at a minimum of five points distributed over the entire test area. Maximum, minimum, and average values should be recorded. To be noted, the laminate specimens need to be positioned correctly to always face the PET side toward the gas inlet. Since the laminate specimens are thick and rigid, more grease is preferred to be applied at the targeted annular area on the surface of bottom chamber to provide good sealing.

5.5.5 Creep Test

Following the ASTM D2990-17, the creep tests were carried out on the MTS machine. Only seam samples were tested, and the specimens tested were cut into 2.54 cm (1 inch) wide strips. The seam specimens were subjected to a constant load of 770 N . And the load ramp time was set to be 2 s , ensuring a fast straining in accordance with the ASTM standard. The load and displacement were measured and recorded in real time with a time interval of 2 min .

6 Results and Discussions

This chapter is divided into three major sections covering the testing results and discussions of lamination parametric study, seam study and helium permeation study. Some critical effects of the variables and parameters investigated in this work were analyzed statistically. A significance level of 5% was selected to reject the null hypothesis.

6.1 Lamination Parametric Study

In this section, we varied the temperature and speed of lamination, as well as the types of Zylon® plain woven fabrics, to be able to understand how these factors affect the tensile strength, peel resistance, tear performance and helium permeation property of the laminates. All samples produced for characterization are listed in Table 6.1, with sample IDs and variable parameters listed. Two replicas were produced for each sample. TY and FY in the table indicate woven fabric from twisted yarns and flat yarns, respectively.

Table 6.1 Sample IDs and their variable parameters of lamination parametric study

ID	Temperature, °C	Dwell Time, s	Fabrics
1	185	2.1	TY
2			FY
3		3.5	TY
4			FY
5	200	2.1	TY
6			FY
7		3.5	TY
8			FY
9	215	2.1	TY
10			FY
11		3.5	TY
12			FY

In this study, the main goal is to find out how changing the lamination parameters and fabric physical structure affects the adhesion property of the laminate. Through the evaluation of the mechanical performances of all the laminate samples, the optimum parameter combinations of the lamination process to produce best composite laminate materials for airship applications can be revealed. Specifically, in this section, the best candidate laminate material with the strongest adhesion property will continue be used for the seam study. Because laminate material with strong adhesion is extremely important for the fabrication of robust and durable seams.

6.1.1 Main Effects of Lamination Parameters on Tensile Property

Uni-axial tensile tests were performed at a constant rate of 0.3 m/min (12 inch/min) up to failure of the specimens. Three specimens from each sample were tested. A representative measured stress-strain curves of uni-axial specimens in the warp and weft directions are shown in Figure 6.1. The nominal stress of this type of thin laminate composite is calculated as load (N) over specimen width (cm). So, the ultimate tensile stress at failure is obtained by applying the peak load of the tensile test.

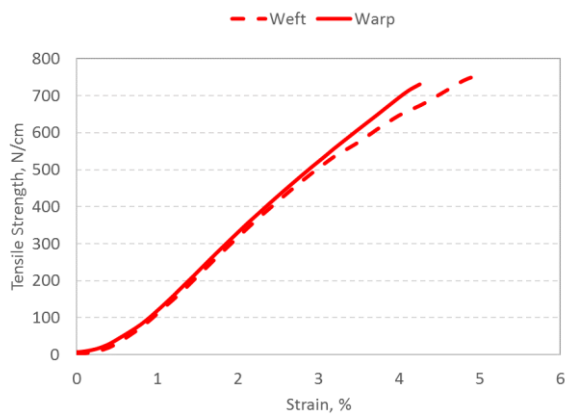


Figure 6.1. Typical Stress vs. strain curves of laminates in warp and weft directions

As can be seen in Figure 6.1, the tensile strength-strain curves are almost identical, indicating that the tensile property in both warp and weft directions are similar, owing to the balanced structure of the fabric reinforcement.

There are three representative regions in the stress-strain curves of both warp and weft directions: a crimp region, a non-linear region, and a linear region with high stiffness. In the crimp region, the stress-strain graph shows a relatively large increase in strain for a very small increase in stress. Woven fabrics inherently have crimp, so the load essentially straightens the yarns by removing the crimp at the beginning. The structural fabric layer and other functional layers are extended together and the whole laminate is with no damage.

As the load increases, the straightened yarns start to take more load, and the stress-strain graph exhibits an increased slope (non-linear region). Yarn-laminate interface debonding may take place at this stage because of different elongation between the film layer and fabric layer. Before reaching the maximum tensile strength, the stress-strain response exhibits linearity in the high stiffness region. The fabric layer becomes the major load bearing structure of the envelope when the films, with poor bonding, may be delaminated in varying degrees.

Macroscopic damage morphologies of the uni-axial tensile testing results with similar mode of failure are shown in Figure 6.2. In the process of tension, Zylon® fibers bear the major stress. Zylon® yarns fractures were the major failure mode of the tensile testing strips. Fractures tend to occur close to the grip where stress concentration is high. Minor damages of the polymeric films were also observed, being distributed randomly across the surface of the laminate.

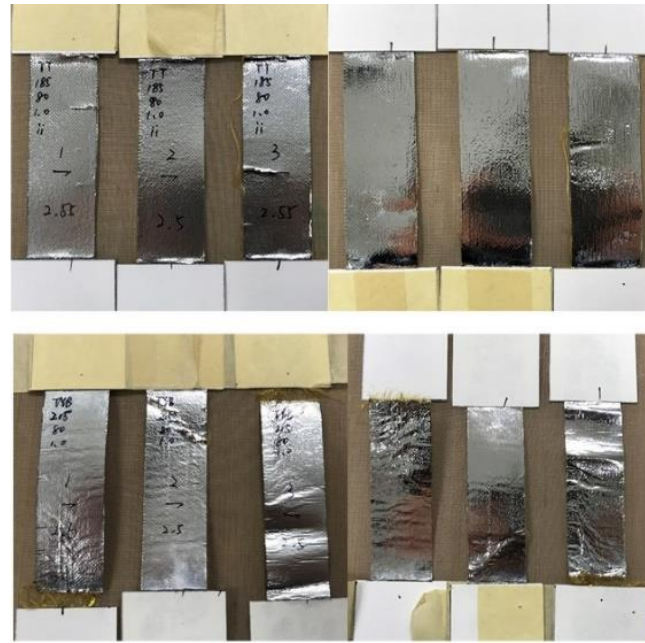


Figure 6.2. Typical modes of failure after tensile test

The results of the tensile test for samples 1 through 12 in warp and weft directions were listed in Table 6.2.

Table 6.2 Laminate tensile test results

ID	Temperature, °C	Dwell Time, s	Fabrics	Tensile Strength, N/cm			
				Warp	CV%	Weft	CV%
1	185	2.1	TY	721.01	3.68	721.97	3.44
2	185	2.1	FY	675.63	6.39	696.96	3.14
3	185	3.5	TY	725.99	3.17	710.88	3.73
4	185	3.5	FY	714.97	7.90	712.52	3.33
5	200	2.1	TY	725.26	3.65	712.15	1.79
6	200	2.1	FY	700.65	5.19	715.35	5.51
7	200	3.5	TY	729.53	1.81	694.70	1.70
8	200	3.5	FY	736.80	2.71	701.50	3.42
9	215	2.1	TY	683.89	3.06	712.31	2.26
10	215	2.1	FY	727.48	2.06	702.02	7.73
11	215	3.5	TY	720.77	2.99	696.79	3.64
12	215	3.5	FY	714.99	4.69	742.54	8.20

The results of the tensile strength of all the specimens were analyzed using univariate analysis of variance to reveal the effect of the lamination parameters (lamination temperature and dwell time) and different woven fabrics on the tensile strength of composite laminates. The results of the univariate analysis of variance test were confirmed using a follow up Tukey-Kramer post hoc test for the three main effects as well as the twelve simple effects. The statistical analysis results of warp and weft specimens are listed in Appendix A and Appendix C, respectively. Further, the main effects of the lamination process and woven fabric difference are plotted in Figure 6.3(a) to (c).

In Figure 6.3(a) to (c), the laminate tensile strength, although with certain variations, were very similar with all the different conditions investigated. The statistical analysis confirmed the observations with all the p-values being more than 0.05, indicating that the tensile strength in both warp and weft directions are not significantly different with the variation of lamination temperature, dwell time as well as the fabric types. However, there is one exception being the effect of dwell time to the laminate tensile strength in the weft direction, shown in Figure 6.3(c). Even though the distinction of tensile strength cannot be obviously seen from the histogram, the ANOVA captured the difference being significant. The p-value obtained is 0.0195, shown in Table C.9. Also, by performing the Tukey-Kramer post hoc test, it was found that the increase of the dwell time during lamination tend to cause the increase of the laminate tensile strength. The results of these two levels of dwell time belong to different subsets as shown in Table C.11.

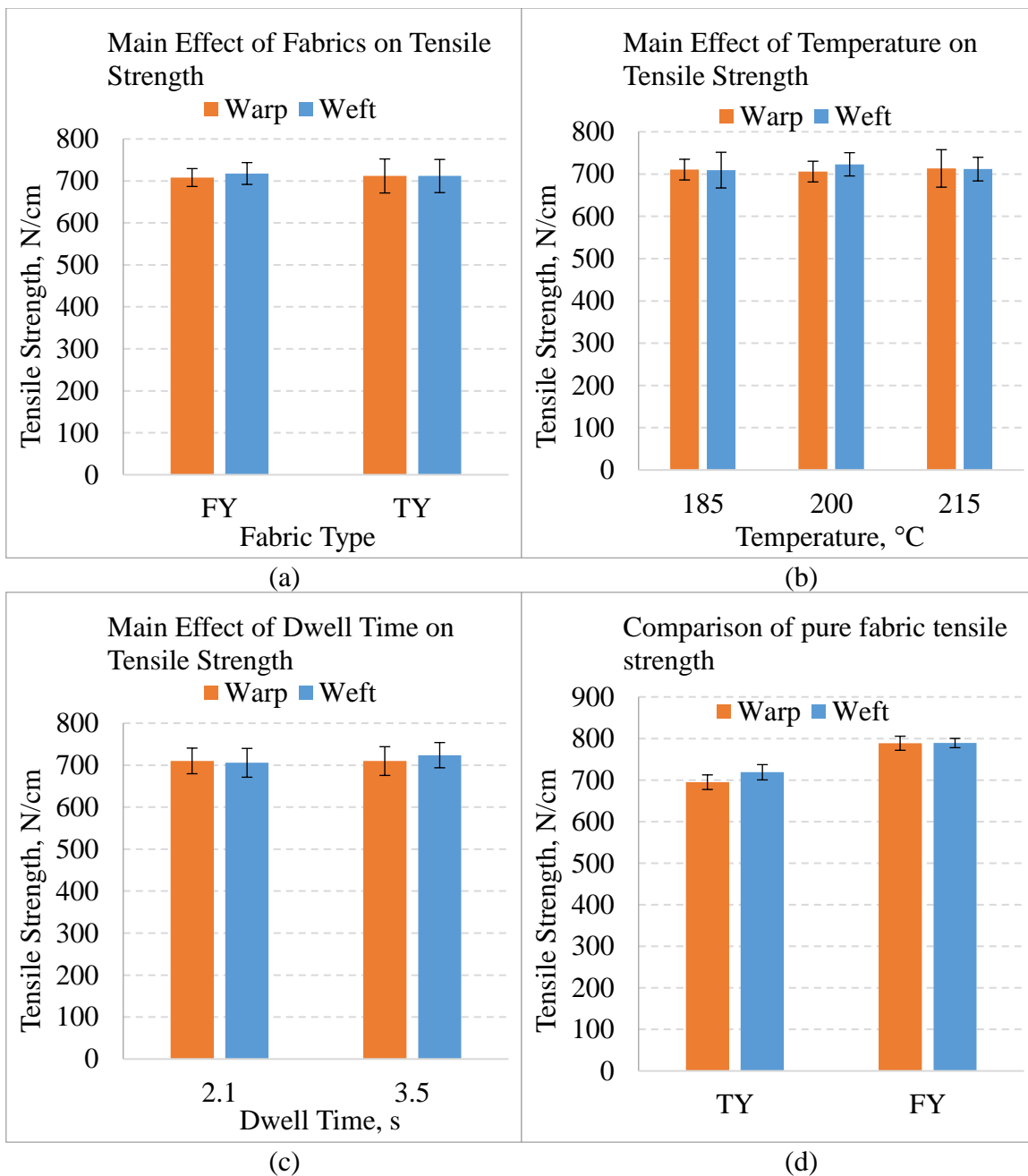


Figure 6.3. Main effects of (a) Fabric types, (b) Temperature and (c) Dwell time on tensile strength of laminate in warp and weft directions; (d) Tensile strength of pure fabrics in warp and weft direction.

Concerning laminated fabrics with high performance fabrics as the major load bearing component, the strength of the yarns is significantly higher than that of other layers of polymeric films. Thus, it is reasonable to believe that the mechanical properties of laminated fabrics, such as tensile strength, is heavily determined by the inherent material properties of

yarns. As is shown in Figure 6.3(d), the tensile strength of both TY and FY fabrics in warp and weft direction exhibited similar. Therefore, it is safe to conclude that the tensile strength of the laminate is predominantly determined by the intrinsic fabric and yarn properties. With both of the fabrics being balanced structure and having similar weave parameters (previously listed in Table 5.1), the strength in warp and weft directions are very close to each other, as is shown in Figure 6.3(d). Likewise, the tensile strength of the laminate should also be balanced in warp and weft direction.

6.1.2 Main Effects of Lamination Parameters on Peel Property

In the case of T-peel test of laminate specimens, the force required to peel the PI film off from the Zylon[®] woven fabric was measured continuously along with the peel propagation. As is clarified in the experimental part, the peel resistance is determined over at least a 12.7 cm (5 inch) length of the bond line after the initial peak. However, the failure analysis of the specimens showed that the PI films tend to be torn and fractured randomly and thus cannot make a minimum of 12.7 cm (5 inch) long peel propagation. In these scenarios, the peel strength/resistance were calculated only with the genuine length of the peel propagation they experienced. Figure 6.4 illustrates the failed T-peel test specimens with complete peel-off of PI film as well as partially peeled, torn and then fractured PI film. The propagation length before PI film fracture vary from specimen to specimen. A close-up view of the peel initiation region is also presented. It is clearly observed that the major peel failure is the exfoliation of the thin VDA coating from PI film. Apparently, the thin VDA coating is not completely separated from the original PI film substrate. The non-uniform pattern of the VDA peel

interface indicates that the adhesion is not consistent over the entire laminated area even with a good appearance.



Figure 6.4. Specimens failed after T-peel test with different mode of failure on PI film.

The tear and fracture of PI film is completely random observation happened at different propagation length and among all the groups of specimens laminated with different combinations of parameters. The shortest PI film fracture occurred right after the peel initiation. It may be an issue of the non-uniformity of the lamination process, bringing good and bad adhesion spots underneath the PI film. The results of the peel testing are listed in Table 6.3.

Table 6.3 Peel strength of laminate

ID	Temperature, °C	Dwell Time, s	Fabrics	Peel Strength, N/cm	
				AVG.	CV%
1	185	2.1	TY	1.966	10.453
2	185	2.1	FY	1.945	16.457
3	185	3.5	TY	2.066	4.577
4	185	3.5	FY	1.925	11.149
5	200	2.1	TY	2.158	4.452
6	200	2.1	FY	2.110	7.749
7	200	3.5	TY	2.085	6.113
8	200	3.5	FY	2.264	7.467
9	215	2.1	TY	2.081	8.401
10	215	2.1	FY	2.347	17.428
11	215	3.5	TY	1.819	6.879
12	215	3.5	FY	2.116	1.110

The results of the peel strength/resistance of all the specimens, were analyzed using univariate analysis of variance to reveal the effect of the lamination parameters (lamination temperature and dwell time) and different woven fabrics on the peel strength of composite laminates. The results of the univariate analysis of variance test were confirmed using a follow up Tukey-Kramer post hoc test. The statistical analysis results are listed in Appendix D. Further, the main effects of the structural parameters are plotted in Figure 6.5.

Figure 6.5(a) indicates that there is no statistically significant difference between the peel strength of the laminates made with different fabrics. Whereas, in Figure 6.5(b) the peel strength is significantly different between the laminate samples made at 185 °C and 200 °C. This is an indication that increasing temperature may help to improve the adhesion strength. However, with a further increase of the temperature to 215 °C, the adhesion doesn't seem to increase accordingly. Because there is no significant difference between the peel strength of the laminate sample made at 200 °C and 215 °C. It is also found from the post hoc test that the peel strength of the laminate samples in the group of 185 °C actually is not significantly

different from the ones in the group 215 °C, indicating that a further increase of temperature can potentially damage the peel strength to some extent. For the different dwell times during the lamination, there is also no statistically significant difference in the peel strength as illustrated in Figure 6.5(c). By performing a post hoc test, the insignificance was confirmed, and that both results belong to the same subset as shown in Table D.11. Therefore, it can be concluded that temperature seems to have more significant impact toward the peel strength than the fabric types and dwell time. A proper temperature control for lamination can be beneficial to produce laminate materials with better adhesion and therefore high peel resistance.

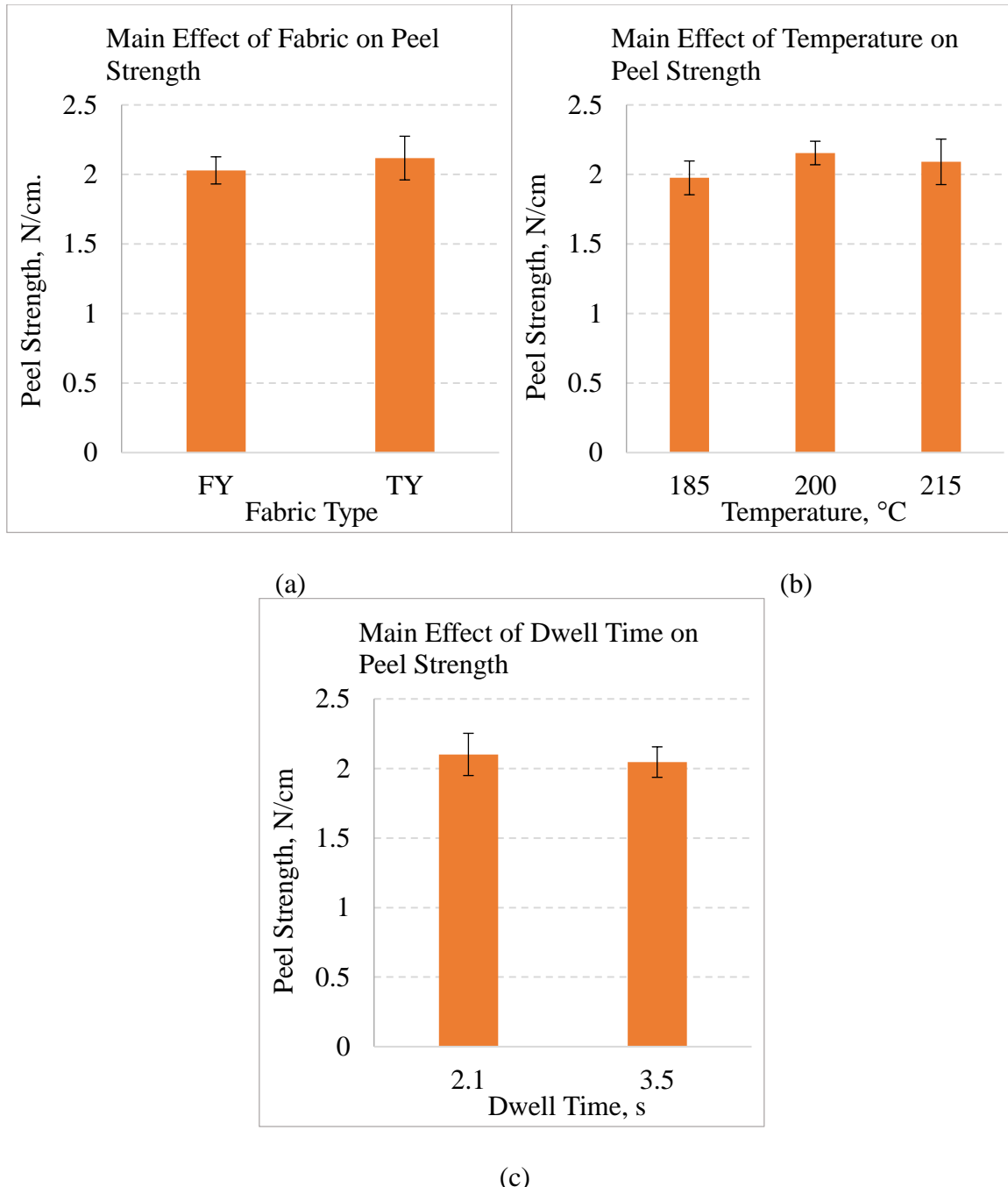


Figure 6.5. Main effects of (a) Fabric types, (b) Temperature and (c) Dwell time on peel strength/resistance of laminate.

Although the T-peel test was originally selected to evaluate the adhesion performance between the polymer films and the Zylon® fabrics, it does not fulfill the purpose completely and correctly. It is noticed that our laminated structure consists of some thin VDA coated

polymer films, where the VDA coating replacing the polymer surface to create direct contact with the adhesives and the fabrics. Therefore, indeed we are investigating the interfacial adhesion between the Zylon® fabric and the VDA coating. However, being an extremely thin layer of coating only vacuum deposited on the polymer film (specifically PI film to our discussion), the VDA coating can be very fragile when facing mechanical force such as peeling. The interaction between the VDA coating and PI film is completely physical and at a relatively low level compared with the adhesion provided by the adhesive of the laminate. Thus, when the peel is initiated, the VDA coating will stay adhered with the adhesive and have to be separated from the PI film, as is shown in Figure 6.4. In this case, it is clear that the interface these T-peel tests were investigating on is mainly the interface between VDA coating and PI film, which is some property irrelevant to the lamination parameters. The results from the T-peel test cannot be directly used for lamination parameters evaluation, but there is still valuable information conveyed through these tests. Firstly, the EVOH film after melting provided decent amount of adhesion to the metallic surface of VDA coating, being at least stronger than the adhesion between the VDA coating and PI film. Secondly, the high lamination process temperature doesn't seem to degrade the adhesion between the VDA coating and PI films.

To effectively evaluate the adhesion performance of the laminate materials determined by the lamination parameters, alternative testing method such as scratch test can be applied. It is also known that the tear behavior of coated and laminated fabrics is significantly affected by the adhesion property. Therefore, the evaluation of tear testing can possibly provide important explanations on the mechanism of inter-layer bonding of laminate composite materials.

6.1.3 Main Effects of Lamination Parameters on Tear Property

Depending on the degree of adhesion within the composite laminate structures, the tear performance of a fabric reinforced composite laminate can be significantly different from pure textile fabrics. In laminated fabrics, the flexible soft polymeric membranes do not hold yarns as firmly, and yarn slippage may occur. During the tearing in laminated fabrics, due to slippage of yarns (mobility), they move to the delta zones and resist the tear load as group rather than individual. The higher the yarn mobility in the laminate due to poor adhesion allows yarn pull-out that result in higher number of yarns that move to the delta zones and resist the tear load.

Concerning laminated fabrics, two types of failure mode were mostly observed in the literature for tear propagation with central slit method: progressive failure and brutal failure (Chen & Chen 2016). Brutal failures always occur in a sudden, with a rapid tear propagation across the specimen where the tear is initiated. A sudden drop of the applied load is therefore associated with this process. For tests involving catastrophic tearing failure, the load at the rupture of first bunch of yarns is usually the maximum load. Then, the tensile load quickly plunges to a very low level following the peak. In contrast, the progressive failure usually take place gradually and is more complicated. In some laminated structures with lower adhesion, a few yarns break at the tip of the crack while the load is still increasing on the specimen owing to yarn grouping and jamming. The initial crack continues to propagate steadfastly and the load either fluctuates at roughly the same level or decreases gradually to the low level (Chen & Chen 2016). In general, only laminate specimens with strong adhesions will be subject to brutal failure. The tear propagates simultaneously in the structural fabric layer and other laminated thin polymeric film layers, and the edges from tear ruptures of the yarns and laminated layers almost completely overlap with each other. However, for samples with poor adhesion, the

edges from tear ruptures of the yarns and other laminated layers do not overlap with each other, which can be attributed to more significant yarn pull-out. A specimen with poor adhesion could show great shear deformation and yarn pull-out in groups, when the tear propagation is initiated. In general, the adhesion properties of the laminate composite materials determine the tear performance. The other way around, by investigating the tear performance of the laminated fabrics, useful information on laminate adhesion can be unfolded as well. Therefore, tear failure mode could be used as a reliable method for assessing adhesion of the laminate component.

Uni-axial tensile load was applied at a constant rate (3.048 m/min , the same with tensile test) up to failure of the tear specimens. Three specimens from each sample were tested. A typical measured load-displacement curves of a central slit tear specimens is shown in Figure 6.6. The tear strength of this type of thin laminate composite is characterized by using the tensile load (N).

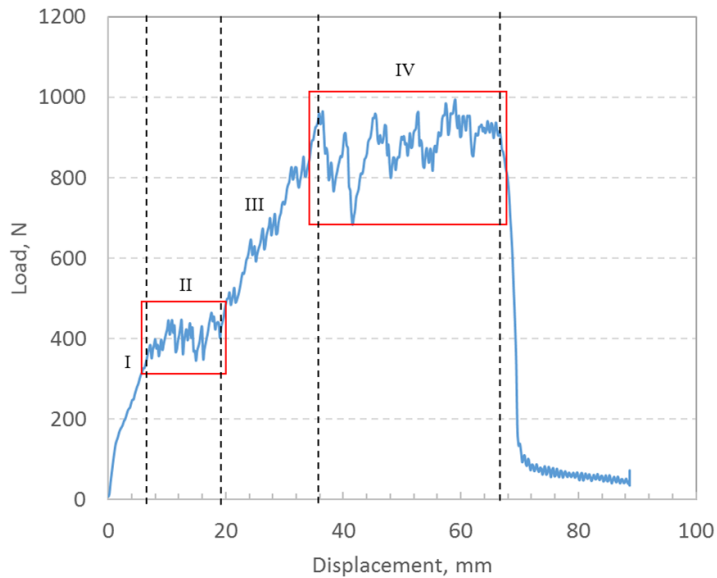


Figure 6.6. Typical load vs. displacement curve of a laminate central slit tear testing specimen (a commercial laminate sample from production line).

The failure of this laminate specimen is considered to be progressive, thus the load-displacement curve of tear propagation can be divided into several distinct regions (regions I-V in Figure 6.6). Each of the regions exhibits certain kind of behavior throughout the complete tear initiation and propagation. Briefly speaking, region I is a slit opening region where no yarn slips and fractures of individual yarns or in small groups hasn't happened yet. Only some of the yarns close to the slit tips are straightened along the loading direction. Region II and IV are both tear propagation regions which are commonly seen in the tearing of laminated fabrics. Yarn slippage and fracture are always involved in these tear propagation regions to give the load curve an appearance of fluctuations. In region II, the load drop is close to single yarn tensile load ($\sim 47 \text{ N/yarn}$) by comparison, showing that yarns are most likely fractured independently without sharing the load. As the tear propagates horizontally, more yarns in vertical direction were brought together to bear the elevated tensile load. Being a transition zone from one tear propagation zone to the other, region III is nonetheless with merely minor yarn fractures, exhibiting a fast load increase (high modulus similar to region I). At a certain high load level, the yarns start to fracture again, leading to the fluctuation of the load curve in region IV. Here, the amplitude of the load fluctuation is larger, indicating the fracture of potentially multiple yarns simultaneously. Lastly, region V represent the post tear propagation region where the load just plunges significantly due to the last group of yarns being pulled out completely since the tear is reaching the edge of the tear specimen. To obtain a more in-depth understanding of the central slit tear propagation mechanism, a more comprehensive discussion explaining those representative features in Figure 6.6 is presented below. Images of the specimen behavior throughout the tear test are also presented to help better understand the tear mechanism.

Region I: Slit opening

As displayed in Figure 6.7(a), the laminate central slit tear specimen was initially gripped on the MTS machine with the regions around the slit being relaxed and free since the tabs applied on the specimen was only 2.54 cm (1 inch) wide, and the gripped area is actually shorter than the slit length, which is $2.54 - 3.175\text{ cm}$ ($1\text{-}1/4\text{ inch}$). Located at the specimen center. So, when the tension is applied onto the specimen, initially there is some tension zone re-shaping. The areas under tension was outlined as the red dashed trapezoid shape right at the moment when tension being applied to the slit specimen. From there on, the slit starts to open up, and the vertical yarns on both side being contracted toward the center, shown by the red arrows. The vertical yarns are squeezed and jammed together. Also, as the slit opens up, the horizontal yarns close to the slit tips were being strained along the load direction. Thus, the tension zone changed shape from trapezoid to rectangular. However, in this particular slit opening process, no yarn slippage and fracture occurred yet. Thus, the load curve in region I shows a smooth increase to displacement.

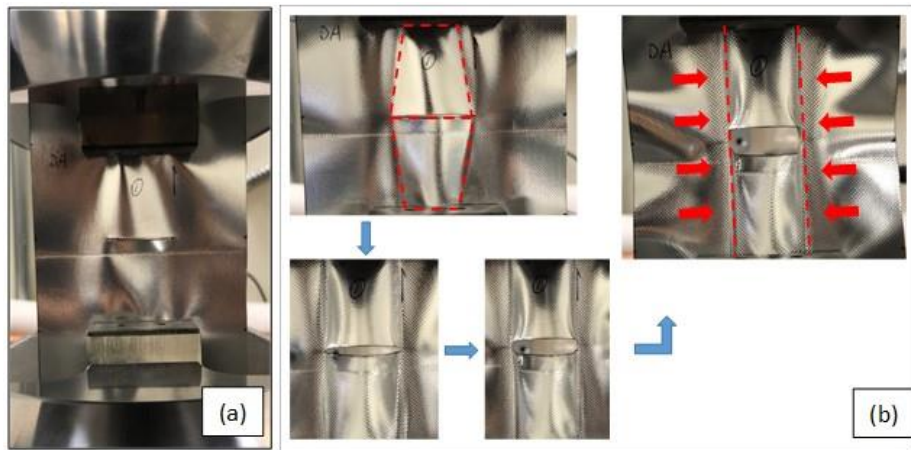


Figure 6.7. (a) Central slit tear test specimen gripped on the MTS machine, (b) The slit opening process.

The tear propagation legitimately started from Region II all the way to specimen failure. A flow chart displaying images of the sequential stages of the progressive tear propagation is shown in Figure 6.8. With that being the guidance, each of the regions from II to V were discussed respectively.

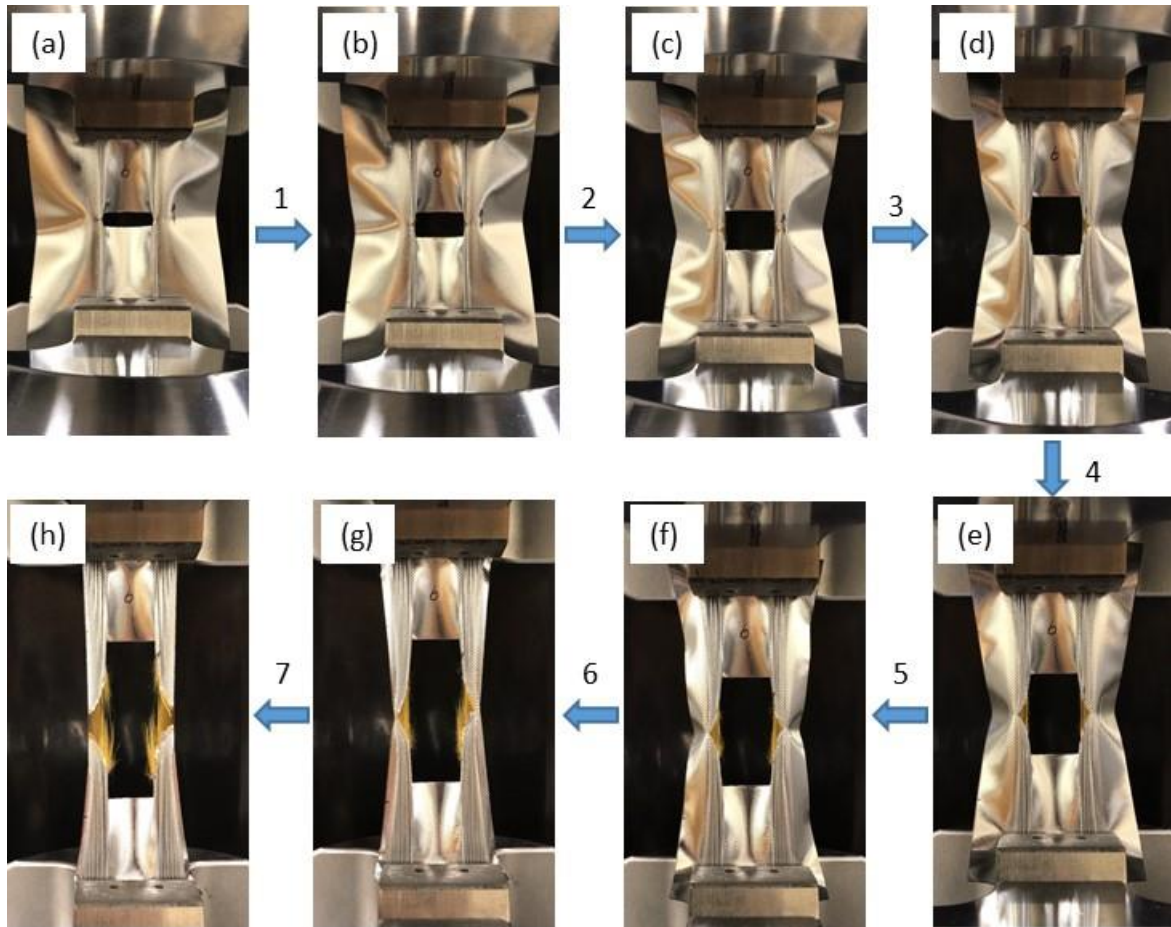


Figure 6.8. Typical tear propagation process of central slit tear testing specimen under uni-axial tensile loading.

Region II: Immediate progressive tear propagation

After the central slit is fully opened up in region I, further extension first initiated the slippage of horizontal yarns against the vertical yarns close to the slit tip. This type of tear behavior revealed that the adhesion of the laminate specimen is not strong enough to hinder the yarns' mobility and force the yarn fracture. Thus, the failure of this specimen will be

progressive rather than brutal. The slippage of horizontal yarns resulted in the fracture of the thin polymeric films bonded to the fabric on both sides. As shown in Figure 6.8(a), the yellowish Zylon® yarns were uncovered following the fracture of the laminated polymeric films. This region is named as immediate progressive tear propagation region owing to the formation of the ‘tear delta zone’ immediately after region I. The tear delta zone of this laminated specimen in this particular method is the delta-shaped opening composed of the stretched vertical yarns bridging the gap between the two separating horizontal yarns. The separation of two horizontal yarns not only caused the polymeric film fracture but also led to the contracting of horizontal yarns, which facilitate the formation and expansion of the tear delta zone. Basically, the yarns in the delta zones can be divided into two categories. The vertical yarns are the principal yarns and the horizontal yarns are secondary ones. It was observed in Figure 6.8(a) – (d) that the initial small tear delta zone of the tear tip developed gradually. As indicated by the load fluctuation zone following the slit opening, it is believed that principal yarns started to break quickly after the slit was fully opened. It was not clearly visible in Figure 6.8(d); yet very soon, principal yarn fractures are obviously observed in Figure 6.8(e). Despite the fact of secondary yarn slippage, the principal yarn fractures are still mainly due to the resistance from laminate adhesion.

Region III: Tear delta zone expansion

As the displacement increases, the secondary yarns continue to slip and be jammed together, causing the size of the delta zone to continuously increase and a large number of frictional points of contact form on and beneath the boundary of the tear delta zone. As the number of these contact points increase, slipping against the principal yarns becomes more and

more difficult, and thus the load is progressively delivered to the secondary yarns. The load transferred by the secondary yarns is delivered to other principal yarns again which are beyond the first batch of intact yarns in the delta zone, and then the size of the delta zone increases quickly, corresponding with a steep load increase shown in Figure 6.6. As being evidently seen from Figure 6.8(f), multiple new principal yarns appeared in the enlarged tear delta zone and were all under tension.

Region IV: Ultimate progressive tear propagation

As the load continues to build up, the principal yarns being locked in the tear delta zone in the previous region start to break, corresponding to the load drop entering this region. With the further increase of the load, some more of the principal yarns fail, and yarns again slip by each other to the delta zone, and so on, in a cycle, until the failure extends over the length tested. This is exactly what is observed in Figure 6.8(g) and (h). The breaking of the previously moved to delta zone principal yarns and incoming of additional ones to the delta zone happened in a cycle. The load is thus fluctuating at a certain level, which is much higher than the previous tear propagation region. That is why this region is called ultimate progressive tear propagation.

Region V: post-peak

A rapid decrease appears in the post-peak region with no fluctuations. Obviously, as the tear propagation reaching the end of the specimen, there is reduction and no more expansion of delta zone. While the load was at such a high level that the rest of the principal yarns were simply pulled out completely, causing the final steep drop of the tensile load. This is due to the yarn-adhesive interface debonding that occurs gradually with producing a partially intact

interface, which allows yarns to be pulled out against the frictional resistance along the debonding interface. It is apparently observed from the failed specimen in Figure 6.9 that several principal yarns close to the specimen edge are pulled out without being fractured.



Figure 6.9. Images of the failed commercial laminate sample from production line after tear test.

However, the tear propagation curves of different laminate specimens may vary significantly. Because the shapes and constituents of the tear propagation curves are determined by the exact adhesion levels of laminate specimens. The tear load-displacement curves of laminate specimens can provide useful information on tear propagation performance. In combination with the image analysis of failed specimens, an accurate evaluation of adhesion level of the laminate specimens can be obtained. With these analyses being applied to EVOH based laminate materials for tear performance evaluations, five most representative behavior of the central slit tear test are identified in order to differentiate the levels of adhesion for different laminate samples. Since the two of the tear performance are similar, the adhesion assessment will be ranked at four different levels, namely excellent, good, fair and poor.

Following this sequence of this adhesion rank, the detailed laminate tear performance analyses and justifications are presented below.

Figure 6.10 shows the tear load-displacement response of a laminate specimen with excellent adhesion obtained from one of the typical central slit tear tests. The load-displacement curve is simple, constituted by only two regions. Region I is the normal slit opening region where the yarns are only straightened with no yarn slippage and yarn fracture observed. Region II is the tear propagation zone showing load decrease throughout the whole region. For this type of laminate specimens, during the tear test, many yarns broke almost simultaneously and therefore the load plunged to a low level nearly immediately after the peak. This also led to shorter overall specimen displacement compared with progressive failure specimen, less peaks and shorter duration of the plateau region because there is minimal to none secondary yarn slippage in the laminate. This is good indication of good adhesion between the reinforcement and the adhesives.

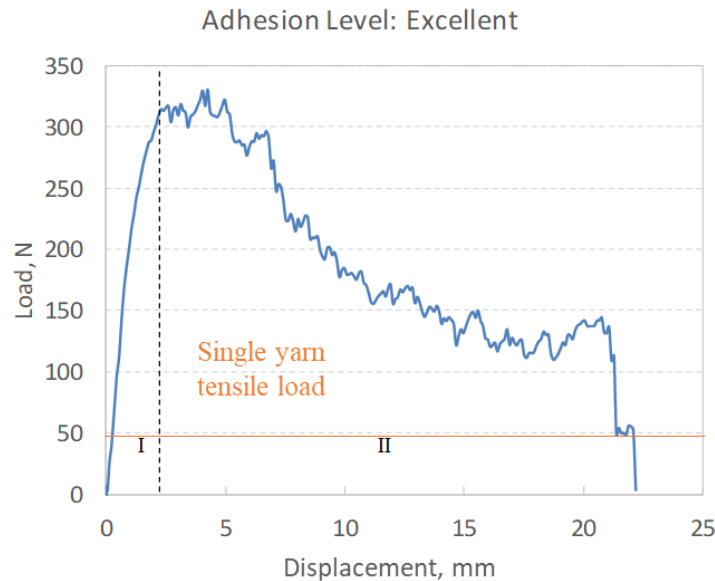


Figure 6.10. The Load-displacement curve of a typical brutal failure of a central slit laminate specimen with excellent adhesion.

By observing the failed specimen in Figure 6.11, the principal yarns break at the tear failure edge and the fracture of the polymeric films and yarns coincide very well. There is simply small tear delta zone with few yarns being formed because the failure happened so fast that the principal yarns just fracture in a fashion of pure tensile. In this case, the adhesion of the laminate is so strong that the principal yarns were completely locked when tension was applied. It is also noted that the secondary yarns have not been jammed together just yet. There is no resistance or anchoring of the principal yarns from the secondary yarns but all from the adhesion of the laminate itself. Therefore, this mode of failure is confirmed as brutal failure and is thus not representative for samples with progressive tear propagation. The adhesion level of this type of laminate specimens are ranked as excellent.



Figure 6.11. Brutal failure of laminate tear test specimen.

Another mode of tear behavior is shown in Figure 6.12. The load-displacement relationship of this type of laminate specimen has three distinct regions. Region I is the normal slit opening region where the yarns are only straightened with no yarn slippage and fracture observed. Region II is the typical immediate tear propagation zone showing load fluctuations throughout the whole region. The amplitude of the load fluctuations is larger than single yarn

tensile load. Therefore, it is apparent that more than one yarn fractured at the same time during the tear propagation, which is an indication of load sharing. At the end, region III is the post-propagation zone exhibiting the failure of the whole specimen. For this type of laminate specimens, the immediate load oscillation after slit opening proved that the principal yarns started to fracture at very low displacement. As discussed above, although the tear delta zone is forming early and propagating gradually, there is still not sufficient frictional resistance provided by jammed secondary yarns at low displacement. Thus, the main resistance to force the yarn fracture at early stage is the resistance from laminate adhesion, indicating that this type of specimens possesses a relatively high level of adhesion.

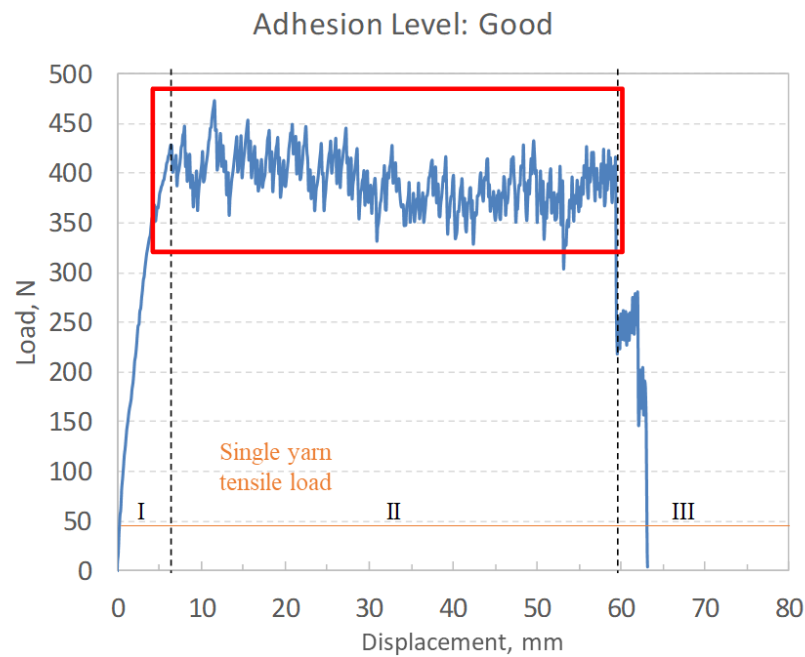


Figure 6.12. The Load-displacement curve of a typical immediate tear propagation of a central slit laminate specimen with good adhesion.

Figure 6.13 shows the specimen after the test was completed. This type of specimen exhibited a more complicated mode of failure compared with the brutal failure. The principal yarns break gradually with relatively short fringes exposed. This indicates that the adhesion of the laminate is good that the principal yarns were broken under tension with minor slippage of

secondary yarns. Polymeric films were cracked with only minor delamination observed around the tear failure boundary. The specimen contracted from edge to the central slit horizontally, causing the yarns to be tightly jammed together. The slippages of the secondary yarns are considered relatively difficult, causing the yarn to fracture only in a small tear delta zone. The adhesion level of this type of laminate specimen is therefore ranked as good.



Figure 6.13. An image showing progressive failure of laminate tear test specimen with immediate tear propagation.

As is shown in Figure 6.14, the tear load-displacement curve of this type of laminate specimen consists of four regions. Region I is the normal slit opening region where the yarns are only straightened with no slippage and fracture observed. Region II is considered as a delta zone expansion region, where the secondary yarns are able to slip more against principal yarns due to relatively weak bonding. The tear delta zone will thus grow continuously, bringing more principal yarns together to bear elevated tensile load. Therefore, in this region, the load continued to increase rapidly with displacement. At certain displacement, the yarns are jammed together so tight that the frictional resistance at the yarns crossover points is very high to cause yarn fractures. The load will then drop, and the curve is transitioned into region III, which is a

typical ultimate tear propagation zone. The amplitude of the load fluctuations is also observed to be significantly larger than single yarn tensile load, proving the simultaneous fracture of multiple yarns during tear propagation. Following the fracture of the first principal yarns, tear propagation will start so on and so forth until the fracture of the whole tear test specimen. Since the tear propagation seems to be delayed, this tear behavior can be called delayed tear propagation in contrast to the previously discussed immediate tear propagation. Both of them are categorized as the progression failure. Lastly, region IV is the post-propagation zone exhibiting the failure of the whole specimen with a plunge of load on the curve.

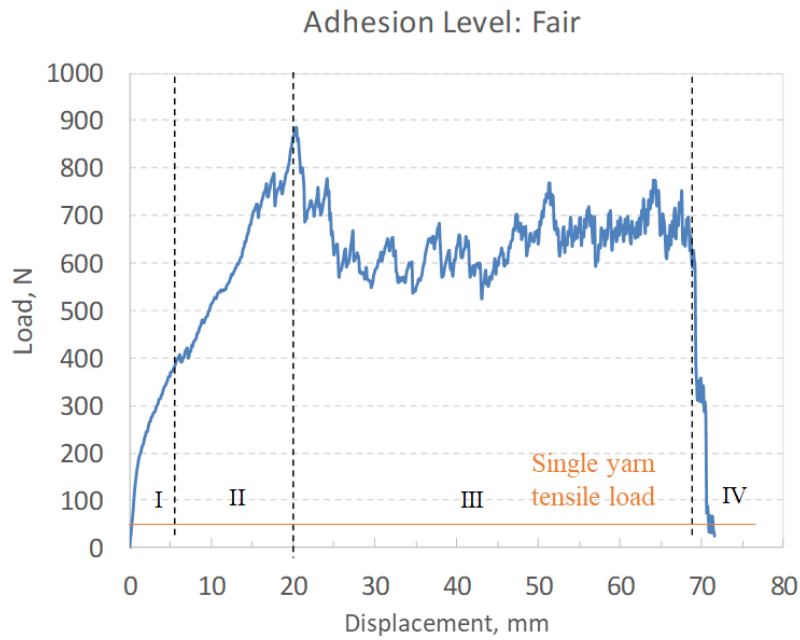


Figure 6.14. The Load-displacement curve of a typical delayed tear propagation of a central slit laminate specimen with fair adhesion.

As observed in Figure 6.15, this type of specimen exhibited a similar as complicated mode of failure compared with the immediate tear propagation specimen. In comparison, the principal yarns break gradually with much longer fringes left on the tear fracture surfaces. This observation validates the discussion of delta zone expansion. The tear propagation and yarn fracture were both delayed until the formation of larger delta zone, where more principal yarns

were free to move and gather and longer distance between the two separating secondary yarns were achieved. Therefore, when the yarn frictional resistance forced the principal yarns to fracture at the delta zone boundary, the fringes will be inevitably longer compared with the case in immediate propagation. This simply indicates that the adhesion of the laminate is weaker than that in the case of the immediate tear propagation, allowing more secondary yarn slippage. Polymeric films were also cracked more aggressively with large areas of delamination observed at load concentrated zone. The horizontal yarn contraction is also significant enough to cause tight yarn jam. The slippage of the secondary yarns is considered relatively easy, causing the yarns to fracture in a large tear delta zone. The adhesion level of this type of laminate specimen is thus ranked only as fair.



Figure 6.15. An image showing progressive failure of laminate tear test specimen with delayed tear propagation.

As is shown in Figure 6.16, the load-displacement curve of this type of laminate specimen consists of three regions. Region I is the normal slit opening region where the yarns are only straightened with no slippage and fracture observed. Region II exhibited a similar trend of load-displacement behavior compared with the delta zone expansion. Yet, the increase of the

load is much slower, indicating that the principal yarns are not picking up the load effectively. This is a sign of principal yarn pull-out in the loading direction. The adhesion is so poor that the principal yarns are slipped and pulled out with low resistant force. Then, with the increase of the displacement, more principal yarns will be pulled out from one end. While, with the tear delta zone being enlarged and more principal yarns pulled out, the tensile load is increasing to displacement but at a much lower rate compared with the previous case. At the end, the load will drop rapidly in Region III when all of the principal yarns are completely pulled out. Since there is no yarn fractures in Region II, the increase of the load-displacement curve is quite smooth and only fluctuate a bit due to slippage of yarns with stick-slip behavior that caused the load fluctuation seen in the load-displacement relationship. Because this type of tear propagation is all about principal yarn pull-out, this tear behavior can be called principal yarn pull-out.

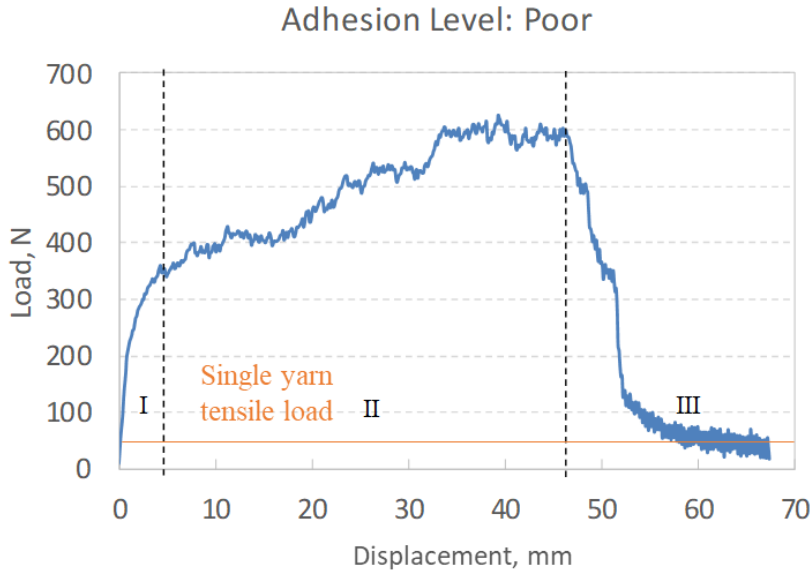


Figure 6.16. The Load-displacement curve of a typical principal yarn pull-out of a central slit laminate specimen with poor adhesion.

As shown in Figure 6.17, this type of specimen exhibited a very self-explanatory failure mode of principal yarn pull-out. This clearly indicates that the adhesion of the laminate is too

poor to stop the principal yarns from slipping. With the weak bonding between yarns and the polymeric films, the damage to these thin films are actually minimal. The horizontal yarn contraction is moderate, and the principal yarns are not significantly jammed together. The adhesion level of this type of laminate specimen is therefore ranked as poor.



Figure 6.17. An image showing progressive failure of laminate tear test specimen with principal yarn pull-out.

The principal yarn pull-out is actually not the worst case of laminate adhesion. As is shown in Figure 6.18, the load-displacement curve of this type of laminate specimen consists of three regions. The overall appearance of the load-displacement curve is very similar to the previous case. However, the load increase rather rapidly to displacement in Region II, which is a lot different from the instance of principal yarn pull-out.

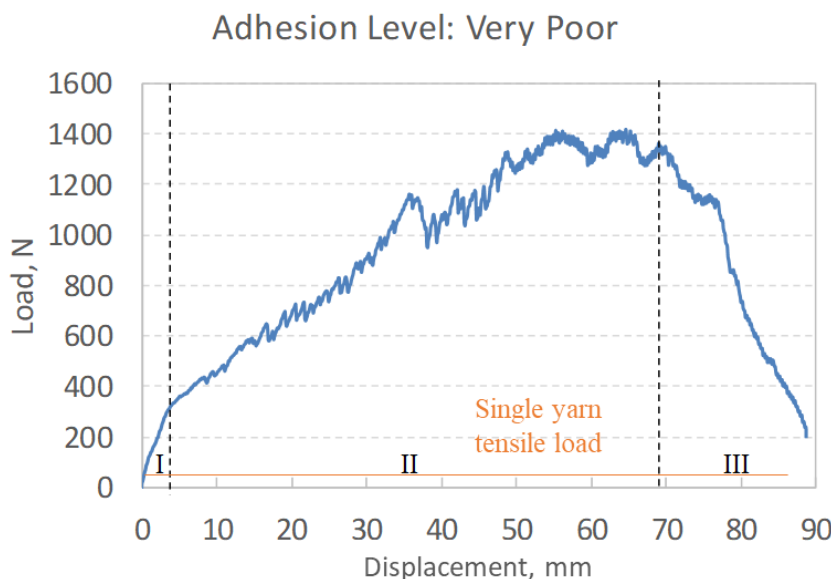


Figure 6.18. The Load-displacement curve of a typical principal yarn pull-out of a central slit laminate specimen with poor adhesion.

In this type of laminate specimen, the adhesion in certain areas are so poor that the interactions between the polymer films and reinforcement fabric barely exist. The polymer films delaminate easily and fracture with the increase of displacement. Therefore, in these areas both of the principal and secondary yarns could slip and rotate somewhat freely at a moderate shear angle and create the fabric-dominated section, resulting in the extension of the material without significant tensile loading of the yarns. The behavior causes a reduction in the slope of the load-displacement curve, transitioning from Region I to II. Once the yarns stop rotating and become locked, the load increases rapidly. This is very similar to the tear behavior of pure fabric specimen, shown in Figure 6.19.

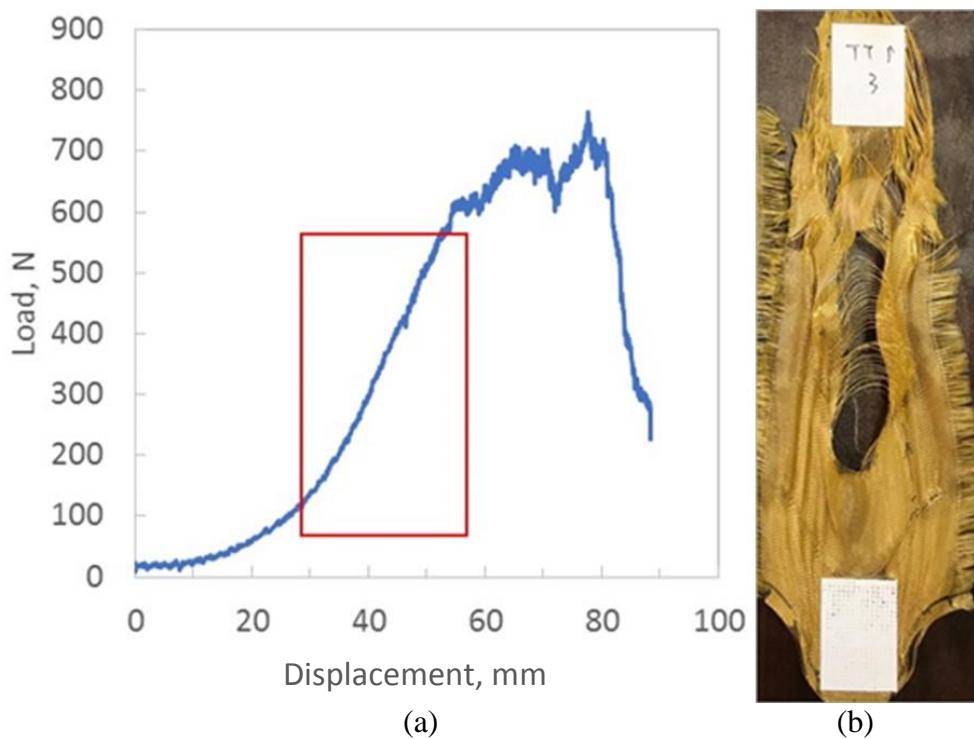


Figure 6.19. (a) Typical Load-Displacement curve of central slit specimen of pure fabric (b) Zylon® fabric failed due to shear.

For the shear behavior of Zylon® woven fabrics in Figure 6.19(a), the concave shape of the curve has several distinct regions: the friction-dominated region at low shear loads; the yarn compaction region, where the slope increases with shear angle; and finally the post-locking angle with a sharp, relatively linear increase in shear load (highlighted in the red rectangle). With the further increase of load, the fabric just crashes due to yarn pull-out in a relatively random fashion. The latter part of the load-displacement curve is more complicated and difficult to identify the exact reason for such behavior. Likewise, the curve of laminate specimen also exhibits some fluctuation of load in Region II, indicating irregular deformation occurring during the test. By observing the failed specimen, one can clearly see the exaggerated delamination and fracture of the polymer films. The laminate simply behaves similarly to a pure fabric with the shearing being the dominant failure mechanism. Some random yarn pull-out can also be observed close to the slit tip and even tab area. Because of the similar mode of

failure to fabric shear, the tear behavior can be named as fabric shear deformation. Overall, the lamination on this type of specimens were significantly inadequate to incorporate all the components into one strong composite as a whole. Therefore, the adhesion level is decided to be even worse than the instance from principal yarn pull-out and ranked as very poor.



Figure 6.20. An image showing progressive failure of laminate tear test specimen with fabric shear deformation.

The results of the tear test for samples 1 through 12 in warp and weft directions are listed in Table 6.4. The results of the tear strength of all the specimens were analyzed using univariate analysis of variance to reveal the effect of the lamination parameters (lamination temperature and dwell time) and different woven fabrics on the tear resistance of composite laminates. The results of the univariate analysis of variance test were confirmed using a follow up Tukey-Kramer post hoc test. The statistical analysis results of warp and weft specimens are listed in Appendix E and Appendix F, respectively. Further, the main effects of the lamination process and woven fabric difference are plotted in Figure 6.21(a) to (c).

Table 6.4 Laminate tear test results

ID	Temperature, °C	Dwell Time, s	Fabrics	Tear Strength, N			
				Warp	CV%	Weft	CV%
1	185	2.1	TY	439.47	27.32	455.64	46.40
2	185	2.1	FY	783.17	27.81	417.54	2.87
3	185	3.5	TY	893.88	37.81	754.75	36.81
4	185	3.5	FY	686.01	48.17	571.67	35.63
5	200	2.1	TY	900.91	55.70	649.90	39.12
6	200	2.1	FY	777.86	20.76	694.41	29.02
7	200	3.5	TY	773.16	48.43	1280.48	31.28
8	200	3.5	FY	789.81	38.07	770.21	58.43
9	215	2.1	TY	625.92	43.11	1042.40	67.46
10	215	2.1	FY	740.36	43.43	434.32	22.59
11	215	3.5	TY	787.94	63.91	651.37	35.35
12	215	3.5	FY	642.17	57.32	645.75	40.22

*Tear strength is the average load of the highest recorded peaks of the five specimens from each sample according to the instructions in FAA 1995

When preparing for the tear test, all specimens need to be carefully fabricated along the yarn orientations, avoiding the loss of yarns. However, it is inevitable to cut one or two yarns during specimen preparation. Also, it is known that laminated fabrics have a significant level of variability across the width of a single roll due to bowing or skewing of the fabric during manufacturing. Therefore, to minimize the negative effect, the cruciform specimens should be cut from the center of the roll (Chen et al. 2015). However, restricted by the sample size of the laminates made on the laminator at NCSU, we have to cut certain number of specimens at areas close to the sample edges. This could partially explain the high CV% of the data we obtained from the tear testing.

Firstly, the tear strength results in the warp direction were analyzed. The results of three-way ANOVA in Table E.1 suggest that the tear strength is not affected by the variations of all these three variables, generating a p-value = 0.6014. Figure 6.21(a) – (c) also indicates that there is no statistically significant difference between the tear strength of the laminate samples

when contrasting all three main effects. While in the weft direction, in Figure 6.21(a), the tear strength is significantly higher for samples laminated with TY fabrics, and by performing a post hoc test this significance was confirmed. On the other hand, changing the lamination temperature had shown a significant effect on the tear strength as illustrated in Figure 6.21(b). Again, by performing a post hoc test this significance was confirmed, and it is indicated that specifically the tear strength of sample laminated at 185 °C is significantly lower than that at 200 °C, as shown in Table F.8. Additionally, it also revealed that the tear strength of sample laminated at 215 °C is not statistically different from either 185 °C or 200 °C. Lastly, there is no significant different observed between the tear strength of samples laminated at two different levels of speed.

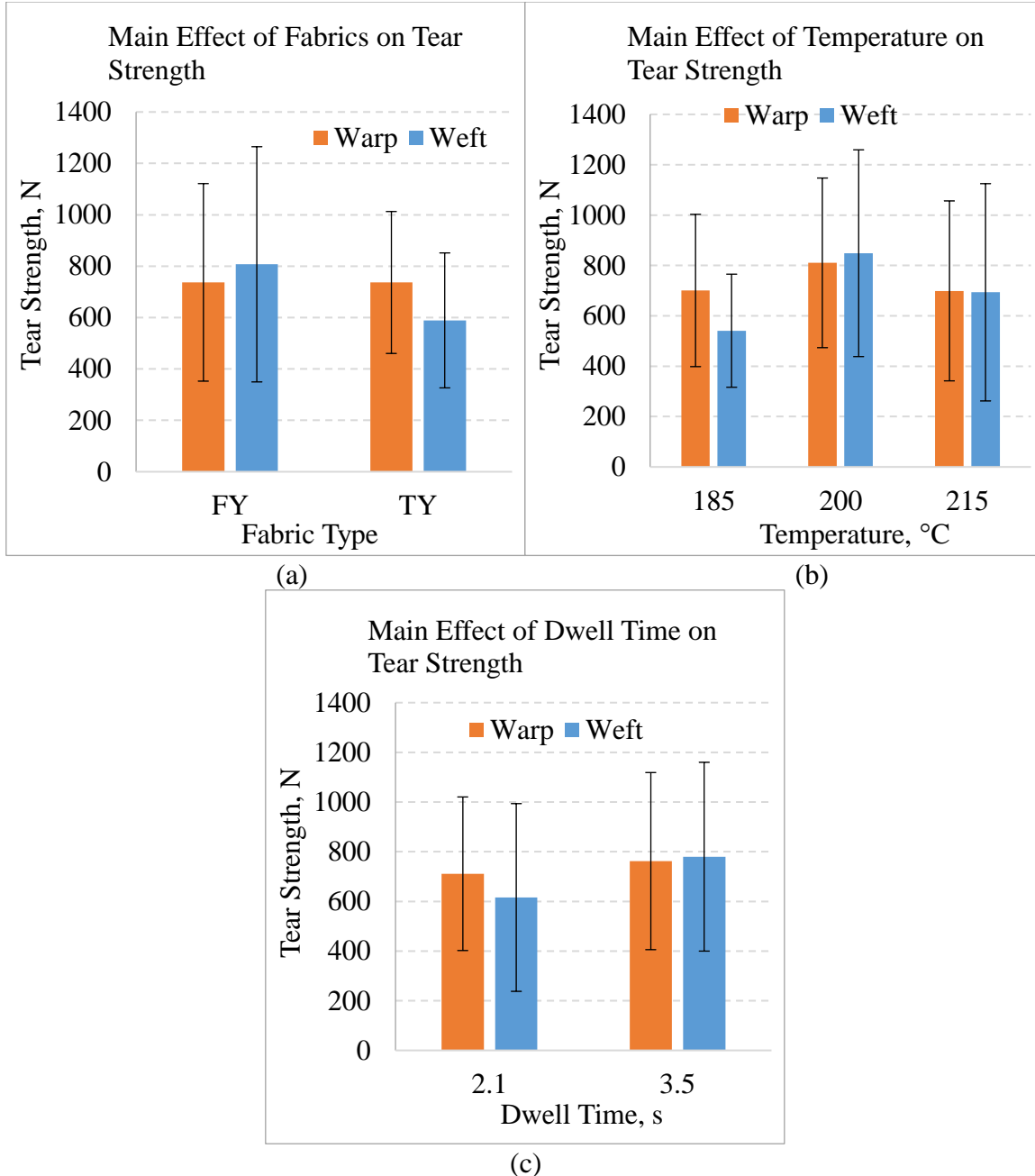


Figure 6.21. Main effects of (a) Fabric types, (b) Temperature and (c) Dwell time on tear strength/resistance of laminate.

Overall, the statistical analysis of particularly the tear strength does not give much useful information to evaluate the tear performance and further adhesion properties of the laminates made in different conditions. Since the laminate samples were already proved balanced structure in the previous tensile testing section, it is controversial to obtain different tear

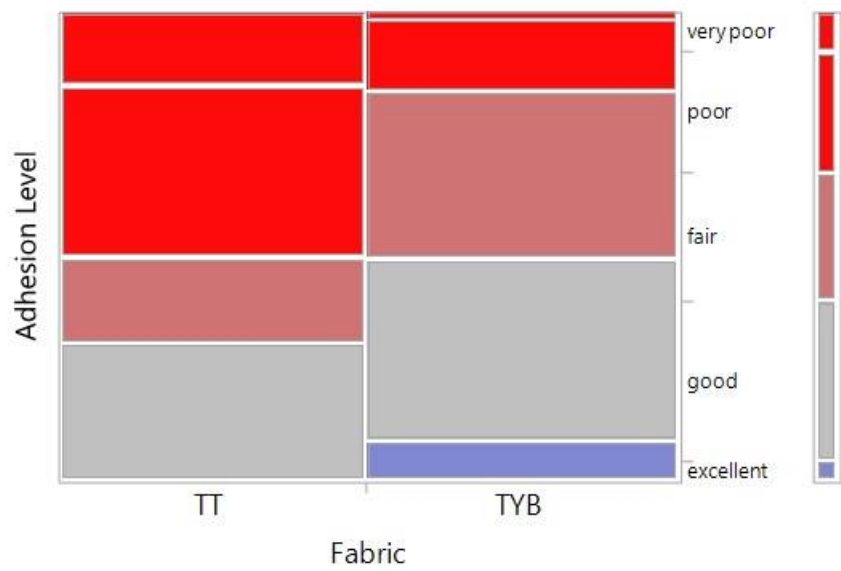
performances in the warp and weft direction according to the statistical analysis. Therefore, it is speculated that considering tear strength alone might not be effective to accurately evaluate the more complicated tear performance of laminated composite structure. Ultimately, it is impossible to obtain correct evaluation of the laminate adhesion from the tear performance. Hence, in order to more accurately assess the adhesion properties of the various laminate samples with the tear testing data, it is decided to carry out statistical analyses of the adhesion levels defined in previous sections with the three groups of laminate parameters as variables. Then, with the adhesion level system, we can correlate back the tear strength as well.

6.1.3.1 Assessing Adhesion Performance using Tear Load-Displacement Relationship

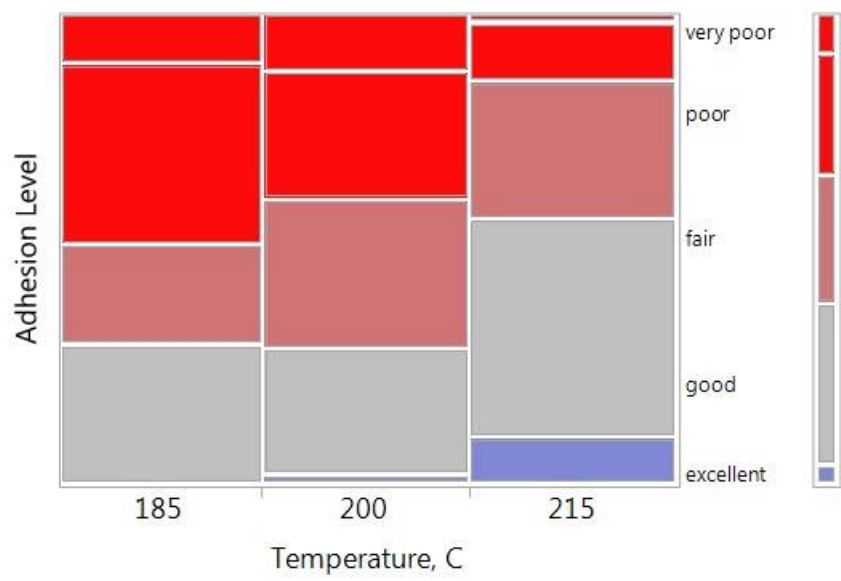
Based on the detailed discussions of the tear load-displacement curve analysis and sample failure analysis of each type of samples, all of the tear testing specimens can be categorized into five different adhesion levels, namely: very poor, poor, fair, good and excellent. With this elaborate classification system, difference between specimens from the same sample can be identified. With this method, all the random variations among the samples introduced by specimen preparation can be maximally eliminated. Now, we have the adhesion levels as a new categorical variable. In order to find the relationship between the three existing variables of the lamination parameters and the new variable of adhesion levels, contingency tables have to be used because the adhesion levels are defined as nominal variables. A chi-square test can then be run on the table to determine if there is a relationship between each of the two variables selected. Chi-square values will be generated after each test. A small value means that there is little relationship between the categorical variables. A large value means that there is a definite correlation between the two variables. As is shown in Figure 6.22(a) – (c), the contingency

tables correlate the fabric types, lamination temperature and dwell time with the adhesion levels, respectively. The results of the contingency tables were evaluated using Chi-square tests in Appendix G.

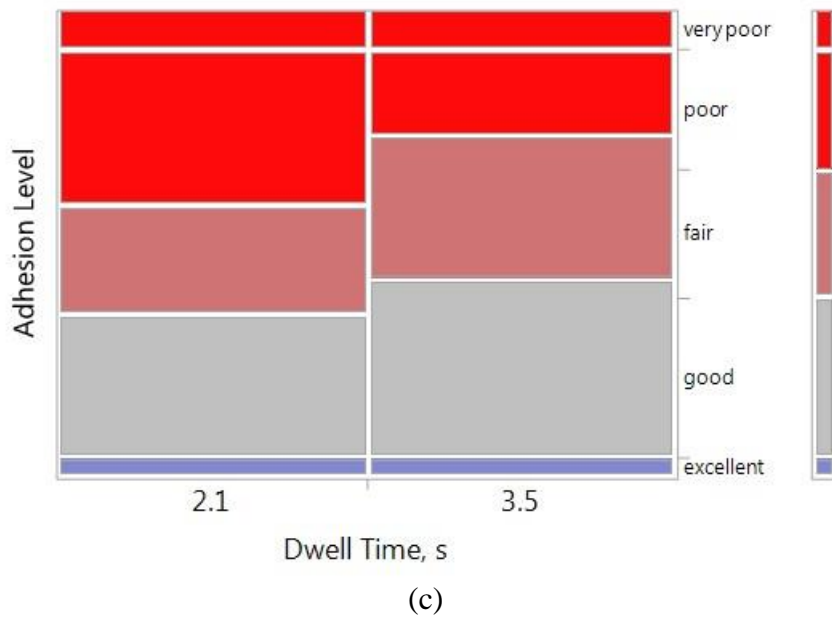
Figure 6.22. Contingency tables correlating adhesion levels with (a) Fabrics, (b) Temperature and (c) Dwell Time.



(a)



(b)



(c)

The contingency tables clearly indicate that the fabric difference and temperature variations do have significant impacts on the adhesion levels of the laminate. Whereas, changing the dwell time will not affect the adhesion level of the laminate. In Figure 6.22(a), it is observed that laminate specimens with FY fabric generally exhibited better adhesion performance over TY fabric. These two types of fabrics are very similar regarding the weave parameters. The only difference is the yarns used in FY fabric are non-twisted flat yarns, while the yarns in TY fabrics are twisted. Therefore, the higher yarn surface exposure of flat yarns promote adhesion due to increased mechanical anchoring of the adhesive polymer. On the other hand, the FY fabrics are 33% thinner than TY fabrics, making the adhesive penetration into the woven structure easier. It was reported by Xu et al. (Xu et al. 2008) that non-twisted yarns are preferably used to weave fabrics for stratospheric airship envelope materials. With twist applied onto the yarns, the cross-section of the yarns become circular, which will increase the thickness of the fabric produced. The space between yarns will thus be increased as well. This will require more adhesives to be used to laminate with other membrane materials, leading to

increased weight of laminate. Moreover, the cover of fabric will be reduced and weaken the bonding of fabric to membrane materials because the overall fabric surface in contact is reduced. There will be a higher chance for the fabrics to be weakly bonded to other film materials. The adhesion strength will be deteriorated as a result. As shown in Figure 6.22(b), the adhesion levels of laminate samples made at 215 °C are significantly better than those at 185 °C and 200 °C. There is not significant difference between the adhesion levels of the laminate samples made at 185 °C and 200 °C. Lamination temperature can influence the adhesion of the laminates in both mechanical and chemical aspects. Mechanically, the higher the temperature, the lower the viscosity of the adhesive. Then, the melted adhesive with lower viscosity can more effectively penetrate into woven fabric interstices and have better chance to wet the structure. Chemically, it is believed that higher temperature surpassing the melting point can further activate the adhesion of the polymer by increasing the mobility of the polymer chains. Thus, stronger bonding can be formed at the fiber/polymer and VDA coating/polymer interfaces. These conclusions are confirmed by the Chi-square tests, showing significantly higher values for the correlations of fabrics and temperature with adhesion levels than that of dwell time. The Chi-square values for the correlations of fabrics, temperature and dwell time with adhesion levels are 29.743, 22.394 and 4.467, respectively.

6.1.4 Main Effects of Lamination Parameters on Gas Barrier Property

Gas leakage is a common phenomenon in flexible composite structure for stratospheric airship due to the inevitable diffusions of tiny gas molecules of lifting gas. It is crucial for the envelope material to be capable of containing the lifting gas (usually Helium and Hydrogen) so that the airship will not lose lifting force over prolonged airship operations. On the other

aspect, the envelope material will be exposed to severe environment in the stratosphere, which will surely cause degradation of the mechanical properties as well as gas permeation property. Helium gas has been predominantly used for airship applications in recent decades due to its inertia nature in comparison with Hydrogen. The upper limit of the acceptable helium permeation rate provided by SCEYE S.A. falls at $80 \text{ cc/m}^2.24\text{h.0.1MPa}$ in order to maintain the high-altitude airship in the stratosphere for long duration (1 – 3 years). However, considering the helium leakage issue will certainly be exacerbated over time, our goal of the initial material helium permeation rate should be as low as possible.

A number of specimens from the 12 laminate samples were selectively tested for helium permeability in order to assess the effect of different variables on permeation property. The helium permeation results (generated by the equipment as GTR) are listed in Table 6.5. Two replicas of samples denoted i and ii were produced with the same combinations of lamination parameters yet at a different time.

Table 6.5 GTR results of selective laminate samples

ID	GTR, $\text{cc/m}^2.24\text{h.0.1MPa}$	
	AVG.	CV%
TY-185-2.1-i	0.420	7.841
TY-185-2.1-ii	0.387	5.390
FY-185-2.1-i	0.435	14.443
TY-185-3.5-i	0.497	11.593
TY-215-2.1-ii	0.351	9.150

Apparently, the helium permeation results of all the laminate sample showed very low values lower than $1 \text{ cc/m}^2.24\text{h.0.1MPa}$, being two orders of magnitude lower than the limit number provided by SCEYE S.A. There are some variations of the data observed between laminate samples made with different parameters. Temperature, dwell time and fabric types

are the major parameters that potentially affect the property of the laminate. Additionally, samples from different replicas are also compared. The main effects of these variables were plotted and compared in Figure 6.23.

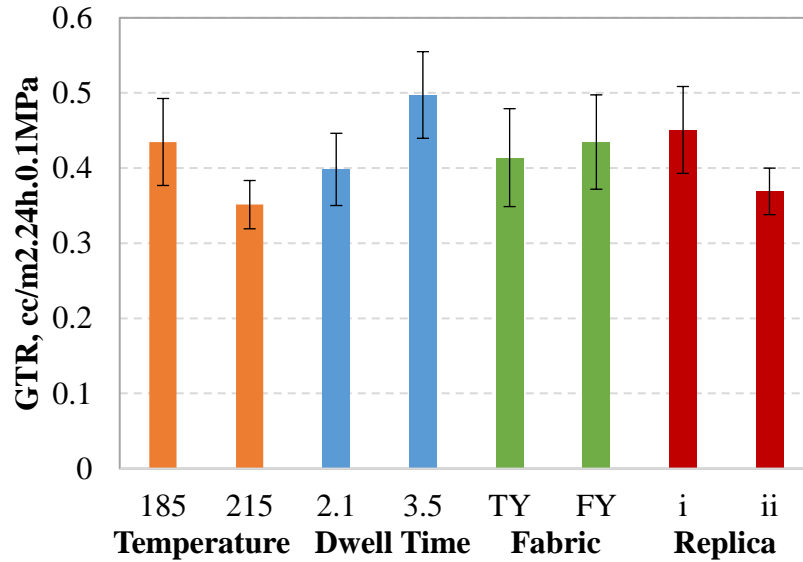


Figure 6.23. Effects of temperature, dwell time, and fabric type on the helium permeation of laminate.

It is clear that the variations of temperature, fabric types and replica did not significantly affect the GTR values of the laminate materials. For the lamination parameters of temperature and dwell time, it seems that by decreasing the heating duration and increasing the temperature, the GTR value went down, showing that the laminate specimens were improved in respect to gas barrier property. As observed in Figure 6.23, the difference of GTR value seems significant enough to confirm that dwell time of heating as well as lamination temperature do have an impact on the helium permeation property. However, with the GTR values being the same order of magnitude and extremely small, the results are practically the same with one another concerning the gas barrier efficiency. It is also reasonable to think that the variations were merely caused by the sample variations. On the other hand, when the GTR values came down to less than $0.5 \text{ cc}/\text{m}^2 \cdot 24\text{h} \cdot 0.1\text{MPa}$, the accuracy of the helium gas transmission measurements

is not guaranteed. For the evaluation of permeation or gas transmission rate, the exact number mostly will not give significant meaning. Since the gas transmission rate is not a real constant, which is characteristic for a polymer, it should only be used as a means of comparing orders of magnitude. Therefore, it is safe to conclude that the helium permeation or transmission rate of the laminate material is consistent regardless of the variables of the lamination or inherent variability of the materials.

6.1.5 Conclusion

The mechanical testing results showed that the tensile strength of the laminate is predominantly determined by the fabric types. Since the two types of fabrics used for lamination possess similar physical property and are both balanced fabrics, the tensile properties of all the different samples are similar and are balanced in the warp and weft directions.

The peel test results showed no significant difference because the adhesion measured is between VDA coating and PI film, which proved to remain at the same level in all conditions.

The tear test results revealed that the fabric types have significant impact on the adhesion of the laminate. Generally, laminate samples made with FY fabrics exhibited stronger adhesion strength than those made with TY fabrics. The variation of dwell time was not affected by the adhesion of the laminate significantly. Thus, faster speed is more beneficial for fabrication efficiency. In regard to the lamination temperature, increase the temperature to 215 °C will significantly enhance the lamination adhesion. Therefore, the best candidate laminate with the highest adhesion strength is FY-2.1-215.

It seems that the Helium permeability of the laminate is not affected by the variations of lamination parameters. It is believed that as long as the EVOH film adhesive is melted into the pinholes in the VDA coating, the helium permeation will be at a good level.

6.2 Seam Evaluation

The evaluations of adhesively bonded seams for airship envelope material consist of two major parts. The first part is a parametric study of the seaming process on the fusing machine, which helped to determine the best combination(s) of parameters to produce seam(s) with the best peel resistant property. With the results of the parametric being the foundation, multiple different butt seams with varied geometrical dimensions were produced for further evaluation regarding the tensile property and long-term creep resistant performance.

6.2.1 Parametric Study of Seaming

Adhesive seams tend to suffer from weak peel resistance, which is mainly determined by the adhesive bonding strength at the seaming interfaces. From our preliminary work, the main parameters during the seaming process affecting the adhesive bonding strength are seaming temperature, seaming speed and pressure applied at the nip roller of the fusing machine. These three seaming parameters are varied at high and low levels to make a range of seam samples with different adhesive bonding strengths to be characterized via T-peel test. To characterize peel resistance of the adhesive used for seaming, T-peel test was applied on MTS Q-Test/5 Universal Testing Machine (Figure 6.24) following ASTM D1876 (ASTM 2015a). Seam samples for T-peel test were made following the instructions mentioned in previous experimental section. Three specimens from each seam sample were tested.



Figure 6.24. Testing samples for T-peel test to determine the adhesive bonding strength.

During the T-peel test, the load applied to pull the sample apart was measured in real time along with the peel propagation. As indicated in the experimental section, the peel resistance is calculated based on the data points over at least a 12.7 cm (5 inch) length of the bond line after the initial load peak. However, it was commonly observed from many specimens that the failure mode changed from cohesive failure quickly to VDA coating being peeled off from the base laminate. As shown in Figure 6.25(a), the peeling was initiated with adhesive failure. However, the adhesive film starts to break apart as the peeling progress in Figure 6.25(b). With further propagation of the peel, the major mode of failure became the delamination between PI film and VDA coating, causing the exposure of plain PI film displayed in Figure 6.25(c). Therefore, the seam adhesive bonding strength was not able to be effectively evaluated by the load variation during the peel propagation. Instead of measuring the adhesive bonding strength, the T-peel test was evaluating the adhesion strength between the VDA coatings and PI film.

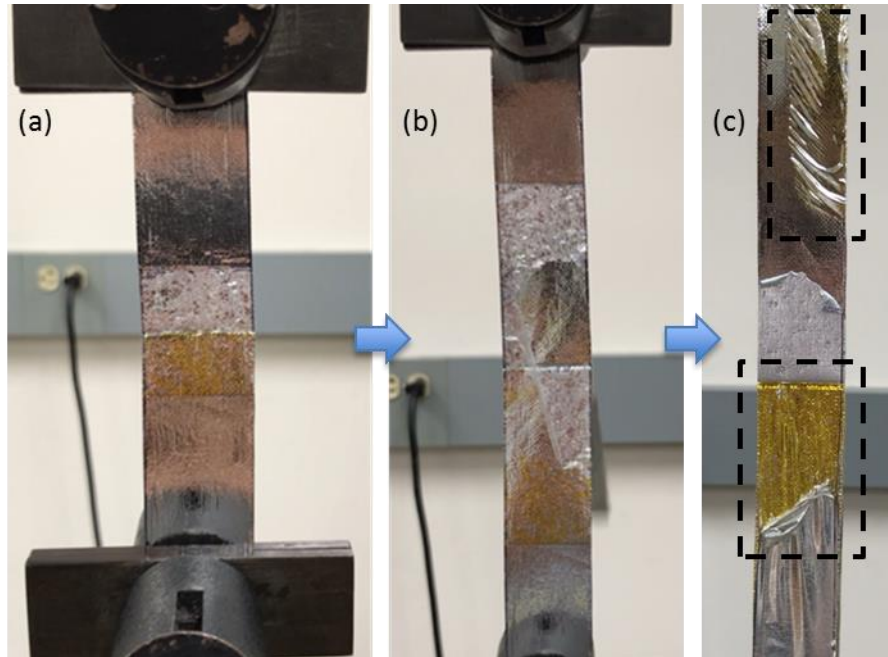


Figure 6.25. T-peel test (a) adhesive failure, (b) adhesive layer fractured and (c) VDA coating peeled off from laminate and PI film delaminated from both VDA coatings (highlighted in the dashed rectangles).

Hence, the load-to-displacement curves of the seam T-peel tests were quite different from typical T-peel test. The load variations captured throughout the peeling process were much more drastic due to changing and thus more complicated failure modes. Some representative measured load-to-displacement curves of seam specimens made with the parameters of $150\text{ }^{\circ}\text{C}$, $100\text{ }KPa$ and $3.0\text{ }m/min$ are shown in Figure 6.26. The drastic fluctuations of the load after the initial peak are probably caused by the adhesive film being torn apart and thus are attributed to the inherent tensile strength rather than bonding strength of the film adhesive. The load fluctuations at relatively lower range were more likely caused by the peel-off of VDA coating from PI film.

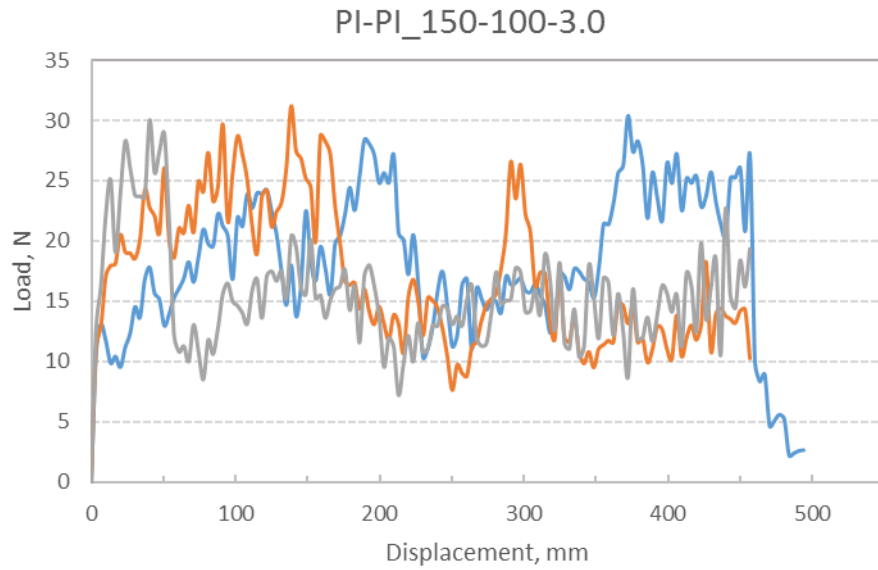


Figure 6.26. Typical load-to-displacement curve of T-peel test.

The load variations of both types of seam failure cannot reflect the true bonding strength of the film adhesive between two base laminates. Thus, it is anticipated that the peel strength measured from all the seam samples in the parametric study will not vary significantly in response to the variations of the seaming parameters. The T-peel testing results of all the samples produced for parametric study are listed in Table 6.6, with respective sample IDs and varied combinations of seaming parameters.

Table 6.6 Peel strength of seams

ID	Temperature, °C	Pressure, KPa	Speed, m/min	Peel Strength, N/cm	
				AVG.	CV%
1	150	100	3.0	7.467	13.05
2	150	100	6.0	9.815	8.978
3	150	400	3.0	6.532	20.88
4	150	400	6.0	5.935	6.256
5	180	100	3.0	5.166	21.43
6	180	100	6.0	7.579	24.54
7	180	400	3.0	7.894	14.69
8	180	400	6.0	4.424	1.651

The results of the peel strength of all the specimens were analyzed using univariate analysis of variance to study the effect of the seaming parameters (temperature, pressure and speed) on the peel resistance property. The statistical analysis results of these seamed specimens are listed in Appendix H. Further, three main effects of seaming process are plotted in Figure 6.27.

With the standard deviations and CV% being considerably high, the differences between the peel strength at different seaming temperature, pressure and speed are not statistically significant. The statistical analysis also exhibits the same results, generating p-values of 0.1286, 0.0868 and 0.8264 for the main effects of seaming temperature, pressure and speed, respectively. However, this also proved that the bonding strength of the seaming adhesive is sufficiently strong to withstand the peeling force and the peeling force only caused the failure of the interfaces with weaker bonding in the laminate structure.

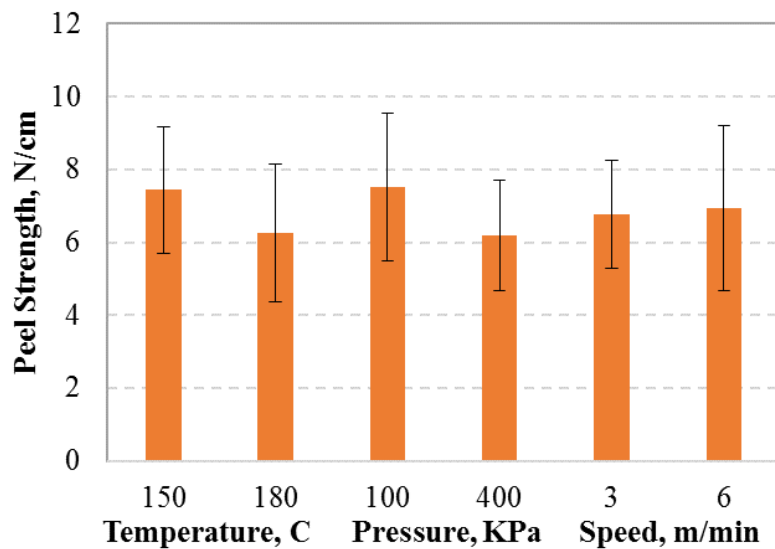


Figure 6.27. Main effects of seaming temperature, pressure and speed on peel strength of seamed samples.

To further determine the seaming parameters for next experiment, the peel strength of the eight seamed samples were compared and contrasted in Figure 6.28. It was found that the peel strength of the seamed sample made with the parameters of $150\text{ }^{\circ}\text{C}$, $100\text{ }KPa$ and $6.0\text{ }m/min$ showed the highest peel strength. Considering the peel strength measured, to some extent, reflect the bonding strength within the laminate, it is speculated that seaming parameters affected the laminate bonding strength and further create some impact on the peel strength indirectly. Because the low temperature, low pressure and fast speed during the seaming process can reduce the potential degradations from high heat. Therefore, it is determined that the seaming parameter combination of $150\text{ }^{\circ}\text{C}$, $100\text{ }KPa$ and $6.0\text{ }m/min$ is to be used for further study regarding tensile and creep property.

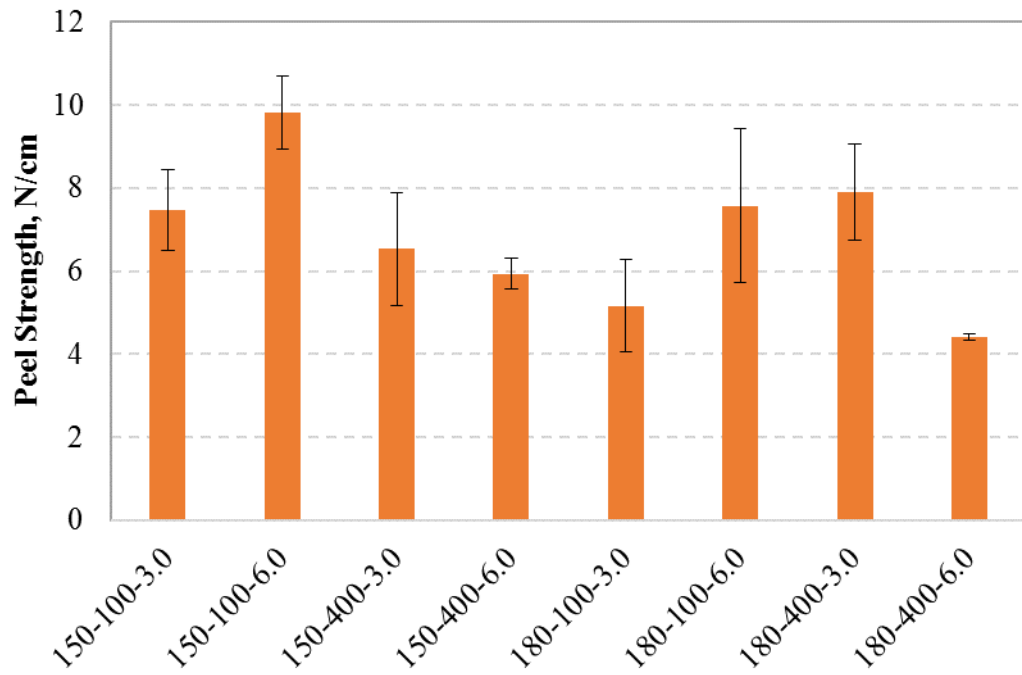


Figure 6.28. Peel strength of all eight seamed samples.

6.2.2 Effect of Seam Configuration on Tensile Property

In this part, seams with firm overlap length of 10.16 cm and varied underlap lengths of 0, 3.81 and 7.62 cm were produced following the same procedure with controlled parameters decided in the previous part of seaming parametric study. Uni-axial tensile tests were conducted at a constant rate of 30.48 cm/min up to failure of the specimens. Three specimens from each sample were tested. In the same principle with laminate tensile testing, the nominal stress is also calculated as load (N) over specimen width (cm). The results of the tensile strength of all the seamed specimens were analyzed using univariate analysis of variance to decide whether the variations of the underlap length have an impact on seam tensile strength. The results of the univariate analysis of variance test were also confirmed by a follow up Tukey-Kramer test. The results were included in Appendix I, showing that there is a statistically difference of strength between the sample with no underlap and the samples with underlap regardless of the length. The difference between the seam strength of samples with 3.81 and 7.62 cm underlap was found not significant. However, the post hoc test confirmed all the conclusions except for the difference between the seam sample with no underlap and 7.62 cm long underlap, indicating that their tensile strengths are not significantly different. At this point, it is still uncertain whether the addition of underlap will create significant difference concerning seam tensile strength. Thus, more analysis on the failure mode of these butt seam samples are necessary.

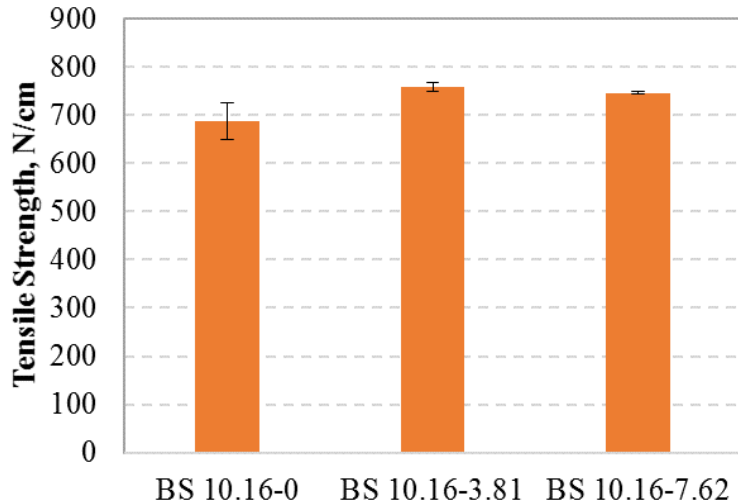


Figure 6.29. Tensile strength of butt seams made in different geometrical configurations.

As is shown in Figure 6.30(a), the down side of the butt seams are clearly shown with the underlap dimensions being different. The overlaps and underlaps were carefully seamed with both being symmetric to the contacting line of the base laminates. It is clearly observed in Figure 6.30(b) that all these butt seam specimens were fractured on the base laminate, which is away from the seamed area. This shows the tensile strength (mainly shearing) of the adhesively bonded seams are stronger than that of the base laminate, which is very desirable. Yet, by looking at the fractured surface closely, one can find the difference between the specimens with and without underlap. Theoretically, the tensile strength of the butt seam specimens should be higher or equal to the tensile strength of the base laminate when fractured cleanly. Assuming the base laminates possess similar failure strength, the lower numbers obtained from the tensile tests can only be attributed to the premature yarn failure, leading to shearing and torsion of the laminate and ultimately lower strength.

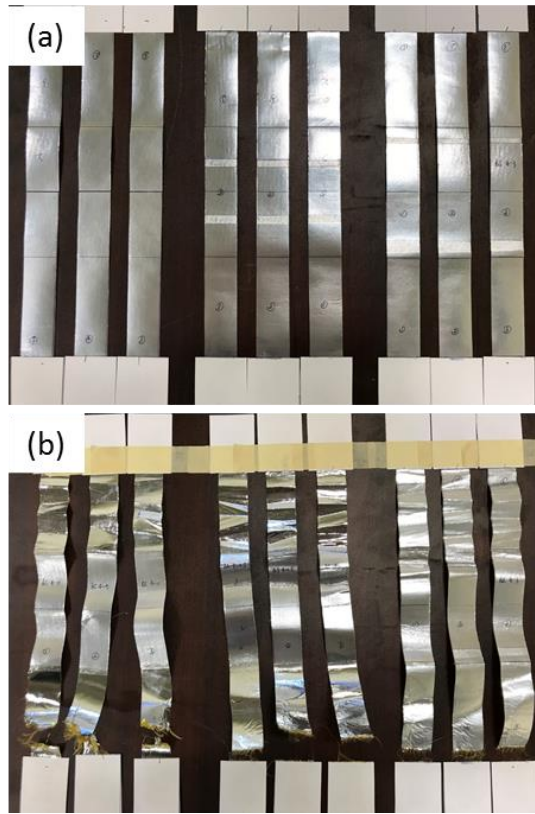


Figure 6.30. (a) Butt seam samples for tensile testing, (b) fractured butt seam samples after tensile testing.

Hence, it is probably safe to conclude that the existence of underlap enhanced the load transfer stability across the butt seam and thus ensure a clean laminate fracture. However, the increase of the underlap length seems not likely to further improve the tensile strength of the butt seam samples.

6.2.3 Seam Creep Properties

In this section, laminates made with a proprietary adhesive and EVOH film adhesive were used for seaming to study the effect of seam dimensions on creep resistance. The performance of seam samples made with different laminates were also compared and contrasted. Being a long-term process, creep test is a more complicated yet very valuable test to investigate on, so as to provide more helpful information for HAA applications. Creep test was performed on

MTS machine in a load control mode. Unlike the dead load applied for common creep test, the load control mode causes fluctuations of load within a small range. The static load was set to 40% of the tensile strength of the laminate material to simulate the operation loading during the airship flight.

Creep properties of laminate material was investigated in our preliminary work and is expected to be control samples, which serve as proper benchmarks for seam creep properties. A *2.54 cm* wide specimen was subject to a constant load of *368 N/cm* for a duration of *137.3 hrs* on the MTS machine in load control mode. The gauge length of the test specimen was *76 mm*. As is shown in Figure 6.31, the creep strain of a laminate sample increases rapidly at the beginning and slows down gradually into nearly a plateau. The overall curve of the creep strain can be fitted by a logarithmic function with an R-squared value of more than 0.97. Therefore, we can make a feasible extrapolation of laminate enduring time under creep based upon the limited data obtained.

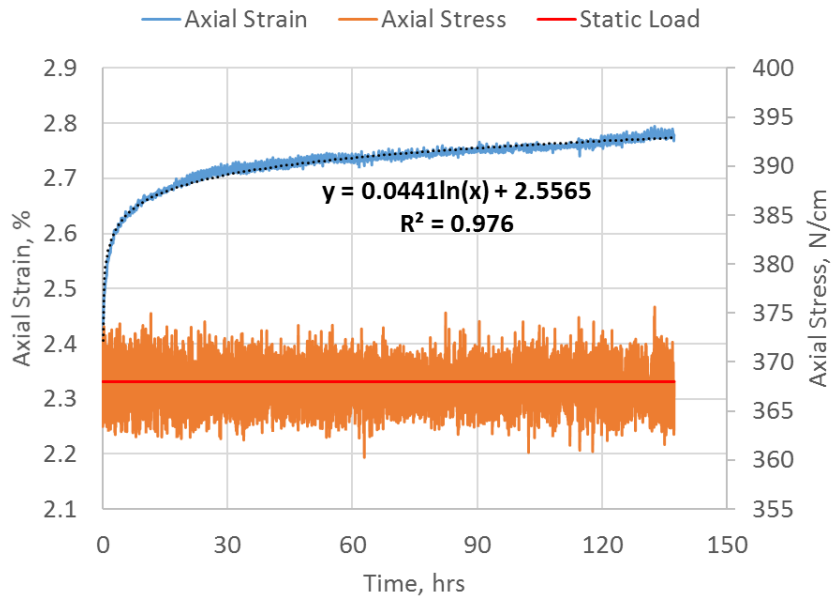


Figure 6.31. Creep strain and stress curves of a laminate sample.

The extrapolation of the creep strain results is listed in Table 6.7. It is predicted that the laminate can last for more than 23,000 *hrs* when the failure occurred at a strain of 3%, which is well below the elongation at break of the laminate tensile test.

Table 6.7 Extrapolation results of laminate creep test

Failure Strain, %	Time, hrs	days
2.7	26	1.1
2.8	250	10.4
2.9	2414	100.6
3	23311	971.3

6.2.3.1 Laminate with Proprietary Adhesive

A typical curve of creep test under a static load of 303 N/cm for a butt seam sample is shown in Figure 6.32. Following an initial rapid elongation upon application of the load, the creep rate first decreases rapidly with time. Then, a steady-state value is reached, followed by a rapid increase and ultimately fracture.

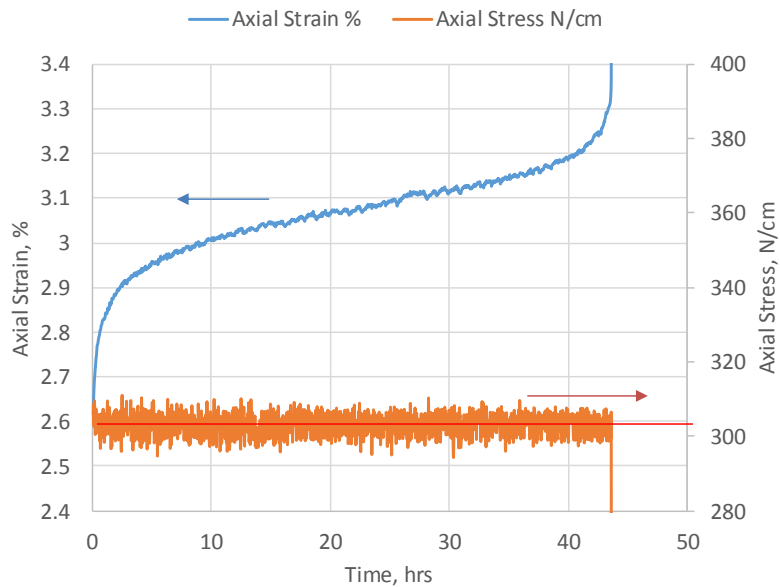


Figure 6.32. A typical curve for creep test of butt seam specimen.

Butt seam with different configurations were made for creep test at the same static load. The overlap length of the butt seam was kept the same at 10.16 cm (4 inch), while the length of the underlap varied from 0 to 10.16 cm . The duration of the creep test until the failure of the seam were recorded for comparison in Figure 6.33.

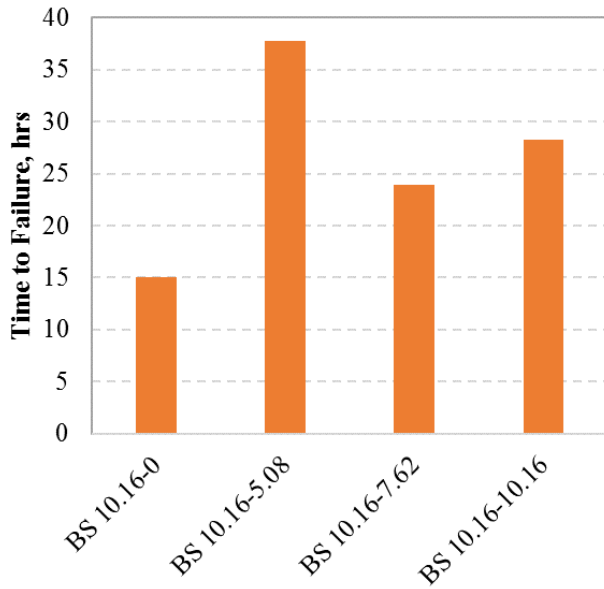


Figure 6.33. Effect of underlap length on time to failure of creep test for 10.16 cm overlap butt seams.

Since the time to failure from sample BS 10.16-0 is significantly lower from the others, it is clear that adding underlaps to make double side butt seam will definitely help to prolong the duration of the creep test. The addition of underlap helped to balance the load transfer across the seamed area and share the load with the overlap part of the seam and thus will help to improve the creep resistance property. The single side butt seam with no underlap can be likened to a combination of two lap seams. Therefore, more peel stress will be generated around the seam edges to accelerate the failure of the seam. In comparison, the load within a double side butt seam will be mainly shear stress. However, it is also apparent that the time to failure of the creep test will not strictly proportionally increase with the increase of the underlap length, with 5.08 cm and 10.16 cm underlap showing significantly better results than 7.62 cm .

underlap. There is not as significant difference between the sample BS 10.16-5.08 and BS 10.16-10.16. Sample BS 10.16-10.16 may be slightly better concerning the creep resistance because with the same length of overlap and underlap, the seam structure is completely balanced. However, the drawback is also very obvious because making a butt seam with 10.16 cm overlap and underlap will consume more materials and cause the seam and the overall airship to be much heavier. The failure mode of the seam samples with different configurations were analyzed by closely examining the specimens shown in Figure 6.34.

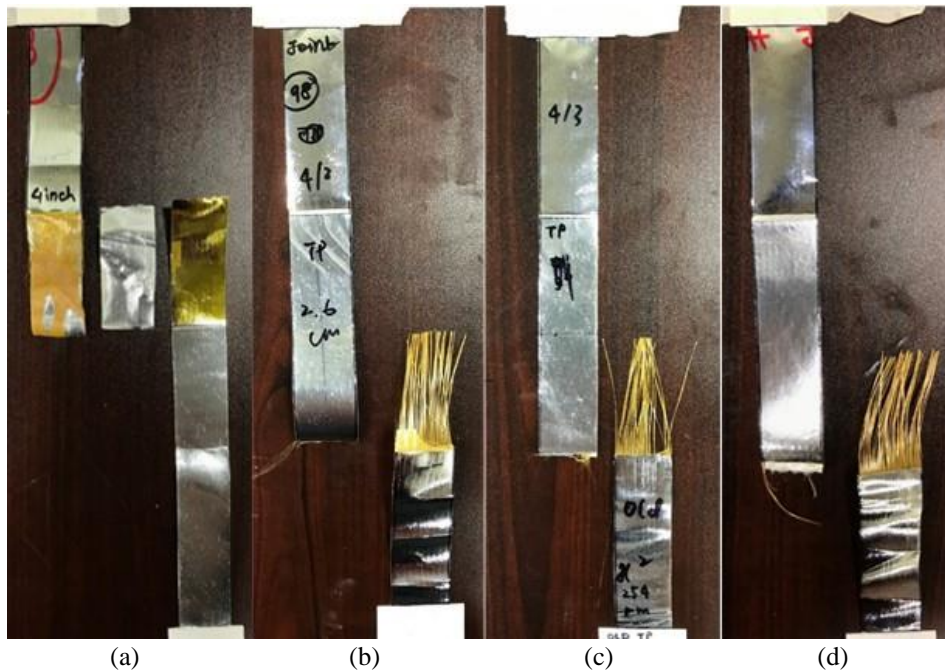


Figure 6.34. Failure analysis after creep test of (a) BS 10.16-0, (b) BS 10.16-5.08, (c) BS 10.16-7.62 and (d) BS 10.16-10.16.

As shown in Figure 6.34(a), the failure mode of BS 10.16-0 is obviously different from the rest of the samples, with the fracture of PI film from one of the base laminate and VDA coating being completely peeled off from the PI film on the overlap. Therefore, it is observed that the Zylon® fabric and PI film were exposed on base laminate and overlap. This indicated that there is indeed considerable amount of peel stress around the seam edges and the adhesion of the laminate is not strong enough to hold the peel stress at the seam edges. In Figure 6.34(b)

– (d), an identical failure mode of base laminate yarn pull-out was observed for all three types of samples with different underlap length. This do prove that with the addition of the underlap, the double side butt seam becomes more balanced structurally, and will not suffer from the peel stress commonly seen in lap seams. The clean yarn pull-out, however, showed that the adhesion within this type of laminate is not sufficiently high to endure long-term static loading. To resolve this issue, there are generally two approaches.

- 1) Increase the overlap and underlap length of the butt seam to make the yarns more difficult to be pulled out because there will be more interactions (frictional resistance against the pull-out) between warp and weft yarns in this scenario, and/or
- 2) Improve the adhesion in the laminate by adjusting the lamination parameters or use different type of adhesive that is capable of providing strong adhesion.

The first solution seems very feasible to do but will lead to very heavy seams which is never desirable for lightweight airship applications. Overall, the second approach may be proved more effective in all aspects.

To extend the overlap length of the butt seam and control the seam weight as well, sample BS 12.7-0 and BS 12.7-2.54 were produced for creep resistance evaluation. The overlap length of the butt seam was increased to *12.7 cm*, while the length of the underlap varied only from 0 to *2.54 cm*. The duration of the creep test until the failure of the seam were recorded for comparison in Figure 6.35.

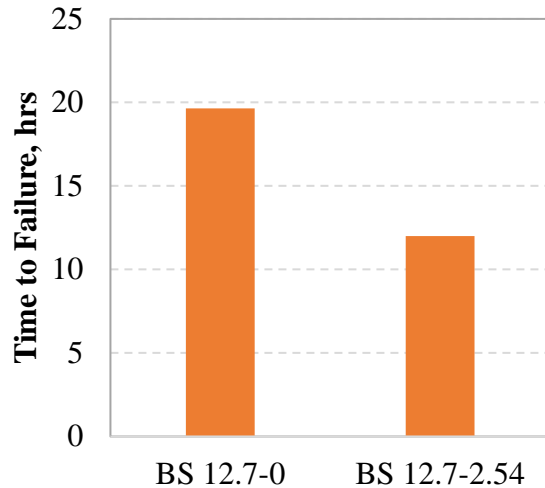


Figure 6.35. Effect of underlap length on creep resistance property for 12.7 *cm* overlap butt seams.

As is shown in Figure 6.35, the increase of underlap length from nothing to 2.54 *cm* doesn't help to improve the creep resistance. However, compared with the creep resistance performance of BS 10.16-0, the increase of the overlap length lead to only small improvement of the creep time to failure. By observing the failure modes of these seam samples in Figure 6.36, it was revealed that the increase of overlap length is effective to enhance the yarn interaction and stop the yarns from pulling out completely. Although, the yarns become more difficult to be pulled out cleanly, the other issue of polymer film delamination becomes more significant type failure mode for both cases. Overall, the failure modes are more complicated than those of 10.16 *cm* overlap butt seams. The yarn pull-out issue may be solved by increase the overlap length, yet the intrinsically weak adhesion of the laminate still exist and remain as a key reason of seam failure in creep test mode.

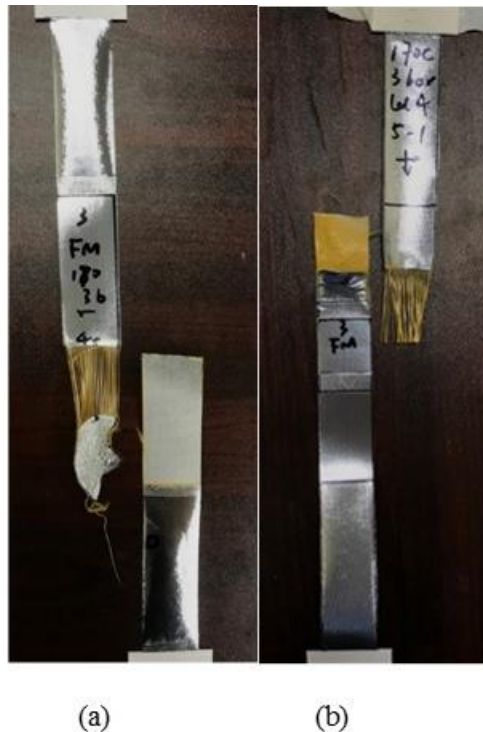


Figure 6.36. Failure analysis after creep test of (a) BS 12.7-0 and (b) BS 12.7-2.54.

6.2.3.2 Laminate with EVOH Film Adhesive

Laminate samples made with EVOH film adhesives were used for seaming and evaluated for the creep resistance property. Butt seam specimens with 10.16 *cm* overlap and 0, 3.81 and 7.62 *cm* underlap were produced for creep test. The specimens tested at the same static load exhibited significantly longer duration and did not fail until unpredictable machine issues or intentional manual interruption after 120, 360 and 231.63 *hrs*, respectively. Restricted by the timeframe of the whole research work and due to the time-consuming nature of creep test (especially performed on MTS machine); only one specimen from each butt seam sample was tested.

Although the tested specimen from BS 10.16-0 endured for more than 120 *hrs*, the software ended up collecting only the data points from the first 67 *hrs* owing to an

unpredictable machine issue. The creep performance of sample BS 10.16-0 under the static load of 303 N/cm over a period of its first 67 hrs is shown in Figure 6.37.

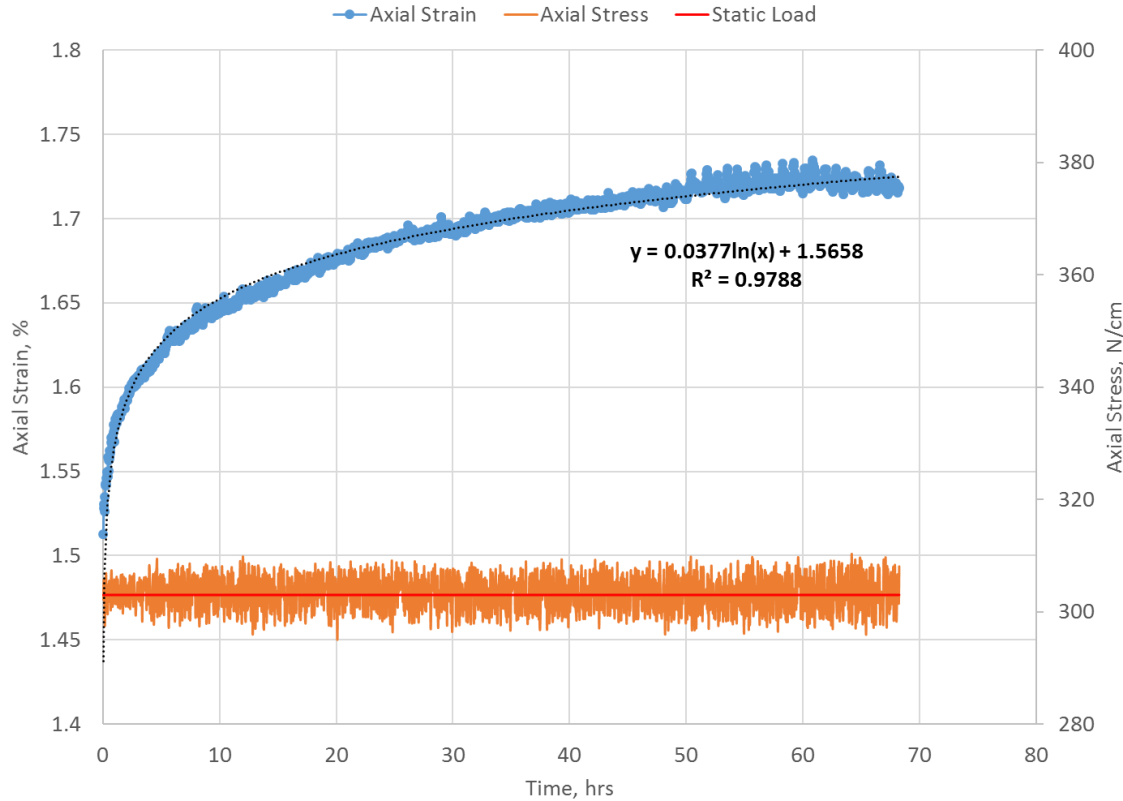


Figure 6.37. Creep strain and stress curves of sample BS 10.16-0 under a static load of 303 N/cm .

A rapid increase of the creep strain is observed at the beginning of the test. Then, the increase rate starts to slow down gradually over time. With the limited amount of data points available, it is a general practice that the test results being extrapolated up to significantly longer period of time. It is found by using curve fitting that creep strain follows logarithmic relation with time. The fitted curve of the creep strain is shown in Figure 6.37 as the black dotted line with an R-squared value of 0.9788. The extrapolation of the creep strain results are listed in Table 6.8. It is predicted that BS 10.16-0 specimens can last for more than 100,000 hrs when the failure occurred at a strain of 2%, which is still within the elongation at break of the seam tensile test.

Table 6.8 Extrapolation results of the creep test of BS 10.16-0

Failure Strain, %	Time, hrs	days
1.8	499	21
1.9	7078	295
2	100433	4185

A specimen from sample BS 10.16-3.81 was also tested for creep resistance at the same static load. The creep strain and stress curves are shown in Figure 6.38. It is observed that the creep strain behaved abnormally within the period from 15 *hrs* to 100 *hrs*, showing a drastic increase initially and then fell quickly back to the original level of strain. It is suspected that some irregular torsions of the specimen might happened during the test since the bottom gripper is free and subjected to motion when irregular force being applied in a sudden. Regardless of what caused the abnormal phenomenon of strain variations, it is certainly not creep induced behavior and thus cannot be counted into the extrapolation of the overall creep performance. Therefore, it is observed in Figure 6.38 that a logarithmic relation showed only a very low R-squared value when the curve fitting is directly applied including all the data points.

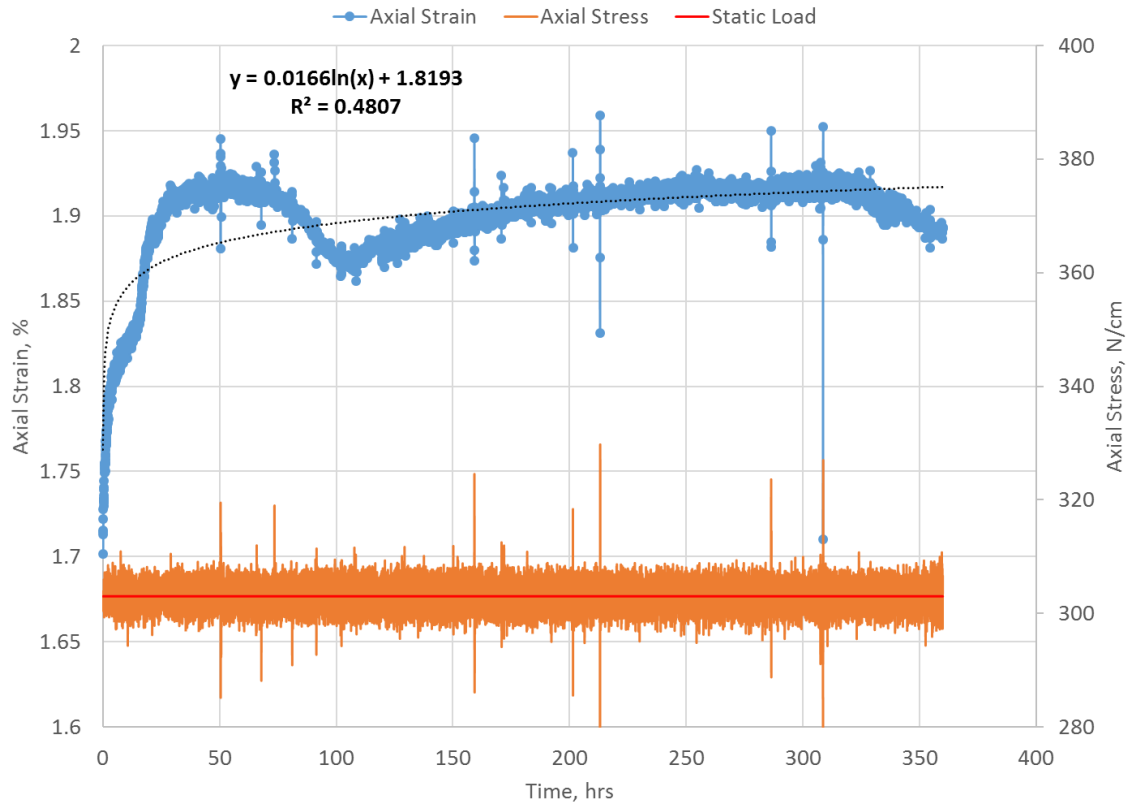


Figure 6.38. Creep strain and stress curves of sample BS 10.16-3.81 under a static load of 303 N/cm.

In order to carry out the extrapolation of the creep strain more accurately, the strain data which is not caused by creep has to be eliminated before deriving the curve fitting. As shown in Figure 6.39, a new logarithmic relation was developed with a significantly better fit (R^2 -squared value of 0.9599) to the creep strain. With the new fitting model, more accurate extrapolation can be generated thereafter.

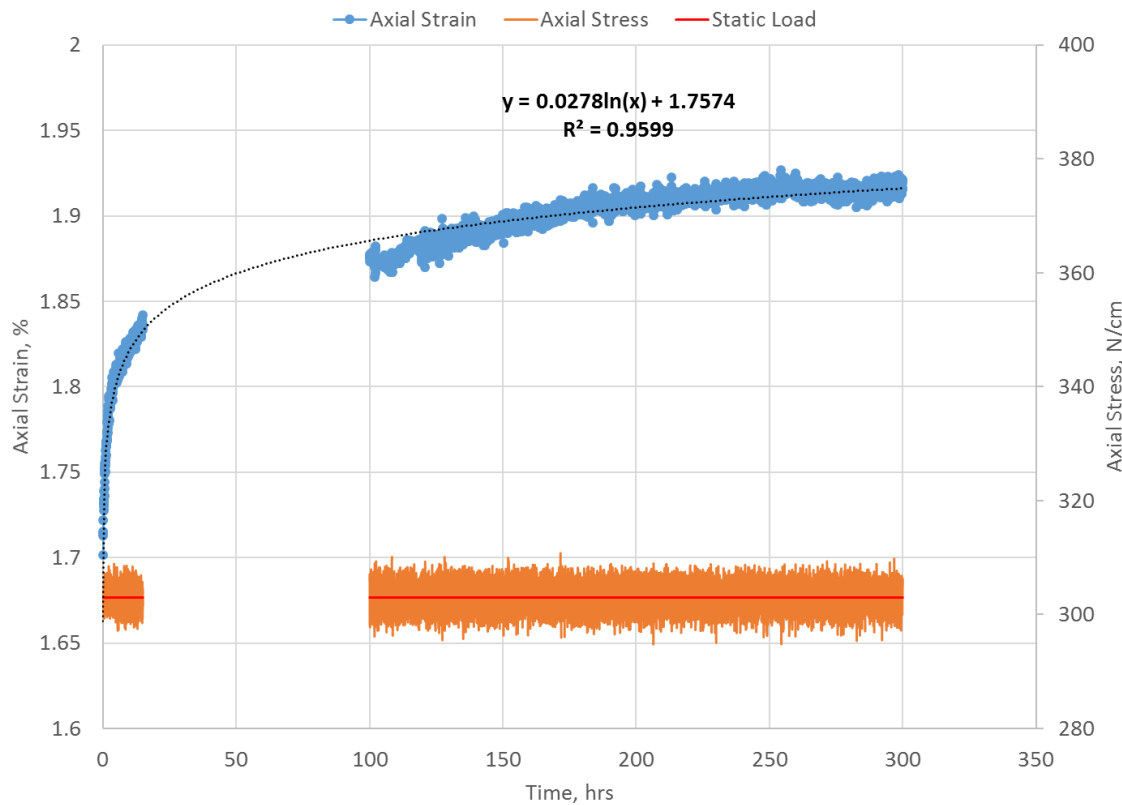


Figure 6.39. Creep strain extrapolation of sample BS 10.16-3.81 with correct curve fitting after data deduction.

The extrapolation of the creep strain results is listed in Table 6.9. It is predicted that BS 10.16-3.81 specimens can last for more than 220,000 *hrs* when the failure occurred at a strain of 2.1%. It is also noted that the initial strain of sample BS 10.16-3.81 is higher than that of sample BS 10.16-0.

Table 6.9 Extrapolation results of the creep test for BS 10.16-3.81

Failure Strain, %	Time, hrs	days
1.9	169	7
2	6165	257
2.1	224974	9374

Although planned in the design of experiment, creep test of sample BS 10.16-7.62 was not able to be conducted due to the time restriction in accessing the equipment. From the creep test results of seam samples with different geometrical configurations for proprietary laminate, the

addition of underlaps was proved to have positive impact on the improvement of seam creep property. However, further increase of underlap length seems not an effective practice to extend the duration of seam samples against creep load. Therefore, it is expected that sample BS 10.16-7.62 will have better creep property than sample BS 10.16-0, and have probably similar creep durations with sample BS 10.16-3.81. Seam samples made with EVOH film adhesive never failed within the testing period, exhibiting much longer duration under creep load. In contrast, seam samples with similar configurations made using proprietary adhesive laminates failed in short period mainly due to yarn pull-out. Thus, it is apparent that the creep property of seams made with two different types of laminates are significantly different, indicating that the adhesive used for lamination played an important role concerning creep property of seams. As shown in Figure 6.32 approaching failure, the continuous increase of axial strain at a faster rate is possibly because of the yarn slippage within the laminate structure with poor bonding from proprietary adhesive. With the constant load applied to the base laminate, the yarns in the loading direction constantly experience pulling and thus will slip gradually over time. The bonding between the yarns will be damaged gradually to certain extent that the frictional resistance generated from those yarn interactions cannot withstand the load anymore. Then the yarns in the loading direction will be completely pulled out. On the contrary, the laminate made with EVOH adhesive is able to provide much stronger bonding between yarns and polymer films. Thus, the yarns within the laminate structure in the loading direction were locked securely and thus slipping is minimized /eliminated. Since the laminate itself (shown in Figure 6.31) have great creep properties owing to excellent creep resistant properties of Zylon® fibers, it was always observed that the increase rate of the creep strain slowed down over time, and the creep strain curve would be well fitted into a logarithmic

function trend line. It is apparent that only the creep strain behavior of the seam samples made with EVOH laminates closely match with what exhibited by the laminate samples. Thus, these seam samples provide the same level or potentially better creep properties than the laminates themselves, which is indeed what desirable seams need to be for long duration high altitude applications.

6.2.4 Conclusion

It is concluded that (1) with the addition of underlap, the double side butt seams become more balanced structure and thus are able to withstand longer time under static load; (2) the increase of overlap length can improve the creep resistance moderately by increasing the yarn to yarn interactions in the laminate; (3) the laminate made with EVOH adhesive can provide strong adhesion in the laminate, successfully preventing the yarns from being pulled out and ultimately make the seam more durable against the static load.

6.3 Helium Permeation Study

6.3.1 Helium Permeation Model of Flexible Composite Laminate

6.3.1.1 Typical Permeability Models

To estimate the permeability of a laminate material structure, the barrier performance of each constituent layer need to be combined. Generally, there are three models that are most commonly used. Figure 6.40 shows a schematic of the permeability is varied with the three basic permeability models (Bishop 2015).

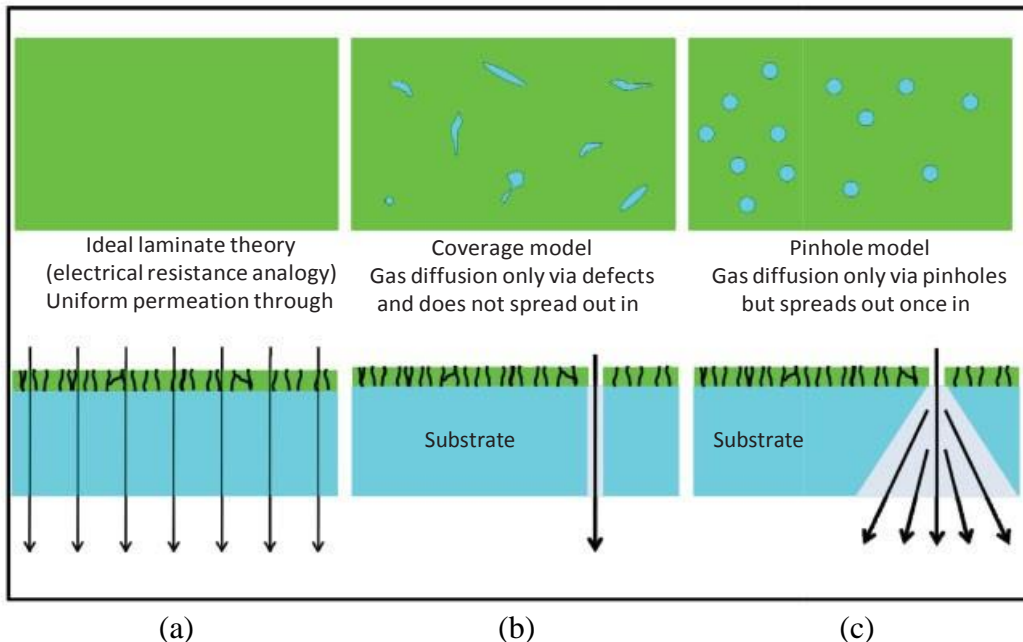


Figure 6.40. A schematic of the three typical model types for gas permeability: (a) Ideal laminate theory, (b) Coverage model and (c) Pinhole model (Bishop 2015).

As shown in Figure 6.40(a), for the ideal laminate theory (ILT), it is assumed that there is uniform permeation through the whole film and substrate. The coverage model, shown in Figure 6.40(b), includes defects and assumes that the diffusion through the coating is only via the defects and does not spread out through the substrate. According to the author in this book chapter (Bishop 2015), the more accurate model is the pinhole model in Figure 6.40(c), where it is also assumed that the diffusion is through the defects but in this case the diffusion spreads out as it goes through the substrate.

The ideal laminate theory equation for calculating the total permeability is often referred to as the electrical analogy model and the equation is in the same form as adding electrical resistors together to find the total resistance of a circuit. This value of total permeability of the multilayer will not be the same as that measured because it assumes there are no defects and the layers are homogeneous, which is not the case in practice. However, this is probably still the most popular used model to estimate the performance of a multilayer barrier structure.

There are multiple papers (Ashford et al. 1973; Yao et al. 2011; Yao et al. 2012; X. Yao et al. 2010) reporting the gas permeation calculation using ILT, but they found quite significant differences between measured and calculated values. Since applying ILT alone is not sufficient, there is a need to study alternative models for predicting the permeability of materials such as the coverage model or the pinhole model.

6.3.1.2 Helium Permeation Evaluation with ILT

Our laminate material is a structure comprising many different components including PI and PET polymer substrate, VDA coatings, EVOH adhesives and Zylon® woven fabric as the reinforcement layer. As shown in Figure 6.41, the highlighted areas by dashed rectangles are the two major gas barrier components, named VDA coated PET film and double side VDA coated PI film. In doing these calculations, it is common to not include thin layers such as the adhesives layers. Since the EVOH films will be melted and lose the film form during lamination process. Thus, it is reasonable to consider it to have no impact on the total performance. The fabric layer is also ignored simply due to its porous structure, which is surely unable to obstruct helium gas molecules.

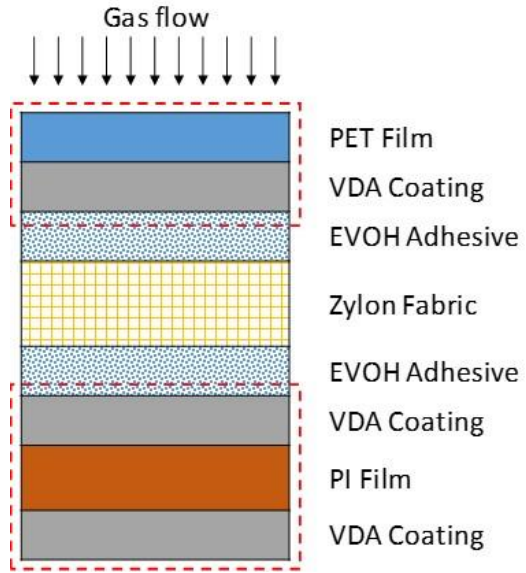


Figure 6.41. A schematic of multilayer structure of the laminate material for ILT.

6.3.1.3 Helium Permeation Evaluation with modified ILT

6.3.1.3.1 Effect of VDA coating

A thin layer of VDA coating can change the mode of gas permeation significantly because the area covered with coating will become theoretically impermeable to the gas molecules. Nevertheless, VDA coating have defects and pinholes over the areas covered, so the gas molecules which are closer to the defects will get through first. Others will have to diffuse in the lateral direction to find the outlet where the pinholes located. A schematic of the gas flow in single side VDA coated PET film is shown in Figure 6.42.

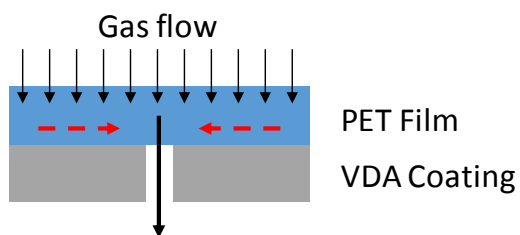


Figure 6.42. A schematic of the gas flow in single side VDA coated PET film.

It is apparent that the coverage model is more suitable to be used for laminate with single VDA or any other thin coating deposited on the polymer substrate. By calculating the ratio of the uncoated area to the whole area, one can easily obtain a more accurate estimate of the permeability. With the addition of a single layer of VDA coating with less defects, the gas permeability will be improved significantly.

Double side coating can be even more beneficial in improving barrier performance. Because if both sides of a polymer film are coated, then a random defect in the coating on one side is unlikely to be directly facing defect in the coating on the other side. As shown in Figure 6.43, the gas molecules will have to diffuse even more along the horizontal direction to find the closest exits.

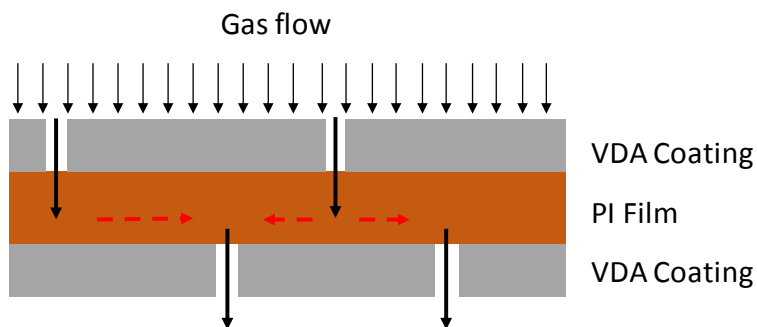


Figure 6.43. A schematic of double VDA coating affecting the gas flow.

Due to the offset of the pinholes, the unidirectional permeations described in the coverage model are unlikely to happen frequently. Thus, the dominant model for this type of structure will be the pinhole model, which taking the spread of gas flow in the polymer layer into account.

6.3.1.3.2 Effect of EVOH Adhesive

The impact of adhesives was ignored in the previous cases. This may not be entirely true as the polymer adhesive may flow into the pinholes in the vacuum deposited coating and substitute adhesive for the air in the pinholes which would change the diffusion through the

pinholes by several orders of magnitude. In our case, the EVOH film adhesive will melt at high temperature and flow into the fabric and pinholes from VDA coatings. With moderate amount of pressure applied during lamination, the EVOH adhesive can quickly flow and fill the pinholes on VDA coatings. With EVOH adhesive being a semi-crystalline polymer, its presence in the pinholes will further increase the difficulty for the gas molecules passing through the tunnel. The crystalline region can potentially force tortuous paths of the gas molecules, increasing their chances of colliding into each other to further slow down the permeation process.

Therefore, the configuration of the laminate can be adjusted differently for the permeability calculation, considering the significant impact of EVOH adhesive. A schematic of the laminate structure with adjustment for calculation is shown in Figure 6.44, with the red dash rectangles highlighting the two parts for modified ILT calculation including the EVOH adhesives.

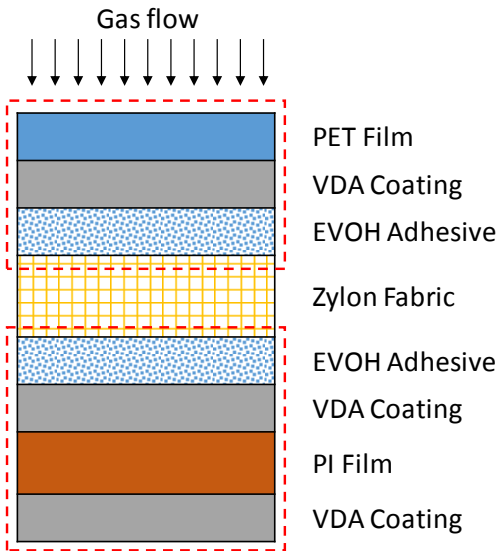


Figure 6.44. A schematic of multilayer structure with detailed compositions of the laminate material for modified ILT.

6.3.2 Experimental Verification of the Models

In laminated multi-layer membrane structures, the total permeability (Q_L) with n layers can be simply expressed using the ideal laminate theory (ILT) as follows:

$$\frac{1}{Q_L} = \frac{1}{x} \sum_{i=1}^{i=n} \frac{x_i}{P_i^*} \quad (22)$$

where x_i is the thickness of each layer and P_i^* is the permeability of each layer (Permeation = Permeability/thickness).

For a laminate with two critical parts for gas barrier, the equation can be written as:

$$\frac{x}{Q_L} = \frac{x_1}{P_1^*} + \frac{x_2}{P_2^*}$$

Since Permeation = Permeability/thickness,

$$\frac{1}{P_L} = \frac{1}{P_1} + \frac{1}{P_2}$$

where P_L , P_1 and P_2 is the total laminate permeation, permeation of part 1 and permeation of part 2, respectively. Here in this study, the permeation is characterized by the gas transmission rate (GTR), which can be directly measured by the gas permeation tester. The units of GTR is $cc/m^2.24h.0.1MPa$ as generated by the equipment. To verify the modelling of the laminate structure, the GTR results of different samples laminated with various combinations of films and fabrics were measured, shown in Table 6.10. The laminations were conducted on the same laminator mentioned in the experimental section, with the temperature, speed and pressure being controlled at $215^\circ C$, $1.6 m/min$ and $80 psi$, respectively. To simulate all the conditions experienced in the lamination process, those as supplied PI, VDA/PI/VDA, PET and PET/VDA films were also passed through the lamination process prior to permeation

measurements. To protect the samples from being damaged in the lamination process, two thin layers of Teflon sheets were applied on the top and bottom of the materials.

Table 6.10 Helium Permeation Results for Modelling

#	Specimen ID	Thickness, μm	Helium GTR, $cc/m^2.24h.0.1MPa$	$1/GTR, \times 10^{-5}$
1	PI	12.5	12616	7.93
2	VDA/PI/VDA	12.8	20.42	4897.16
3	VDA/PI/VDA-EVOH	37.13	3.45	28985.51
4	VDA/PI/VDA-EVOH-Zylon®	121.07	5.31	18832.39
5	PET	6	10945	9.14
6	PET/VDA	6.8	41.48	2410.80
7	PET/VDA-EVOH	31.43	2.38	42016.81
8	PET/VDA-EVOH-Zylon®	126.4	14.76	6775.07
9	PET/VDA-EVOH-Zylon®-EVOH-VDA-PI-VDA	163.73	1.45	68965.52

For the purpose of discussion, we define the $1/GTR$ as resistance of permeation (R). Thus, the ILT equation can be further rewritten as $R_L = R_1 + R_2$ for the calculations of two-component laminate.

As shown in Table 6.10, the resistance of permeation for both PI and PET films with VDA coating increase by three orders or magnitude when comparing to plain polymer films. It is also clearly observed that the double side VDA coating on PI film is more effective than the single side VDA coating on PET film, improving the resistance of permeation more significantly. Further, with the addition of EVOH adhesive, the resistance of permeation increased by one order of magnitude for both PI and PET samples, proving that the EVOH adhesives can fill the pinholes to provide significant hindrance to the permeation of gas molecules. Therefore, according to ILT model only, the effect of adhesive and fabric will be ignored, and the estimated resistance of permeation for the laminate will be the total of R #2

(VDA/PI/VDA) and R #6 (PET/VDA), which is only 7307.96. This is one order of magnitude lower than that of the measured resistance of permeation for the whole laminate. Whereas, based on the coverage and pinhole models, the effect of adhesives were decided to be included into the calculation. Thus, the estimated laminate resistance of permeation will be the total of R #3 (VDA/PI/VDA-EVOH) and R #7 (PET/VDA-EVOH), which is 71002.32. This number falls into the same order of magnitude with that of the measured whole laminate R_L (68965.52).

6.3.3 Conclusion

By comparing the results from all the samples laminated with certain designs, the effects of VDA coating and EVOH adhesive on improving helium permeation barrier property are verified. The modified ILT is also proved to be significantly more effective to estimate the helium permeability of the whole laminate structure. On the other hand, results from this study can be very useful to guide the material selection for laminate design to meet certain permeation requirement. Since the permeability of the laminate will surely be lower than the estimated value based on ILT model, we can use the estimated value from ILT model as a caliber to select or drop certain materials with no need for forming and testing final laminates, a matter that reduces/eliminates the trial and errors.

7 Overall Summary

A multi-layer laminate envelope material for stratospheric airship with high strength-to-weight ratio and high gas barrier property were successfully produced based on a unique structural design and material combination. A parametric study of the lamination process to understand the effects of lamination parameters i.e. temperature and speed, as well as the fabric structure on the properties of the laminate was conducted. It was found that:

1. The tensile strength of the laminate is predominantly determined by the reinforcement layer type (woven fabric). Since the two types of fabrics used for lamination possess similar physical property and are both balanced fabrics, the tensile properties of all different samples are similar and are balanced in the warp and weft directions.
2. The peel test results showed no significant difference because the adhesion measured is between VDA coating and PI film, which proved to remain at the same level in all conditions.
3. The tear test results revealed that the fabric types have significant impact on the adhesion of the laminate. Generally, laminate samples made with FY fabrics exhibited stronger adhesion strength than those made with TY fabrics. The variation of dwell time will not affect the adhesion of the laminate significantly. Thus, faster speed is more beneficial for fabrication efficiency. For the lamination temperature, increase the temperature to 215 °C significantly enhanced the lamination adhesion. Therefore, the best candidate laminate was FY-2.1-215.
4. It seems that the Helium permeability of the laminate is not affected by the variations of lamination parameters. It is believed that as long as the EVOH film adhesive is well

melted, the gas would flow into the pinholes in the VDA coating and thus the helium permeation will be at a required low level.

It is concluded that: (1) with the addition of underlap, the double side butt seams become more balanced structure and thus are able to withstand longer time under static load; (2) the increase of overlap length can improve the creep resistance moderately by increasing the yarn to yarn interactions in the laminate; (3) the laminate made with EVOH adhesive can provide strong adhesion in the laminate, successfully preventing the yarns from being pulled out and ultimately make the seam more durable against the static load.

By comparing the results from all the samples laminated with certain designs, the effects of VDA coating and EVOH adhesive on improving helium permeation barrier property are verified. The modified ILT is also proved to be significantly more effective to estimate the helium permeability of the whole laminate structure. On the other hand, results from this study can be very useful to guide the material selection for laminate design to meet certain permeation requirement. Since the permeability of the laminate will surely be lower than the estimated value based on ILT model, we can use the estimated value from ILT model as a caliber to select or drop certain materials without the need to form and test laminates.

REFERENCES

- Anderson, M. & Whitcomb, P., 2007. Chapter 3: Two-Level Factorial Design. In DOE Simplified: Practical Tools for Effective Experimentation. pp. 41–43.
- Ashford, R.L., Bata, B.T. & Walsh, E.D., 1973. Measurement of Helium Gas Transmission Through Aerostat Material. , pp.101–107.
- ASTM, 2015a. ASTM D1876 - 08 Standard Test Method for Peel Resistance of Adhesives (T Peel Test), D1876 - 08. ASTM International, pp.1–3. Available at: <http://www.astm.org/Standards/D1876.htm>.
- ASTM, 2015b. Standard Test Method for Breaking Strength and Elongation of Textile Fabrics (Strip Method), D5035 - 11. ASTM International, pp.1–8.
- ASTM, 2015c. Standard Test Method for Breaking Strength and Elongation of Textile Fabrics (Strip Method), D5035 - 11. ASTM International, pp.1–8. Available at: <http://www.astm.org/Standards/D5035 - 11.htm>.
- ASTM, 2015d. Standard Test Method for Determining Gas Permeability Characteristics of Plastic Film and Sheeting, D1434 - 82. ASTM International, pp.1–13. Available at: <http://www.astm.org/Standards/D1434 - 82.htm>.
- Auras, R., Harte, B. & Selke, S., 2004. Effect of water on the oxygen barrier properties of poly(ethylene terephthalate) and polylactide films. *Journal of Applied Polymer Science*, 92(3), pp.1790–1803.
- Bishop, C.A., 2015. Roll-to-Roll Vacuum Deposition of Barrier Coatings,
- Boersma, A., Cangialosi, D. & Picken, S.J., 2003. Mobility and solubility of antioxidants and oxygen in glassy polymers. III. Influence of deformation and orientation on oxygen permeability. *Polymer*, 44(8), pp.2463–2471.
- Bonnici, M., Tacchini, A. & Vucinic, D., 2014. Long permanence high altitude airships: The opportunity of hydrogen. *European Transport Research Review*, 6(3), pp.253–266.
- Chen, J. et al., 2015. Mechanical responses and damage morphology of laminated fabrics with a central slit under uni-axial tension: A comparison between analytical and experimental results. *Construction and Building Materials*, 101(200), pp.488–502. Available at: <http://dx.doi.org/10.1016/j.conbuildmat.2015.10.134>.
- Chen, J. & Chen, W., 2016. Central Crack Tearing Testing of Laminated Fabric Uretek3216LV under Uni-axial and Bi-axial Static Tensile Loads. *Journal of Materials in Civil Engineering*, 28(7), p.4016028. Available at: [http://dx.doi.org/10.1061/\(ASCE\)MT.1943-5533.0001537](http://dx.doi.org/10.1061/(ASCE)MT.1943-5533.0001537).

Chen, J., Chen, W. & Wang, M., 2017. Mechanical Behaviors and Elastic Parameters of Laminated Fabric URETEK3216LV Subjected to Uni-axial and Bi-axial Loading. *Applied Composite Materials*. Available at: <http://dx.doi.org/10.1007/s10443-016-9576-2>.

Chen, J., Chen, W. & Zhang, D., 2014. Experimental study on uni-axial and bi-axial tensile properties of coated fabric for airship envelopes. *Journal of Reinforced Plastics and Composites*, 33(7), pp.630–647. Available at: <http://jrp.sagepub.com/cgi/doi/10.1177/0731684413515540>.

Cole, P.J. & Macosko, C.W., 2000. Polymer-Polymer Adhesion in Melt-Processed Layered Structures. *Journal of Plastic Film and Sheeting*, 16(3), pp.213–222. Available at: <http://techpub.metapress.com/link.asp?target=contribution&id=6N2BV63L32AW4JYD>.
Colozza, A. et al., 2005. High-Altitude, Long-Endurance Airships for Coastal Surveillance. , (February).

Crank, J., 1975. *The mathematics of diffusion*. Oxford University Press, p.414.
D’Oliveira, F.A., De Melo, F.C.L. & Devezas, T.C., 2016. High-altitude platforms - Present situation and technology trends. *Journal of Aerospace Technology and Management*, 8(3), pp.249–262.

Dartman, T. & Shishoo, R., 1993. Studies of Adhesion Mechanisms Between PVC Coatings and Different Textile Substrates. *Journal of Coated Fabrics*, 22, pp.317–335.

DSM, 2008. Technical brochure: Dyneema in marine and industrial applications. , 31(46), p.4. Available at: http://www.pelicanrope.com/pdfs/DyneemaSK75_Tech_Sheet.pdf.

Duncan, B., Urquhart, J. & Roberts, S., 2005. Review of Measurement and Modelling of Permeation and Diffusion in Polymers. *Engineering*, (January), p.73. Available at: http://resource.npl.co.uk/materials/polyproc/iaq/october2005/depc_mpr_012.pdf.

FAA, 1995. Airship Design Criteria. US. Department of Transportation, pp.119–120.

Farboodmanesh, S. et al., 2005. Effect of Coating Thickness and Penetration on Shear Behavior of Coated Fabrics. *Journal of Elastomers and Plastics*, 37(3), pp.197–227. Available at: <http://jep.sagepub.com/cgi/doi/10.1177/0095244305047987>.

Fesen, R. & Brown, Y., 2015. A method for establishing a long duration , stratospheric platform for astronomical research. , pp.475–493.

Fung, W., 2002. Coated and Laminated Textiles,
Gledhill, R. a., Kinloch, a. J. & Shaw, S.J., 1980. A Model for Predicting Joint Durability. *The Journal of Adhesion*, 11(1), pp.3–15.

Gorrasí, G. et al., 2003. Vapor barrier properties of polycaprolactone montmorillonite nanocomposites: Effect of clay dispersion. *Polymer*, 44(8), pp.2271–2279.

- Gouzman, I. et al., 2010. Thin Film Oxide Barrier Layers: Protection of Kapton from Space Environment by Liquid Phase Deposition of Titanium Oxide. , 2(7), pp.1835–1843.
- Gu, Z., 2007. Research of Stratospheric Airships. Skin Material. Spacecraft Recovery& Remote Sensing, 28(1), pp.62–66.
- Guchi, K.E. et al., 2000. 2000 Overview of Stratospheric Platform Airship R & D Program in Japan. , pp.12–15.
- Isida, M., 1973. Analysis of Stress Intensity Factors for the Tension of a Centrally Cracked Strip with Stiffened Edges. Engineering Fracture Mechanics, 5, pp.647–665.
- Islam, S. & Bradley, P., 2012. Materials. In Airship Technology. pp. 113–148.
- Jacob, K., Seemann, R. & Herminghaus, S., 2008. Polymer Thin Films,
- Jamison, L., Sommer, G. & Porche, I., 2005. High-Altitude Airships for the Future Force Army,
- Kang, W. et al., 2006. Mechanical property characterization of film-fabric laminate for stratospheric airship envelope. Composite Structures, 75, pp.151–155.
- Komotsu, K., Sano, M. & Kakuta, Y., 2003. Development of high-specific-strength envelope materials.pdf. In AIAA's 3rd Annual Aviation Technology, Integration, and Operations (ATIO) Tech 17-19 November 2003, Denver, Colorado. Denver, pp. 17–19.
- Lagaron, J.M., Catalá, R. & Gavara, R., 2004. Structural characteristics defining high barrier properties in polymeric materials. Materials Science and Technology, 20(1), pp.1–7.
- Laven, C.K. & Kelly, D.J., 2005. Flexible Material for Lighter-Than-Air Vehichles. , pp.1–7.
- Li, B., Xing, L. & Zhou, Z., 2010. Study on Mechanical Properties of High Performance Envelope Materials. , pp.1–5.
- Liao, L. & Pasternak, I., 2009. A review of airship structural research and development. Progress in Aerospace Sciences, 45(4–5), pp.83–96. Available at: <http://dx.doi.org/10.1016/j.paerosci.2009.03.001>.
- Lin, G., Tan, H. & Materials, A., 2011. The Influence of Ozone on the Property of Envelop Materials of Near Space Vehicle. , pp.1413–1416.
- Liu, L.B., Cao, S. & Zhu, M., 2015. Mechanical characteristics of stratospheric airship envelope of vectran fibre-reinforced-laminated composite. Materials Research Innovations, 19(S5), pp.S5-606-S5-612. Available at: <http://www.scopus.com/inward/record.url?eid=2-s2.0-84941344971&partnerID=tZOTx3y1>.

Maekawa, S. et al., 2008. Tear Propagation of a High-Performance Airship Envelope Material. *Journal of Aircraft*, 45(5), pp.1546–1553. Available at: <http://www.scopus.com/inward/record.url?eid=2-s2.0-54549096949&partnerID=tZOTx3y1>.

Maekawa, S., Nakadate, M. & Takegaki, A., 2007. Structures of the Low-Altitude Stationary Flight Test Vehicle. *Journal of Aircraft*, 44(2), pp.662–666.

Mater, E.C. & Hartly, K., 1992. Laminate Material Particularly Adapted for Hull of Aerostats. , p.6.

McDaniels, K. et al., 2009. High Strength-to-Weight Ratio Non-Woven Technical Fabrics for Aerospace Applications. , pp.1–9. Available at: http://www.cubictechnology.com/Technical_Fabrics_for_Aerospace_Applications.pdf.

Meng, J. et al., 2016. Mechanical properties of woven fabric composite for stratospheric airship envelope based on stochastic simulation. *Journal of Reinforced Plastics and Composites*, 35(19), pp.1434–1443. Available at: <http://jrp.sagepub.com/cgi/doi/10.1177/0731684416652947>.

Michaeli, W., GOBEL, S. & Dahlmann, R., 2004. The Influence of Strain on the Properties of Plazma Polymerized Permeation Barriers. *Journal of Polymer Engineering*, 24(1–3), pp.107–122.

Miller, T. & Mandel, M., 2000. Airship Envelopes: Requirements, Materials and Test Methods. 3rd International Airship Convention and Exhibition, pp.1–5.

Mokwena, K.K. & Tang, J., 2012. Ethylene vinyl alcohol: a review of barrier properties for packaging shelf stable foods. *Critical reviews in food science and nutrition*, 52(7), pp.640–50. Available at: <http://www.ncbi.nlm.nih.gov/pubmed/22530715>.

Nakadate, M., Maekawa, S. & Kurose, T., 2011. Investigation of Long Term Weathering Characteristics on High Strength and Light Weight Envelope Material Zylon® In 11th AIAA Aviation Technology, Integration, and Operations (AITO) Conference. pp. 1–6.

Petrie, E.M., 2003. Improving the Low Temperature and Temperature Cycling Properties of Adhesives and Sealants. SpecialChem.

Petrie, E.M., 2003. The Importance of Glass Transition Temperature in formulating adhesives and sealants. SpecialChem.

Said, M.A. et al., 2006. Investigation of ultra violet (UV) resistance for high strength fibers. *Advances in Space Research*, 37(11), pp.2052–2058.

Schwartz, P., 2008. Structure and Mechanics of Textile Fibre Assemblies, Available at: <http://www.scopus.com/inward/record.url?eid=2-s2.0-84904144301&partnerID=tZOTx3y1>.

- Shim, E., 2010. Smart Textile Coatings and Laminates. In W. C. Smith, ed. Smart Textile Coatings and Laminates. Woodhead Publishing Limited and CRC Press LLC, pp. 10–41. Available at: <http://www.sciencedirect.com/science/article/pii/B9781845693794500055>.
- Silverstein, M.S. & Breuer, O., 1993. Adhesive properties and failure of etched UHMW-PE fibres. *Journal of Materials Science*, 28(17), pp.4718–4724.
- Smith, S. et al., 2011. HiSentinel80: Flight of a High Altitude Airship. In 11th AIAA Aviation Technology, Integration, and Operations (ATIO) Conference. pp. 1–14. Available at: <http://arc.aiaa.org/doi/10.2514/6.2011-6973>.
- Triton, 2001. More Than Just a Polymer. NASA SPINOFF, p.110.
- Vallabh, R. et al., 2016. Improving high-altitude UV-Vis resistance of PBO braided tendons of NASA's super pressure balloons. *Journal of the Textile Institute*, 107(1), pp.136–143.
- Wang, F. et al., 2016. Experimental study on uni-axial tensile and welding performance of a new coated fabric for airship envelopes. *Journal of Industrial Textiles*, 0(0), pp.1–24.
- Wang, F.X. et al., 2016. Tearing analysis of a new airship envelope material under uni-axial tensile load. *IOP Conference Series: Materials Science and Engineering*, 137(1).
- Wicks, Z.W. et al., 2007. *Organic Coatings: Science and Technology* 3rd ed., Hoboken: Wiley & Sons.
- Xu, C., 2009. Fabrication and Investigation of Envelope Materials for Stratospheric Aircraft with PBO Fabric as Load-carriers. *Hi-Tech Fiber & Application*, 34(4), pp.0–5.
- Xu, C., Zhengming, G. & Weizhi, W., 2008. Weave and Performance Investigation of PBO Fabric for Stratosphere Airship Envelope. *Spacecraft Recovery& Remote Sensing*.
- Yao, X. et al., 2010. Experimental Study of Helium Leakage Parameters in Flexible Composite. *Journal of Applied Polymer Science*, 116, pp.3562–3568.
- Yao, X.F. et al., 2010. Experimental Study on Damage-induced Helium Leakage in Flexible Composites. *Journal of Reinforced Plastics and Composites*, 29(19), pp.2936–2945. Available at: <http://jrp.sagepub.com/cgi/doi/10.1177/0731684409357800>.
- Yao, X.F. et al., 2012. Mechanics Analysis on Helium Leakage of Flexible Composites. *Mechanics of Advanced Materials and Structures*, 19(8), pp.603–612. Available at: <http://www.tandfonline.com/doi/abs/10.1080/15376494.2011.563412>.
- Yao, X.F. et al., 2011. Theoretical and Experimental Investigation on Helium Leakage Characterization of Flexible Film-Fabric Laminated Composites. , 19(7), pp.619–624.

Zhai, H. & Euler, A., 2005. Material challenges for lighter-than-air systems in high altitude applications. In AIAA 5th Aviation, Technology, Integration, and Operations Conference (ATIO). pp. 1–12. Available at: <http://arc.aiaa.org/doi/pdf/10.2514/6.2005-7488>.

Zhang, Y. et al., 2012. Simulational Study on Bi-axial Tensile Test of the Envelope Material of Stratospheric Airship., 593, pp.1006–1011.

APPENDICES

Appendix A Preliminary Work

Laminate Development and Modification

A.1 Concept of Design

The structure of typical airship materials is well established in the literature and turned out to be effective approach to achieve strong and lightweight hull materials. After a thorough literature search and review, it is decided that the laminate design concept (Figure A.1) consists of multiple functional component layers. Various material and structural options are available for the functional layers.

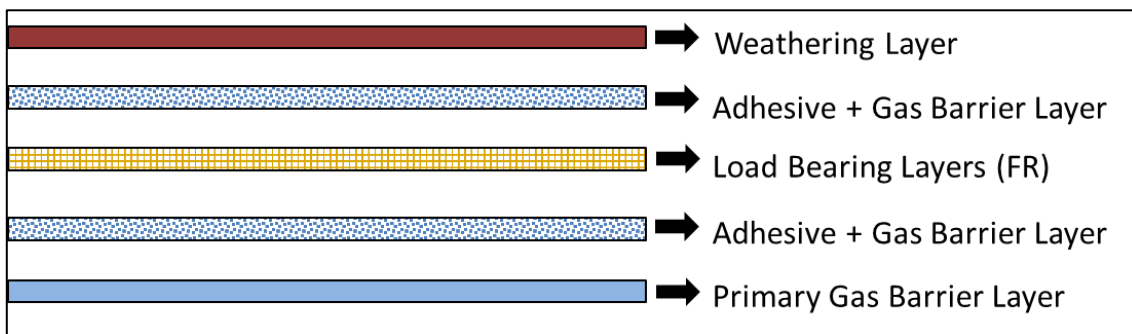


Figure A.1. General design concept of the laminate material.

Depending on the temperature rating of the laminate, different material and material combinations can be used for the weathering layer, adhesive layer and primary gas barrier layer. For example, in case of high temperature rated laminates, a metallized polyimide (PI) film can be used, whereas for a lower temperature rated laminate a metallized polyvinyl fluoride (PVF) film can be used. The primary load bearing layer is in the form of a lightweight fiber reinforcement such as a woven fabric. The fiber reinforcement (FR) has an unbalanced construction to provide the required strength in the longitudinal and hoop direction of the stratospheric airship. Zylon® fibers, which have the highest specific strength, was used for the fiber reinforcement layer. A metallized/non-metallized PET film is used as the primary gas

barrier layer. In general, the metallized side of the film faces the adhesive layer to prevent damage to the metallized coating. EVOH film has been used as the primary gas barrier layer in LTA laminates materials developed by prior research (Komotsu et al. 2003), however, to date, it has not been used as an adhesive layer. The novel idea of using EVOH as an adhesive layer also serves to enhance the overall gas barrier properties (including the reduction of in-plane gas permeability) of laminate material. This novel idea of using EVOH, both as the adhesive layer and the primary/secondary gas barrier layer, has been used in examples of laminate materials described above.

A.2 Laminate Fabrication

Initially, the method of operating hot-press machine to make laminate is to place securely stacked materials in between two Aluminum plates and press the assembly at controlled temperature in order to melt the bonding agent. Various components of the laminate were secured over a 30.48 cm x 30.48 cm aluminum plate by using heat resistant tapes. After the layering steps, 19.05 cm x 19.05 cm aluminum plate was places on the top (as shown in Figure A.2) and hot pressed at 175 – 178 °C under 1965 KPa pressure for 15 min. The use of smaller size top plate allowed lamination pressure to be applied only to central area where no tapes were present. Consequently, a uniform lamination pressure could be applied.

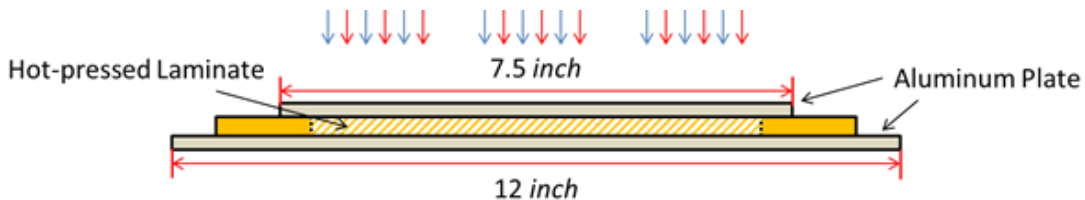


Figure A.2. Schematic of laminate between aluminum plates during hot press lamination

Modification of Laminate Fabrication

All the unbalanced laminate prototypes (P4, P9 and P10) produced through hot-press encountered delamination issues at different levels. Thus, we started to look into the influence of processing parameters variations on lamination bonding. The same setup was carried on making new laminates with the newly woven balanced Zylon® fabrics, only altering the parameters of temperature, pressure and dwell time for a parametric study. On the other hand, the trial lamination with a new set of parameters on a lab scale lamination machine succeeded in producing laminates with stronger bonding. In this trial, the 99-denier unbalanced woven fabrics (used in P10) were still used as the FR layer for lamination. The details of the layer notations were demonstrated in Figure A.3.

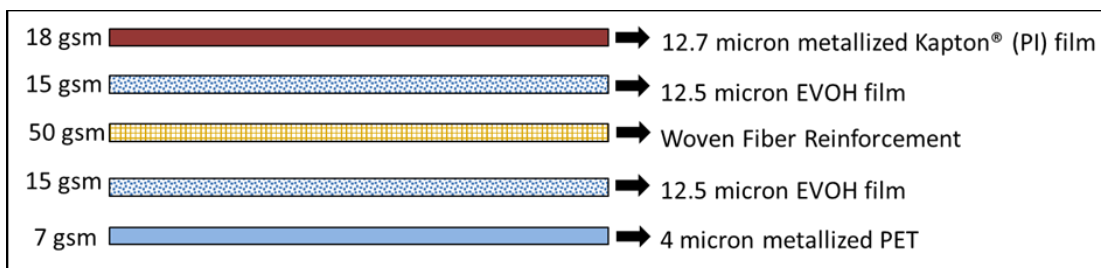


Figure A.3. Layer notations of the laminate fabricated on lab-scale lamination machine.

Strong adhesion between woven fabric and PET/PI films were observed at the well laminated areas by hand peel test. The polymer films were extremely difficult to be peeled off and would be fractured immediately once peeling was initiated.

In this trial, heated nip roller was used to heat the materials at 196 °C (385 °F) and apply the pressure at 414 KPa for ~2 s. The tensile testing also generated tensile strengths of 661 N/cm and 481 N/cm at hoop and longitudinal direction, respectively. According to our observation, the yarns in the fabric were not straightened out before lamination. This resulted in the weft yarns (in the hoop direction) to be wavy and not aligned to the test direction.

Consequently, the tensile strength in the hoop direction is lower than expected due to the unequal load sharing among the yarns in the test direction. Proper tension control during the lamination process will help to align the yarns and therefore lead to higher strength. This set of parameters developed in the lab-scale trial provided us with some precious information to further investigate on. The lamination parametric study was enlightened in the direction to increase the temperature further above the EVOH film melting point as well as shorten the dwell time. While, the pressure was determined to be controlled at 414 KPa in alignment with the lab-scale trial.

In the hot-press set-up, two Aluminum plates were used to transfer the heat from the hot-press machine. However, due to the thickness of the plates, the heat transmission from hot platen through the Aluminum plates then ultimately to the materials would be delayed. Thus, the target temperature set on the hot-press machine would not be instantly reached at the position of stacked materials. After realizing the issue of heating delay hot-press process, we turned to use the laminator with heated roller to simulate the continuous lamination process.

A.3 Laminate Prototype Development

The schematic design of laminate prototype P4 (shown in Figure A.4) uses an unbalanced cross-ply (two-ply) non-crimp fabric as the FR. The fabric has *250 denier* PBO yarns in longitudinal and cross directions. The basis weight of the fabric is *48 gsm* with yarn density of *30 ypi* in warp direction and *15 ypi* in weft direction. In order to achieve lower laminate weight, the design uses two layers of EVOH film and a bottom layer of a lightweight metallized Mylar[®] film which serves as the primary gas barrier layer. The estimated and measured weight of this

laminate prototype is 103 gsm. Images of outside and inside of the laminate prototype P4 is shown in Figure A.5.

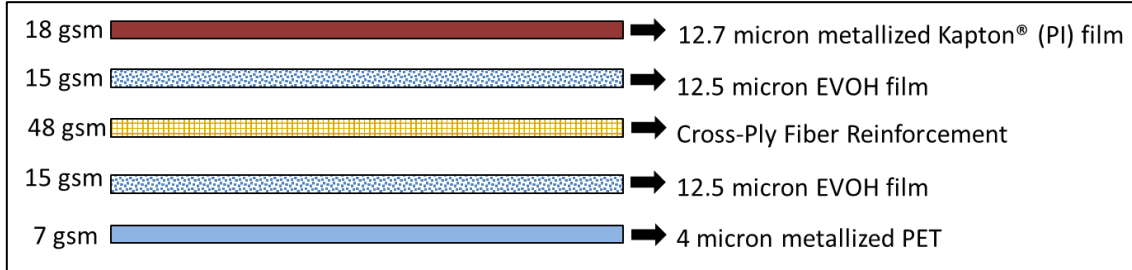


Figure A.4. Schematic design of laminate prototype P4

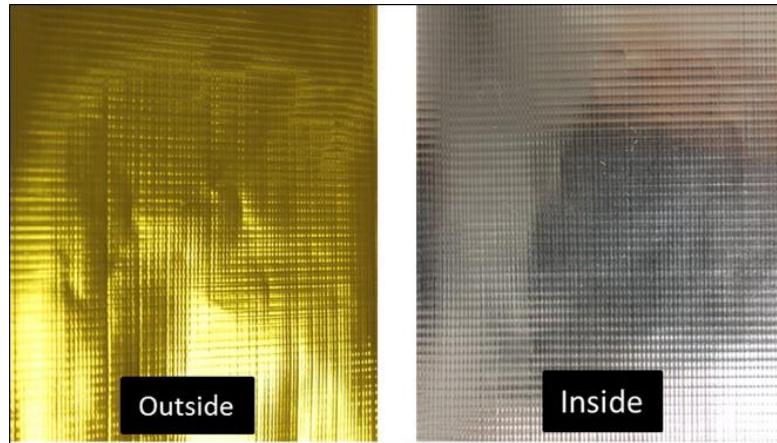


Figure A.5. Outside and inside of laminate prototype P4

The schematic design of laminate prototype P9 (shown in Figure A.6) uses an unbalanced woven fabric as the FR. The woven fabric has low twist 99 *denier* Zylon® yarns and non-twisted 250 *denier* Zylon® yarns in warp and weft directions, respectively. The basis weight of the fabric is 50 gsm with yarn density of 40 *ypi* in warp direction and 30 *ypi* in weft direction. Like prototype P4, the bottom layer is a lightweight metallized Mylar® film which serves as the primary gas barrier layer. Though the lamination temperature of 175 °C produced satisfactory adhesion between the layers, increasing the lamination temperature to 178 °C improved the adhesion between layers. The estimated and measured weights of this laminate

prototype were found to be 105 *gsm*. Images of outside and inside of the laminate prototype P9 is shown in Figure A.7.

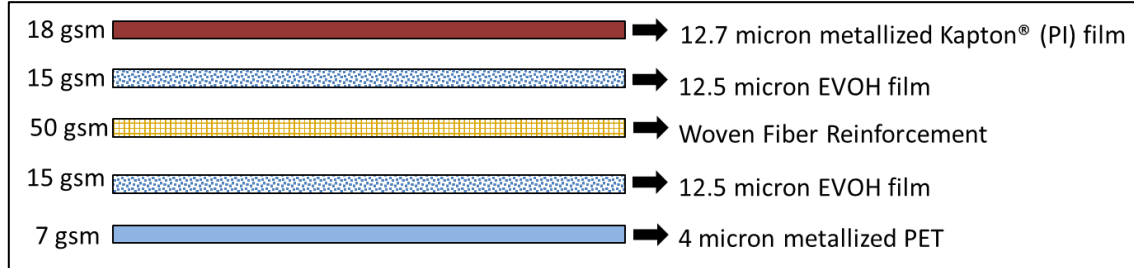


Figure A.6. Schematic design of laminate prototype P9

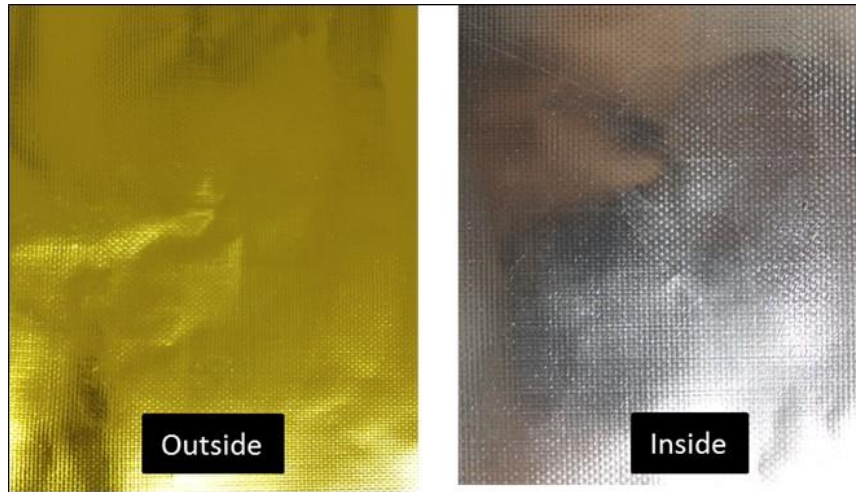


Figure A.7. Outside and inside of laminate prototype P9

The schematic design of laminate prototype P10 (shown in Figure A.8) uses an unbalanced woven fabric as the FR. Unlike the prototype P9, prototype P10 uses woven fabric with low twist and non-twisted 99 *denier* Zylon® yarns in warp and weft directions, respectively. The basis weight of the fabric is 50 *gsm* with yarn density of 40 *ypi* in warp direction and 75 *ypi* in weft direction. The higher *ypi* in the weft direction is expected to form a more stable fabric structure with smoother surface texture. In the initial trials, lamination temperature of 175 °C was used, however, this resulted in poor lamination quality with weak adhesion of the metallized PI film. Increasing the lamination temperature to 178 °C improved the lamination quality, but the adhesion was not as good as prototype P9. The estimated

and measured weight of this laminate prototype were found to 105 gsm. Images of outside and inside of the laminate prototype P10 is shown in Figure A.9.

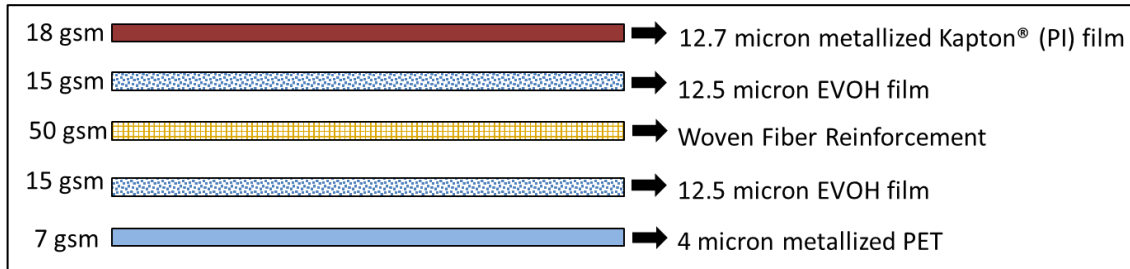


Figure A.8. Schematic design of laminate prototype P10



Figure A.9. Outside and inside of laminate prototype P10

A.4 Characterizations

A.4.1 Laminate Tensile Strength

The warp and weft direction tensile strength of laminate prototypes P4, P9, and P10 are shown in Table A.1. Three specimens of each prototype (except P10) were tested in the warp and weft direction.

Table A.1 Tensile Strength of laminate prototypes P4, P9, and P10

Laminate Prototype	Laminate Weight, gsm	Tensile Strength, N/cm				Tensile Strength, gf/denier				Elongation% @ break			
		Warp		Weft		Warp		Weft		Warp		Weft	
		Avg.	cv%	Avg.	cv%	Avg.	cv%	Avg.	cv%	Avg.	cv%	Avg.	cv%
P4	103	945.4	5.5	507.8	7.9	32.1	5.7	35.3	5.0	3.17	7.3	2.91	5.0
P9	105	486.9	6.0	970.8	3.7	32.0	5.5	32.9	4.5	3.01	7.8	3.29	8.8
P10	105	476.8	-	956.4	-	30.7	-	33.3	-	2.68	-	3.41	-

The estimated tensile strengths (calculated based on the yarn strength and fiber reinforcement construction parameters) are 1033 N/cm and 516 N/cm in the two directions. The measured tensile strength of the prototypes is slightly lower than the estimated values. The lower tensile strengths compared to the estimated tensile strength is attributed to manual preparation of laminate prototypes which causes (a) lack of complete alignment of yarns and (b) non-uniform tension in the yarns. These imperfections result in non-uniform load sharing among the load-bearing yarns which ultimately causes pre-mature rupture of specimens during the tensile test.

A comparison of the strength and weight of the new laminate prototypes and laminate materials developed in other studies in the literature is shown in Figure A.10. Comparison of strength-to-weight ratio of the new laminate with the laminates developed by other studies is shown in Figure A.11. The new laminate prototypes are not only significantly lighter than any other laminates with similar tensile strength, but also significantly stronger than any laminate with the similar weight. The strength-to-weight ratios of the new laminate prototypes are higher than all the laminates developed in other studies.

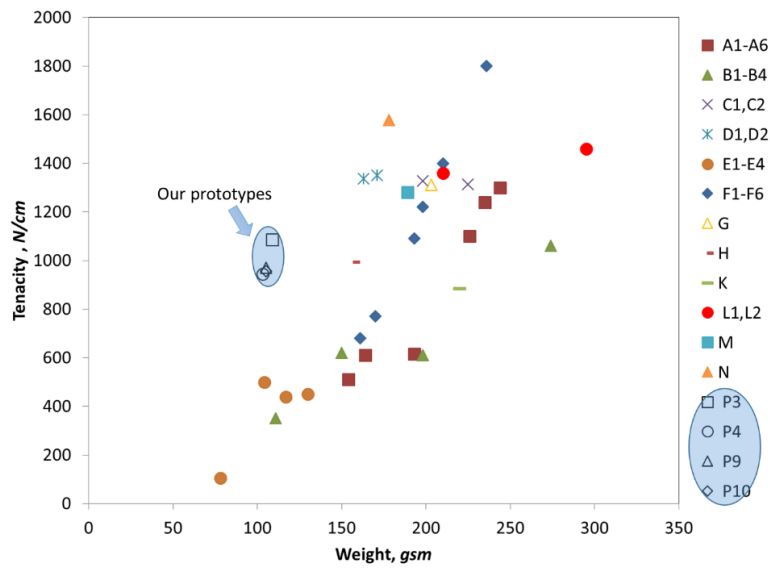


Figure A.10. Comparison of the strength and weight of the new laminate prototypes and laminate materials developed in other studies

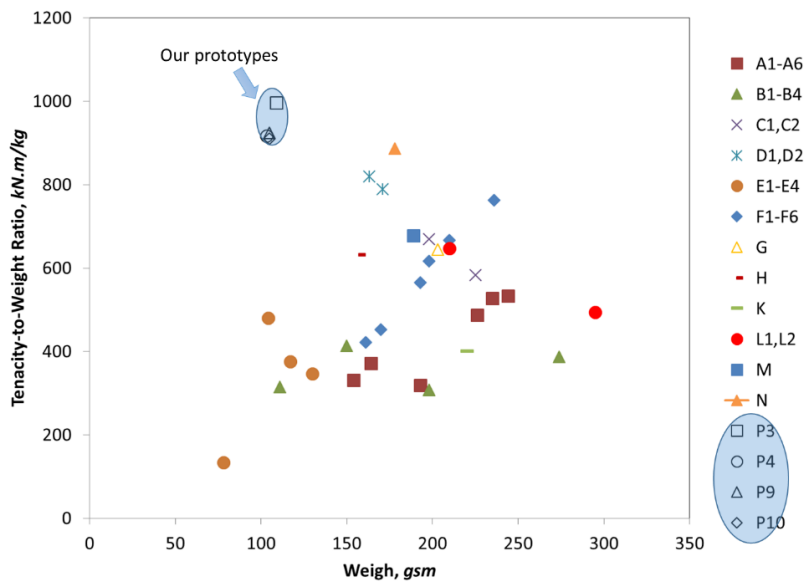


Figure A.11. Comparison of the strength-to-weight ratio of the new laminate prototypes and laminate materials developed in other studies

A.4.1.1 Effect of Thermal and UV Weathering

Laminate prototypes P4, P9, and P10 were subjected to two different weathering conditions. In one weathering exposure the prototypes were subjected to thermal exposure for

24 hrs in an oven at 80 °C. The other weathering exposure involved the accelerated exposure to UV and Visible light (UV-Vis) spectrum of ~275 to 700 nm for a duration of 170 hrs (~ 60 days of real time exposure at an altitude of 10 km). The prototypes were exposed in an Atlas Ci 3000+ Weather-Ometer with the irradiance level of 1.1 Watts/m² @ 340 nm. During the UV-Vis weathering, the temperature of the prototypes was maintained at about 80 °C. For UV-Vis weathering the specimens were mounted on metal frames and the inner side (Mylar® side) of the samples was covered with two layers of black card paper to prevent any exposure to the inner side (Figure A.12). The frames were then mounted on round rails inside the weathering chamber of Atlas Ci 3000+ Weather-Ometer such that the outside of the specimens was facing towards the UV and visible light source as shown in Figure A.13.

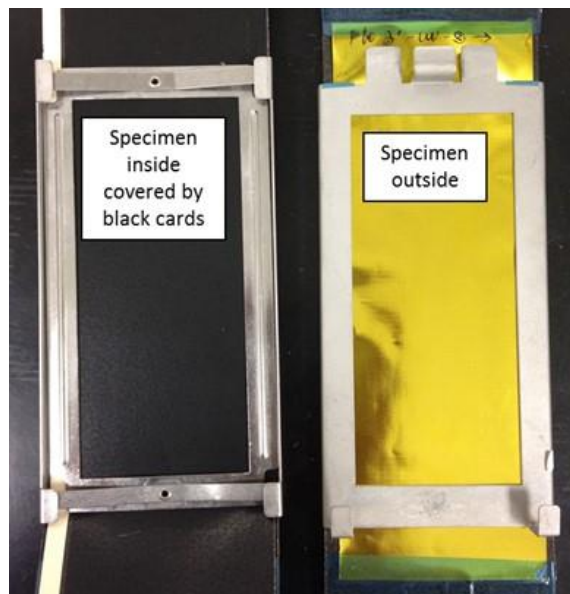


Figure A.12. Specimens mounted on metal frames for UV-Vis weathering

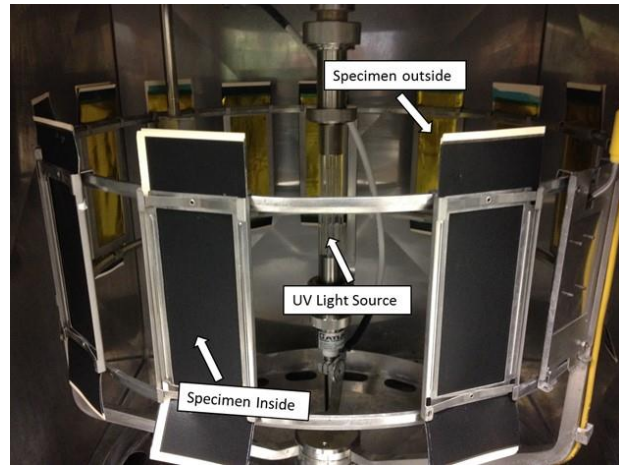


Figure A.13. Specimen frames mounted inside the weathering chamber of Atlas Ci 3000+ Weather-Ometer

A graphical comparison of tensile strengths of prototypes P4, P9, and P10 before and after thermal exposure and UV-Vis weathering is shown in Figure A.14. Strength loss % in prototypes P4, P9 and P10 after thermal exposure and accelerated UV-Vis weathering is shown in Figure A.15. The average tensile strength before and after thermal exposure and UV-Vis weathering were found to be statistically same (statistical analysis was performed suing t-test at 95% confidence level). It can therefore be concluded that there is negligible degradation caused by thermal and UV-Vis weathering.

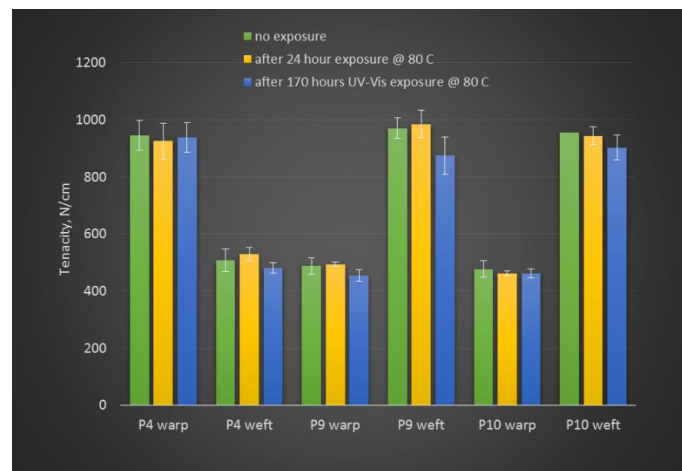


Figure A.14. Comparison of tensile strength of prototypes before and after thermal exposure and accelerated UV-Vis weathering

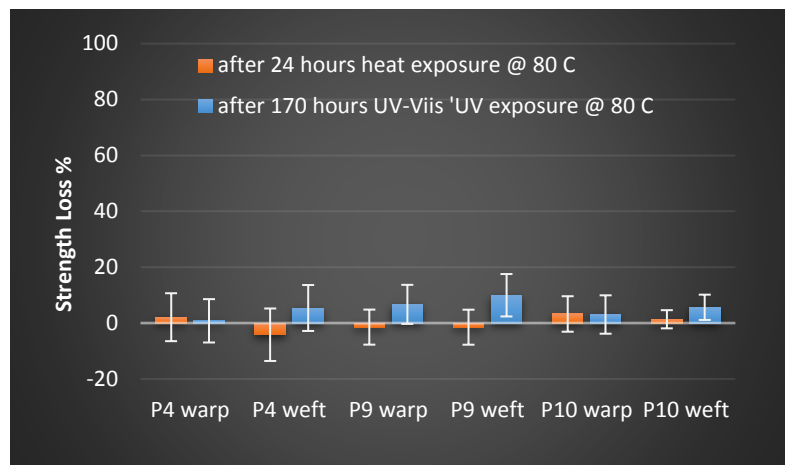


Figure A.15. Strength loss after thermal exposure and accelerated UV-Vis weathering

A.4.2 Laminate Tear Strength

Tear strength of a specimen was calculated by averaging the 5 highest peak loads during a tear test (as shown in Figure A.16). Three specimens per sample were tested in warp and weft directions. The tear strength results of prototype P4 and P9 are shown in Table A.2.

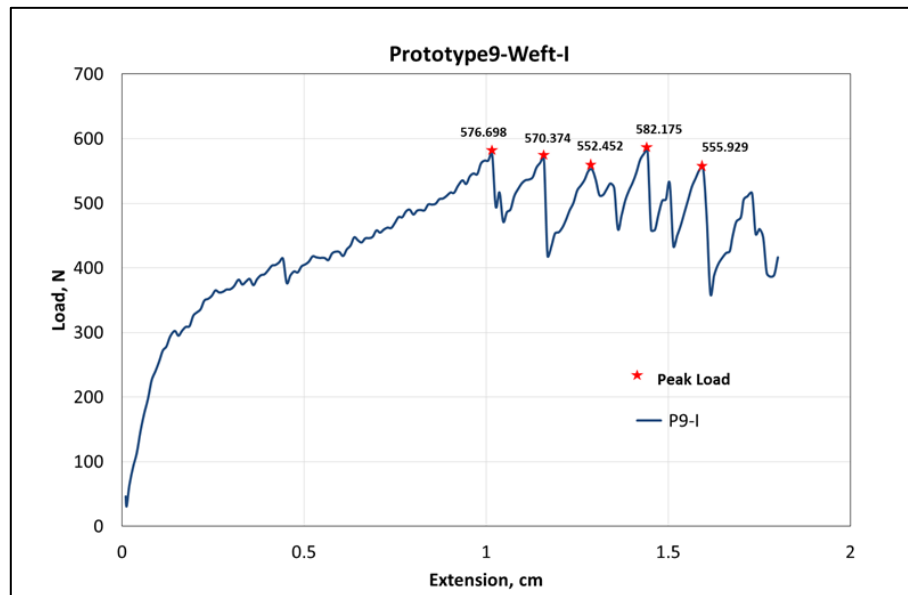


Figure A.16. Example of cut-slit tear test load-displacement curve (prototype P9 weft)

Table A.2 Tear Strength of laminate prototypes P4 and P9

Laminate Prototype	Tear Strength, N			
	Warp		Weft	
	Avg.	cv%	Avg.	cv%
P4	330.7	9.5	403.5	9.7
P9	290.0	6.6	533.7	5.2

The reason for the higher tear in warp direction of prototype P4 compared to prototype P9 is due to the difference in warp yarn linear density used to construct the two structures. In prototype P4, 250 *denier* yarns was used while in prototype P9, 99 *denier* was used. It is well established in the literature that the tear load increases by increasing the yarn breaking load.

A.4.3 Laminate Creep Resistance

A 2.54 cm wide specimen of prototype P4 was subject to a constant load of 1250 N for a duration of 1 day on a MTS load frame (running in load control mode). The gauge length of the test specimen was 7.62 cm (3 inch). The load and displacement curve of the test is shown in Figure A.17. After an instantaneous extension of 1.6%, the P4 specimen showed a very small creep extension of 0.02%.

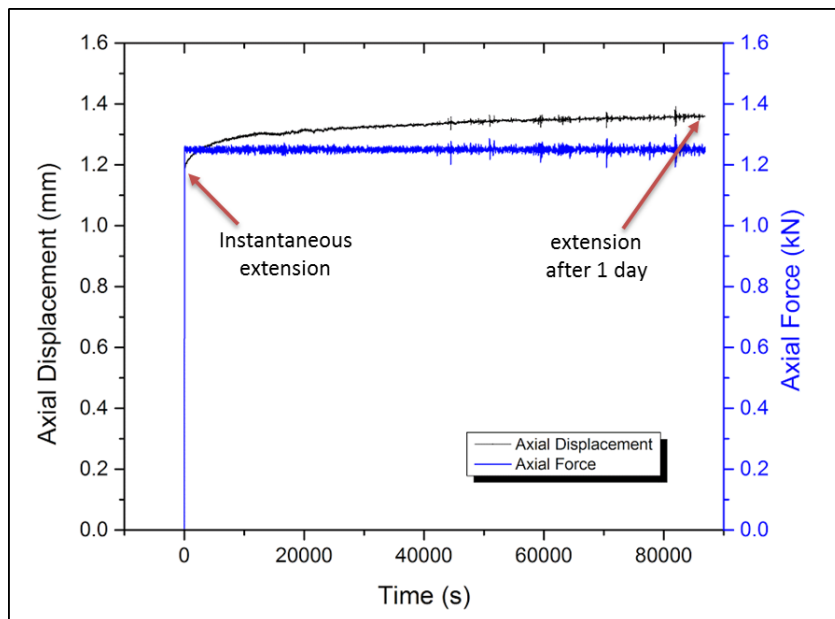


Figure A.17. Load-displacement curve of prototype subjected to a constant load of 1250 N

A.4.4 Helium permeation

Helium permeability test results (Table A.3) shows that while both the laminate prototypes P3 and P4 have much lower helium permeability than the target value of $80 \text{ cc}/\text{m}^2.24\text{h}.0.1\text{MPa}$ (provided by SCEYE S.A.), laminate prototype P4 has significantly lower helium permeability compared to that of prototype P3. The lower permeability of prototype P4 is attributed to the presence of the metallized Mylar® layer which also reduced the overall weight of the prototype P4. Given the same layering schemes, helium permeability values of prototypes P9 and P10 are expected to be same as that of prototype P4.

Table A.3 Helium permeability of laminate prototype P3 and P4

Laminate Prototype	Laminate Weight, gsm	Gas (He) Permeability, $\text{cc}/\text{m}^2.24\text{h}.0.1\text{MPa}$
P3	109	23
P4	103	8

Helium Permeation Modification

To make new laminate with improved helium permeation performance, one extra layer of VDA coating was added to the weathering layer, shown in Figure A.18.

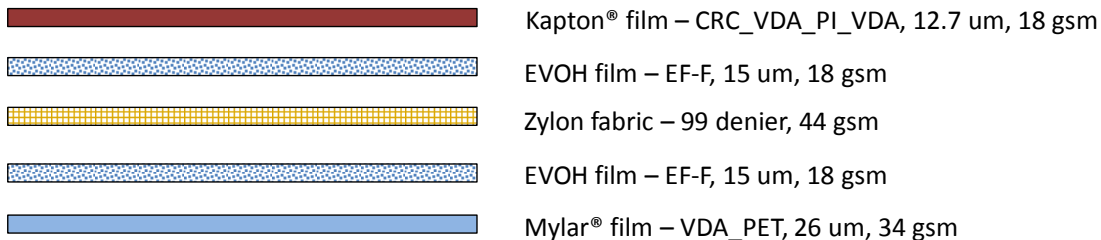


Figure A.18. Schematic design of modified laminate prototype.

The measured Helium permeability results of the modified laminate prototype is listed in Table A.4.

Table A.4 Helium Permeability of Modified Laminate Prototype.

Laminate ID	Laminate Weight, gsm	Gas (He) Transmission Rate, $cc/m^2 \cdot 24h \cdot 0.1MPa$
DL #1	132	0.64

It is apparent that the addition of an extra layer of VDA coating cause the helium gas transmission through the laminate structure to decrease an order of magnitude. Moreover, the extra layer of VDA coating toward the atmosphere can help to more effectively reflect the sun radiation. So, the surface temperature of hull material won't increase drastically and the strength of light-sensitive Zylon® fabric won't be easily degraded. However, the VDA coating when exposed to the stratosphere, will be attacked by Ozone and singlet oxygen. In order to prevent this layer of VDA coating being damaged, another layer of CRC coating which is anti-singlet oxygen, needs to be applied right over VDA coating. Therefore, the modified laminate structural design was determined to be optimal and was continued to be used for further study.

A.4.5 Ozone Resistance

Laminate samples were sent out to Akron Rubber Development Lab (ARDL) for Ozone resistance testing. The tests were performed according to ASTM D 1149-16, per Method B, procedure B1. Considering Ozone resistance performance of the laminate materials used on the airship, we decided to concentrate on the outmost layer (PI) which is in direct contact with the Ozone as well as the edges of the laminates due to the unavoidable exposure in the seamed areas. Therefore, the samples were partially masked using a type of special masking tape. According to the standard requirement of test specimens, rectangular strips 25 mm (1 inch) in width by 152.4 mm (6 inch) in length were precisely cut, masked and mounted onto a fixture made with Ozone resistant materials. The schematic of the sample set-up is shown in Figure A.19, where Sample #1 was masked on the Mylar surface as well as all the laminate edges while Sample #2 was intentionally masked on Mylar surface only to be able to expose the edges.

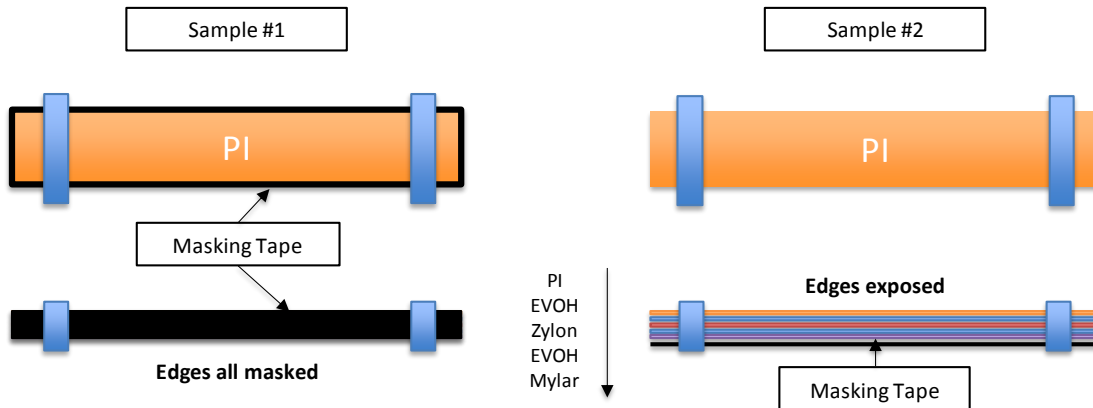


Figure A.19. The schematic of the sample set-up of Ozone resistance exposure testing.

The samples were exposed in the Ozone atmosphere for 72 hrs at an Ozone concentration of 500 *pphm* (parts per hundred million) and 70 °C. The Ozone concentration was selected as 500 *pphm* to more or less reflect what is at the stratosphere ranging from 200 to 800 *pphm*.

between about 20 to 40 kilometers. Observations were made during the testing at a frequency of 7x magnification, which is sufficient to detect the first appearance of ozone cracking. The sample weights before and after ozone aging were also measured to confirm the material degradation if there is any ozone etching occurred. The test results were shown in Table A.5, which apparently showing good ozone resistant performance of both samples. The testing results showed that the outmost PI film as well as the laminate edges survived from the ozone degradation even after a total of 216 *hrs* exposure. According to the before and after weights of the samples, there is no weight loss at all, demonstrating that no etching was happening on the PI surface and laminate edges. On the other hand, the ozone molecules were not able to cause internal damages of other components through the laminate edges, and delamination of the laminates were not observed after ozone aging.

Table A.5 Ozone resistance testing results

	Results	Weight before	Weight after	Pass/Fail
Sample #1*	No Cracks	0.95 g	0.95 g	Pass
Sample #2**	No Cracks	0.75 g	0.75 g	Pass

* All edges and Mylar side masked

** Only Mylar side masked, edges exposed

A.5 Summary

At this stage, it is safe to say that the laminate prototypes we developed have significantly superior properties compared to the current state-of-the-art materials. The new laminate prototypes are not only significantly lighter than any other laminates with similar tensile strength, but also significantly stronger than any laminate with the similar weight. The specific strength (strength-to-weight ratio) of the new laminate prototypes is significantly higher than

the current state-of-the-art. The laminates prototypes also have excellent resistance to thermal degradation, photo and ozone degradation, outstanding gas barrier properties, and excellent resistance to creep elongation.

Appendix B Statistical analysis of laminate tensile test in warp direction for lamination parametric study

Table B.6 Between subject-effects on tensile strength – Analysis of Variance

Source	DF	Sum of Squares	Mean Square	F Ratio	Prob > F
Model	11	11774.755	1070.43	1.0403	0.4238
Error	60	61735.127	1028.92		
C. Total	71	73509.882			

Table B.7 Between subject-effects on tensile strength – Effect Tests

Source	Nparm	DF	Sum of Squares	F Ratio	Prob > F
Temperature, C	2	2	686.5925	0.3336	0.7176
Dwell Time, s	1	1	1.626	0.0016	0.9684
Temperature, C*Dwell Time, s	2	2	2434.897	1.1832	0.3133
Fabric	1	1	243.9841	0.2371	0.6281
Temperature, C*Fabric	2	2	2611.4565	1.269	0.2885
Dwell Time, s*Fabric	1	1	3722.9821	3.6183	0.0619
Temperature, C*Dwell Time, s*Fabric	2	2	2073.2173	1.0075	0.3712

Table B.8 ANOVA of fabric effect on tensile strength

Source	DF	Sum of Squares	Mean Square	F Ratio	Prob > F
Fabric	1	243.984	243.98	0.2331	0.6307
Error	70	73265.898	1046.66		
C. Total	71	73509.882			

Table B.9 Means for one-way ANOVA – Estimates of fabric effect on tensile strength

Level	Number	Mean	Std Error	Lower 95%	Upper 95%
TT	36	708.132	5.392	697.38	718.89
FY	36	711.814	5.392	701.06	722.57

Table B.10 Tukey-Kramer HSD post hoc test of fabric effect on tensile strength

Level		Mean
FY	A	711.81389
TT	A	708.13222

Table B.11 ANOVA of temperature effect on tensile strength

Source	DF	Sum of Squares	Mean Square	F Ratio	Prob > F
Temperature, C	2	686.593	343.3	0.3253	0.7234
Error	69	72823.289	1055.41		
C. Total	71	73509.882			

Table B.12 Calculated means for one-way ANOVA – Estimates of temperature effect on tensile strength

Level	Number	Mean	Std Error	Lower 95%	Upper 95%
185	24	710.581	6.6314	697.35	723.81
200	24	705.924	6.6314	692.69	719.15
215	24	713.414	6.6314	700.18	726.64

Table B.13 Tukey-Kramer HSD post hoc test of temperature effect on tensile strength

Level		Mean
215	A	713.41417
185	A	710.58125
200	A	705.92375

Table B.14 ANOVA of dwell time effect on tensile strength

Source	DF	Sum of Squares	Mean Square	F Ratio	Prob > F
Dwell Time, s	1	1.626	1.63	0.0015	0.9687
Error	70	73508.26	1050.12		
C. Total	71	73509.88			

Table B.15 Calculated means for one-way ANOVA – Estimates of dwell time effect on tensile strength

Level	Number	Mean	Std Error	Lower 95%	Upper 95%
2.1	36	710.123	5.4009	699.35	720.9
3.5	36	709.823	5.4009	699.05	720.59

Table B.16 Tukey-Kramer HSD post hoc test of dwell time effect on tensile strength

Level		Mean
2.1	A	710.1233
3.5	A	709.8228

Table D.17 ANOVA of simple effects on tensile strength

Source	DF	Sum of Squares	Mean Square	F Ratio	Prob > F
Model	11	11774.76	1070.43	1.0403	0.4238
Error	60	61735.13	1028.92		
C. Total	71	73509.88			

Table D.18 Tukey-Kramer HSD post hoc test of simple effects on tensile strength

	Level		Least Sq Mean	SE	Lower 95%	Upper 95%
1	185,2,1,TY	A	721.9650	13.0953	695.7705	748.1595
2	185,2,1,FY	A	696.9583	13.0953	670.7639	723.1528
3	185,3,5,TY	A	710.8817	13.0953	684.6872	737.0761
4	185,3,5,FY	A	712.5200	13.0953	686.3255	738.7145
5	200,2,1,TY	A	712.1467	13.0953	685.9522	738.3411
6	200,2,1,FY	A	715.3450	13.0953	689.1505	741.5395
7	200,3,5,TY	A	694.7033	13.0953	668.5089	720.8978
8	200,3,5,FY	A	701.5000	13.0953	675.3055	727.6945
9	215,2,1,TY	A	712.3083	13.0953	686.1139	738.5028
10	215,2,1,FY	A	702.0167	13.0953	675.8222	728.2111
11	215,3,5,TY	A	696.7883	13.0953	670.5939	722.9828
12	215,3,5,FY	A	742.5433	13.0953	716.3489	768.7378

Appendix C Statistical analysis of laminate tensile test in weft direction for lamination parametric study

Table C.1 Between subject-effects on tensile strength – Analysis of Variance

Source	DF	Sum of Squares	Mean Square	F Ratio	Prob > F
Model	11	23167.78	2106.16	2.269	0.0217
Error	60	55694.426	928.24		
C. Total	71	78862.206			

Table C.2 Between subject-effects on tensile strength – Effect Tests

Source	Nparm	DF	Sum of Squares	F Ratio	Prob > F
Temperature, C	2	2	2556.8905	1.3773	0.2601
Dwell Time, s	1	1	5955.2241	6.4156	0.0139
Temperature, C*Dwell Time, s	2	2	334.5883	0.1802	0.8355
Fabric	1	1	645.7819	0.6957	0.4075
Temperature, C*Fabric	2	2	6723.7742	3.6218	0.0327
Dwell Time, s*Fabric	1	1	142.4391	0.1535	0.6966
Temperature, C*Dwell Time, s*Fabric	2	2	6809.0816	3.6677	0.0314

Table C.3 ANOVA of fabric effect on tensile strength

Source	DF	Sum of Squares	Mean Square	F Ratio	Prob > F
Fabric	1	645.782	645.78	0.5779	0.4497
Error	70	78216.424	1117.38		
C. Total	71	78862.206			

Table C.4 Calculated means for one-way ANOVA – Estimates of fabric effect on tensile strength

Level	Number	Mean	Std Error	Lower 95%	Upper 95%
TT	36	717.743	5.5712	706.63	728.85
FY	36	711.753	5.5712	700.64	722.86

Table C.5 Tukey-Kramer HSD post hoc test of fabric effect on tensile strength

Level		Mean
TT	A	717.7425
FY	A	711.75278

Table C.6 ANOVA of temperature effect on tensile strength

Source	DF	Sum of Squares	Mean Square	F Ratio	Prob > F
Temperature, C	2	2556.891	1278.45	1.156	0.3207
Error	69	76305.315	1105.87		
C. Total	71	78862.206			

Table C.7 Calculated means for one-way ANOVA – Estimates of temperature effect on tensile strength

Level	Number	Mean	Std Error	Lower 95%	Upper 95%
185	24	709.398	6.7881	695.86	722.94
200	24	723.062	6.7881	709.52	736.6
215	24	711.783	6.7881	698.24	725.32

Table C.8 Tukey-Kramer HSD post hoc test of temperature effect on tensile strength

Level		Mean
200	A	723.06208
215	A	711.7825
185	A	709.39833

Table C.9 ANOVA of dwell time effect on tensile strength

Source	DF	Sum of Squares	Mean Square	F Ratio	Prob > F
Dwell Time, s	1	5955.224	5955.22	5.7178	0.0195
Error	70	72906.98	1041.53		
C. Total	71	78862.21			

Table C.10 Calculated means for one-way ANOVA – Estimates of dwell time effect on tensile strength

Level	Number	Mean	Std Error	Lower 95%	Upper 95%
2.1	36	705.653	5.3788	694.93	716.38
3.5	36	723.842	5.3788	713.11	734.57

Table C.11 Tukey-Kramer HSD post hoc test of dwell time effect on tensile strength

Level			Mean
3.5	A		723.8422
2.1		B	705.6531

Table C.12 ANOVA of simple effects on tensile strength

Source	DF	Sum of Squares	Mean Square	F Ratio	Prob > F
Model	11	23167.78	2106.16	2.269	0.0217
Error	60	55694.43	928.24		
C. Total	71	78862.21			

Table C.13 Tukey-Kramer HSD post hoc test of simple effects on tensile strength

	Level		Least Sq Mean	SE	Lower 95%	Upper 95%
1	185,2,1,TY	AB	721.0117	12.4381	696.1317	745.8916
2	185,2,1,FY	B	675.6250	12.4381	650.7451	700.5049
3	185,3,5,TY	AB	725.9900	12.4381	701.1101	750.8699
4	185,3,5,FY	AB	714.9667	12.4381	690.0867	739.8466
5	200,2,1,TY	AB	725.2633	12.4381	700.3834	750.1433
6	200,2,1,FY	AB	700.6500	12.4381	675.7701	725.5299
7	200,3,5,TY	AB	729.5333	12.4381	704.6534	754.4133
8	200,3,5,FY	A	736.8017	12.4381	711.9217	761.6816
9	215,2,1,TY	AB	683.8883	12.4381	659.0084	708.7683
10	215,2,1,FY	AB	727.4800	12.4381	702.6001	752.3599
11	215,3,5,TY	AB	720.7683	12.4381	695.8884	745.6483
12	215,3,5,FY	AB	714.9933	12.4381	690.1134	739.8733

Appendix D Statistical analysis of T-peel test for lamination parametric study

Table D.1 Between subject-effects on peel strength – Analysis of Variance

Source	DF	Sum of Squares	Mean Square	F Ratio	Prob > F
Model	11	0.3858246	0.035075	2.6102	0.0108
Error	48	0.6450024	0.013438		
C. Total	59	1.030827			

Table D.2 Between subject-effects on peel strength – Effect Tests

Source	Nparm	DF	Sum of Squares	F Ratio	Prob > F
Temperature, C	2	2	0.10714493	3.9868	0.025
Dwell Time, s	1	1	0.01488375	1.1076	0.2979
Temperature, C*Dwell Time, s	2	2	0.0894348	3.3278	0.0443
Fabric	1	1	0.03845602	2.8618	0.0972
Temperature, C*Fabric	2	2	0.10858413	4.0403	0.0239
Dwell Time, s*Fabric	1	1	0.00257415	0.1916	0.6636
Temperature, C*Dwell Time, s*Fabric	2	2	0.0247468	0.9208	0.4051

Table D.3 ANOVA of fabric effect on peel strength

Source	DF	Sum of Squares	Mean Square	F Ratio	Prob > F
Fabric	1	0.038456	0.038456	2.2476	0.1392
Error	58	0.992371	0.01711		
C. Total	59	1.030827			

Table D.4 Means for one-way ANOVA – Estimates of fabric effect on peel strength

Level	Number	Mean	Std Error	Lower 95%	Upper 95%
TT	30	1.1587	0.02388	1.1109	1.2065
FY	30	1.20933	0.02388	1.1615	1.2571

Table D.5 Tukey-Kramer HSD post hoc test of fabric effect on peel strength

Level		Mean
FY	A	1.2093333
TT	A	1.1587

Table D.6 ANOVA of temperature effect on peel strength

Source	DF	Sum of Squares	Mean Square	F Ratio	Prob > F
Temperature, C	2	0.1071449	0.053572	3.3059	0.0438
Error	57	0.9236821	0.016205		
C. Total	59	1.030827			

Table D.7 Means for one-way ANOVA – Estimates of temperature effect on peel strength

Level	Number	Mean	Std Error	Lower 95%	Upper 95%
185	20	1.12805	0.02846	1.0711	1.185
200	20	1.23015	0.02846	1.1732	1.2871
215	20	1.19385	0.02846	1.1369	1.2508

Table D.8 Tukey-Kramer HSD post hoc test of temperature effect on peel strength

Level			Mean
215	A		1.23015
185	A	B	1.19385
200		B	1.12805

Table D.9 ANOVA of dwell time effect on peel strength

Source	DF	Sum of Squares	Mean Square	F Ratio	Prob > F
Dwell Time, s	1	0.0148837	0.014884	0.8497	0.3605
Error	58	1.0159432	0.017516		
C. Total	59	1.030827			

Table D.10 Means for one-way ANOVA – Estimates of dwell time effect on peel strength

Level	Number	Mean	Std Error	Lower 95%	Upper 95%
2.1	30	1.19977	0.02416	1.1514	1.2481
3.5	30	1.16827	0.02416	1.1199	1.2166

Table D.11 Tukey-Kramer HSD post hoc test of dwell time effect on peel strength

Level		Mean
2.1	A	1.1997667
3.5	A	1.1682667

Appendix E Statistical analysis of laminate tear test in warp direction for lamination parametric study

Table E.1 Between subject-effects on tear strength – Analysis of Variance

Source	DF	Sum of Squares	Mean Square	F Ratio	Prob > F
Model	11	1046629	95148	0.8402	0.6014
Error	60	6794784	113246		
C. Total	71	7841413			

Table E.2 Between subject-effects on tear strength – Effect Tests

Source	Nparm	DF	Sum of Squares	F Ratio	Prob > F
Temperature, C	2	2	195642.88	0.8638	0.4267
Dwell Time, s	1	1	46594.89	0.4114	0.5237
Temperature, C*Dwell Time, s	2	2	171069.27	0.7553	0.4743
Fabric	1	1	1.82	0	0.9968
Temperature, C*Fabric	2	2	46128.34	0.2037	0.8163
Dwell Time, s*Fabric	1	1	225852.48	1.9943	0.1631
Temperature, C*Dwell Time, s*Fabric	2	2	361339.35	1.5954	0.2113

Table E.3 ANOVA of fabric effect on tear strength

Source	DF	Sum of Squares	Mean Square	F Ratio	Prob > F
Fabric	1	1.8	1.82405	0	0.9968
Error	70	7841411.2	112020		
C. Total	71	7841413			

Table E.4 Means for one-way ANOVA – Estimates of fabric effect on tear strength

Level	Number	Mean	Std Error	Lower 95%	Upper 95%
TT	36	736.881	55.782	625.63	848.14
FY	36	736.563	55.782	625.31	847.82

Table E.5 Tukey-Kramer HSD post hoc test of fabric effect on tear strength

Level		Mean
FY	A	736.88111
TT	A	736.56278

Table E.6 ANOVA of temperature effect on tear strength

Source	DF	Sum of Squares	Mean Square	F Ratio	Prob > F
Temperature, C	2	195642.9	97821	0.8828	0.4182
Error	69	7645770.1	110808		
C. Total	71	7841413			

Table E.7 Means for one-way ANOVA – Estimates of temperature effect on tear strength

Level	Number	Mean	Std Error	Lower 95%	Upper 95%
185	24	700.633	67.949	565.08	836.19
200	24	810.436	67.949	674.88	945.99
215	24	699.097	67.949	563.54	834.65

Table E.8 Tukey-Kramer HSD post hoc test of temperature effect on tear strength

Level		Mean
215	A	810.4358
185	A	700.6333
200	A	699.0967

Table E.9 ANOVA of dwell time effect on tear strength

Source	DF	Sum of Squares	Mean Square	F Ratio	Prob > F
Dwell Time, s	1	46594.9	46595	0.4184	0.5198
Error	70	7794818.1	111355		
C. Total	71	7841413			

Table E.10 Means for one-way ANOVA – Estimates of dwell time effect on tear strength

Level	Number	Mean	Std Error	Lower 95%	Upper 95%
2.1	36	711.283	55.616	600.36	822.21
3.5	36	762.161	55.616	651.24	873.08

Table E.11 Tukey-Kramer HSD post hoc test of dwell time effect on tear strength

Level		Mean
2.1	A	762.16111
3.5	A	711.28278

Appendix F Statistical analysis of laminate tear test in weft direction for lamination parametric study

Table F.1 Between subject-effects on tear strength – Analysis of Variance

Source	DF	Sum of Squares	Mean Square	F Ratio	Prob > F
Model	11	4175262	379569	3.6093	0.0006
Error	59	6204698	105164		
C. Total	70	10379960			

Table F.2 Between subject-effects on tear strength – Effect Tests

Source	Nparm	DF	Sum of Squares	F Ratio	Prob > F
Temperature, C	2	2	1047019.3	4.978	0.0101
Dwell Time, s	1	1	472330.8	4.4914	0.0383
Temperature, C*Dwell Time, s	2	2	623595.6	2.9649	0.0593
Fabric	1	1	831965.7	7.9111	0.0067
Temperature, C*Fabric	2	2	114613.3	0.5449	0.5828
Dwell Time, s*Fabric	1	1	4655.7	0.0443	0.8341
Temperature, C*Dwell Time, s*Fabric	2	2	1031994.5	4.9066	0.0107

Table F.3 ANOVA of fabric effect on tear strength

Source	DF	Sum of Squares	Mean Square	F Ratio	Prob > F
Fabric	1	845169	845169	6.1162	0.0159
Error	69	9534791	138185		
C. Total	70	10379960			

Table F.4 Means for one-way ANOVA – Estimates of fabric effect on tear strength

Level	Number	Mean	Std Error	Lower 95%	Upper 95%
TT	35	807.214	62.834	681.86	932.57
FY	36	588.983	61.955	465.39	712.58

Table F.5 Tukey-Kramer HSD post hoc test of fabric effect on tear strength

Level			Mean
FY	A		807.214
TT		B	588.98333

Table F.6 ANOVA of temperature effect on tear strength

Source	DF	Sum of Squares	Mean Square	F Ratio	Prob > F
Temperature, C	2	1112723	556362	4.0824	0.0212
Error	68	9267237	136283		
C. Total	70	10379960			

Table F.7 Means for one-way ANOVA – Estimates of temperature effect on tear strength

Level	Number	Mean	Std Error	Lower 95%	Upper 95%
185	23	540.993	76.976	387.39	694.6
200	24	848.748	75.356	698.38	999.12
215	24	693.462	75.356	543.09	843.83

Table F.8 Tukey-Kramer HSD post hoc test of temperature effect on tear strength

Level			Mean
215	A		848.74833
185	A	B	693.46167
200		B	540.99348

Table F.9 ANOVA of dwell time effect on tear strength

Source	DF	Sum of Squares	Mean Square	F Ratio	Prob > F
Dwell Time, s	1	477471	477471	3.327	0.0725
Error	69	9902489	143514		
C. Total	70	10379960			

Table F.10 Means for one-way ANOVA – Estimates of dwell time effect on tear strength

Level	Number	Mean	Std Error	Lower 95%	Upper 95%
2.1	36	615.703	63.139	489.74	741.66
3.5	35	779.731	64.034	651.99	907.48

Table F.11 Tukey-Kramer HSD post hoc test of dwell time effect on tear strength

Level		Mean
2.1	A	779.73086
3.5	A	615.70306

Appendix G Statistical analysis of varied laminate adhesion levels for lamination parametric study

Table G.1 Chi-Square test for correlation of adhesion level and fabrics

Test	ChiSquare	Prob>ChiSq
Likelihood Ratio	29.743	<.0001
Pearson	25.742	<.0001

Table G.2 Chi-Square test for correlation of adhesion level and temperature

Test	ChiSquare	Prob>ChiSq
Likelihood Ratio	22.394	0.0042
Pearson	20.417	0.0089

Table G.3 Chi-Square test for correlation of adhesion level and dwell time

Test	ChiSquare	Prob>ChiSq
Likelihood Ratio	4.467	0.3465
Pearson	4.415	0.3528

Appendix H Statistical analysis of peel strength for seaming parametric study

Table H.1 Between subject-effects on seam peel strength – Analysis of Variance

Source	DF	Sum of Squares	Mean Square	F Ratio	Prob > F
Model	3	18.715701	6.23857	2.0077	0.1453
Error	20	62.145169	3.10726		
C. Total	23	80.86087			

Table H.2 ANOVA of temperature effect on seam peel strength

Source	DF	Sum of Squares	Mean Square	F Ratio	Prob > F
Temperature, C	1	8.232201	8.2322	2.4936	0.1286
Error	22	72.62867	3.3013		
C. Total	23	80.86087			

Table H.3 Calculated means for one-way ANOVA – Estimates of temperature effect on seam peel strength

Level	Number	Mean	Std Error	Lower 95%	Upper 95%
150	12	7.43723	0.52451	6.3495	8.525
180	12	6.26589	0.52451	5.1781	7.3537

Table H.4 Tukey-Kramer HSD post hoc test of temperature effect on seam peel strength

Level		Least Sq Mean
150	A	7.437227
180	A	6.265888

Table H.5 ANOVA of seaming pressure effect on seam peel strength

Source	DF	Sum of Squares	Mean Square	F Ratio	Prob > F
Pressure, KPa	1	10.302841	10.3028	3.2124	0.0868
Error	22	70.558029	3.2072		
C. Total	23	80.86087			

Table H.6 Means for one-way ANOVA – Estimates of seaming pressure effect on seam peel strength

Level	Number	Mean	Std Error	Lower 95%	Upper 95%
100	12	7.50676	0.51698	6.4346	8.5789
400	12	6.19636	0.51698	5.1242	7.2685

Table H.7 Tukey-Kramer HSD post hoc test of seaming pressure effect on peel strength of the seams

Level		Least Sq Mean
100	A	7.5067559
400	A	6.1963589

Table H.8 ANOVA of seaming speed effect on seam peel strength

Source	DF	Sum of Squares	Mean Square	F Ratio	Prob > F
Speed, <i>m/min</i>	1	0.180659	0.18066	0.0493	0.8264
Error	22	80.680211	3.66728		
C. Total	23	80.86087			

Table H.9 Means for one-way ANOVA – Estimates of seaming speed effect on seam peel strength

Level	Number	Mean	Std Error	Lower 95%	Upper 95%
3	12	6.7648	0.55282	5.6183	7.9113
6	12	6.93832	0.55282	5.7918	8.0848

Table H.10 Tukey-Kramer HSD post hoc test of seaming speed effect on peel strength of the seams

Level		Least Sq Mean
6	A	6.9383183
3	A	6.7647965

Appendix I Statistical analysis of tensile strength of butt seams with different seam configurations

Table I.1 ANOVA of seaming speed effect on seam peel strength

Source	DF	Sum of Squares	Mean Square	F Ratio	Prob > F
Underlap, cm	2	8337.657	4168.83	5.5342	0.0434
Error	6	4519.668	753.28		
C. Total	8	12857.325			

Table I.2 Tukey-Kramer HSD post hoc test of seaming speed effect on seam peel strength

Level			Least Sq Mean
3.81	A		757.973
7.62	A	B	746.19967
0		B	688.33